UNIVERSITY OF LEEDS

The circumstellar matter distribution of massive young stellar objects

Fernando Andres Olguin Choupay

School of Physics and Astronomy

University of Leeds

Submitted in accordance with
the requirements for the degree of

Doctor of Philosophy

December 2016

The candidate confirms that the work submitted is his own, except where work which has formed part of jointly authored publications has been included. The contribution of the candidate and the other authors of this work has been explicitly indicated. The candidate confirms that appropriate credit has been given within this thesis where reference has been made to the work of others.

Preface

This thesis presents include text published in the following papers:

I. "*Herschel* Hi-GAL imaging of massive young stellar objects" – **F. A. Olguin**, M. G. Hoare, H. E. Wheelwright, S. J. Clay, W.-J. de Wit, I. Rafiq, S. Pezzuto, S. Molinari, 2015, MNRAS, 449, 2784.

For paper I, the author obtained the results and wrote the results, discussion and conclusion sections. The author commented in the other sections and made the figures, as such part of the text was edited for this thesis. The text includes comments from the co-authors of the paper and the referee. This paper constitutes the Section 2 of this thesis.

Acknowledgements

First and foremost, I would like to thank my supervisor, Prof. Melvin Hoare, for giving me the opportunity to work on this research project and for being a constant source of support during my PhD. Most importantly, thanks for sharing all your knowledge on both star formation and ales. I would also like to thank Katharine Johnston for all the help on the final chapters of this thesis.

This PhD would not have been finished without all the good times I had with my office mates. Thanks to Karim Ababakr and Jacob Close for the day to day conversations and coffee time games. Special thanks go to: Simon Purser, Robert Pomohaci, Marc Evans and Harrison Steggles, for all the fun times and the discussions about science and life. To all the people left out of this list, thanks for sharing your time with me and making Leeds a great place to study.

Finally, I would like to thank my family for supporting me in the distance. In particular, thanks to Laura, Fernando and Alicia for keeping me update, and my grandparents for all the support.

Abstract

A multiwavelength study of the circumstellar matter distribution of massive young stellar objects (MYSOs) was conducted. First, the potential of the new *Herschel* 70 μm data to resolve MYSOs in the Hi-GAL survey was analysed. These data have the highest resolution achieved at far infrared wavelengths where the spectral energy distribution of MYSOs peaks. These data showed that relatively isolated sources with high $\sqrt{L}/d$, where L is the luminosity and d the distance of the source, are resolved at 70 μm. The analysis of these data and 1-D spherically symmetric radiative transfer modelling of three sources in the $l = 30^\circ$ and 59° fields showed that they have a shallower density power law index than expected for infalling material. This suggests that the far-IR emission may be dominated by warm dust from the outflow cavity walls rather than rotational flattening as suggested by earlier studies.

In order to explain the 70 μm observations, the circumstellar matter of the proto-typical MYSO AFGL 2591 was studied by utilising and modelling full resolution *Herschel* data from the HOBYS survey and other multi-wavelength dust continuum observations including high-resolution near-IR and mm interferometric data. A 2-D axi-symmetric radiative transfer model was used to find the density and temperature

distributions that better reproduce the observations. The model that best fits the continuum observations has a rotationally flattened envelope, paraboloidal outflow cavities and a flared disc with a mass of 1 $M_{\odot}$. As a result it was found that the extended emission observed at 70 μm can be explained in part by dust emission from the envelope outflow cavity walls. The modelling was able to reproduce most of the other multi-wavelength observations.

Finally, the velocity structure of gas in the envelope of AFGL 2591 was studied by modelling methyl cyanide observations in the CH_3CN J=12–11 transition at 1.3 mm. The transition K-ladder was fitted assuming a constant density and isothermal distribution of gas, and an excitation temperature ranging between 100-300 K was found. In addition, the first moment (velocity) maps are consistent with rotation of the inner envelope, and its linear velocity gradient is slower than the one observed at smaller scales. The radiative transfer modelling of the methyl cyanide data with a velocity structure of a rotating and infalling envelope suggests that rotation is faster than predicted by the model. This may be solved by magnetic fields transporting angular momentum from the accretion disc.

Abbreviations

AGB	Asymptotic Giant Branch
ALMA	Atacama Large Millimeter Array
APEX	Atacama Pathfinder Experiment
ATLASGAL	APEX Telescope Large Area Survey of the Galaxy
arcsec	Second of arc
au	Astronomical unit
CMB	Cosmic Microwave Background
CMF	Core Mass Function
FWHM	Full width at half-maximum
GLIMPSE	Galactic Legacy Infrared Mid-Plane Survey Extraordinaire
GMC	Giant Molecular Cloud
Hi-GAL	Herschel IR Galactic Plane Survey
HIFI	Heterodyne Instrument for the Far-IR
HOBYS	Herschel OB Young Stellar Objects Survey
HST	Hubble Space Telescope
IMF	Initial Mass Function
IR	Infrared
IRAC	Infrared Array Camera
IRDC	Infrared Dark Cloud
ISM	Interstellar Medium
JCMT	James Clerk Maxwell Telescope

LABOCA	Large APEX Bolometer Camera
LAMDA	Leiden Atomic and Molecular Database
LTE	Local Thermodynamic Equilibrium
mas	Milliarcsecond
MCMC	Markov Chain Monte Carlo
MIPS	Multiband Imaging Photometer
MYSO	Massive Young Stellar Object
MSX	Mid-course Space Experiment
NICMOS	Near IR Camera and Multi-object Spectrometer
NIRI	Near IR Imager
NOEMA	Northern Extended Millimeter Array
PACS	Photoconductor Array Camera and Spectrometer
PdBI	Plateau de Bure Interferometer
PDF	Probability Distribution Function
PN	Planetary Nebula
PSF	Point Spread Function
pv	Position-velocity
RMS	Red MSX Source
RT	Radiative Transfer
SAO	Special Astrophysical Observatory
SCUBA	Submillimetre Common-User Bolometer Array
SDP	Science Demonstration Phase
SED	Spectral Energy Distribution
SPIRE	Spectral and Photometric Imaging Receiver
submm	Submillimetre
UCH II	Ultra compact H II
UKIDSS	UKIRT Deep Sky Survey

UKIRT	United Kingdom IR Telescope
UV	Ultraviolet
VLA	Very Large Array
WFCAM	Wide Field Camera
ZAMS	Zero Age Main Sequence
2MASS	Two Micron All-Sky Survey

Contents

List of Figures

List of Tables

Chapter 1

Introduction

High-mass stars ($M > 8$ $M_{\odot}$; Zinnecker & Yorke 2007) play an important role in galaxy evolution. During the different stages of their lives, from their formation until they die, they are a source of feedback processes which modify the interstellar medium (ISM). Early in their formation, they can trigger star formation by compressing the ISM through outflows or restrict the formation of new stars by heating the matter in their natal clouds. Once formed, they become one of the main sources of ultraviolet (UV) photons, disrupting the ISM in their surroundings through winds. At the end of their lives, they explode as supernova which not only has the potential to trigger star formation, but it also enriches the ISM with heavy elements, which are then depleted into molecules and dust grains, thus providing material for the formation of new stars and planets.

However, the formation of high-mass stars is not understood as well as their low-mass counterparts. None of the theories proposed to explain the formation of high-mass stars have been proved so far, and several questions remain open. The main question that will be addressed in this thesis is whether or not massive

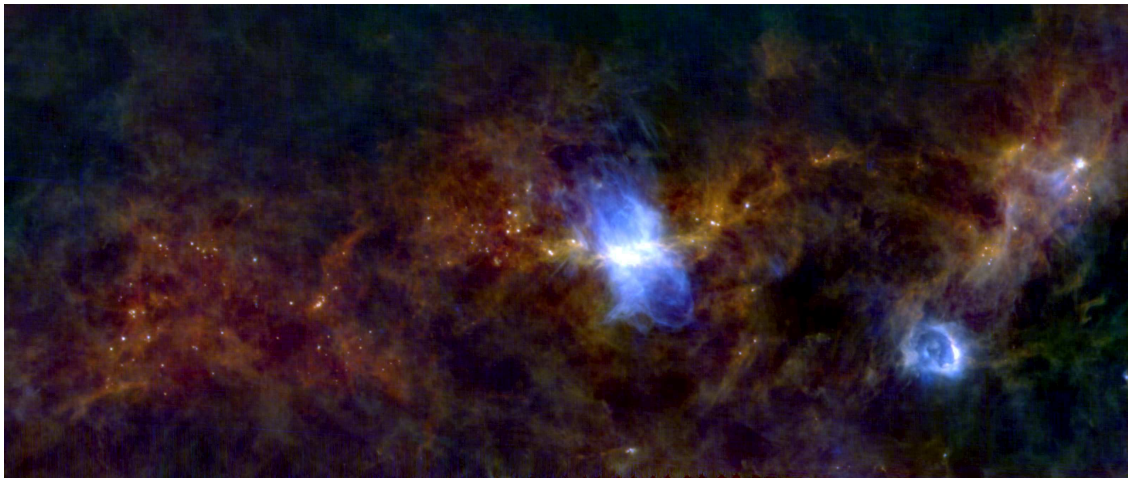

Figure 1.1: Three colour image of the Vela C molecular cloud as observed by *Herschel* at 70 (blue), 160 (green) and 250 μm (red) from Hill *et al.* (2011).

stars form as a scaled-up version of low-mass star formation.

1.1 Galactic high-mass star formation

1.1.1 Environmental properties

Massive stars form in the densest regions of giant molecular clouds (GMCs), which are large clouds of molecular gas and dust located in the spiral arms (e.g. Kolpak *et al.* 2003). Fig. 1.1 shows a colour image of the Vela C molecular cloud, where several sub-structures can be observed. These are the result of the gravitational collapse of the GMC, which forms the filamentary structure observed in the same figure. The physical conditions in these filaments allow the formation of clumps, which are in turn fragmented into cores. The typical physical conditions of GMCs, clumps and cores are listed in Table 1.1.

Clumps will likely form stellar clusters whereas cores will probably form a single or a multiple system (Williams *et al.* 2000). High-mass stars form in

Table 1.1: Average properties of GMCs, clumps and cores

Structure	Mass ($M_\odot$)	Size (pc)	T (K)	n (cm^{-3})
GMC	$10^4 - 10^6$	50	10	10^2
Clump	$10^3 - 10^5$	0.5	$10 - 20$	10^3
Core	$1 - 10^2$	$\leqslant 0.1$	$10 - 20$	10^5

References. Churchwell (2002), Williams *et al.* (2000), Mac Low & Klessen (2004), McKee & Ostriker (2007), Zinnecker & Yorke (2007).

dense and cold cores within clumps, thus most massive stars belong to larger associations or stellar clusters (e.g. Lada *et al.* 1991). Since massive stars form embedded in these structures, the radiation released during the gravitational collapse and later by the star is absorbed by dust and then re-emitted at longer wavelengths ($\lambda > 1$ μm).

Massive stars are also rare in comparison with low-mass stars. The amount of stars as a function of their mass, or initial mass function (IMF), can generally be described by several power laws (Kroupa 2001). For the high-mass end ($M_\star > 1$ $M_\odot$), the observed IMF function for field stars is $dN \propto M^{-2.3}\, dM$ (Salpeter 1955; Kroupa 2001). The physical mechanism by which this distribution is obtained it is still not well understood. However, the number of molecular cores relative to their masses, or core mass function (CMF), seems to resemble the IMF shape (e.g. Alves *et al.* 2007). Thus it has been proposed that the shape of the IMF may be determined by the fragmentation process, but this a subject of current debate (Offner *et al.* 2014).

Additionally, regions forming massive stars are generally located at larger distances than their low-mass counterparts. Therefore, the study of individual cores requires high-resolution observations in order to resolve them.

1.1.2 Observational stages

Different evolutionary stages of the clumps/cores are recognised from observations of high-mass star forming regions. Infrared dark clouds (IRDCs) are believed to be the earliest observable stage following the fragmentation of GMCs (e.g. Rathborne *et al.* 2006). These are infrared (IR) quiet and cold regions, with temperature distributions which decrease towards their densest regions (e.g Wilcock *et al.* 2011), and with sizes of clumps (Rathborne *et al.* 2006).

The loss of potential energy during the gravitational collapse of a core heats its gas and a proto-star is formed. This phase is known as the hot core phase (Kurtz *et al.* 2000). The core should flatten towards the mid-plane perpendicular to the rotation axis. This rotation is induced by the initial angular momentum of the parental material. The final result is the formation of a disc or disc-like structure (e.g. Cesaroni *et al.* 2005; Beltrán *et al.* 2006b) and release of the angular momentum through molecular outflows (e.g. Henning *et al.* 2000). In general, these outflows seem to be less collimated than their low-mass counterparts (e.g. Richer *et al.* 2000). However, Beuther *et al.* (2002b) obtained collimation ratios consistent with the low-mass star formation ones, and Arce *et al.* (2007) argue that the lower collimation ratios may be due to confusion along the line of sight because most high-mass star forming regions are located in crowded regions. Due to the high temperatures reached during the gravitational collapse (> 100 K), several molecular species are observed which are not observed at equivalent stages in low-mass star forming cores (van Dishoeck 2003).

Inflow and outflow processes during the formation of massive stars are driven by gravitational collapse, rotation, turbulence, magnetic fields and radiation. The

imprints left by these processes in the parental material can be well studied in early stages of massive young stellar objects (MYSOs), when the ionising nature of the star radiation has not started to dissipate the parental core, i.e. MYSOs are late hot cores. Hence MYSOs are a useful probe of the physical processes dominating the early stages of star formation.

MYSOs are radio quiet, unresolved in the mid-IR at 1 arcsec resolution and have luminosities $L > 10^4$ $L_{\odot}$ (Mottram *et al.* 2011a). Lower effective temperatures than their zero age main sequence (ZAMS) counterparts are thought to be responsible for the lack of ionising radiation given their luminosity (Hoare & Franco 2007; Davies *et al.* 2011).

Finally, when the bulk of the accretion has halted, the recently formed star starts to ionise the circumstellar matter forming an ultra compact H II region (UCH II; Churchwell 2002). From here on the ionising radiation and stellar winds will disrupt the molecular cloud forming a compact H II region (Yorke 1986) and later a classical H II region.

1.2 Theory of star formation

One of the important questions that this research project is trying to address is whether the formation of massive stars is a scaled-up version of the formation of low-mass stars. The following sub-sections describe the theories that try to explain the formation of low- and high-mass stars.

1.2.1 The Low-Mass Case

During the gravitational collapse of a GMC, large scale turbulence is dissipated into smaller scales generating self-similar substructures, namely clumps and cores (McKee & Ostriker 2007). Assuming that these substructures are isothermal, they will collapse gravitationally if their mass, M, is higher than the Jeans mass (or Bonnor-Ebert mass, e.g. Stahler & Palla 2005):

$$M_{\rm J} = \frac{1.18}{\rho^{1/2}} \left(\frac{kT}{G\mu m_{\rm H}} \right)^{3/2} \tag{1.1}$$

where T is the temperature, k is the Boltzmann constant, G is the universal gravitational constant, μ is the mean molecular weight, $m_{\rm H}$ the mass of the hydrogen atom and ρ the density.

Magnetic fields can also provide support against gravitational collapse. In order to overcome the magnetic pressure, cores must have masses $M > M_{\rm cr} = c_\Phi \Phi / G^{1/2}$ (Mouschovias & Spitzer 1976) where Φ is the magnetic flux and the coefficient $c_\Phi \approx 0.13 - 0.18$ depends on the distribution of gas and the magnetic field (Crutcher 1999; McKee & Ostriker 2007). However, magnetically sub-critical cores may still gather matter through ambipolar diffusion to increase the mass-to-flux ratio and collapse or otherwise expand and merge with the surrounding medium (Vázquez-Semadeni *et al.* 2005). The ambipolar diffusion phenomena may be important in the formation of low-mass cores (e.g. Crutcher & Troland 2000), but it is not clear whether ambipolar diffusion or turbulence is the dominant process during low-mass star formation (e.g. Crutcher *et al.* 2009).

The density distribution of a spherically symmetric isothermal core in hydrostatic equilibrium and confined by an external pressure is described by a Bonnor-

Ebert sphere (Ebert 1955; Bonnor 1956). The exact shape of the density distribution can be obtained by the degree of concentration (e.g. Johnstone *et al.* 2000), but it generally consists of a constant central density distribution followed by a decrease in density after a radius determined by the properties of the sphere (density and temperature). An unstable Bonnor-Ebert sphere with a degree of central concentration towards infinity gives a density distribution described by a singular isothermal sphere (Shu 1977):

$$\rho = \frac{c_{\rm s}^2}{2\pi G r^2} \tag{1.2}$$

where $c_{\rm s} = \sqrt{kT/\mu m_{\rm H}}$ is the isothermal speed of sound.

At the on-set of collapse, a density wave travels from the centre outwards at the isothermal speed of sound. The density distribution inside the wave front follows that of free-falling material, i.e. $\rho \propto r^{-3/2}$ (Larson 1972; Shu 1977). Once enough material has been accumulated, the core becomes optically thick and the isothermal phase is followed by an adiabatic phase. In general, the predictions of this model agree with observations of low-mass star forming cores (e.g. Motte & André 2001).

Other approaches to gravitational collapse of isothermal cores find a density distribution that is constant in the central region and then follows a power law $\rho \propto r^{-1}$ by considering an equation of state that reproduces the mass and radius vs. line-width relations (McLaughlin & Pudritz 1996).

The different stages during the formation of low-mass stars are divided in classes by the appearance of their spectral energy distributions (SEDs), as is shown in Fig. 1.2. The earliest stage Class 0 objects are cold embedded proto-

stars which emit mostly at longer wavelengths (submm/mm) and are obscured at wavelengths shorter than mid-IR (Andre *et al.* 1993). Class I objects have mid-IR emission and are associated with sources accreting material from a large envelope through a disc (e.g. Brinch *et al.* 2007). Discs and magnetic fields are thought to be important in the transport of angular momentum from the star (e.g. Tomisaka 2000) and the generation of jets/outflows (e.g. Shu *et al.* 1994), which are also observed in these early stages (e.g. Andre *et al.* 1993; Reipurth *et al.* 1999). The accretion rates range between $10^{-6} - 10^{-4}$ $M_{\odot}$ yr^{-1}, thus the formation process lasts $\sim 10^6$ yr (e.g. Stahler *et al.* 1980; Plunkett *et al.* 2015) whilst outflow rates are estimated to be $\sim 10 - 30$ per cent the accretion rate (Pelletier & Pudritz 1992; Lee *et al.* 2007). Class II objects correspond mainly to T Tauri stars, and during this stage the stellar wind blows the large scale envelope. Finally, Class III objects are pre-main sequence stars and the dusty disc is photo-evaporated (Dullemond *et al.* 2007).

The gravitational collapse of a slowly rotating gas cloud was studied by Ulrich (1976, hereafter Ulrich envelope) in order to reproduce P Cygni profiles from spectral lines (e.g. hydrogen recombination lines) of T Tauri stars. In their work, the velocity distribution, which is obtained from the parabolic trajectories of free-falling gas particles, are used in order to derive the density distribution of the core. The same distribution was found by Terebey *et al.* (1984), who used a semi-analytic perturbational approach to follow the collapse of a slowly rotating singular isothermal sphere. Both solutions do not include the effects of e.g. magnetic fields or stellar radiation. This solution has been used to study the envelopes of earlier Class I objects (e.g. Eisner *et al.* 2005).

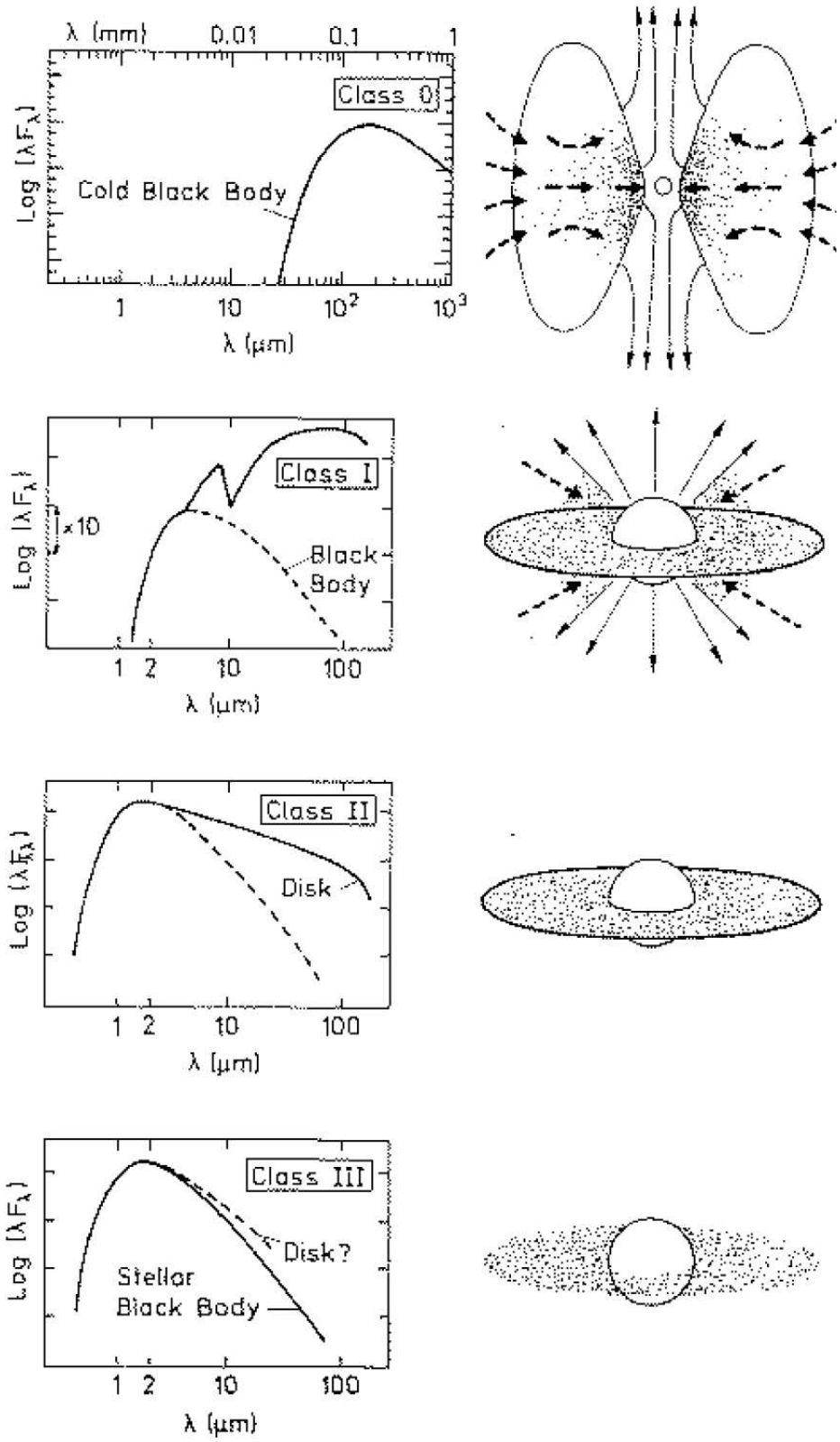

Figure 1.2: Gravitational collapse of low-mass star forming cores and the evolution of their SED. Figure adapted from André (1994).

1.2.2 The high-mass case

Unlike low-mass star formation, none of the theories proposed for the formation of high-mass stars have been able to describe successfully all the physical processes involved in their formation. Observations of binary systems have shown that O stars can reach masses of about 60 $M_\odot$ (Gies 2003). However, the formation of such massive stars may not be possible under the spherical collapse paradigm of star formation, even though high-mass cores are magnetically critical or super-critical (Crutcher 2005). Indeed, Larson & Starrfield (1971) studied the effects of radiative heating, radiation pressure and the formation of an H II region during the gravitational collapse of a high-mass core and identified the last two as the main processes that can halt the accretion during the formation of stars with masses larger than $20 - 40$ $M_\odot$. These processes are more important in the formation of massive stars than in the low-mass case because massive stars have higher luminosities and temperatures. The free-fall times of massive cores are also larger than their Kelvin-Helmholtz times (Larson & Starrfield 1971), resulting in a faster formation than in the low-mass case ($10^4 - 10^5$ yr, e.g. Mottram *et al.* 2011a). Hence each observable stage is short lived.

The effects of radiation pressure on dust were further studied by Kahn (1974) and found that for stellar masses larger than about 40 $M_\odot$ the pressure can reverse the inflow of matter. Wolfire & Cassinelli (1987) then analysed the effects of the dust size distribution on the stellar mass upper limit and found that high accretion rates ($\sim 10^{-3}$ $M_\odot$ yr^{-1}) and a reduction of the maximum dust grain size in the Mathis *et al.* (1977) size distribution are needed in order to form massive stars under the spherical collapse paradigm. Following these results, Yorke &

Sonnhalter (2002) included rotation together with a wavelength dependent treatment of the dust opacity and high accretion rates in their 2-D simulations, and found that stars as massive as 40 $M_{\odot}$ can be formed from massive cores. In their simulations the presence of a disc helps the accretion process allowing the release of radiation through the polar regions in what they denominated as the flash-light effect. High accretion rates as the determined by these models have been estimated for massive cores ($10^{-4} - 10^{-3}$ $M_{\odot}$ yr^{-1}, e.g. from infall velocities derived from NH_3 observations and assuming free-fall by Beltrán *et al.* 2006b).

The evolution of theoretical models and better initial conditions and more physical processes (e.g. turbulence) included in 3-D simulations have resulted in two main theories that could explain the formation of massive stars: monolithic collapse (also called turbulent core accretion) and competitive accretion. In the monolithic collapse theory, the mass of the cores formed as a consequence of the large scale turbulence determines the available material to form stars. In hydrostatic equilibrium, the pressure at the surface of the core equals the pressure of the clump which can be expressed as a function of the effective sound speed (McKee & Tan 2002). The observed line widths of molecular clouds increase with radius (Larson 1981), hence the effective sound speed in a high-mass core is dominated by the turbulence velocity and the accretion rate should increase with time (McKee & Tan 2003). In order to prevent the fragmentation of massive clumps into cores with Jeans masses, which may not be enough to form a massive star, radiation and feedback from newly formed stars change the physical conditions in the clump allowing the formation of massive cores (Krumholz *et al.* 2012). The accretion process is a scaled-up version of the low-mass one, where bipolar cavities opened by outflows and accretion from a disc help to overcome

the effects of the radiation pressure (Krumholz *et al.* 2005; Kuiper *et al.* 2010; Cunningham *et al.* 2011).

In the competitive accretion model, the turbulence cascade forms cores with masses of the order of the Jeans mass which grow by accreting gas funnelled from other regions of the clump (Bonnell *et al.* 2001). Massive stars are formed in the central region of the clump, where the gravitational potential is large enough to pull the material from other regions of the clump. The gas is accreted by the core through Bondi-Hoyle accretion (e.g. Wang *et al.* 2010), i.e. through the dynamical interaction between the core and the clump gas (Bondi & Hoyle 1944). The presence of filaments also helps the transport of gas from distant regions within the clump (Smith *et al.* 2009, 2012).

Both theories predict accretion through a disc with an accretion rate growing with time. However, higher accretion rates are predicted for the monolithic collapse (Tan *et al.* 2014). Simulations of disc accretion at high accretion rates ($10^{-4} - 10^{-3}$ $M_{\odot}$ yr^{-1}) have shown that the proto-star swells during the accretion process as the entropy is transported from the interior to the surface (Hosokawa *et al.* 2010). Therefore, even if the luminosity is high, the temperature of the proto-star is lower than its ZAMS counterpart. This has been proposed as an explanation for the lack of ionisation in MYSOs (Hoare & Franco 2007; Davies *et al.* 2011). The more dynamical nature of the competitive accretion implies that the density distribution of the core will be determined by the interaction with other cores, e.g. it may produce truncated accretion discs (Tan 2015), whilst in the turbulent core accretion matter distribution is determined by the gravitational collapse. Therefore, the study of the circumstellar matter in MYSOs can shed light on which accretion model explains the observations.

1.2.3 Jets and outflows

All the models of low- and high-mass star formation predict the presence of outflows. In the formation of high-mass stars, simulation show that outflows open bipolar cavities (e.g. Banerjee & Pudritz 2007) where radiation can escape relieving the radiation pressure on the infalling material (e.g. Yorke & Sonnhalter 2002). However, the mechanism by which jets/outflows are created is still not well understood.

The main proposed models for ejection of material require the presence of a magnetic field threading a rotating accretion disc. In these magneto-centrifugal models a fraction of the disc angular momentum is released through a wind. How the mass is loaded into the wind determines the strength of the toroidal magnetic field component, which in turn determines the collimation of the wind (Pudritz *et al.* 2006). In the X-wind model, the wind is loaded close to the point of intersection between the (proto-)stellar magnetic field and the disc magnetic field, which is located close to the dust sublimation radius (Shu *et al.* 1994). In the wind model however, the wind is loaded in the surface of the disc, i.e. can be loaded at larger distances than the X-wind, as long as the material is partially ionised (Blandford & Payne 1982; Pudritz & Norman 1983). The loading position imply that X-winds are less collimated than disc winds (Pudritz *et al.* 2007).

The way the circumstellar material is swept by the wind depends on the degree of collimation. In jet-driven bow shock models, a jet generated by a collimated disc wind interacts with the ISM and forms a bow shock structure when the high pressure gas, which was pushed to the side by the jet, interacts with the ambient medium (Cabrit *et al.* 1997). Whilst in the wind-driven shell models, material is

swept by a radially expanding wind at a constant velocity in each direction, i.e. a Hubble-law expansion (Shu *et al.* 1991).

1.3 Multi-wavelength view of MYSOs

Different emission mechanisms can be traced as a function of wavelength. In the near-IR the dominating mechanism is the scattered radiation from dust in the outflow cavity (e.g. Maud *et al.* 2013). *JHK*-band observations can thus trace the structure of the outflow cavity. Fig. 1.3(a) shows an example of K-band observation of the MYSO IRAS 20126+4104 made with the Large Binocular Telescope (resolution 90 mas). The cavity emission and its bipolar nature can be observed while a dark lane is observed at the position of the star (Sridharan *et al.* 2005), whose emission is extincted probably by a disc (Cesaroni *et al.* 2013). Observations at near-IR wavelengths with current telescopes can reach $\sim$100 mas resolutions by using adaptive optics or speckle interferometry.

At mid-IR wavelengths the emission from warm dust is optically thick. Interferometric or single dish diffraction limited observations, with instruments like the Very Large Telescope or Subaru, can resolve the mid-IR emission of MYSOs (Wheelwright *et al.* 2012). The emission traced correspond to that of the disc and outflow cavity (Boley *et al.* 2013). Fig. 1.3(b) shows the IRAS 20126+4104 as observed at 24.5 μm with Subaru (resolution 0.6 arcsec). The dark lane in this case is seen in emission whilst the extended emission coincides with the outflow (de Wit *et al.* 2009).

On the other side of the spectrum, at (sub)mm wavelengths, dust emission is optically thin. Single dish observations trace the cold dust emission from

the circumstellar material whilst interferometric observations may be able to resolve the disc emission. Fig. 1.3(c) shows the 1.4 mm continuum emission of IRAS 20126+4104 as mapped by the Plateau de Bure Interferometer (PdBI; resolution 0.4 arcsec). The observed structure is extended perpendicular to the outflow direction, which is probably tracing a disc as also pointed out by the molecular line emission which is consistent with Keplerian rotation (Cesaroni *et al.* 2005, 2014). With the Atacama Large Millimeter Array (ALMA) subarcsec resolutions can also be obtained in order to map regions closer to the star, but extended emission can also be recovered by also observing with its compact array.

Ionised gas can be observed at radio wavelengths and traces shocked gas or gas being accelerated by the jet/wind. Fig. 1.3(d) shows a 3.6 cm map of IRAS 20126+4104 as observed by the Very Large Array (VLA, resolution $\sim$0.2 arcsec). The emission traced by this observation is consistent with free-free emission (Hofner *et al.* 2007). Maser emission can also be observed at radio wavelengths in the disc and the outflow walls (e.g. Trinidad *et al.* 2005).

1.4 Radiative transfer modelling

Radiative transfer (RT) combined with multi-wavelength observations, like the ones showed in the previous section, is a powerful tool to study the physical properties of the circumstellar matter during the formation of massive stars, and compare theoretical/numerical models with real observations. In the following subsections, the theory behind RT is described and the use of RT modelling in the study of star formation is reviewed.

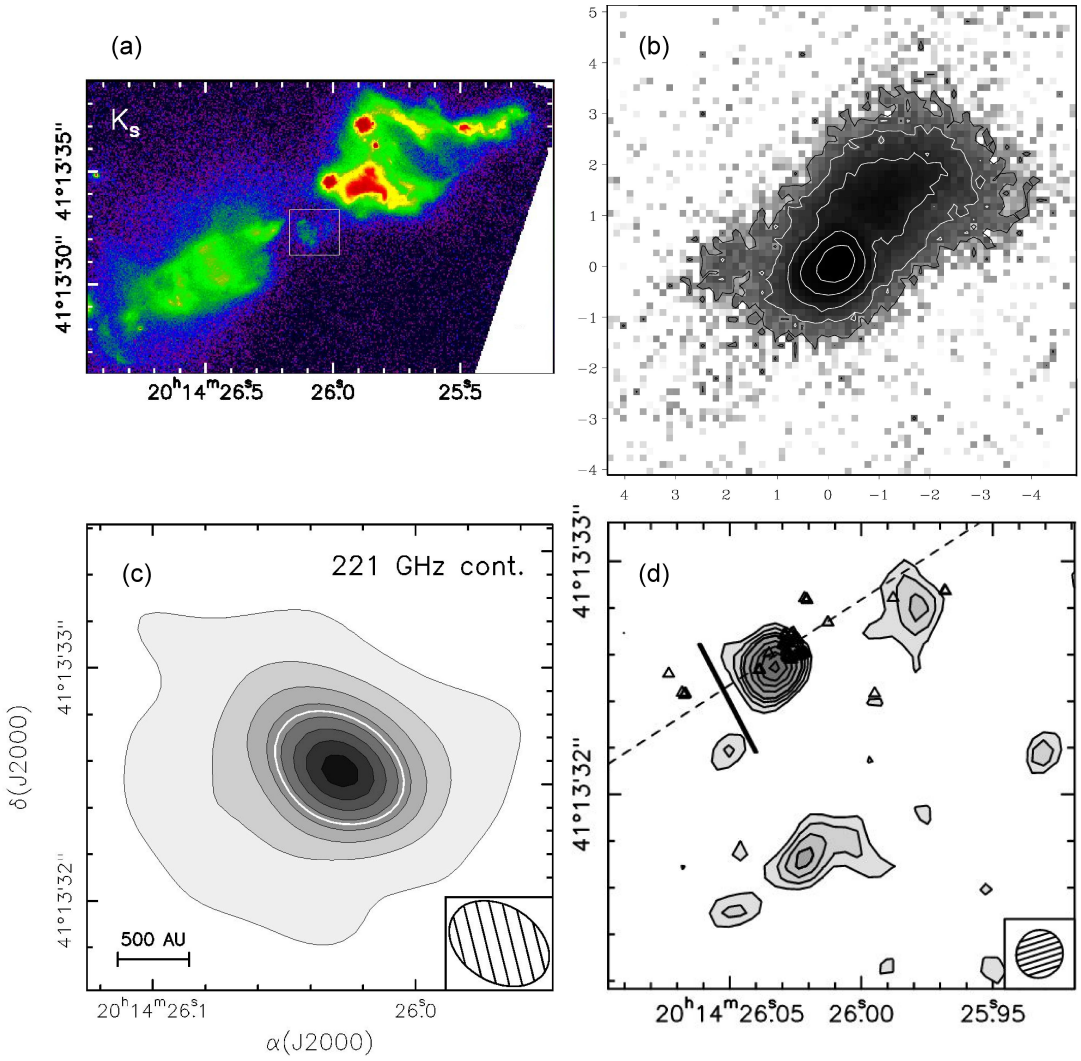

Figure 1.3: Multi-wavelength observations of IRAS 20126+4104. (a) K_s image from the Large Binocular telescope, taken from Cesaroni *et al.* (2013). (b) Subaru 24.5 μm interferometric observation taken from de Wit *et al.* (2009). Axes are in arcsec offset from the peak. (c) 1.4 mm interferometric observation from Cesaroni *et al.* (2014). (d) 3.6 cm interferometric observation from Hofner *et al.* (2007). The continuous black line marks the position of the dark lane observed in the near-IR images, the dashed line follows the outflow direction and the triangles mark the maser emission.

1.4.1 Theory and methods

The amount of energy per unit time, area, solid angle and frequency emitted from any astronomical source, also known as intensity I_ν, is the result of several physical processes that depend on physical properties like the temperature and chemical composition of the source as well as the interactions of the light with material between the source and the observer. Following Rybicki & Lightman (1986), the shape of the intensity function can be obtained by solving the radiative transfer equation:

$$\frac{dI_\nu}{d\tau_\nu} = -I_\nu + S_\nu \tag{1.3}$$

where τ_ν is the optical depth and S_ν is the source function defined as the ratio between the emissivity j_ν and the absorption coefficient α_ν, which in turn depend on the probabilities of the transitions with frequency ν. In local thermodynamic equilibrium (LTE), the source function equals the Plank function for black body radiation, $B_\nu(T)$, where the temperature T is a function of the position. The optical depth is related to the absorption coefficient by

$$d\tau_\nu = \alpha_\nu ds = \rho\kappa_\nu ds \tag{1.4}$$

where s is the path travelled by the light, ρ is the mass density and κ_ν is the opacity. When only absorption processes take place, the solution of the RT equation is:

$$I_\nu(s) = I_\nu(s_0)\exp[-\tau_\nu(s)] \tag{1.5}$$

whilst when only emission processes take place, the solution to eq. 1.3 is:

$$I_\nu(s) = I_\nu(s_0) + \int_{s_0}^{s} j_\nu(s)\, ds \tag{1.6}$$

where s_0 is the origin of the light beam.

If scattering is included, an extinction coefficient defined as the sum of the absorption coefficient α_ν and the scattering coefficient σ_ν can be introduced in eq. 1.3. There are different sources of scattering, e.g. dust grains or electrons. The solution of the RT equation can only be found numerically in this case (Rybicki & Lightman 1986).

For more complicated 3-D geometries and radiation sources, the Monte Carlo method can be used to find the radiation field that solves the RT equation from a given density distribution and dust/gas properties. Fig. 1.4 shows in general how a Monte Carlo RT code works. In Monte Carlo RT, the propagation, i.e. the path travelled by a photon packet, is drawn randomly from a probability distribution function (PDF) which is based on the properties of the gas/dust in the grid (Whitney 2011). In the diagram in Fig. 1.4, the method of Lucy (1999) is used to find the temperature distribution. Another method to find the temperature is that of Bjorkman & Wood (2001), which does not do several iterations but updates the temperature during the main iteration and the photon is emitted from a cell with a corrected emissivity probability distribution.

The post-processing at the end of the diagram includes the averaging of the properties, e.g. exit direction and optical depth, of the $N_{\rm tot}$ photon packets used, where $N_{\rm tot}$ is generally a large number so the average is statistically significant. Finally, the properties of the exiting photons can be used to calculate images and

the SED. In order to produce higher signal-to-noise images, other two methods can be used rather than the binning of the exiting photons (e.g Robitaille 2011). One is the peel-off method, whereby a photon packet is propagated in the direction of the observer weighted by the probability that it can go in that direction. The other is the ray tracing method, which solves the RT equation based on the physical properties of the grid along the line of sight.

Solving eq. 1.3 implies a knowledge of the density, temperature and chemical composition of the emission source. However, observations give us information about the intensity function that can be used to constrain these properties. We will distinguish two types of modelling: dust and line emission modelling.

1.4.1.1 Dust emission modelling

The gas density and temperature distribution can be found by modelling the dust emission. The advantage of using the dust emission is that the models are less susceptible to the chemical models and does not depend on the kinematics of the gas.

A commonly used solution of eq. 1.3 is that of a constant distribution of dust in LTE at temperature T_d:

$$I_\nu(T_d) = B_\nu(T_d)(1 - e^{-\tau_\nu}) \tag{1.7}$$

where it has been assumed that the contribution from the cosmic microwave background (CMB) is negligible. Physical properties of MYSOs, like the average dust temperature and column density, can be obtained by modelling their far-IR/submm dust emission by using this equation (e.g. Morales *et al.* 2009; Sadavoy

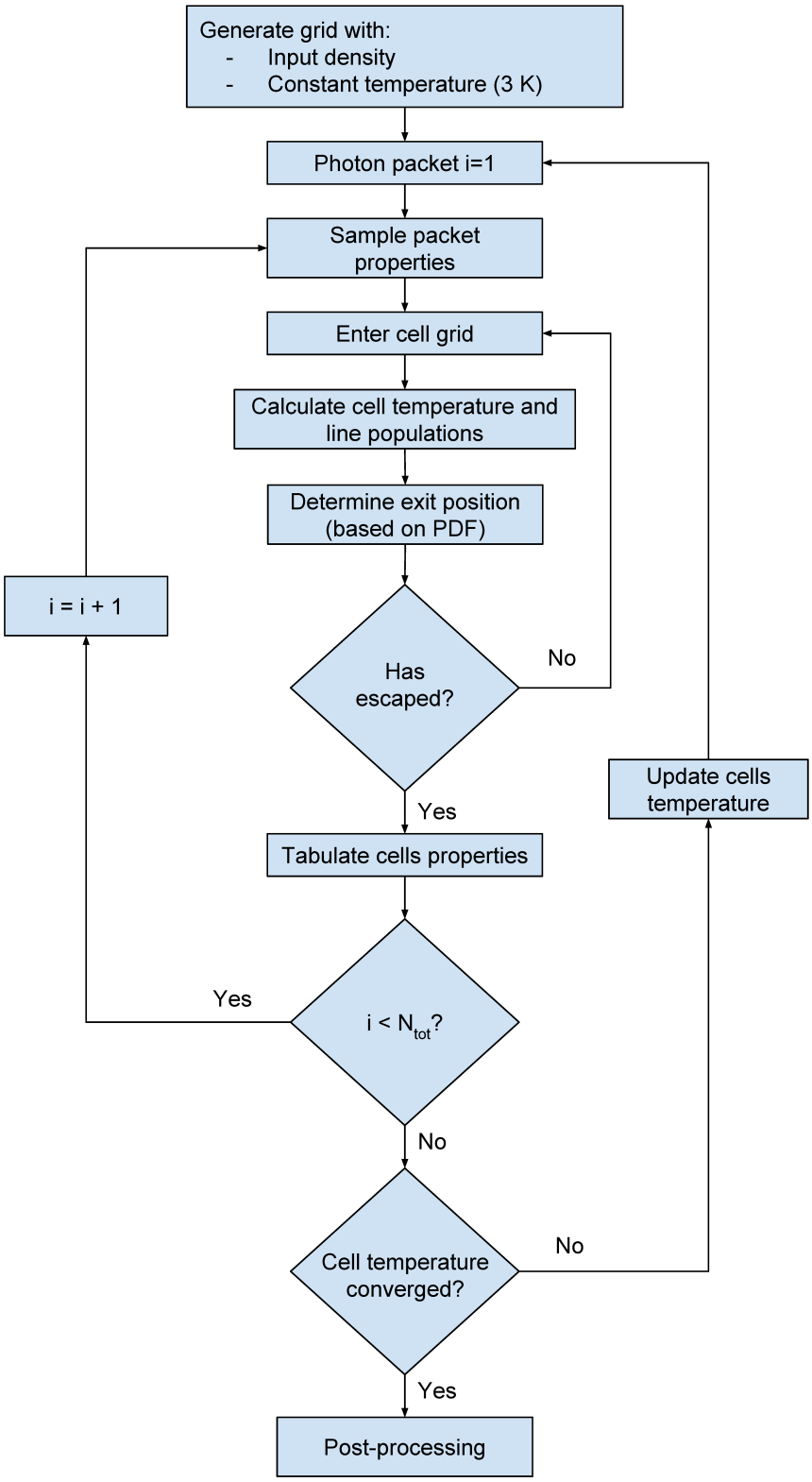

Figure 1.4: Monte Carlo RT flow diagram following the Lucy (1999) method for determining the cell temperature. $N_{\rm tot}$ stands for the total number of photon packets per iteration. The probability distribution function (PDF) determines where the photon is likely to move to and is related to the optical depth and scattering angles. The sampled packet properties include spectral and initial direction properties.

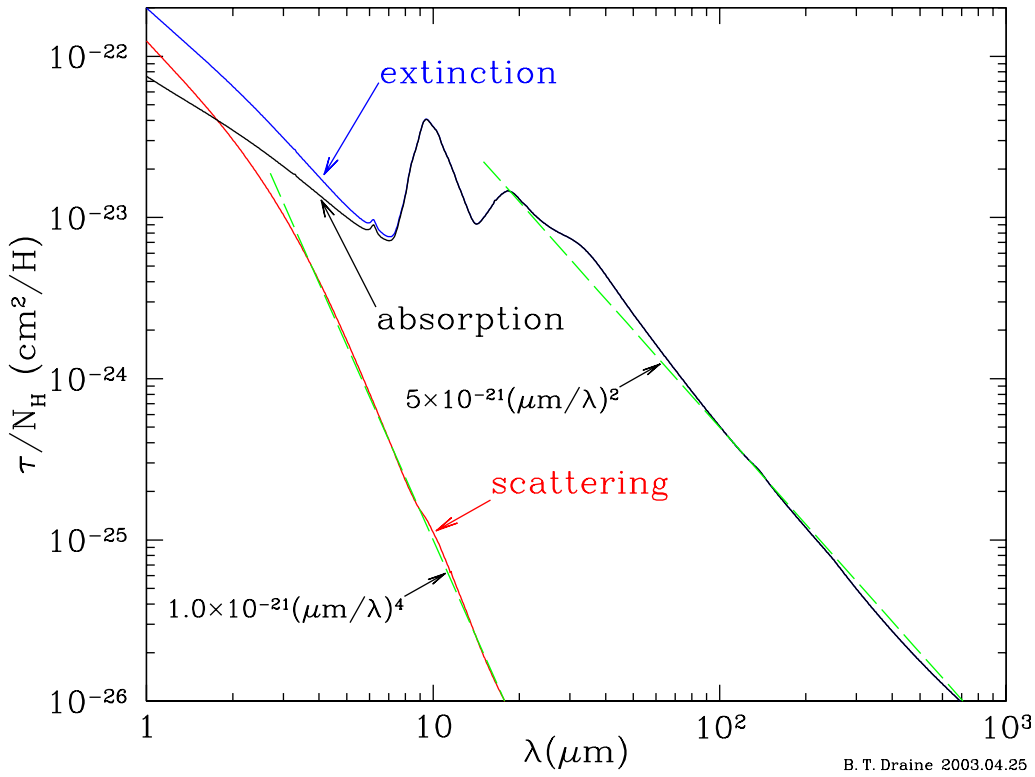

Figure 1.5: Example of dust extinction curve from Weingartner & Draine (2001) for a visual reddening $R_V = 3.1$. Figure from Draine (2003).

et al. 2013). This modelling assumes a certain knowledge of the dust opacity, which is assumed to be constant along the line of sight. For wavelengths larger than ~ 100 μm, the dust opacity is usually approximated by a power law $\kappa_\nu \propto \nu^\beta$ where β is the dust opacity index. This is supported by dust models as is shown in Fig. 1.5.

For a spherically symmetric dust distribution heated by a central source, a numerical scalable solution to eq. 1.3 can be found (Ivezic & Elitzur 1997). Therefore, a grid of solutions can be computed for different configurations of the dust distribution for modelling the SED and images of several sources. This method gives 1-D density and temperature distributions instead of average properties as

the previous solution.

For 2-D and 3-D distributions of dust, scattering has to be taken into account. As is shown in Fig. 1.5, Rayleigh scattering by dust grains is important at wavelengths $\lambda \lesssim 10$ μm.

1.4.1.2 Line emission modelling

Unlike dust emission modelling, to model spectral line emission the abundances of the emitting species are needed in addition to the velocity, density and temperature distributions. Density, temperature and abundances are used to calculate the populations of the different excitation levels, which determine the emissivity and absorption coefficient, in order to find the source function and optical depth.

For a cloud similar to that in Section 1.4.1.1, an analytical solution to eq. 1.3 can be found:

$$I_\nu = (B_\nu(T_{\rm CMB})e^{-\tau_{\rm dust}} + I'_\nu(T_d))e^{-\tau_{\rm gas}} + B_\nu(T_{\rm ex})(1 - e^{-\tau_{\rm gas}}) \qquad (1.8)$$

where $T_{\rm CMB} = 2.7$ K is the CMB temperature, $\tau_{\rm dust}$ and $\tau_{\rm gas}$ are the optical depths of dust and gas at frequency ν, $I'_\nu(T_d)$ is given by eq. 1.7 and $T_{\rm ex}$ is the excitation temperature. In practise, the continuum is fitted and subtracted from the observations, and the observed intensity includes a term subtracting the intensity of the CMB as a result of the chopping of the telescope. The excitation temperature and the column density of the molecule can be found by fitting this function to the observed spectra. As in the dust modelling case, these values will be averages along the line of sight.

In the general non-LTE solution, collisions with other molecules/particles

must be considered. A critical density $n_{\rm cr}$ for which the radiative and collisional de-excitations are equal can be defined. In non-LTE, the number densities are $n \lesssim n_{\rm cr}$, hence the kinetic temperature of the gas $T_{\rm K}$ is not the same as its excitation temperature $T_{\rm ex}$. To find the opacity and kinetic temperature, the population of the different energy levels is determined by achieving statistical equilibrium between collisional and radiative transitions. This in turn depends on the radiation field, through the average intensity, which is not local. The radiation field calculations can be separated from the level population ones by introducing a function that determines the probability that a photon escapes. This escape probability depends on the geometry of the system, e.g. for a expanding envelope the large velocity gradient approximation can be used. Since collisions depend also on the density of the collisional partner, the number of free parameters increases for non-LTE modelling. For the cases analysed in this thesis, the main collisional partner is molecular hydrogen, whose density distribution can be obtained from the dust RT modelling and collision rates tables for different molecules can be found in the literature (e.g. Schöier *et al.* 2005).

1.4.2 RT modelling of MYSOs

Dust continuum 1-D spherically symmetric modelling of MYSOs have been used to model SED and submm intensity radial profiles. Power law density distributions $\rho \propto r^{-p}$ are generally assumed in order to compare with the low-mass star formation theory. Mueller *et al.* (2002) found an average density exponent $p = 1.8$ for their sample of 31 objects by using 350 μm observations, whilst Williams *et al.* (2005) found a flatter average exponent $p = 1.3$ for their sample of 39 objects by

using 850 μm data. The modelling of 14 MYSOs by de Wit *et al.* (2009) gave an exponent of $p = 1.0$ for the inner $\sim 10^3$ au as mapped by their 24.5 μm diffraction limited observations. This flattening in the inner region was interpreted as an effect of rotational flattening of the envelope.

Dust continuum modelling by 2-D axisymmetric models has the disadvantage of increasing the number of free parameters, hence modelling of a large sample is limited. de Wit *et al.* (2010) modelled the MYSO W33A and found that outflow cavities are key in order to reproduce N-band (~ 10 μm) visibilities. Their results were used by Wheelwright *et al.* (2012) to successfully model a larger sample of MYSOs. Grids of 2-D RT models (e.g. Robitaille *et al.* 2006) have also been used to study other physical properties of MYSOs, like the bolometric luminosity (e.g. Mottram *et al.* 2011b).

In general, dust continuum RT modelling focuses on reproducing the SED and one or two observations. In some approaches a scattered emission image is used to constrain the outflow cavity shape and density for 2-D modelling, but this image is not included in the final modelling (e.g. de Wit *et al.* 2010; Maud *et al.* 2013).

1-D line modelling has been used to model the spectra of cores in order to study their physical conditions (e.g. Johnston *et al.* 2015) or chemical composition/evolution (e.g. van der Tak *et al.* 2006; San José-García *et al.* 2016), either by assuming a constant density along the line of sight or by using a spherically symmetric temperature and density distribution. For 2-D modelling, Wiles *et al.* (2016) have used a spherical distribution described by different temperature components as an initial condition for the modelling of high-mass cores in G333 in order to study their kinematics. In other studies, like Johnston *et al.* (2015), dust

and line emission are modelled simultaneously.

1.5 Multi-wavelength surveys

In order to overcome the observational challenges described in Section 1.1, large regions of the sky have been mapped at high angular resolution by ground- and space-based telescopes, e.g. United Kingdom IR Telescope (UKIRT), *Spitzer* and *Herschel*, from near-IR to submm wavelengths. These observations are also complemented by interferometric observations of specific sources at even higher resolutions, which allow the study of regions closer to the proto-star.

1.5.1 The RMS survey

The Red *MSX*[1] Source (RMS; Lumsden *et al.* 2013) survey has been dedicated to catalogue a well selected sample of objects by their *MSX* IR colours. Using the colour criteria of Lumsden *et al.* (2002) the survey has obtained a sample of ∼2000 candidate MYSOs. However, this sample is contaminated by evolved stars, proto-planetary nebualae (PNe) and UCH II regions. Follow-up observations were done in order to classify the objects in the initial sample. These allowed the identification of ∼650 MYSOs, mostly located in the Galactic plane as is shown in Fig. 1.6.

Unlike MYSOs, UCH II regions and PNe are not radio quiet and can be resolved at 1 arcsec resolutions in the mid-IR. Radio continuum (Urquhart *et al.* 2007a, 2009) and mid-IR (Mottram *et al.* 2007) observations were used to separate these populations. Dusty evolved stars are identified by their near-IR spectra

[1] *Midcourse Space Experiment*

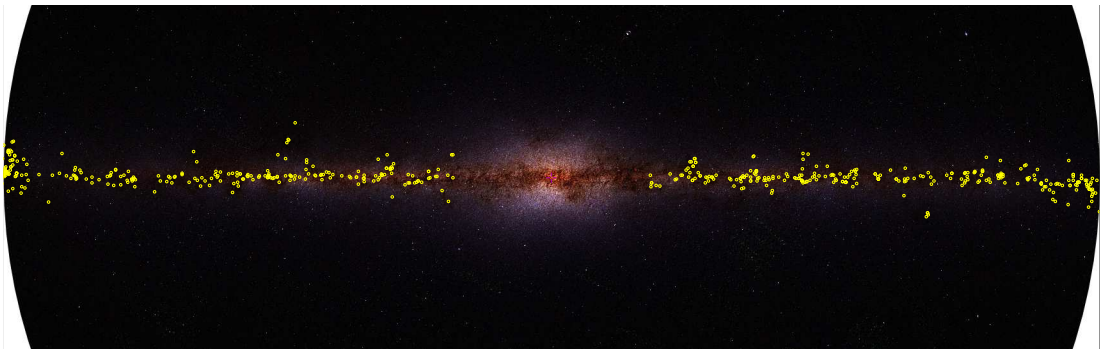

Figure 1.6: Galactic MYSOs from the RMS survey in the $l = \pm 90°$ range overlaid the near-IR emission from the Two Micron All-Sky Survey (2MASS).

(Cooper *et al.* 2013). Additionally, ^{13}CO line emission observations were used to determine the kinematic distances to the sources in the RMS survey (Urquhart *et al.* 2007b, 2008, 2012). Finally, Mottram *et al.* (2011b) estimated their luminosities by using the synthetic SED database of Robitaille *et al.* (2007), and Mottram *et al.* (2011a) estimated the Galactic luminosity function (number of objects per unit volume per unit luminosity) of MYSOs and estimated their lifetime. A summary of the main results of the RMS survey can be found in Lumsden *et al.* (2013).

All the follow-up observations, distances and luminosities are available in the RMS database. This database also contains public data from other surveys, which includes the UKIRT IR Deep Sky Survey (UKIDSS; Lucas *et al.* 2008), the APEX[1] Telescope Large Area Survey of the Galaxy (ATLASGAL; Contreras *et al.* 2013) and the SCUBA[2] Legacy Catalogue (Di Francesco *et al.* 2008). This database is one of the main sources for the multi-wavelength study of MYSOs in this thesis.

[1]Atacama Pathfinder Experiment
[2]Submillimetre Common-User Bolometer Array

1.5.2 *Herschel* surveys

The *Herschel Space Observatory* mapped several star-forming regions in the continuum and spectroscopically at far-IR/submm wavelengths. This work will focus on the continuum observations, which were made by the Photoconductor Array Camera and Spectrometer (PACS) at 70 and 160 μm and the Spectral and Photometric Imaging Receiver (SPIRE) at 250, 350 and 500 μm. In particular, the 70 μm observations will be of particular interest as they have the highest resolution in the far-IR, where the SED of MYSOs peaks.

The Galactic plane was mapped by the *Herschel* IR Galactic Plane Survey (Hi-GAL; Molinari *et al.* 2010b). To accomplish this, the observations used a high scan speed (60 arcsec s^{-1}) resulting in an asymmetrical PSF which does not allow a detailed study of the circumstellar matter. However, a selected group of molecular clouds forming high-mass stars were observed by the *Herschel* OB Young Stellar Objects Survey (HOBYS; Motte *et al.* 2010) at a slower scan speed which produce a more symmetrical PSF, thus allowing a detailed study of the circumstellar matter distribution.

1.6 Thesis motivation and structure

This introduction has shown that MYSOs are important for testing the predicted physical conditions from theoretical models during the formation of high-mass stars. In particular, if the formation of high-mass star is an scaled-up version of low-mass star formation. The increasing amount of data and the improvements on resolution at key wavelengths allow a detailed study of these models through RT.

First, high-resolution *Herschel* 70 μm observations are explored to determine whether MYSOs can be spatially resolved at this wavelength. Previous studies of far-IR emission towards MYSOs required deconvolution in order to extract spatial information as the observations were unresolved (e.g. Campbell *et al.* 1995). In Chapter 2 Hi-GAL images of three MYSOs are analysed and a criterion is defined in order to select objects which are likely to be resolved at 70 μm.

The origin of the 70 μm continuum emission is analysed in Chapter 3. This emission has not been analysed in detail before, thus it is not clear which structures are traced: a rotationally flattened envelope and/or the outflow. 2.5-D RT models are used to explain the 70 μm data and high-resolution data from IR to mm wavelengths.

The density and temperature distributions constrained by the multi-wavelength continuum data are then used to study the kinematics of the envelope of AFGL 2591 in Chapter 4. The methyl cyanide distribution and velocity structure is explored on scales between envelope and disc by RT modelling of interferometric data.

Finally, the conclusions of this thesis are presented in Chapter 5.

Chapter 2

Herschel Hi-GAL imaging of MYSOs

2.1 Introduction

At increasingly longer wavelengths the emission of colder dust can be observed. This emission becomes more extended as we move from the mid-IR to mm wavelengths, where it is usually resolved by single-dish telescopes. By definition, MYSOs are usually unresolved sources at $\sim$1 arcsec resolution in the mid-IR (e.g. Cooper *et al.* 2013). However, sub-arcsec mid-IR interferometric observations have shown that MYSOs can be partially resolved. Using 40 mas resolution 8–13 μm interferometric observations, de Wit *et al.* (2007, 2010, 2011) and Boley *et al.* (2013) have studied a sample of MYSOs at scales of roughly 100 au, which is a few times the expected dust sublimation radius. The interferometric visibilities can be well reproduced by 2-D axisymmetric models including a low density outflow cavity. These models show that most of the emission arises from warm

dust along the cavity walls with a compact component needed in order to fit the 8 μm visibilities.

Diffraction limited observations at 24.5 μm at 0.6 arcsec resolution can also partially resolve MYSOs (de Wit *et al.* 2009; Wheelwright *et al.* 2012). The RT modelling with spherically symmetric dust distributions of de Wit *et al.* (2009) showed that the density of these sources scales with distance to the source as $n \propto r^{-1}$. This is flatter than the expected distribution for free-falling material, $n \propto r^{-1.5}$, and was argued to be produced by the rotation of the cores. The 2-D axisymmetric modelling of Wheelwright *et al.* (2012) also showed that the 20 μm emission is dominated by warm dust in the envelope cavity walls.

The transition between mid-IR to submm, where the dust becomes optically thin, has the potential of providing further spatial information of warm dust at scales between the larger cold extended envelope and the somewhat hotter dust mapped by the mid-IR observations. Following the results from the mid-IR studies, it is expected that the dust emission at these scales comes from warm material in the cavity walls, which are being heated by the stellar radiation escaping from an optically thin cavity.

The highest resolution observations to date around the optically thick/thin transition come from the *Herschel* space telescope. Its nominal resolution at 70 μm is 5 arcsec and offers the best chance to resolve MYSOs in the far-IR. As part of the efforts to map star forming regions with *Herschel*, the Hi-GAL survey (Molinari *et al.* 2010b) has the largest coverage of the Galactic plane where most stars are formed. The study of these released data can determine whether MYSOs can be resolved at 70 μm. If this emission is extended, is it elongated in the disc plane due to rotational flattening of the envelope or in the outflow direction due

to heating of dust along cavity wall.

In this chapter the data from two Hi-GAL fields observed during the Science Demonstration Phase (SDP; Molinari *et al.* 2010a) are examined. The observational technique utilised to map these 2 deg^2 fields is described in Section 2.2 together with a discussion of the consequences of such technique on the 70 μm point spread function (PSF). In Section 2.3, the 70 μm imaging of 3 RMS MYSOs is analysed, and then modelled with RT models in Section 2.4. The results of this chapter are discussed in Section 2.5 and conclusions are drawn in Section 2.6.

2.2 Herschel Hi-GAL observational technique

2.2.1 The parallel mode

The parallel mode is a special observational technique developed for scanning fields simultaneously with the PACS and SPIRE instruments on-board the *Herschel Space Observatory*. In this mode, the three bands of SPIRE are available (250, 350 and 500 μm) and only two of the three bands of PACS are available (either 70, 100 or 160 μm). The scan speeds can be 20 or 60 arcsec s^{-1}. Fig. 2.1 shows the orientation of the PACS array in the sky and defines the angles relevant for the orientation of the PSF. In particular, the array-to-map angle determines the orientation of the structure supporting the secondary mirror, which in turn determines the diffraction pattern projected on the instruments.

For the Hi-GAL survey, PACS 70 and 160 μm bands and a scan speed of 60 arcsec s^{-1} were selected in order to maximise the survey area of the observations (Molinari *et al.* 2010b). Each field in the survey was observed twice with

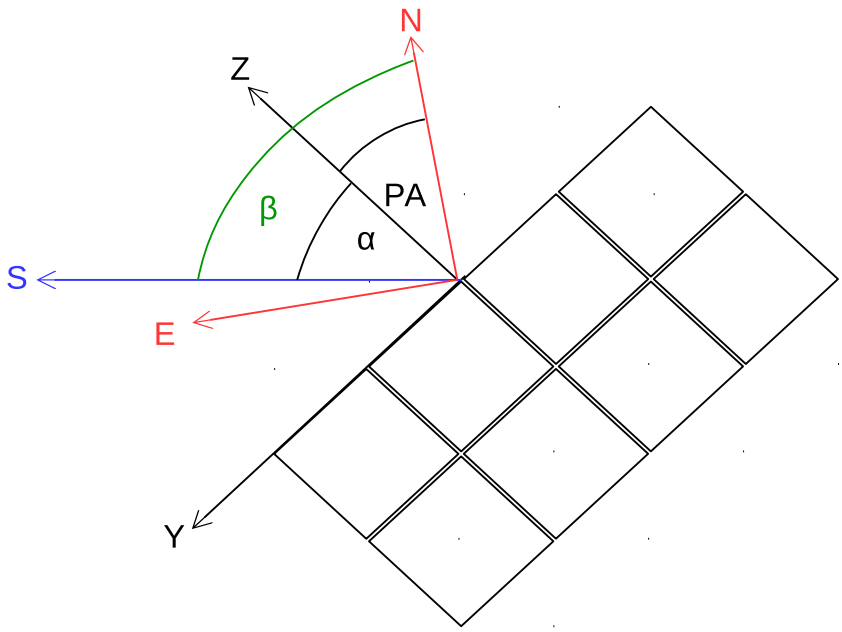

Figure 2.1: PACS array orientation. Axis S points the direction of the scan leg, Z and Y are the axes of the array, and N and E the north and east directions. The angles defined by these axes are the array-to-map angle α, the position angle of the array PA, and the map orientation angle $\beta \equiv \mathrm{PA} + \alpha$. In parallel mode $\alpha = \pm 42\overset{\circ}{.}5$ for nominal or orthogonal directions.

an array-to-map angle $\alpha = 42\overset{\circ}{.}5$ for the so-called nominal direction and with $\alpha = -42\overset{\circ}{.}5$ for the orthogonal direction. These were then aligned and combined in what it is called the naive map.

During an observation, the detector sweeps the observed field in parallel legs. These can be named positive or negative depending on the leg direction with respect to the first scan leg direction. Fig. 2.2 shows the scan legs used in the observations of the $l = 30°$ Hi-GAL SDP field with PACS in the nominal direction. Note that some patches are observed twice, which affects the PSF of sources located in these intersections.

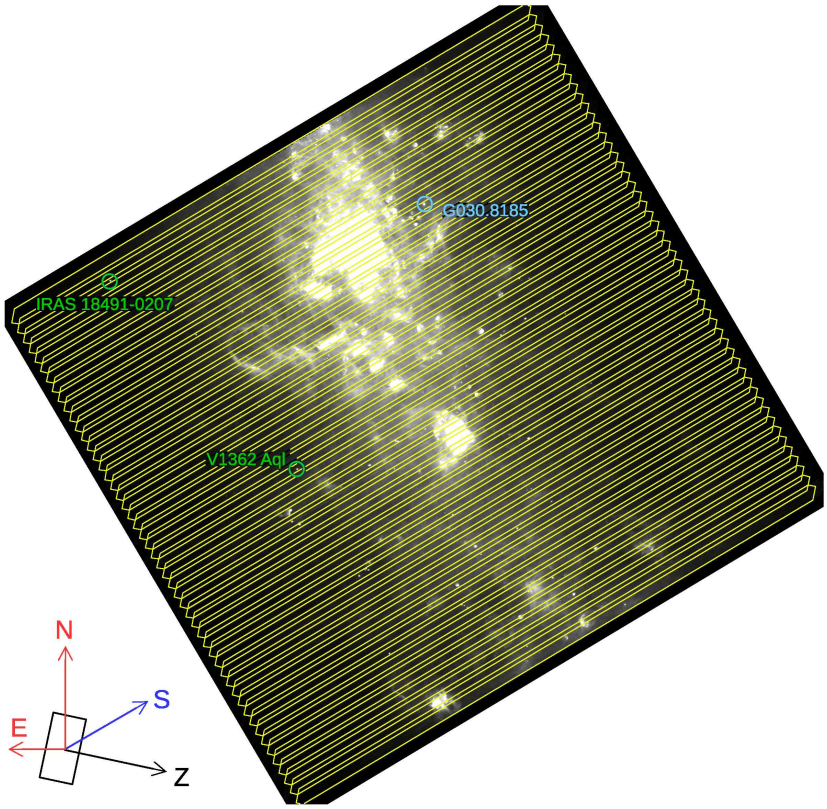

Figure 2.2: Scanning of the $l = 30°$ SDP field with PACS. Scanning legs are shown in yellow. The PACS array orientation is shown in the lower left corner with PA = 258° and $\alpha = 42.^{\circ}5$ (cf. Fig. 2.1). Sources in green are the PSF candidates, and the MYSO studied is in blue.

2.2.2 70 μm PSF characterisation

The high velocity speed chosen for the Hi-GAL survey produces a PSF which is smeared out along the scan direction. Fig. 2.3 shows a high signal-to-noise ratio image of the asteroid Vesta made as part of the telescope performance verification phase in order to study the behaviour of the PSF (see Lutz 2012). The PSF size (FWHM) derived from Vesta observations is $5.''8 \times 12.''1$ (Lutz 2012). Two dark spots can also be observed along the scan direction and they are a result of the

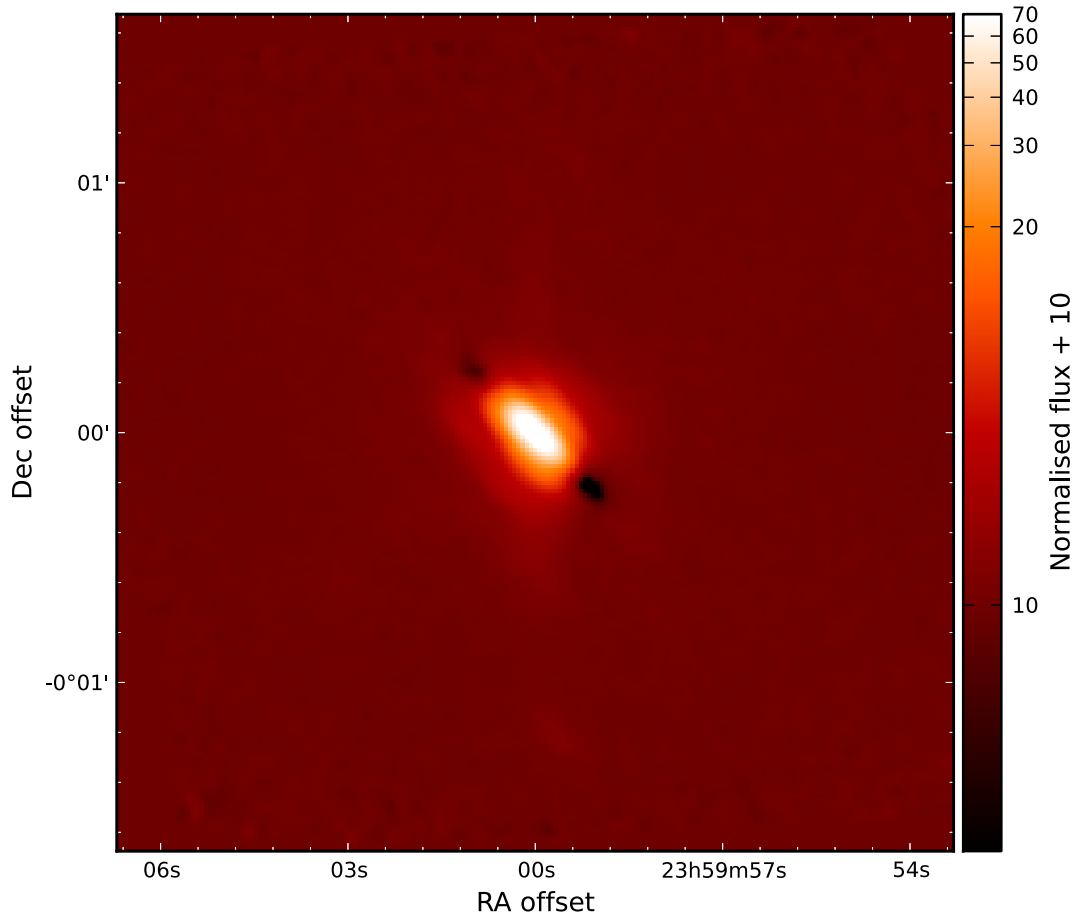

Figure 2.3: Image of Vesta taken in parallel mode with a scan speed of 60 arcsec s^{-1} and array-to-map inclination angle of $\alpha = 42.^{\circ}5$ showing the details of the PSF. In order to use a logarithmic stretch, a constant value of 10 was added to the normalised fluxes.

undershooting of the signal due to the scan speed.

In order to study the suitability of Vesta images as a PSF, four bright unresolved sources were identified in both Hi-GAL SDP fields. Table 2.1 lists the details of these PSF candidates. These are isolated asymptotic giant branch (AGB) and post-AGB stars. Although these are unresolved sources, they can have extended envelopes (de Wit *et al.* 2009) and may not be good PSF objects. Therefore, they are only used to check the consistency between them and the

Table 2.1: Parameters of the PSF objects found within the two Hi-GAL SDP fields at 70 μm.

Name	Nature	RA	Dec	$f_{70\mu m}$
		(J2000)		(Jy)
V1362 Aql	Mira	18:48:41.9	−02:50:28	66
IRAS 18491−0207	PAGB	18:51:46.2	−02:04:12	80
IRAS 19374+2359	PAGB	19:39:35.5	+24:06:27	29
IRAS 19348+2229	?	19:36:59.8	+22:36:08	32

Note. '?' stands for unclassified or unknown nature.

Vesta PSF after taking into account all the features introduced by the parallel mode.

Since nominal and orthogonal maps are almost perpendicular in parallel mode, the PSF of the naive map will be dominated by the major axes of the nominal and orthogonal map PSFs. Fig. 2.4 shows the effect of combining nominal and orthogonal maps on the PSF object V1362 Aql. The result is a cross-shaped PSF with the dark spots in the extremes of the cross. This decreases the probability of resolving the 70 μm emission from MYSOs. Fig. 2.5 shows that the PSF objects have similar features as the Vesta PSF shown in Fig. 2.3. Therefore, the best way to compare the Vesta PSF with the PSF objects, and later with models, is along the minor axis direction, i.e. the direction perpendicular to the scan direction.

In order to do the comparison, slices across the PSF minor axis were obtained from nominal and orthogonal observations. As shown in the diagram presented in Fig. 2.6, the Vesta image was rotated so the scan direction coincides with the horizontal and it points to the right, and then rebinned to the coarser Hi-GAL pixel scale (3.2 arcsec). Then the average and standard deviation of three columns centred on the intensity peak were calculated, thus defining the slice and its error. The columns were normalised to their peak values before combining them. Finally, a subpixel correction to the slice offset was applied by aligning the

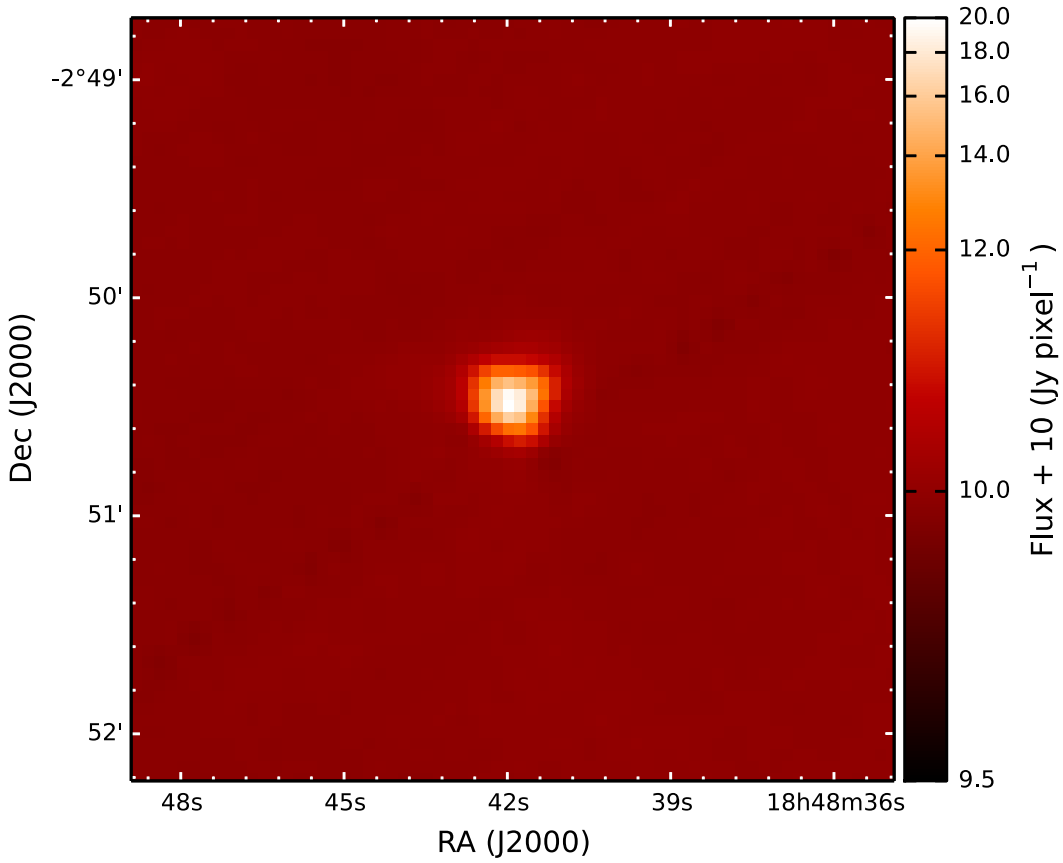

Figure 2.4: Image of the PSF star V1362 Aql in the naive map of the $l = 30°$ region. Note the offset cross shape caused by the addition of the nominal and orthogonal scans each of which has an elongated PSF.

slice zero offset to the peak obtained from a 2-D Gaussian fitted to the image.

A similar procedure was applied for the Hi-GAL PSF objects. First, each SDP field was rotated so the scan direction coincides with the Vesta one, i.e. the positive scan direction pointing to the right. Then, cut-outs of each object were obtained, and a mean sky level calculated over an annulus surrounding each object was subtracted from each of them. Finally, the slices were extracted following the same procedure as for Vesta.

The comparison between the PSF objects and Vesta slices is shown in Fig. 2.7.

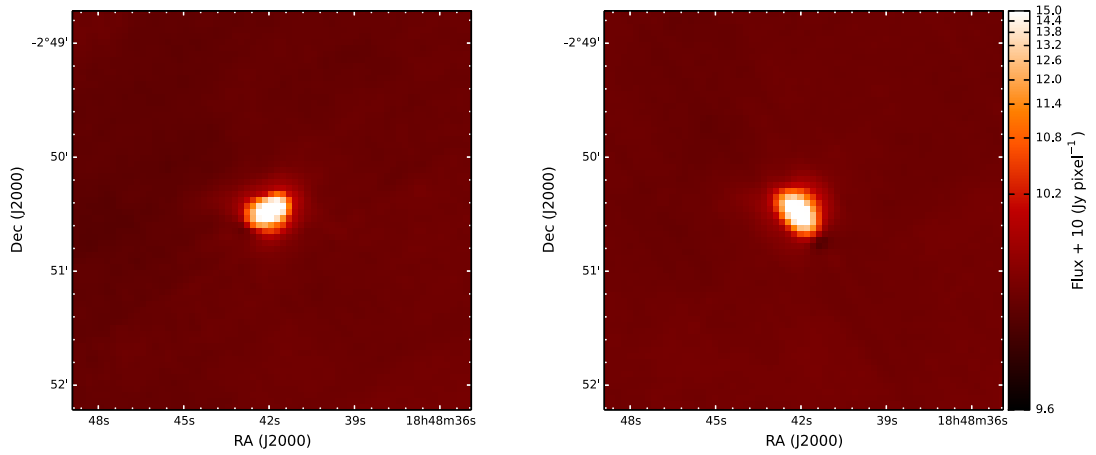

Figure 2.5: Nominal (left) and orthogonal (right) scan image of the PSF star V1362 Aql. The flux scale is the same for both images.

Objects V1362 Aql, IRAS 18491–0207 and IRAS 19374+2359 show a similar intensity distribution as Vesta down to 1 per cent of the peak value, whilst IRAS 19348+2229 seems to be extended in the nominal direction. Below 1 per cent the background noise starts to dominate. Since the shape of Vesta is similar to that of the PSF objects and has a higher signal-to-noise ratio, to allow a better determination of whether MYSOs are extended at 70 μm, then Vesta will be compared to the MYSOs in the SDP fields.

As described in Section 2.2.1, some objects can be observed twice due to the overlap of scans legs. In Fig. 2.7, IRAS 18491–0207 is scanned on one leg in the orthogonal map and by two legs in the nominal map. However there is not a significant deviation from the Vesta slice. Fig. 2.8 shows the Vesta slices compared with a slice from the Vesta image averaged with its reflection along the major axis, i.e. a PSF for an object scanned twice. The difference between the slices is less than 10 per cent. Although this is not a major difference, for the purpose of modelling the 70 μm emission, the reflected averaged Vesta PSF will

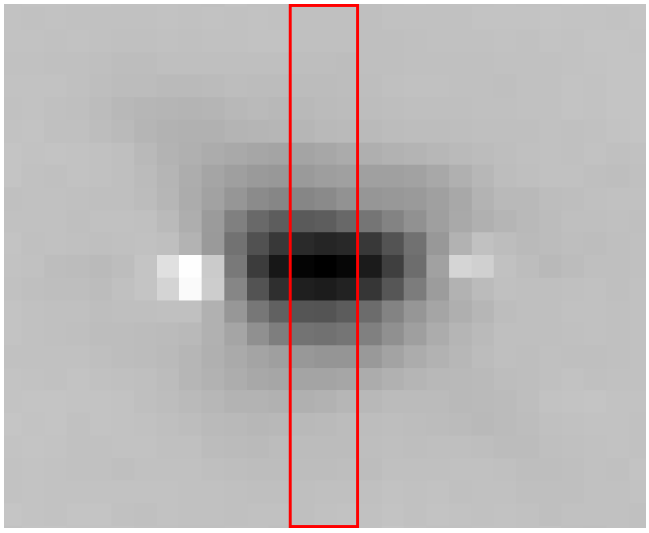

Figure 2.6: Image of Vesta ($\alpha = 42\overset{\circ}{.}5$) rotated and rebinned to Hi-GAL resolution showing the slice along the minor axis used in this work (red box). Each pixel has a size of 3.2 arcsec and the image is 29×23 pixels in size.

be used with objects scanned twice.

2.3 Observations

2.3.1 70 μm Imaging of RMS MYSOs

Of the 19 RMS MYSOs in the $l = 30$ and 59° fields only 3 are relatively isolated. Fig. 2.9 shows examples of an isolated source, G030.8185+00.2729, and a source located in a region with complex background and with nearby sources, G030.4117–00.2277. Isolated objects offer better conditions in order to study whether or not MYSOs are resolved at 70 μm. The details of the only source in the $l = 30^\circ$ and the two sources in the $l = 59^\circ$ fields that are isolated are given in Table 2.2.

Although these sources are isolated at 70 μm, 2–4 sources are identified at

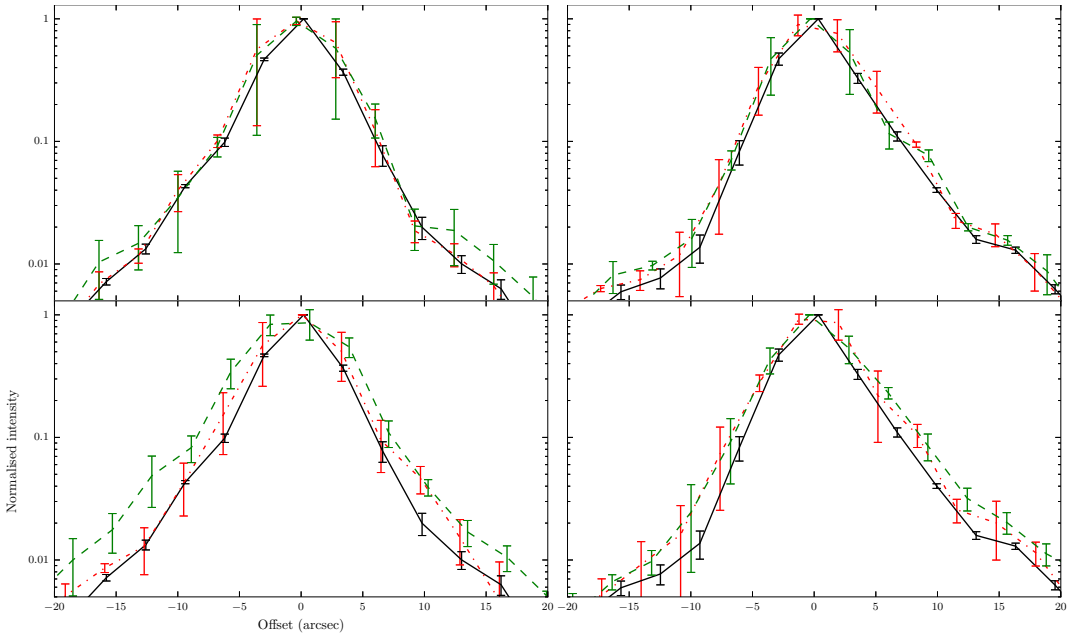

Figure 2.7: A comparison of the intensity profile of Vesta (solid black line) and PSF stars V1362 Aql (dash–dotted red line) and IRAS 18491−0207 (dashed green line) slices in the nominal (left) and orthogonal (right) map directions in the upper panel, and IRAS 19374+2359 (dash–dotted red line) and IRAS 19348+2229 (dashed green line) in the lower panel. Note the agreement within the errors between Vesta and the PSF objects out to about the 1 per cent level.

8 μm in the Galactic Legacy Infrared Mid-Plane Survey Extraordinaire/Infrared Array Camera (GLIMPSE/IRAC) observations within the *Herschel* 70 μm resolution ($\sim$6 arcsec). However, the fraction of the emission from the MYSO at 8 μm is $\gtrsim$50 per cent and *Spitzer* Multiband Imaging Photometer (MIPS) observations show that the MYSOs largely dominate the emission at 25 μm. Therefore, multiplicity should not be a major concern.

The naive map of G030.8185+00.2729 in Fig. 2.9 shows that the pattern imprinted by the PSF, like the one in Fig. 2.4 for V1362 Aql, is not clear and therefore the object should be more extended. The same is observed in the nominal and orthogonal images of G030.8185+00.2729 in Fig. 2.10, where the Airy rings

Table 2.2: Parameters of the isolated RMS MYSOs found within the two Hi-GAL SDP fields at 70 μm.

Name	RA	Dec	d (kpc)	L ($L_\odot$)	$\sqrt{L}/d$ [b] ($L_\odot^{1/2}$ kpc^{-1})	$f_{70\mu m}$ (Jy)	$f_{170\mu m}$ (Jy)	$f_{250\mu m}$ (Jy)	$f_{350\mu m}$ (Jy)	$f_{500\mu m}$ (Jy)
G030.8185+00.2729	18:46:36.6	−01:45:22	5.7	1.1×10^4	18.4	321	269	131	57.6	22.7
G058.7087+00.6607	19:38:36.8	+23:05:43	4.4	4.4×10^3	15.1	30.9	70.5	44.4	23.2	12.2
G059.8329+00.6729	19:40:59.3	+24:04:44	4.2	1.9×10^{3a}	10.4	150	361	150	61.0	25.2

[a] Note this object is in a cluster with several other YSOs within about 5 arcsec. Its GLIMPSE 8 μm flux is only 20 per cent of the larger *MSX* beam 8 μm flux and its total luminosity has therefore been reduced by this amount to reflect the fact there may be other luminosity sources in the large beam far-IR measurements of bolometric luminosity (see Mottram *et al.* 2011b).

[b] The physical size of a spherical dusty cloud heated to a particular temperature by a central source depends on the square root of the heating source luminosity which determines the spatial scales of the solution to the RT equation (Ivezic & Elitzur 1997). The angular size is then inversely proportional to the distance. Therefore, it is an indicator of how resolved is a source (see Section 2.5).

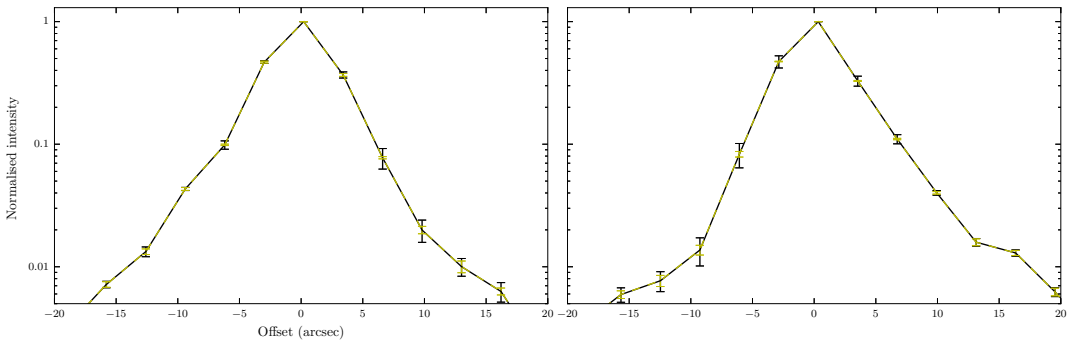

Figure 2.8: A comparison of the intensity profile of Vesta scanned once (solid black line) and Vesta scanned by a positive and negative scan leg (dashed yellow line) in the nominal (left) and orthogonal (right) directions.

which appear in Fig. 2.3 of Vesta are not observed in the MYSO images, indicating that the emission perpendicular to the scan direction is extended. Moreover, slices for the selected MYSOs were obtained following the same procedure as for the PSF objects, and are shown in Figs. 2.11–2.13. These are compared to Vesta slices and clearly show that the objects are more extended than the PSF in the minor axis direction.

2.3.2 Submm Radial Profiles

The three MYSOs were observed by APEX/LABOCA[1] (Contreras *et al.* 2013) at 870 μm as part of ATLASGAL, and one MYSO by JCMT/SCUBA[2] at 450 μm, which was obtained from the SCUBA Legacy Catalogue (Di Francesco *et al.* 2008). These ground-based observations have higher resolution than the longer wavelength observations available in Hi-GAL (500 μm). In order to compare the colder and more extended matter distribution mapped by these submm observa-

[1]LABOCA: Large APEX Bolometer Camera
[2]JCMT: James Clerk Maxwell Telescope

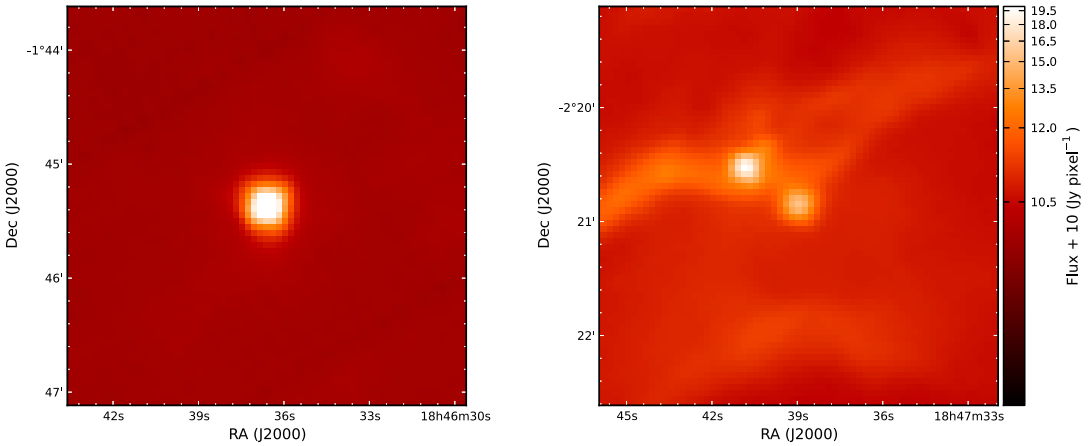

Figure 2.9: Image of the RMS MYSOs G030.8185+00.2729 (left) and G030.4117–00.2277 (right) from the naive map of the $l = 30°$ region. Note the partially resolved nature of G030.8185+00.2729 compared to the PSF star in Fig. 2.4 and the background level and morphology compared to G030.4117–00.2277.

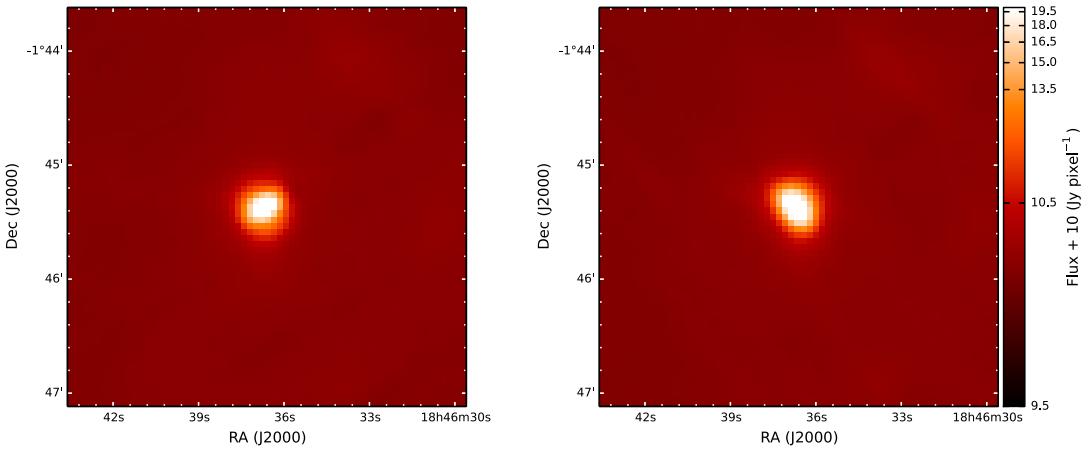

Figure 2.10: Nominal (left) and orthogonal (right) scan images for the RMS MYSO G030.8185+00.2729. The flux scale is the same for both images.

tions with the distribution of the somewhat hotter matter mapped by the 70 μm observations, azimuthally averaged radial profiles (hereafter radial profiles) were obtained and are shown in Fig. 2.14. In these radial profiles each data point is the mean flux within an annulus of width 1.5 times the pixel size (6 arcsec at 870 μm and 3 arcsec at 450 μm) centred in the intensity peak. The standard deviation of the annulus accounts for the noise in the flux and any asymmetry in the source.

2.4 Results

The modelling procedure used by de Wit *et al.* (2009) has been adapted in order to interpret the extended emission seen at 70 μm. The same grid of spherical RT models for MYSOs that was calculated by de Wit *et al.* (2009) using the DUSTY code (Ivezic & Elitzur 1997) was used, which solves the eq. 1.3 numerically. The grid of 120 000 models spans a range in density law exponent p where $n(r) \propto r^{-p}$ with p varying from 0 to 2 in steps of 0.5, A_V from 5 to 200 in steps of 5, and the ratio of outer radius to sublimation radius, $Y \equiv R_{\rm outer}/R_{\rm sub}$, varying from 10 to 5000. For this study, other model grid parameters were kept constant. These include the stellar effective temperature that was kept at 25 000 K corresponding to a B0 V star as the IR emission is insensitive to this parameter. For the dust model, the "ISM" model as described in de Wit *et al.* (2009) that consists of Draine & Lee (1984) graphite and silicate with an MRN size distribution (Mathis *et al.* 1977) was used. This has a submm emissivity law with a slope of $\beta = 2$. The dust sublimation temperature was kept constant at 1500 K.

Each model was scaled to the appropriate luminosity and distance for the

MYSOs in Table 2.2. A circular image of the emergent 70 μm emission from the spherical model was generated and then convolved with the Vesta PSF rebinned to the Hi-GAL pixel scale. As before, an intensity profile slice was generated from an average of the three rows across the minor axis of the PSF direction normalised to the peak pixel. These model slices were then compared to the observed ones, both in the nominal and orthogonal scan directions.

Simultaneously with fitting the intensity profile slice we also fitted the SED. The luminosity used to scale the models comes from fitting the SED. The data points in the SEDs in Figs 2.11–2.13 are from 2MASS (Skrutskie *et al.* 2006), GLIMPSE (Churchwell *et al.* 2009), *MSX* (Price *et al.* 2001), *Herschel* (this work), submm (Di Francesco *et al.* 2008; Contreras *et al.* 2013) and millimetre observations (Beuther *et al.* 2002a; Beltrán *et al.* 2006a). Errors of 10 per cent were adopted for all the SED data points to account for uncertainties in the absolute calibration across different data sets.

During the fitting procedure reduced-χ^2 (hereafter χ^2) values were calculated for both the fits to the intensity slice and SED, where the degrees of freedom were the number of fitted points minus one. These are each placed in order of increasing χ^2 and the model that is top of the combined order is considered to be the best-fitting model. This method was used by de Wit *et al.* (2009), but no justification was given. Jørgensen *et al.* (2002), who similarly combined SED and submm intensity profiles, argue that the χ^2 values cannot be combined because the observations are not completely independent, thus it is not statistically correct to combine them. They also argue that intensity profiles and SEDs constrain different parameters of the density distribution (see also Section 2.5). Williams *et al.* (2005) add that the χ^2 values are in different numerical scales, thus they

should be compared in an ordinal way. It can also be added that profiles can have a number of data points comparable to the SED, thus certain wavelengths will carry more weight in a total χ^2.

The best combined fits to the 70 μm intensity profile and SED for each direction are shown in Figs 2.11–2.13 whilst the parameters are listed in Table 2.3. In what follows, the results are not referred to any particular scan direction unless otherwise stated. Reasonable combined fits to the intensity profile of most of the objects are obtained with the models, with χ^2 near 1 for the 70 μm profile. The SED fit shows that fluxes at $\lambda < 3$ μm are always underestimated. This is common for spherical models as they do not account for near-IR light being scattered and escaping from the bipolar outflow cavities (de Wit *et al.* 2010). The average power-law index of the best-fitting models is $p = 0.5$.

Fig. 2.14 shows the profiles at 450 and 870 μm as seen in the combined fit of the SED and 70 μm intensity profile. Submm radial profiles were also used instead of the 70 μm slices to analyse the effects of the spatial information from different wavelengths on the density distribution fit. These profiles constrain the density distribution of the cool outer regions. The combined 870/450 μm profile and SED best fits have an average exponent $p = 0.5$, which is consistent with the combined 70 μm profile and SED fit.

Finally, fits to each individual observation were also calculated. The results show that the best fits to radial profiles have exponents between 1 and 2, whilst the fits to SEDs have exponents between 0 and 0.5. In addition, the exponent of the best-fitting models to the radial profiles is independent of A_V and the size of the cloud.

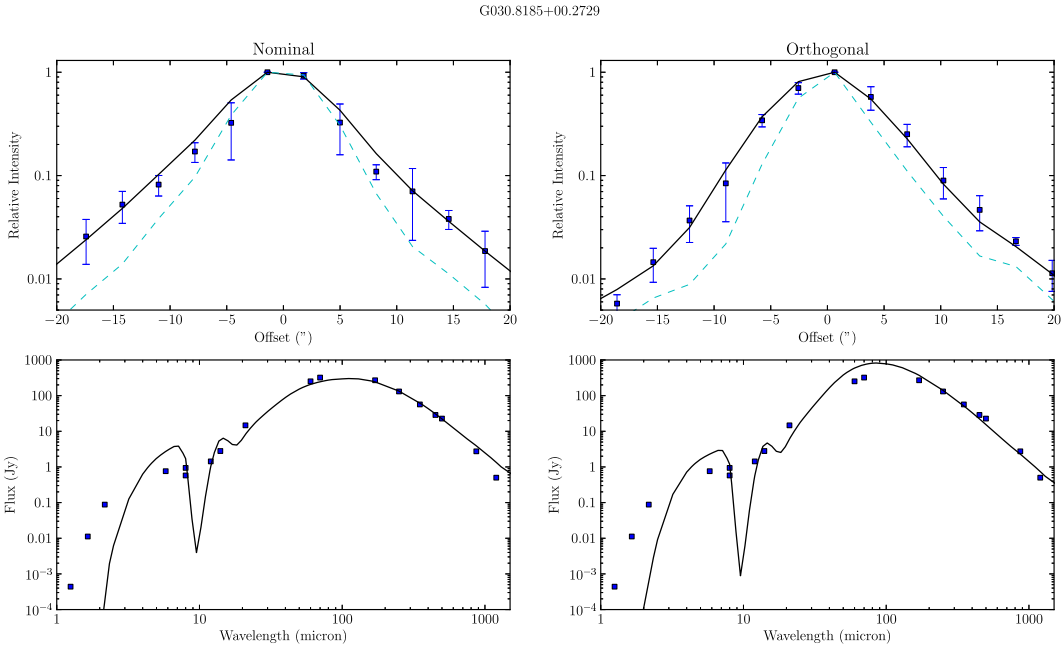

Figure 2.11: The combined best-fitting model (solid black) in terms of the 70 μm scan profile (top) and SED (bottom) compared to the data (blue squares) for G030.8185+00.2729. The left-hand panels are for the scan in the nominal direction whilst the right-hand panel is for the scan in the orthogonal direction. The Vesta PSF scan is shown in the top panel (dashed cyan) to illustrate the extended nature of the MYSO emission. An error of 10 per cent of the total observed fluxes was considered in the observed SED.

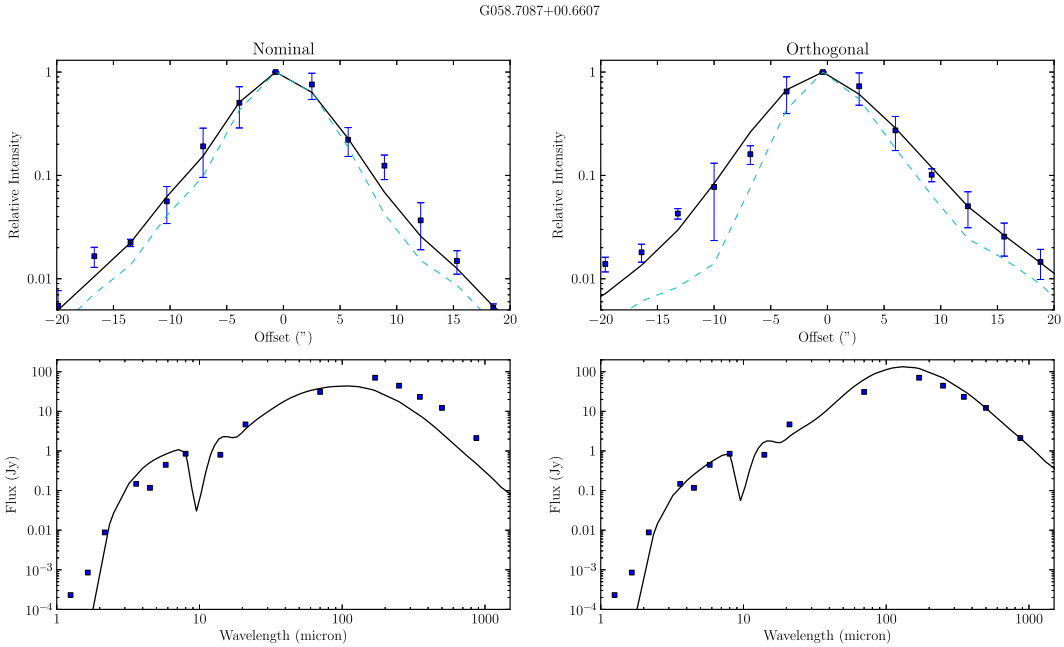

Figure 2.12: As in Fig. 2.11 but for G058.7087+00.6607.

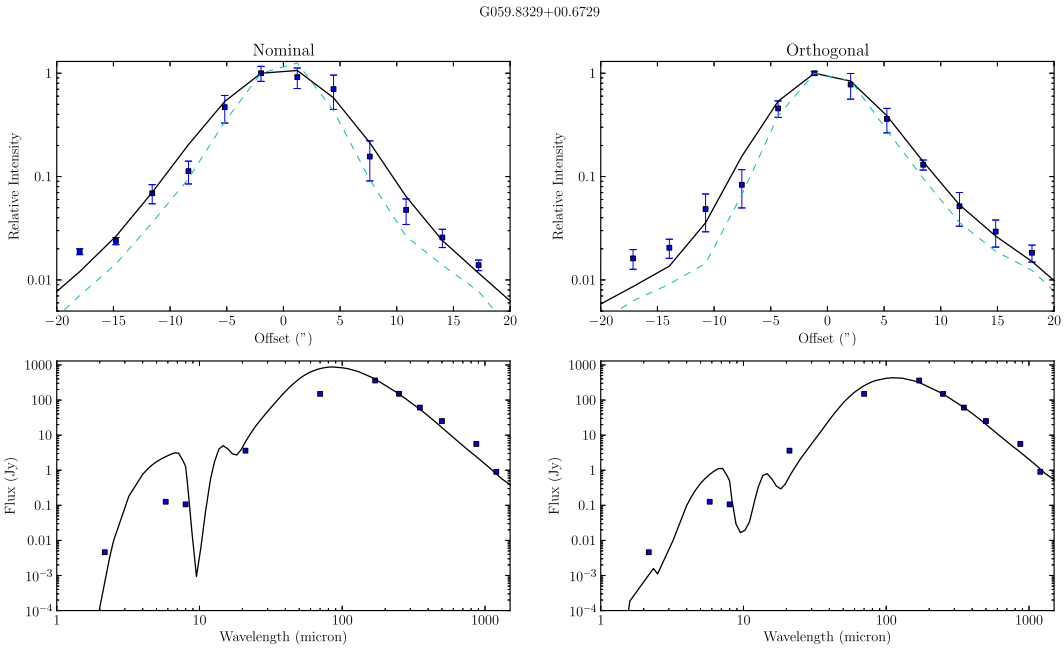

Figure 2.13: As in Fig. 2.11 but for G059.8329+00.6729.

2.5 Discussion

The average power-law index is shallower than the $p \sim 1$ exponent in the sample of de Wit *et al.* (2009) who fitted 24.5 μm intensity profiles and the SED. In addition, the averages do not agree in general with other works which have found that the values of the power-law index vary between 1 and 2 by combining SED and submm observations (e.g. Mueller *et al.* 2002). Nevertheless, in the particular case of G030.8185+00.2729, Williams *et al.* (2005) obtained an exponent of 0.5 by using the SED and 850 μm radial profile, which agrees with the results of this work. The results of Williams *et al.* (2005) where obtained by including in the SED points with $\lambda \geqslant 12$ μm whilst Mueller *et al.* (2002) included points with $\lambda \geqslant 30$ μm. Fitting only data with $\lambda \geqslant 30$ μm was also experimented upon and the results are listed in Table 2.4. It was found that in general values of exponents are 0.5 lower than using the whole SED, and therefore the exponents are still between 0 and 1. However, these fits do not necessarily match the luminosity of the source because they fit mostly submm points. It is obviously not expected to match the average results of Mueller *et al.* and de Wit *et al.* since the sample has only 3 objects.

The power-law indexes for the 70 μm slice only and 870 μm only cases vary between 1.5 and 2, whilst in the 450 μm only cases its value is $p = 1$. These values are consistent with those obtained by Beuther *et al.* (2002a), who found an average value of $p = 1.6$, even though they derived their values from a power-law fitted to the radial profiles instead of doing the RT. Of course, these models do not fit the SED well.

On the other hand, the power-law indexes for the fits to the SED only vary

between 0 and 0.5. This is similar to previous studies that use a dust emissivity law with a slope of $\beta = 2$ (e.g. Chini *et al.* 1986). As discussed by Hoare *et al.* (1991), a shallower dust emissivity law allows fits with a steeper density distribution. In fact, inspection of the SED fits at $\lambda > 100$ μm in Fig. 2.12 shows that the λ^{-2} emissivity law used in the modelling is slightly too steep. Moreover, a study of the dust emissivity law in these two regions by Paradis *et al.* (2010) shows that the emissivity slope should be $\sim$1.5 in $l = 30°$ and $\sim$1 in $l = 59°$ for a dust temperature of 30 K. The higher value of the slope found in this work would also explain the large values of A_V, for steeper emissivity laws need more dust mass to match the dust emission in the far-IR/submm.

The values of A_V range between 95 and 200 for the combined SED and slice fit, but most of the sources have an A_V of 200. This is consistent with them being massive, young and embedded objects in their parental clouds. However, de Wit *et al.* (2009) found lower values than this work. In the particular case of G030.8185+00.2729, Williams *et al.* (2005) found a value $\sim$4 times larger than the one in Table 2.3, and using the method of Mueller *et al.* (2002) similar values of A_V as those obtained by considering all the points in the SED are obtained. Either way, all these results point towards values of A_V greater than 90 mag, and the inclusion of points at smaller wavelengths does not determine the value of A_V though it helps to constrain it. The value of A_V seems to be determined by the amount of dust necessary to reproduce the far-IR/submm dust emission given its emissivity law.

Table 2.2 shows the values of the $\sqrt{L}/d$ ratio, which has previously found to be a good indicator of how resolved these objects are (e.g. Wheelwright *et al.* 2012). This ratio is proportional to the angular size of the inner rim of the spherical

Table 2.3: Best-fitting model parameters for the fits to the 70 μm intensity slice and the 450 and 870 μm radial profiles.

Name	Scan	Fit	p	A_V	Y^a	$\chi^2_{\rm SED}$	$\chi^2_{70\mu{\rm m}}$	$\chi^2_{450\mu{\rm m}}$	$\chi^2_{870\mu{\rm m}}$	$\chi^{2\ b}_{\rm SED30}$
G030.8185+00.2729	Nominal	SED + 70 μm	1.0	200	5000	109	1.4	4.7	0.23	37
		SED + 450 μm	0.5	170	2000	40	3.2	0.4	1.48	9.4
		SED + 870 μm	0.5	120	5000	73	3.6	4.1	0.04	50
		70 μm only	2.0	170	2000	2.3×10^{6}	0.3	1.1	0.14	5.6×10^{3}
		450 μm only	1.0	60	2000	1.1×10^{4}	4.9	0.2	1.04	103
		870 μm only	1.5	140	2000	2.1×10^{5}	4.3	2.0	0.001	572
		SED only	0.5	165	2000	35	2.8	0.5	1.60	9.2
	Orthogonal	SED + 70 μm	0.5	200	1000	77	0.7	1.9	2.17	40
		SED + 450 μm	0.5	170	2000	40	1.6	0.4	1.48	9.4
		SED + 870 μm	0.5	120	5000	73	13.6	4.1	0.04	50
		70 μm only	2.0	10	200	1.3×10^{11}	0.5	2.0	2.29	9.7×10^{4}
		450 μm only	1.0	60	2000	1.1×10^{4}	7.8	0.2	1.04	103
		870 μm only	1.5	140	2000	2.1×10^{5}	42.0	2.0	0.001	572
		SED only	0.5	165	2000	35	1.1	0.5	1.60	9.2
G058.7087+00.6607	Nominal	SED + 70 μm	1.0	120	5000	132	0.6	–	0.48	121
		SED + 870 μm	0.5	150	5000	62	3.2	–	0.25	6.7
		70 μm only	1.5	180	1000	1.1×10^{5}	0.6	–	0.8	2.4×10^{4}
		870 μm only	2.0	185	5000	9.7×10^{4}	1.1	–	0.01	2.9×10^{4}
		SED only	0.0	75	5000	33.4	5.0	–	0.5	12
	Orthogonal	SED + 70 μm	0.0	95	5000	45	2.6	–	0.35	7.6
		SED + 870 μm	0.5	150	5000	62	2.8	–	0.25	6.7
		70 μm only	1.5	200	5000	4.7×10^{4}	0.7	–	0.57	1.6×10^{3}
		870 μm only	2.0	185	5000	9.7×10^{4}	4.8	–	0.01	2.9×10^{4}
		SED only	0.0	75	5000	33.4	3.0	–	0.5	12
G059.8329+00.6729	Nominal	SED + 70 μm	0.5	200	1000	4800	4.8	–	1.42	313
		SED + 870 μm	0.5	200	5000	101	6.2	–	0.57	24
		70 μm only	2.0	85	50	7.2×10^{11}	4.6	–	1.61	2.1×10^{5}
		870 μm only	2.0	200	500	1.1×10^{10}	220.3	–	0.19	4.3×10^{4}
		SED only	0.0	200	5000	46	5.5	–	0.76	28
	Orthogonal	SED + 70 μm	0.0	200	2000	403	1.5	–	1.88	13
		SED + 870 μm	0.5	200	5000	101	2.0	–	0.57	24
		70 μm only	2.0	130	50	2.6×10^{11}	1.3	–	1.88	1.5×10^{5}
		870 μm only	2.0	200	500	1.1×10^{10}	40.6	–	0.19	4.3×10^{4}
		SED only	0.0	200	5000	46	2.5	–	0.76	28

Notes. The values of χ^2 correspond to the reduced χ^2.

[a] $Y \equiv R_{\rm outer}/R_{\rm sub}$ with $R_{\rm outer}$ the outer radius and $R_{\rm sub}$ the sublimation radius of the envelope.

[b] Reduced χ^2 for points with $\lambda \geqslant 30$ μm. The values in this column were scaled using these points, thus the scaling and luminosity of these models are different than the ones in the other columns. See Table 2.4 for the best-fitting models using these SED data points.

Table 2.4: Best-fitting model parameters for the fits to the 70 μm intensity slice and the SED for points with $\lambda \geqslant 30$ μm.

Name	Scan	Fit	p	A_V	Y^a	$\chi^2_{\rm SED30}$	$\chi^2_{70\mu{\rm m}}$
G030.8185+00.2729	Nominal	SED + 70 μm	0.0	160	2000	11	1.8
		SED only	0.0	105	2000	7.8	5.0
	Orthogonal	SED + 70 μm	0.5	195	2000	10	0.7
		SED only	0.0	105	2000	7.8	2.3
G058.7087+00.6607	Nominal	SED + 70 μm	0.0	140	5000	3.8	0.6
		SED only	0.0	175	5000	2.5	0.7
	Orthogonal	SED + 70 μm	0.5	65	5000	40	1.9
		SED only	0.0	175	5000	2.5	5.3
G059.8329+00.6729	Nominal	SED + 70 μm	0.0	195	2000	19	5.4
		SED only	0.0	45	5000	7.7	569
	Orthogonal	SED + 70 μm	0.0	200	2000	13	1.5
		SED only	0.0	45	5000	7.7	140

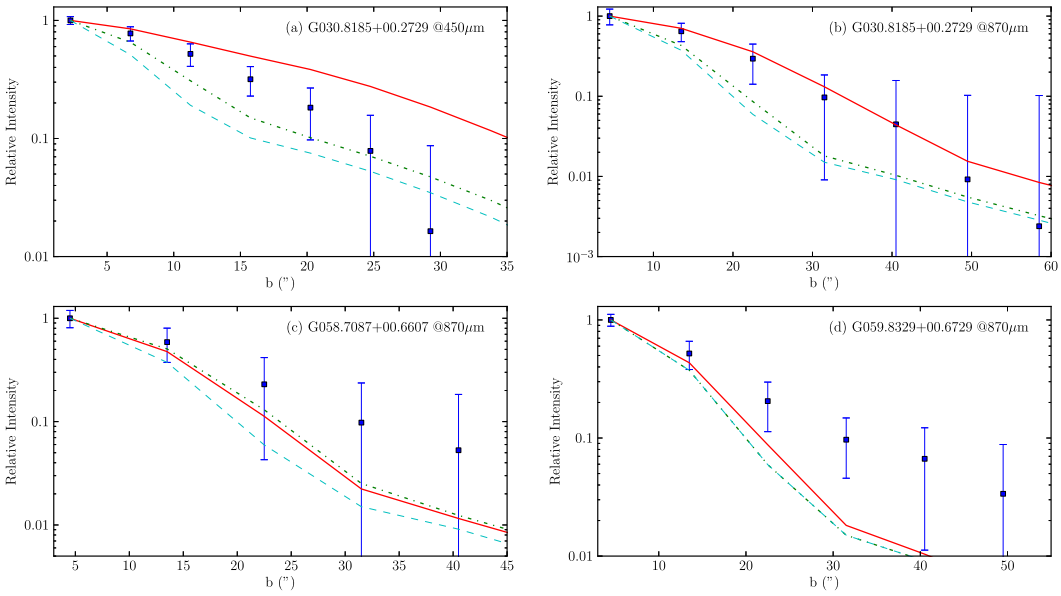

Figure 2.14: Azimuthally averaged radial profiles of submm observations for each source (blue squares). The radial profiles from the best-fitting models using the 70 μm intensity profile and SED for nominal (solid red line) and orthogonal (dash–dotted green line) directions are also shown. (a) and (b) show G030.8185+00.2729 radial profiles for 450 and 870 μm, respectively. (c) and (d) show the 870 μm radial profile of G058.7087+00.6607 and G059.8329+00.6729, respectively. The dashed cyan line corresponds to the PSF. The impact parameter b corresponds to the angular distance to the peak of the emission in the plane of the sky.

envelope (Ivezic & Elitzur 1997) and, as is shown in Table 2.3, the envelopes have sizes a few thousand times the sublimation radius ($\sim$25 au for $L = 10^4$ $L_\odot$), and should therefore be resolved at longer wavelengths. Figs 2.11–2.13 show the degree to which the objects are resolved at 70 μm agrees with this.

To explore whether this extends to the other 16 MYSOs with more complex background/neighbouring sources, the procedures used in the previous sections are repeated to obtain slices from the other sources in the Hi-GAL fields and from two models with similar physical properties as those obtained by the RT results, and then fitted 1-D Gaussian to measure the FWHM of these slices to see how resolved the sources are. Fig. 2.15 shows the relation between the FWHM and the $\sqrt{L}/d$ ratio. All observed sources are consistent with the models with some of them more extended due to the complex background.

2.6 Conclusions

70 μm observations made with the *Herschel* PACS instrument as part of the Hi-GAL survey towards two regions of the Galactic plane were investigated and three relatively isolated MYSOs were studied in detail. The peculiarities of the Hi-GAL survey PSF and its effects on the MYSOs observations were analysed. The sources in the sample are all partially resolved at 70 μm.

Using spherical RT models to simultaneously fit the 70 μm profile and SED, a density law exponent of around 0.5 is needed. This is shallower than previously found from fitting partially resolved 24.5 μm ground-based imaging, though both observations give an exponent between 0 and 1. It is also shallower than expected for infalling material ($p = 1.5$). This could be due to rotational support, but since

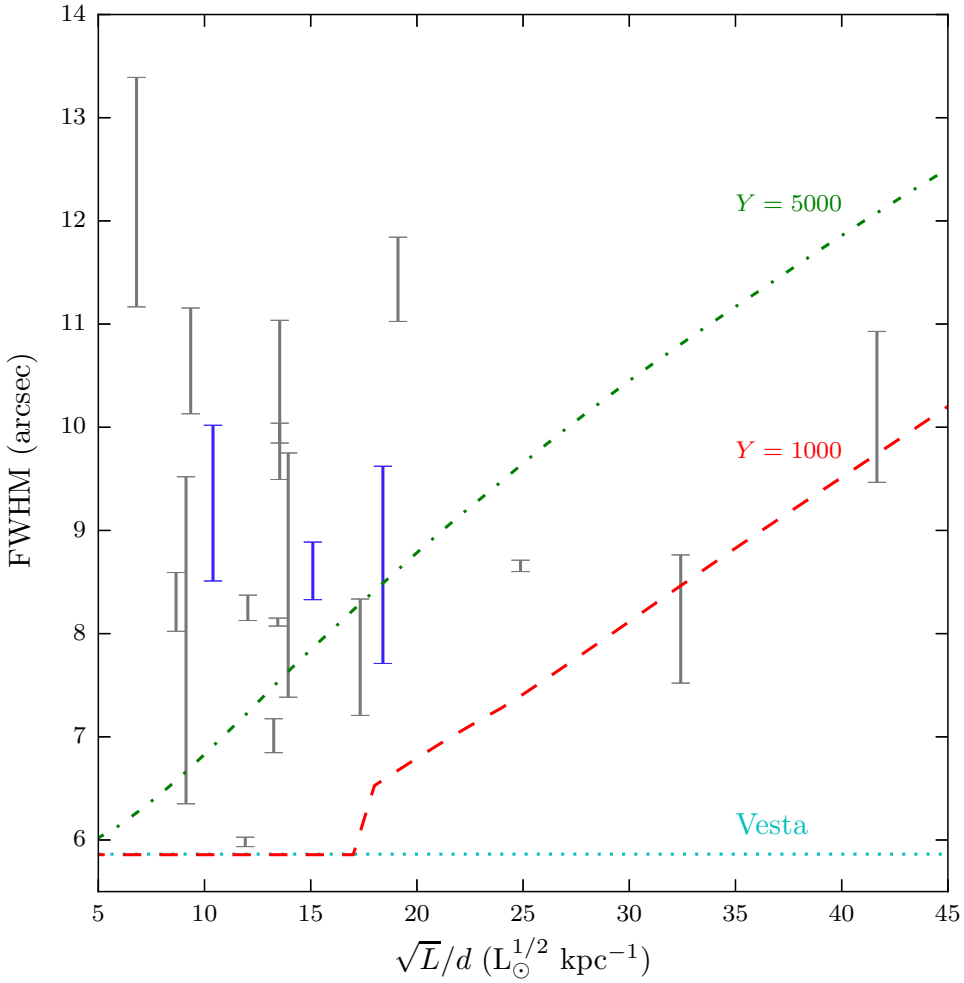

Figure 2.15: Relation between $\sqrt{L}/d$ and FWHM of a 1-D Gaussian fitted to the 70 μm slices from MYSOs in the $l = 30°$ and $59°$ fields and models. The bar ranges are defined by the FWHM of the fit to the nominal and orthogonal directions, and the blue bars correspond to the 3 MYSOs sample. The predicted relation from two models with $p = 0.5$ and $A_V = 200$ is shown in dashed red line for $Y = 1000$ and in dot–dashed green line for $Y = 5000$. Model images were convolved with the nominal Vesta PSF and a mean error of 1.2 arcsec is estimated for the Gaussian fit. The horizontal dotted cyan line represents the FWHM of the Vesta nominal slice.

the emitting region is well outside of the expected disc/centrifugal radius (less than a few thousand au, e.g. Zhang 2005) this is unlikely. It is more likely due to warm dust along the outflow cavity walls as seen in the mid-IR. This will be investigated further using 2-D axisymmetric models in the next chapter. Intrinsic asymmetry could explain why the results are not always the same on any given object from the nominal and orthogonal scan directions.

Finally, the images at 70 μm were smeared along the scan direction due to the scan speed. Moreover, the lack of PSF stars in the fields does not allow a characterisation of the PSF specific for these observations. Therefore, slow scan data, with a better behaved PSF, will be better to map and constrain the matter distribution of MYSOs. In particular, if the dust emission at 70 μm comes from a non-spherical structure like bipolar cavity walls, data at 70 μm can provide useful insights for 2-D models.

Chapter 3

Dust density and temperature distributions of the proto-typical MYSO AFGL 2591

3.1 Introduction

In the light of the results from the previous chapter and the release of *Herschel* data from other surveys, a multi-wavelength study of MYSOs can provide further constraints to the dust density and temperature distributions of their circumstellar matter. One of the sources with the highest $\sqrt{L}/d$ in the RMS survey sample, as shown in Table 3.1, and relatively isolated from other luminous IR/submm sources is AFGL 2591. It is located in the Cygnus X sky region, and it was covered by the *Herschel*/HOBYS survey[1] (Motte *et al.* 2010). The HOBYS data

[1]The *Herschel* imaging survey of OB Young Stellar objects (HOBYS) is a *Herschel* key programme. See `http://hobys-herschel.cea.fr`

Table 3.1: Top 10 RMS MYSOs sorted by $\sqrt{L}/d$.

MSX Name	RA (J2000)	Dec (J2000)	d (kpc)	L ($L_\odot$)	$\sqrt{L}/d$ ($\sqrt{L_\odot}$ kpc^{-1})
G133.7150+01.2155	02 25 40.77	+62 05 52.4	2.0	2.10×10^5	229.13
G345.4938+01.4677	16 59 41.61	–40 03 43.3	2.4	1.50×10^5	161.37
G061.4736+00.0908A	19 46 47.60	+25 12 45.4	2.8	1.40×10^5	133.63
G078.8867+00.7087	20 29 24.86	+40 11 19.4	3.3	1.90×10^5	132.09
G109.8715+02.1156	22 56 17.98	+62 01 49.7	0.7	8.40×10^3	130.93
G017.6380+00.1566	18 22 26.37	–13 30 12.0	2.2	5.30×10^4	104.64
G192.6005–00.0479	06 12 54.01	+17 59 23.1	2.0	3.60×10^4	94.87
G339.8838–01.2588	16 52 04.66	–46 08 33.6	2.7	6.40×10^4	93.70
G343.1261–00.0623	16 58 17.20	–42 52 07.1	2.8	6.60×10^4	91.75
G337.4050–00.4071A	16 38 50.21	–47 28 18.3	3.1	7.80×10^4	90.09

Notes. AFGL 2591 MSX name is G078.8867+00.7087. The units of right ascension are hours, minutes and seconds and the units of declination are degrees, arcmin and arcsec.

for the Cygnus X region were published by Schneider *et al.* (2016), however there is no published close up study of this source to date. The HOBYS survey was designed to map specific star forming regions at lower scan speeds than in the Hi-GAL survey. Therefore, it is one the best candidates to resolve the 70 μm emission since the observations will not be smeared out as in Hi-GAL.

AFGL 2591 is a well studied luminous ($L \sim 10^5$ $L_\odot$) source located at 3.3 ± 0.1 kpc (Rygl *et al.* 2012). Several radio continuum sources have been identified in this region as shown in Fig. 3.1: four sources have been classified as H II regions (VLA 1, 2, 4, 5; see Trinidad *et al.* 2003; Johnston *et al.* 2013), and one as a MYSO (VLA 3; Trinidad *et al.* 2003); and an unknown source(s) powering maser emission has also been detected (VLA 3-N Trinidad *et al.* 2013). The MYSO (AFGL 2591 VLA 3) will be referred to as AFGL 2591 as it is the one that dominates the SED from the near-IR to millimetric wavelengths (Johnston *et al.* 2013). Molecular line observations have revealed the presence of a bipolar outflow cavity in the E-W direction (Hasegawa & Mitchell 1995). The blue shifted outflow

cavity can also be observed in scattered light in the K-band (e.g. Preibisch *et al.* 2003), whilst shocked H_2 bipolar emission is detected in the same band (Tamura & Yamashita 1992; Poetzel *et al.* 1992). The blue shifted cavity K-band emission presents several features (loops) formed probably by entrainment of material (e.g. Parkin *et al.* 2009).

The qualitative analysis of CO emission by Hasegawa & Mitchell (1995) limited the full cavity opening angle to be less than 90° and its inclination with respect to the line of sight $\leqslant$45°. van der Tak *et al.* (2006) limited the inclination angle between 26 and 38° based on geometrical considerations from their Gaussian fits to molecular line emission maps and assuming that this emission traces a disc (e.g. SO_2). The near-IR polarization study by Minchin *et al.* (1991) found that a cone with an inclination of 35° can reproduce their data, however Simpson *et al.* (2013) found an inclination angle of 15° by fitting the SED and then modifying this model in order to match the morphology of their polarization data. van der Tak *et al.* (1999) fitted a 1-D spherically symmetric power law density distribution to CS isotopologues observations and then modified their best model to include an empty bipolar cavity, and found that an opening angle of 60° can better fit their data. However, the opening angle may be wider at the base of the cavity ($\theta_c \sim 100°$) as implied by the spatial distribution and proper motion of water maser emission (Sanna *et al.* 2012). The detailed RT modelling of Johnston *et al.* (2013), whose objective was to fit the SED and *JHK* 2MASS slices along and perpendicular to the outflow direction, found that the inclination angle with respect to the line of sight is constrained to be between 30–65°, and that the real cavity opening angle is not well constrained by observations as it is degenerated with the inclination angle. The position angle of the Herbig-Haro

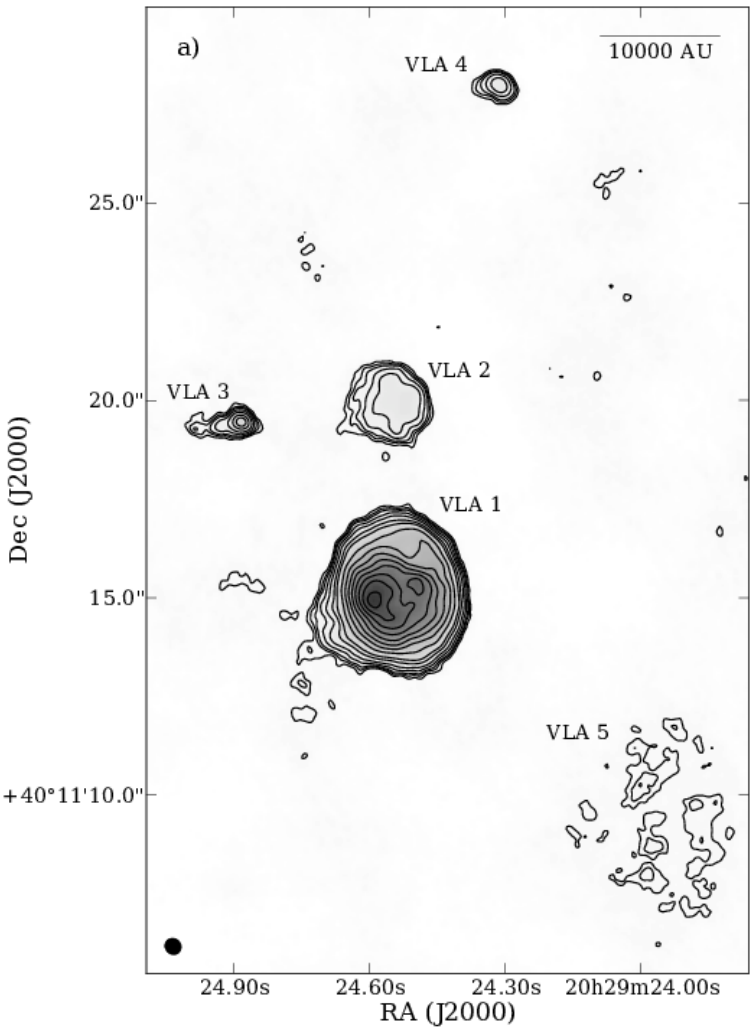

Figure 3.1: VLA 3.6 cm radio continuum from Johnston *et al.* (2013) showing the radio continuum sources in the AFGL 2591 region.

objects observed in the near-IR varies between $258 - 261°$ (Poetzel *et al.* 1992), whilst Preibisch *et al.* (2003) adopted a value of 259° for the outflow cavity symmetry axis even though the position angle of the loops ranges between $263 - 265°$ as determined from their K-band speckle interferometric observations.

The presence of a disc in AFGL 2591 is still uncertain. Through 2-D axisymmetric radiative transfer modelling of the SED and 2MASS observations,

Johnston *et al.* (2013) found that models with and without a disc can reproduce the observations. However, HDO, $H_2^{18}O$ and SO_2 interferometric observations at millimetric wavelengths point towards the presence of a sub-Keplerian disc-like structure and expanding material in the inner ∼1000 au, and the continuum is extended nearly perpendicular to the jet/outflow direction (Wang *et al.* 2012). The partially resolved source identified in the K-band speckle interferometric visibilities of Preibisch *et al.* (2003) seems to be tracing the inner rim of this disc, which has a size of ∼120 au at 3.3 kpc as derived from their modelling. The inclusion of millimetric interferometry observations into the RT modelling can help constrain the disc properties (if any) as found by other studies of MYSOs (e.g. Maud & Hoare 2013; Maud *et al.* 2013).

Zhang & Tan (2011) calculated SED and synthetic images at several near and far-IR wavelengths for a core with luminosity 10^3 $L_\odot$. The core density distribution includes a disc with accretion luminosity, vacuum outflow cavities and an envelope, all of which are integrated self-consistently and satisfy the turbulent core physical conditions. The images were convolved with PSFs of several instrument including *Herschel*/PACS. The model was then modified to include a more accurate physical description of the cavity density distribution (Zhang *et al.* 2013). In these studies, the cavity wall emission is an important feature for wavelengths up to 70 μm. However in Zhang & Tan (2011) it is not clear whether the 70 μm is extended along or perpendicular to the outflow at inclination angles similar to those above for AFGL 2591 because of the wide opening angle used (roughly twice the values stated above for AFGL 2591). In Zhang *et al.* (2013) the 70 μm emission is extended along the outflow but this is dominated by the relatively symmetrical core rather than the outflow, which extends beyond the

core radius into the empty surrounding medium. These models also have not been compared with observations of MYSOs.

The aim of this chapter is to explain the *Herschel* 70 μm emission and determine from which structure it is coming from: the rotationally flattened envelope or the outflow cavity walls. RT modelling is used in order to explain the 70 μm data. In order to constrain the density distribution used in the modelling, multi-wavelength near-IR and (sub)mm resolved high-resolution data are included. Thus the modelling uses more high-resolution constraints to study the distribution of the circumstellar matter than in Johnston *et al.* (2013). The data are presented in Section 3.2 and the modelling procedure in Section 3.3. The results of the modelling are presented in Section 3.4 and discussed in Section 3.5. Finally, the conclusions are presented in Section 3.6.

3.2 Data

3.2.1 *Herschel* 70 μm

New resolved data from *Herschel* observed as part of the HOBYS survey was used at 70 μm. The reduced data mapped using procedures from the HOBYS team was provided by F. Motte (private communication), and details of the reduction are given in Schneider *et al.* (2016). These data were taken by the PACS photometer in the parallel mode of the telescope at a scan speed of 20 arcsec s^{-1}. This produces a more symmetrical PSF ($6\farcs51 \times 5\farcs44$), which is shown in Fig. 3.2, with fewer artefacts than Hi-GAL data scanned at 60 arcsec s^{-1}, which has a $12\farcs58 \times 5\farcs85$ PSF (Lutz 2012, see previous section also). A zoom on AFGL 2591 is

Table 3.2: 70 μm angular sizes

	2-D Gaussian		Horizontal slice		Vertical slice	
Type	FWHM	PA	FWHM	FW1%	FWHM	FW1%
	(arcsec)	(deg)	(arcsec)	(arcsec)	(arcsec)	(arcsec)
Observed	14.5×12.9	253.1 ± 0.7	12.2	58.0	11.3	47.7
Model	11.0×10.0	245 ± 2	8.4	50.7	8.1	43.2
PSF	6.6×5.9^a	56 ± 1	6.1	22.9	5.9	20.7

Notes. An error of 0.02 arcsec is estimated for the semi-axes of the 2-D Gaussian fit. FW1% stands for full width at 1 per cent the peak intensity.
[a] Note this value is from the PSF binned to the observed pixel size and rotated to match the observations, hence it is different from the one presented in Table 3.3.

shown in Fig. 3.3 and provides the highest resolution in the far-IR so far. Table 3.2 lists the observed size of the 70 μm emission as obtained from a 2-D Gaussian fitted to the data, which shows that the source is well resolved by *Herschel* and that the Gaussian position angle is also close to the outflow direction. The former is also true for the horizontal and vertical slices shown in Fig. 3.3 side panels. The emission peak is shifted $\sim$3.2 arcsec to the west of the radio source position (Trinidad *et al.* 2003). However, the *Herschel* astrometry error[1] is $\sim$2 arcsec, hence the shift is not significant. In what follows it will be assumed that the emission peak at 70 μm coincides with the radio one.

3.2.2 Other multi-wavelength data

Multi-wavelength observations were used to constrain the dust density and temperature distributions. Since these images were previously reduced, only the sky level was subtracted when necessary. Table 3.3 presents a summary of the observations described below.

[1] `http://herschel.esac.esa.int/Docs/PACS/pdf/pacs_om.pdf`

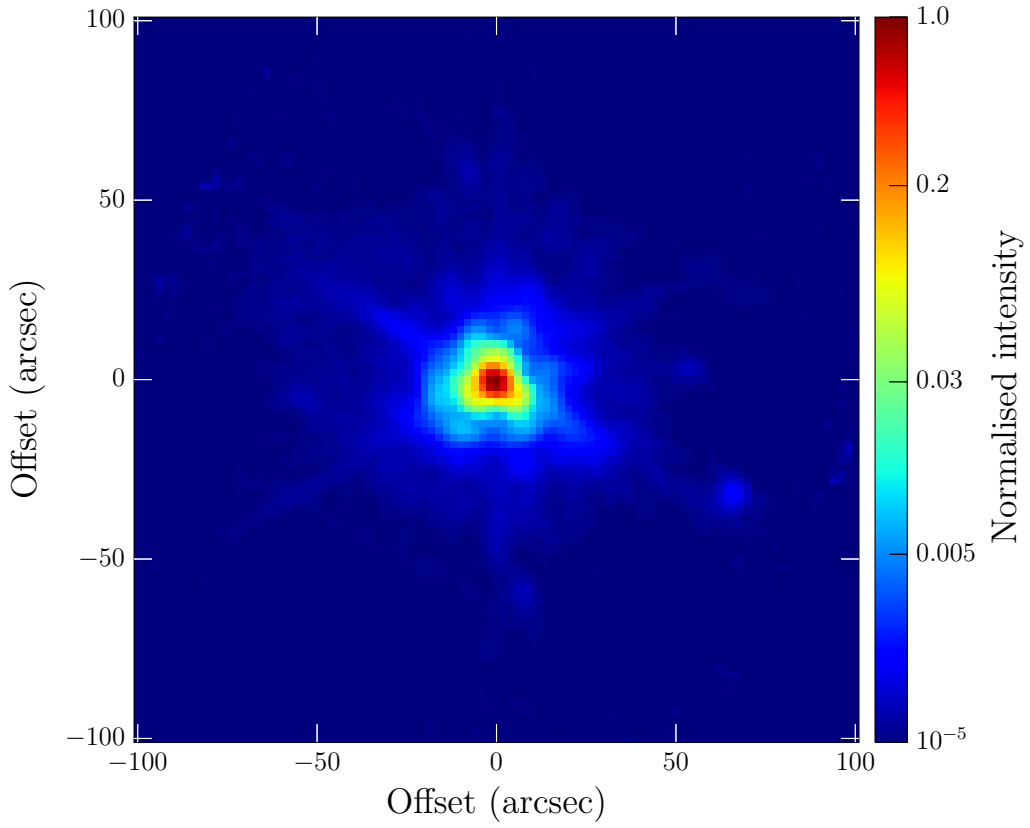

Figure 3.2: *Herschel* 70 μm PSF for the scan speed of HOBYS (20 arcsec s^{-1}). The image was produced by combining the nominal and orthogonal Vesta observations from Lutz (2012), and rotated and binned to match the HOBYS observations of AFGL 2591.

Near-IR imaging

Near-IR images from the UKIRT Wide Field Camera (WFCAM) at 1.2, 1.6 and 2.1 μm, J, H and K bands respectively, were obtained from UKIDSS and are presented in Fig. 3.4. These data have higher resolution than the 2MASS data used by Johnston *et al.* (2013), which had a resolution of $\sim$2.5 arcsec. The images were flux calibrated and error maps were obtained by using Poisson statistics on

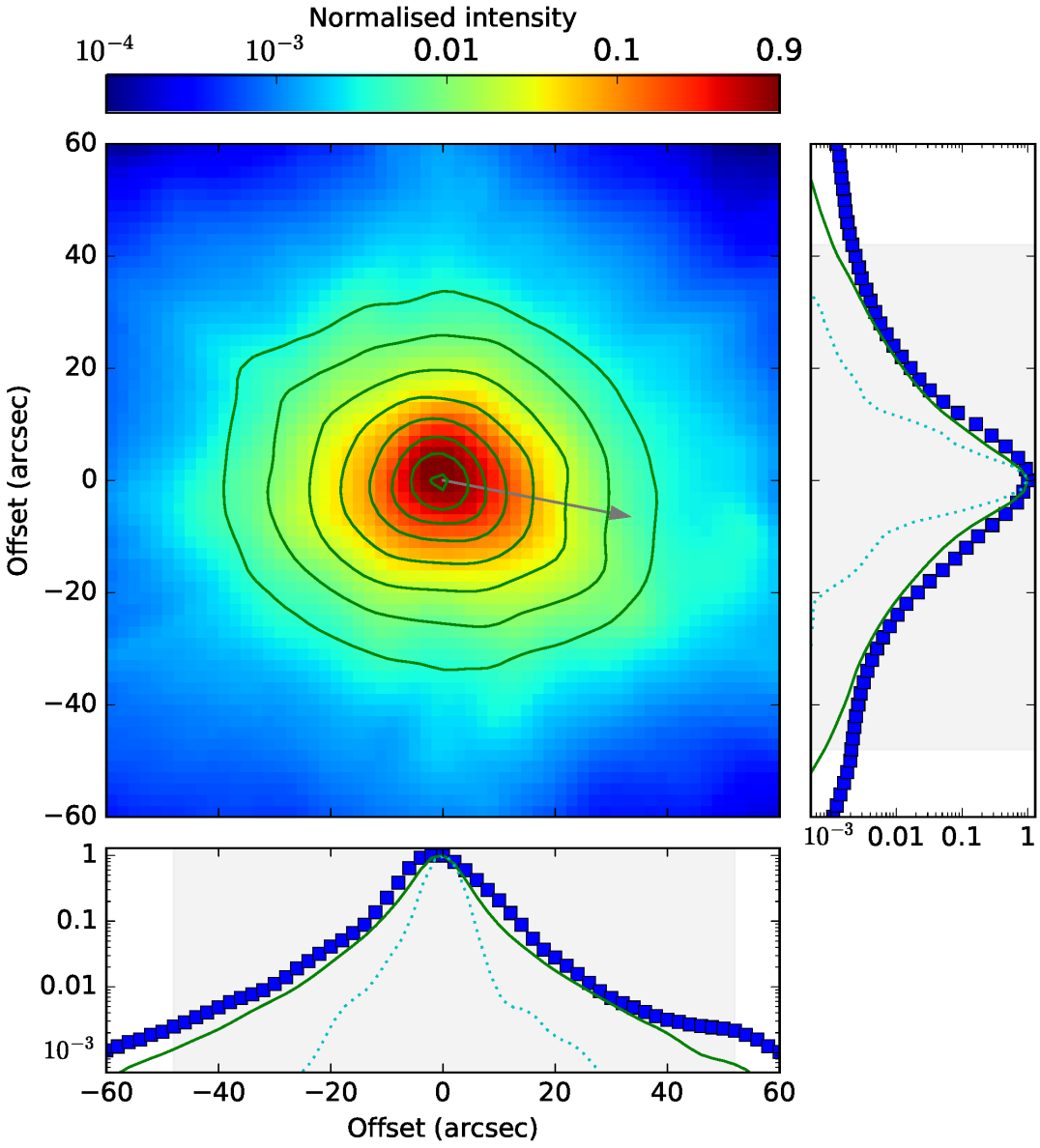

Figure 3.3: Observed (colour scale) and model (green contours) 70 μm maps of AFGL 2591. Contour levels, in intensity normalised to peak value, are 0.003, 0.006, 0.013, 0.031, 0.072, 0.167, 0.385 and 0.891. The grey arrow shows the outflow direction. Bottom and right panels show a slice through the peak in the horizontal and vertical directions, respectively. Blue squares in the side panels correspond to the observations (errors are smaller than the point size), continuous green line is the best-fitting model presented in Section 3.4 and dotted cyan line is the PSF. The shaded region enclose the points higher than 5σ with $\sigma = 50$ mJy.

Table 3.3: Summary of observations used.

λ (μm)	Instrument	Resolution	Type[a]
1.2	UKIRT/WFCAM	$0\farcs9$	I
1.6	UKIRT/WFCAM	$0\farcs9$	I
2.1	UKIRT/WFCAM	$0\farcs9$	I
2.1	SAO/6 m	$0.17''$	V
70	*Herschel*/PACS	$6\farcs51 \times 5\farcs44$	I
450	JCMT/SCUBA	$9''$	P
850	JCMT/SCUBA	$14''$	P
1300	PdBI (5Dq)	$2\farcs3 \times 1\farcs6$ PA $88\fdg7$	V
1300	PdBI (6Aq+6Bq)	$0\farcs51 \times 0\farcs33$ PA 18°	V

[a] Type of data product used: I for images, V for visibility profiles and P for azimuthally averaged radial profiles.

the un-calibrated data converted to counts. A Moffat function (Moffat 1969):

$$P(x,y) = A\left(1 + \frac{(x-x_0)^2 + (y-y_0)^2}{\gamma^2}\right)^{-\alpha} + B \tag{3.1}$$

where (x_0, y_0) is the position of the peak and B is the sky level, was fitted to several saturated and unsaturated nearby point-like sources to produce a PSF image. This function has been proven reliable in reproducing the PSF wings (e.g. McDonald *et al.* 2011). The FWHM of the Moffat function is given by:

$$\mathrm{FWHM} = 2\gamma\sqrt{2^{1/\alpha} - 1} \tag{3.2}$$

where the parameter γ and the atmospheric scattering coefficient α were obtained from the fit. The core of saturated sources were masked in order to fit better the PSF wings. The FWHMs of the fitted Moffat functions are 0.9 ± 0.1, 0.9 ± 0.2 and 0.9 ± 0.2 arcsec and the atmospheric scattering coefficients are 3.0 ± 0.4, 2.7 ± 0.4 and 2.7 ± 0.7 for the J, H and K-bands, respectively. These widths are consistent with the observed seeing FWHM of 0.8 arcsec, as recorded in the header of the

images.

In order to study the regions close to the MYSO, which are saturated in the UKIRT images, Special Astrophysical Observatory (SAO) 6m telescope K-band speckle interferometric visibilities from Preibisch *et al.* (2003) were used. The visibilities were radially averaged following the same procedure described in the previous chapter for the submm radial profile. The standard deviation of the data in each annulus was used as measure of the errors. Fig. 3.5 shows the visibility radial profile. It is worth noticing that the visibilities are reasonably symmetric which results in relatively small errors (see Preibisch *et al.* 2003, their fig. 2).

AFGL 2591 was also observed by the *Hubble Space Telescope* (*HST*) with Near IR Camera and Multi-Object Spectrometer (NICMOS) instrument. The observations were made using the polarization filters and have a resolution of 0.2 arcsec (Simpson *et al.* 2013). The published Stokes I map was provided by J. Simpson. The observations were made using a coronagraph to mask the central source emission (i.e VLA 3) and then replacing the coronagraph hole of the PSF subtracted image with the source emission observed during the same run. Although the *HST* data have a higher resolution than the UKIRT observations, they were not used in the modelling because the UKIRT data map better the extension of the blue shifted cavity.

The compatibility between the UKIRT and speckle K-band observations with the *HST* observations was investigated. The *HST* data was first aligned and binned to the UKIRT pixel size, and convolved to match the UKIRT resolution. Since the polarization band has a slightly different wavelength, the intensity of the *HST* data was scaled using the emission from the outflow cavity emission. The scaling factor was determined from the average ratio of the intensity on a pixel-

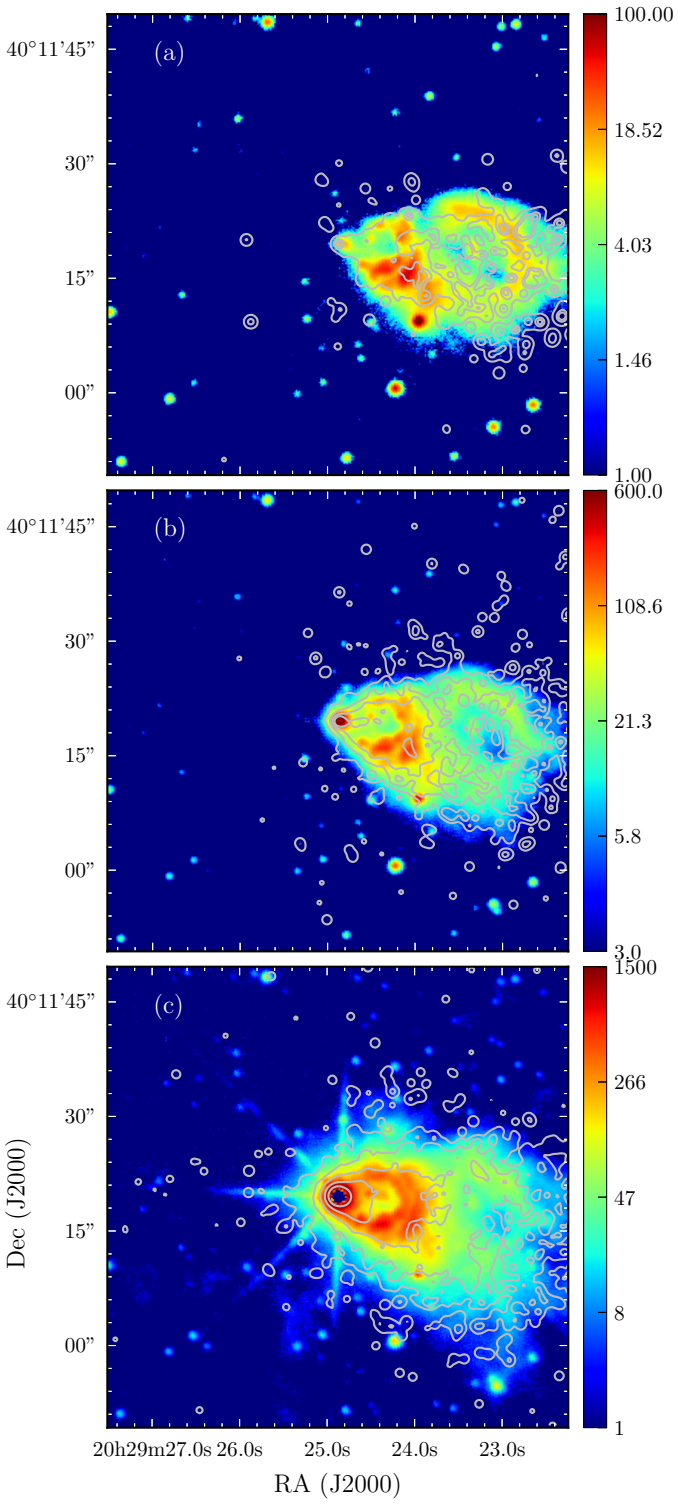

Figure 3.4: Observed (colour map) and model (white contours) near-IR maps of AFGL 2591. The J-band data and model are shown in (a) and contour levels are 1, 5 and 10 MJy sr^{-1}. (b) shows the H-band data and model in contours at levels 3, 10, 25 and 50 MJy sr^{-1}. (c) shows the K-band data and model in contours at levels 8, 30, 110, 405 and 1500 MJy sr^{-1}. The colour maps are in units of MJy sr^{-1}.

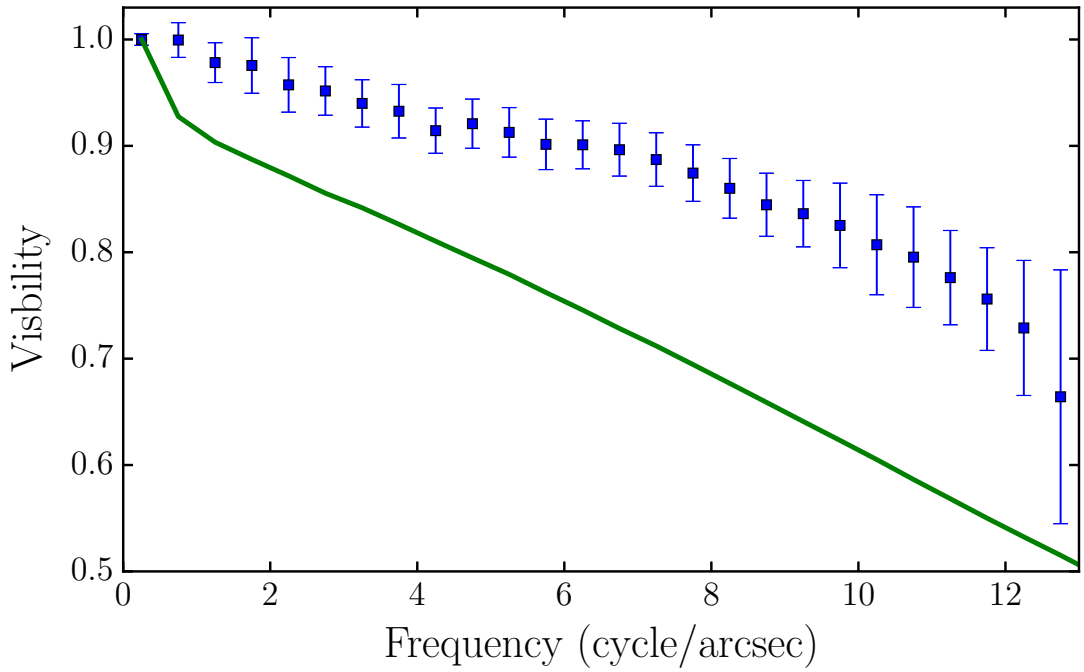

Figure 3.5: *K*-band interferometry visibilities radial profile. Observed points are represented by blue squares and the best-fitting model by a continuous green line.

by-pixel basis. Figure 3.6(a) and (b) show the degree of agreement between the UKIRT and *HST* observations for slices in the horizontal and vertical directions. Then the un-calibrated speckle observation was aligned, binned and convolved to match the *HST* data. The speckle intensity was scaled to the *HST* one by using the outflow cavity emission and the peak emission within 2 arcsec. Figure 3.6(c) and (d) show a good agreement in the regions used for the scaling. The scaling factor was used to scale the un-calibrated (high resolution) image, i.e. to produce a calibrated speckle image. Finally, the calibrated speckle image was binned and convolved to match the UKIRT observation and the comparison is shown in Figure 3.6(a) and (b).

The un-saturated region close to the star in the UKIRT observation is well

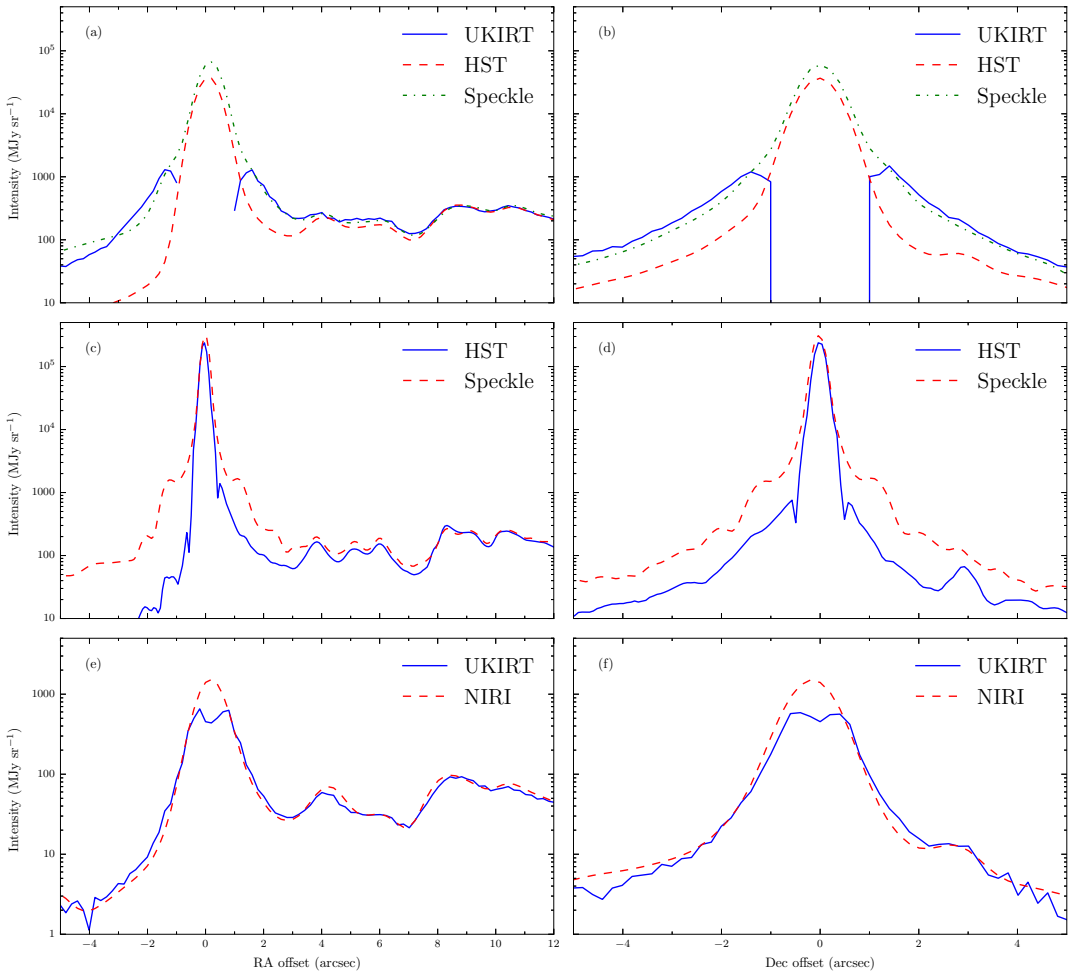

Figure 3.6: Near-IR comparison between high-resolution observations. (a) and (b) show a comparison between horizontal and vertical slices of K-band images matching the UKIRT resolution. Similarly, (c) and (d) show slices of K-band images matching the *HST* resolution. Figures (e) and (f) show slices from H-band UKIRT and Gemini/NIRI observations.

fitted by the speckle image, unlike the *HST* one which underestimates the intensity. However, the peak of the *HST* observation is consistent with the speckle one. These differences in the *HST* image may be explained by the slightly different wavelength band of the *HST* combined with the effects of the coronagraph and PSF subtraction in the central region.

A similar approach was taken in order to compare un-saturated H-band Gemini/NIRI[1] data, which has a resolution of 0.4 arcsec, and the UKIRT equivalent. The NIRI observations were made as part of the commissioning of the instrument and were not flux calibrated. Figure 3.6(e) and (f) show that there is a good agreement between both observations.

(Sub)mm

In the submm, images were obtained from the JCMT Legacy Catalogue which were taken by SCUBA at 450 and 850 μm. As in the previous chapter, a PSF composed of two Gaussians which reproduce the main and secondary lobes was used. The main lobes have a FWHM of 9 and 14 arcsec at 450 and 850 μm respectively, whilst 2-D Gaussians fitted to observed emission towards AFGL 2591 have a FWHM of $37\farcs1 \times 28\farcs5$ PA$= 247^\circ \pm 1^\circ$ and $47\farcs6 \times 38\farcs7\times$ PA$= 233^\circ \pm 1^\circ$ respectively. Hence the source is elongated with position angles of the 2-D Gaussian major axis consistent with the outflow cavity direction, as in the 70 μm data. However, since the real PSF is known to be more complicated and changes between nights (e.g. Hatchell *et al.* 2000), azimuthally averaged radial intensity profiles (hereafter radial intensity profiles) were fitted. The intensity radial profiles shown in Fig. 3.7 were calculated as the average flux of concentric

[1]NIRI: Near Infrared Imager

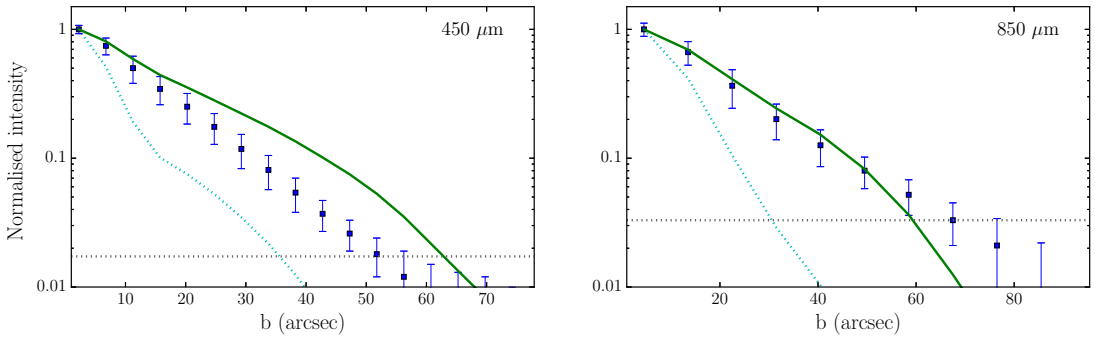

Figure 3.7: Normalised intensity radial profiles at 450 and 850 μm. Observed profiles are represented with blue squares and the best-fitting model by a continuous green line. The horizontal dotted line represents the 3σ level above zero, where σ is the noise level. Observed points above this level were compared with the model ones. The dotted cyan line shows the PSF profile.

annuli regions of constant width and their errors are the standard deviation of the enclosed fluxes.

The source has been observed in 1.3 mm dust continuum. These continuum observations were taken in August and October 2014 as part of the CORE[1] project with the Northern Extended Millimeter Array (NOEMA) in its most compact configuration. Vector-averaged radial visibility profiles were extracted, where the standard error of the mean of the points in each uv-distance bin was used as measure of the errors. A higher resolution 1.3 mm interferometric visibility profile from Plateau de Bure Interferometer (PdBI) observations was extracted from data published by Wang *et al.* (2012). The visibility profiles of both datasets are shown Fig. 3.8.

[1] `http://www2.mpia-hd.mpg.de/core/Overview.html`

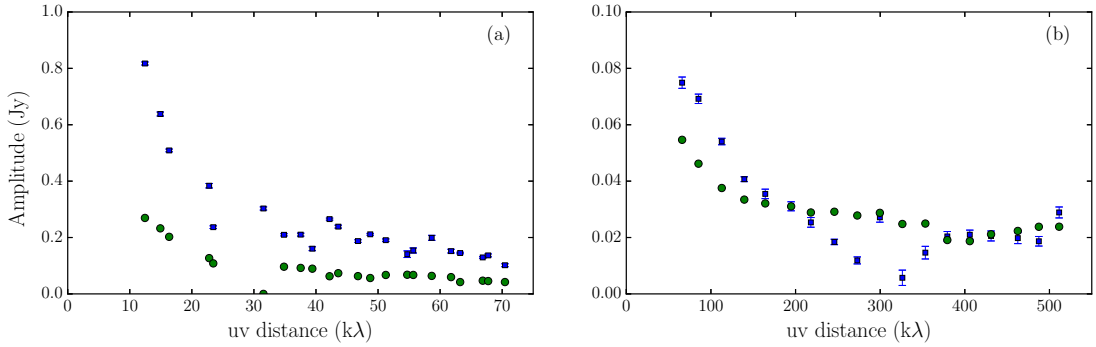

Figure 3.8: Observed (blue squares) and simulated (green circles) NOEMA and PdBI 1.3 mm interferometry visibility profiles. (a) NOEMA/CORE observations in 5Dq (compact) configuration. (b) Wang *et al.* observations in A and B (extended) configurations.

SED

Finally, the SED consists of data points from Johnston *et al.* (2013) for $\lambda < 60$ μm and the data points in Table 3.4 for longer wavelengths. The whole SED is shown in Fig. 3.9. The fluxes for the *Herschel* bands, observed by PACS and SPIRE and shown in Fig. 3.10, were obtained from the sum of all pixels with intensity higher than three times the image noise. This filters out the filamentary emission observed in SPIRE data whilst the fluxes are within the calibration uncertainties of the ones calculated with an aperture covering the whole region. The flux calibration uncertainties for PACS and SPIRE in the literature range from ∼5 to 15 per cent (e.g. Sadavoy *et al.* 2013; Roy *et al.* 2014, and Herschel online documentation[1]). A calibration error of 10 per cent was adopted for both. Despite the large number of points in the mid-IR, the best-fitting model in the RT modelling does not change if the points are weighted by the density of points in bins of $\log \lambda$ or if some points are deleted (but still following the shape of the

[1]SPIRE: `http://herschel.esac.esa.int/twiki/bin/view/Public/SpireCalibrationWeb`
PACS: `http://herschel.esac.esa.int/twiki/bin/view/Public/PacsCalibrationWeb`

Table 3.4: SED points for $\lambda \geqslant 60$ μm.

Wavelength (μm)	Flux (Jy)	Instrument	Ref.
70	5600 ± 560	*Herschel*/PACS	(1)
160	4055 ± 400	*Herschel*/PACS	(1)
250	1250 ± 125	*Herschel*/SPIRE	(1)
350	426 ± 43	*Herschel*/SPIRE	(1)
450	222 ± 110	JCMT/SCUBA	(2)
500	123 ± 12	*Herschel*/SPIRE	(1)
850	26.8 ± 5.2	JCMT/SCUBA	(2)
1200	8.1 ± 0.8	IRAM 30m/MAMBO	(3)

(1) This work. Data from PACS and SPIRE were obtained from the HOBYS observations, with SPIRE data from high gain dedicated observations.
(2) Di Francesco *et al.* (2008)
(3) Roy *et al.* (2011) based on Motte *et al.* (2007)

SED and depth of the 10 μm silicate feature).

3.3 Modelling

3.3.1 Fitting procedure

In order to explain the *Herschel* emission and the dust density and temperature distributions, the 3-D Monte Carlo radiative transfer code HYPERION (Robitaille 2011) was used to calculate SEDs and images produced by a dust distribution heated by a given heating source. HYPERION uses the Lucy (1999) approximation to find the energy field for the given input parameters and computes images using the peel-off method (mainly for scattering) and ray tracing to increase the signal-to-noise ratio of the continuum images. Ray tracing is not used for scattering. Table 3.5 presents the different density distribution types considered here. For type A, the nomenclature and fiducial values in Johnston *et al.* (2013, see also Table 3.7) were used in order to compare the results with the aforementioned

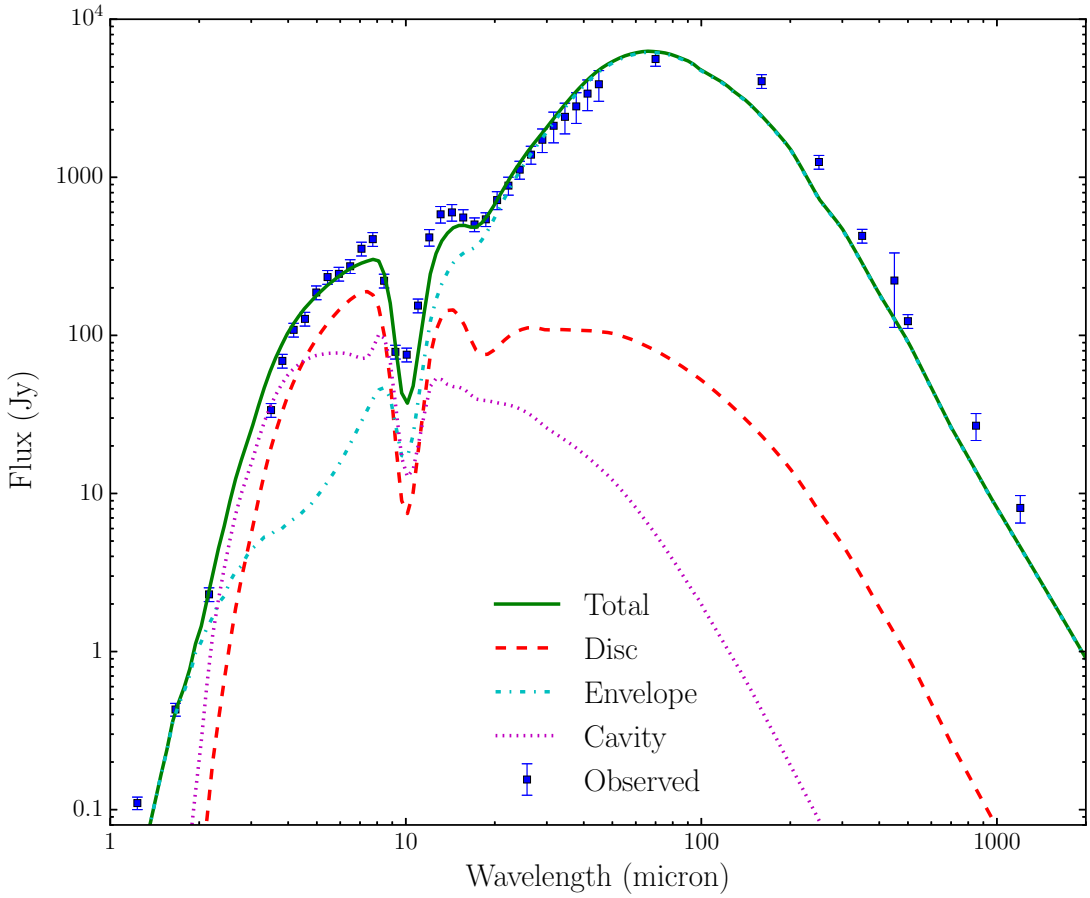

Figure 3.9: SED of AFGL 2591 and the best-fitting model. The emission from each of the different components included in the model are also shown (see legend).

paper. Types B and C are used to study the effects of different types of envelope and disc distributions on the fit.

Types A and B use the Ulrich (1976) analytical solution for rotating, infalling material. Its density distribution is given in spherical coordinates by:

$$\rho(r,\theta) = \frac{\dot{M}_{\rm env}}{4\pi(GM_\star R_{\rm c}^3)^{1/2}} \left(\frac{r}{R_{\rm c}}\right)^{-3/2} \left(1+\frac{\mu}{\mu_0}\right)^{-1/2} \left(\frac{\mu}{\mu_0}+\frac{2\mu_0^2 R_{\rm c}}{r}\right)^{-1} \qquad (3.3)$$

where $\mu \equiv \cos\theta$, $\dot{M}_{\rm env}$ is the envelope infall rate, $M_\star$ is the mass of the star, $R_{\rm c}$ is

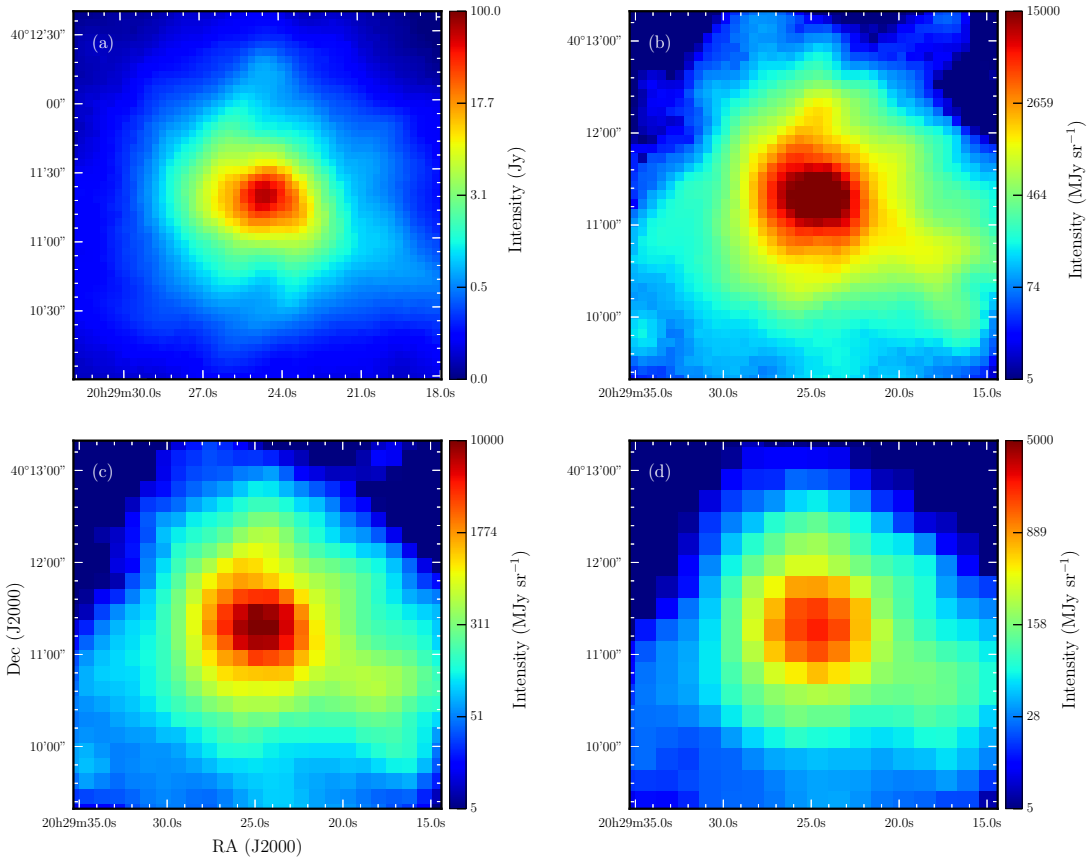

Figure 3.10: *Herschel* PACS 160 μm (a) and SPIRE 250 (b), 350 (c) and 500 μm (d) observations from the HOBYS survey.

the centrifugal radius and μ_0 can be obtained by solving the streamline equation:

$$\mu_0^3 + \mu_0 \left(\frac{r}{R_c} - 1 \right) = \mu \frac{r}{R_c} \tag{3.4}$$

This density behaves like a power law $n(r) \propto r^{-1.5}$ for distances r larger than the centrifugal radius R_c, i.e. like free-falling material, while at shorter distances the density is relatively constant.

Type B models were used to study the MYSO W33A (de Wit *et al.* 2010), and unlike type A they have an alpha disc with accretion luminosity. The disc

density distribution also differs between type A and B models. The flared disc in type A models have a density distribution described in cylindrical coordinates by:

$$\rho(\varpi, z) = \rho_0 \left(\frac{\varpi_0}{\varpi}\right)^{\alpha} \exp\left[-\frac{1}{2}\left(\frac{z}{h(\varpi)}\right)^2\right] \tag{3.5}$$

where α is the flaring exponent and the scale-height function is given by:

$$h(\varpi) = h_0 \left(\frac{\varpi}{\varpi_0}\right)^{\beta} \tag{3.6}$$

with h_0 the scale-height at $\varpi_0 = 100$ au and β the vertical density exponent. The density scale factor ρ_0 is calculated to obtain the disc mass (M_d) of a given model. The alpha-disc used in type B models have a factor $(1 - \sqrt{R_\star/\varpi})$, where $R_\star$ is the stellar radius, in the density distribution given by eq. 3.5 (see also HYPERION documentation[1]). Its accretion luminosity is given by:

$$L_\mathrm{acc} = \frac{GM_\star \dot{M}_\mathrm{acc}}{2}\left[3\left(\frac{1}{R_\mathrm{in}} - \frac{1}{R_\mathrm{c}}\right) - 2\left(\sqrt{\frac{R_\star}{R_\mathrm{in}^3}} - \sqrt{\frac{R_\star}{R_\mathrm{c}^3}}\right)\right] \tag{3.7}$$

where $\dot{M}_\mathrm{acc}$ is the accretion rate and R_in is the disc inner radius. This luminosity is obtained by integrating (Whitney *et al.* 2003):

$$\frac{d\dot{E}_\mathrm{acc}}{dV} = \frac{3GM_\star \dot{M}_\mathrm{acc}}{\sqrt{32\pi^3}\varpi^3 h(\varpi)}\left(1 - \sqrt{\frac{R_\star}{\varpi}}\right)\exp\left[-\frac{1}{2}\left(\frac{z}{h(\varpi)}\right)^2\right] \tag{3.8}$$

where $\dot{E}_\mathrm{acc}$ is the accretion energy and V the volume.

Type C is one of the proposed solutions to increase the underestimated near and mid-IR fluxes, which results from 1-D spherically symmetric envelopes used

[1] `http://docs.hyperion-rt.org`

Table 3.5: Density distributions.

Type	Density structures[a]	N^{b}_{model}
A	Ulrich envelope[c] + flared disc	514
B	Ulrich envelope[c] + alpha disc	131
C	Power law envelope[d] + flared disc	52

[a] All models include bipolar cavities.
[b] Total number of models for each type.
[c] Ulrich (1976).
[d] $n \propto r^{-p}$ with n the density and r the distance to the source.

to model SEDs and submm intensity radial profiles of MYSOs (e.g. Williams *et al.* 2005). The density distribution of this type of models is parametrised as a power law in spherical coordinates:

$$\rho(r) = \rho_0 \left(\frac{r}{r_0} \right)^{-p} \tag{3.9}$$

with $r_0 = 0.5 R_{\rm out}$, $R_{\rm out}$ the envelope radius and the density reference value ρ_0 is determined by the mass of the envelope.

All the models include outflow bipolar cavities. The cavity shape is defined by:

$$z(\varpi) = z_{\rm ref} \left(\frac{\varpi}{\varpi_{\rm ref}} \right)^{b_{\rm cav}} \tag{3.10}$$

where $z_{\rm ref} = r_0 \cos\theta_{\rm cav} \equiv 10^4$ au is the reference height where the cavity half-opening angle, $\theta_{\rm cav}$, and the reference cavity density, $\rho_{\rm cav}$, are defined, and $\varpi_{\rm ref} = z_{\rm ref} \tan\theta_{\rm cav}$. The dust density distribution in the cavity is defined by a power law as in eq. 3.9 but with $r_0 = z_{\rm ref} / \cos\theta_{\rm cav}$.

For the density distributions, the built-in HYPERION functions were used. The values of the distributions were calculated at each cell of an spherical coordinate grid. The densities of all the components are defined between the inner and outer radii, though the maximum radius of the grid can be larger or shorter than the

envelope radius. In the modelling the maximum radius of the grid was fixed to 3×10^5 au, i.e. larger than the envelope radius. To calculate the density distribution, HYPERION calculates the density distribution of each component in all the cells. Then it sums the envelope and disc components, and finally replaces the cells within the bipolar outflow cavities, which were set initially to the envelope density, by the density of the cavity component. The model grid consisted of 700 cells with a logarithmic distribution in the radial direction and 200 cells with a sinusoidal distribution in the elevation direction, thus improving the number of cells close to the inner radius and mid-plane. For most of the models 5×10^6 photons were used for all the calculations (specific energy calculation and imaging).

Table 3.3 lists the data product type that is compared for each observation. To obtain each of these data products from the synthetic images and compare them with the observed ones, the model images were binned to match the observed pixel size, rotated to match the cavity position angle (259°; Preibisch *et al.* 2003) and convolved with the respective PSF.

When images are used, these are compared on a pixel-by-pixel basis by aligning the emission peak. For the UKIRT images, the observed World Coordinate System information in the image headers is used to align the images because the peak emission is saturated. The images are convolved with the respective PSF, where the PSF rotation has also been taken into account. To compare the images, they were also masked to isolate the source and exclude emission which cannot be reproduced by the model because of its symmetry. In the H and K bands this includes features in the outflow cavity (the so-called 'loops'), other stars sources inside and outside the cavity and the saturated central region.

The Monte Carlo noise in these two bands was reduced in a 2-step process.

First, isolated pixels were identified by approximating pixels with fluxes lower than 10^{-10} Jy sr^{-1} to zero and using a median filter of size 2. This filters out pixels which are located in the outskirts of the cavity and in other regions alike. Then, to recover the pixels in the outskirts of the cavity, the local density of pixels with values larger than zero was calculated in a 7×7 pixel^2 box. The percentile 75 of the local density values of any given image was used as threshold so pixels in high density regions, like the outflow cavity, are not filtered out. The total flux of the noise reduced image is within $\sim$20 per cent of the original image.

A similar procedure was followed to obtain the images used for the model radial intensity profiles. These images were not rotated since the PSF is symmetric and only radial profiles are compared. With these images the same steps utilised to obtain the observed profiles were followed (see §3.2). In these cases, points whose observed intensity is higher than three times the image noise are compared.

In the particular case of the K-band speckle interferometric visibilities the model image was Fourier transformed and then the visibility radial profile was obtained. For the mm interferometric data, CASA (McMullin *et al.* 2007) was used to simulate the observed visibilities from the model images. Noise was added to the simulated observations. For reproducing the observed PSF properties as close as possible, the on-source integration time, antenna configurations and hour angle of the observations are utilised. The simulated observations have a PSF FWHM of $2\farcs3 \times 1\farcs8$ with PA$= 93^\circ$ and $0\farcs51 \times 0\farcs40$ with PA$= 20^\circ$ in the NOEMA and PdBI observations respectively (cf. Table 3.3).

In order to determine the best model, the reduced χ^2 was first calculated for each of the types of data in Table 3.3 and the SED. Similarly to Williams

et al. (2005), the rank of the models for each of these reduced χ^2 was calculated, i.e. the rank of the models for each of the types of data. Finally, these ranks were combined to obtain an average rank per model. In the particular cases of the K-band and 1.3 mm observations, where there are two measurements for the same wavelength, the average rank of the two observations was calculated at each wavelength before they were combined with the results from the other observations. The best model is the one with the lowest average rank.

Most initial parameters values were taken from the results of Johnston *et al.* (2013), where the average values of the two envelope with disc models were used, like the disc scale height and density in the cavity, and those obtained for the MYSO W33A by de Wit *et al.* (2010), like the envelope infall rate. The cavity density distribution ($\rho \propto r^{-e}$) and shape parameters ($z \propto \varpi^{b_{\rm cav}}$) were taken from observations and theoretical models of outflows (e.g. Preibisch *et al.* 2003; Cantó *et al.* 2008). These parameters were varied and new models computed based on the fitting statistics and a visual inspection of the results, rather than building a grid of models. Since analyses of the effects of changing each parameter in the model images and SED already exist (e.g. Alvarez *et al.* 2004), the models were built from this knowledge and the previous studies of this source.

3.3.2 Constraints on parameter space

Models with an envelope and a cavity were used to determine the stellar luminosity that best fits the SED peak. A stellar luminosity value of $L = 1.6 \times 10^5$ $L_\odot$was obtained, which is slightly lower than the value in the literature ($L = 2 \times 10^5$ $L_\odot$; Lumsden *et al.* 2013). The luminosity was kept constant during most of the it-

erations and the models were calculated with stellar temperatures $T_\star = 10000 - 40000$ K. Models with other luminosities were also calculated in order to improve some fits, e.g. $L = 1.4 \times 10^5$ $L_\odot$ for models with WD01 dust (see below), or to compare with the literature value. The stellar spectrum was assumed to be that of a black body and its radius, $R_\star$, was calculated self-consistently with the temperature and luminosity.

Based on Davies *et al.* (2011) calculations, a ZAMS stellar mass of $M_\star \sim 40$ $M_\odot$ was estimated for a stellar luminosity of $L = 1.6 \times 10^5$ $L_\odot$. However, as the envelope density has the form:

$$n = n_0 f(\mathbf{r}, R_c) \propto \frac{\dot{M}_{\rm env}}{\sqrt{M_\star}} f(\mathbf{r}, R_c) \tag{3.11}$$

for a given envelope density, the stellar mass and the infall rate are degenerate parameters. The stellar mass becomes important only in models with an alpha disc with accretion luminosity ($L_{\rm acc} \propto M_\star$). All the results presented here use a stellar mass of 40 $M_\odot$, which in turn decides the determined infall rate.

The empirical expression found by Whitney *et al.* (2004) was utilised to estimate the dust sublimation radius:

$$R_{\rm sub} = R_\star \left(\frac{T_{\rm sub}}{T_\star} \right)^{-2.1} = \left(\frac{L}{4\pi\sigma} \right)^{0.5} T_\star^{0.1} T_{\rm sub}^{-2.1} \tag{3.12}$$

where σ is the Stefan-Boltzmann constant and the sublimation temperature was fixed to $T_{\rm sub} = 1500$ K. The second equality was obtained by assuming that the star radiates as a black body. For a luminosity of $L = 1.6 \times 10^5$ $L_\odot$ and stellar temperatures $T_\star = 10000 - 40000$ the sublimation radius from eq. 3.12 ranges

between 30–40 au. The model inner radius $R_{\rm in}$ was set to this value for all the density distributions explored. Sublimation of dust was allowed during HYPERION iterations by decreasing the dust density in those cells exceeding an upper limit dust sublimation temperature of 1600 K. Although this value is higher than the one used to estimate the inner radius, from eq. 3.12 the range of sublimation radius values are in a similar range. This upper limit was reached by most models at each density component.

The disc mass was kept $M_{\rm disc} \lesssim 0.1 M_{\star}$ and its radius below 1000 au, which are close to the values found by Wang *et al.* (2012), which were determined from the total flux of their interferometric observations at 1.3 mm. For most models, parameters describing the disc flaring and vertical density distribution were fixed to the values in Johnston *et al.* (2013, $\alpha = 2.25$ and $\beta = 1.25$), and the disc radius was fixed to the centrifugal radius in most cases. In the few cases where they were varied, their lower limits were those of a steady Keplerian disc in Alvarez *et al.* (2004), i.e. $\alpha = 1.88$ and $\beta = 1.13$, and upper limits of $\alpha = 2.5$ and $\beta = 1.5$. The scale height was chosen to produce a physically thin disc.

The cavity density distribution exponent took values of 0, 1.5 and 2, but for most models the exponent was 2. For its shape, values of 1.5 and 2 were used in most models. The full opening angle was varied between 50–80°, whilst the inclination angle took values between 20–40° in steps of 5°.

For type B models, the α-disc parameters were fixed to their flared disc equivalent in type A models, whilst the envelope and cavity parameters were constrained in the same ranges as type A models. The disc accretion rate, which determines the accretion luminosity, was 1×10^{-4} $\mathrm{M}_{\odot}$ yr^{-1} in most models, which is $\sim$10 per cent the envelope infall rate. For a typical disc with an inner radius of

35 au, outer radius of 100 au and 1 $M_\odot$, an accretion luminosity of $\sim$15 $L_\odot$ is obtained from eq. 3.7. Therefore, the main difference with the flared disc model is the density distribution.

The density power law exponent of type C models was fixed to $p = 2$. Their mass was varied between $1 \times 10^3 - 5 \times 10^3$ $M_\odot$, which is close to the envelope mass of type A models. Disc and cavity parameters are constrained in the same ranges as type A models.

In total there are 15 free parameters defining each density distribution and heating source for model types A–C without including the dust models, the stellar mass and stellar radius. The inner radius depends on other parameters, and a few of them are not expected to be well constrained by the modelling based on the observations available. These include the parameters defining the disc flaring and density structure (3 parameters) and the stellar temperature. The latter converged to different values for the three types of models presented in Johnston *et al.* (2013), but their inner radius, which was not well constrained, did not depend on this parameter. Therefore, there are 10 free parameters which can be constrained by the observations.

The observed SED has 41 measurements. In the images, the independent data points can be approximated as the area of the pixels within each observation mask divided by the solid angle of the PSF. If the PSF is assumed Gaussian then the solid angle is $\Omega_{\rm PSF} = 2\pi\sigma^2_{\rm PSF}$ with $\sigma_{\rm PSF}$ the standard deviation of the PSF. This gives roughly 160 independent points for the 70 μm observation and 2700 for each UKIRT masked observation. For the other observations the number of fitted points ranges between 7–24, but the number of independent points should be around half of those. Therefore, the number of independent points,

and considering that the observations trace different emitting regions, should be enough to constrain the effective 10 free parameters.

3.3.3 Dust models

Models including dust libraries with different dust optical properties were calculated. The purpose of using different dust libraries is two-fold. On the one hand, changing the dust properties can improve the fit. On the other hand, they can provide information about the dust properties of each density component (e.g. disc, envelope). Table 3.6 lists the dust models used for each density component.

For the WD01 dust model, the dust properties were calculated by using Mie theory[1] together with the dust size distribution as calculated by the available online scripts[2] and the dust optical properties of Laor & Draine (1993), so the dust properties are close to the published ones.

Other dust libraries with different far-IR slopes were also used on a few models (e.g. KMH dust with ice mantles), but they did not improve the fit and are not included here. Models 1 and 2 from Wood *et al.* (2002) were not included in order to reduce the parameters in the fit, and only model 3 was used in order to analyse the effect of grain growth and because it is the dust model with the flattest emissivity index.

[1] HYPERION's bhmie code wrapper
[2] `http://physics.gmu.edu/~joe/sizedists.html`

Table 3.6: Different dust libraries used in the models and their locations.

Dust	Structures	β^{a}	$a_{\rm min}$ (μm)	$a_{\rm max}$ (μm)	Size dist.	Ref.
OHM92	envelope, disc, cavity	2.0	0.005	0.25	MRN+CDE	(1)
KMH	envelope, cavity	2.0	0.0025	–	MEM	(2)
WD01	envelope	1.7	0.00035	$\sim$1	pl + log-normal	(3)
W02-3	disc	0.4	–	1000	pl	(4)

Notes. MRN is a power law with index –3.5, CDE stands for continuous distribution of ellipsoids, MEM corresponds to maximum entropy method fitted to data and which can be approximated by a power law plus an exponential, and pl stands for power law.
[a] Dust emissivity index measured between $100 - 1000$ μm.
References. (1) Ossenkopf *et al.* (1992) silicates and MRN amorphous carbon grains (Mathis *et al.* 1977), see also de Wit *et al.* (2010); (2) Kim *et al.* (1994); (3) Weingartner & Draine (2001) for $R_V = 5.5$; (4) Wood *et al.* (2002) model 3.

3.4 Results

The extended emission observed at 70 μm is relatively well fitted by the model up to $\sim$40 arcsec from the centre as shown in Fig. 3.3. In general, the model matches the elongation in the data. At 1 per cent of the peak intensity, where the model has a better fit, the horizontal slice, which cuts through the cavity, is more elongated than the vertical one in the model and the observations as listed in Table 3.2. This cannot be explained by any asymmetry in the 70 μm PSF, which is relatively symmetric as shown in the same table. Fig. 3.11 shows the 70 μm image before convolution with the PSF, where the contribution of the cavity to the elongation can be observed. The emission is underestimated close to the source and along the cavity axis (PA= 259°). As a result, the angular sizes at the FWHM from slices and 2-D Gaussian fit listed in Table 3.2 are similar between each direction. Figs. 3.12 and 3.13 show how the 70 μm extended emission changes with different inclination and opening angles. Although the changes seem to be small, models with larger inclination angles ($\sim$40°, cf. Fig. 3.12b) or wider

opening angles ($\sim$80°, cf. Fig. 3.12d) provide a better fit at 70 μm. In addition, Fig. 3.13 shows that the inclination angle affects mainly the extension of the emission along the outflow cavity whilst the change in opening angle affects both directions but the change is more subtle. However, the increase in these angles do not increase the emission closer to the source as observed. The increase in these angles also do not reproduce the J and H-band observations well as shown in Figs. 3.14(b), (d) and 3.15 because their cavities are wider than observed or the emission of the red shifted cavity starts to increase as shown in the model K-band image in Fig. 3.16. Furthermore, higher inclinations produce a deeper silicate feature as shown in the SED in Fig. 3.17(a) whilst a higher opening angle overestimates the fluxes between $\sim 2 - 8$ μm as shown in Fig. 3.17(b).

The best-fitting model is a type A model. Its parameters are listed in Table 3.7 and the ranking and reduced χ^2 values for each observation are listed in Table 3.8. Fig. 3.18 shows the density and temperature distribution of the best-fitting model at different scales. Its envelope has a radius roughly a factor 1.4 shorter than the initial one and has a similar size to the model with disc of Johnston *et al.* (2013). The disc mass did not change from the initial parameters, which is around one order of magnitude smaller than in Johnston *et al.* (2013). The disc scale height and the radius are also smaller roughly one and two order of magnitude to those in Johnston *et al.* (2013), respectively. The shape of the cavity changed from the initial exponent of 1.5 to 2.0, and its reference density decreased a $\sim$15 per cent from its initial value and its density exponent did not change. The cavity opening angle was slightly smaller than the initial one ($2\theta_{\rm cav} = 60°$).

The model SED agrees reasonably well with the observations as shown in Fig. 3.9. The total mass of the model, $M = 1.4 \times 10^3$ M$_\odot$, is enough to fit the

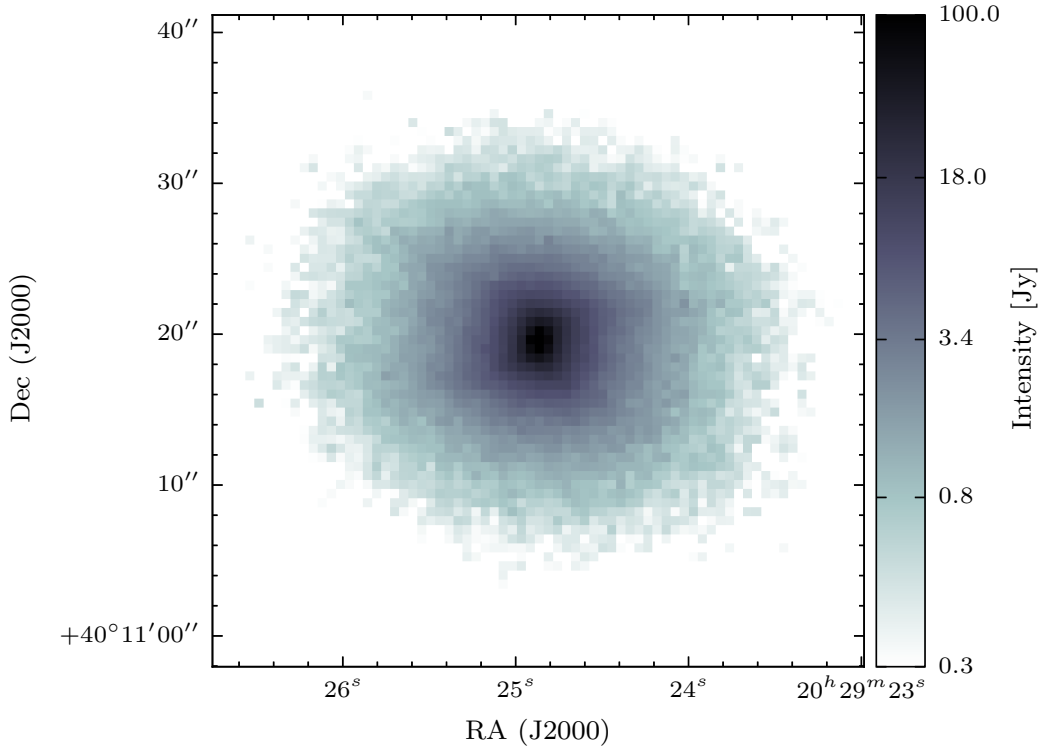

Figure 3.11: Best-fitting model 70 μm image before convolution. Note the elongation along the cavity axis oriented at PA= 259°.

10 μm silicate feature relatively well at an inclination of 30°, but it is not high enough to closely fit the submm points. This is 200 $M_{\odot}$ more massive than the model with disc of Johnston *et al.* (2013). Models with WD01 dust can improve the fit in the submm, however they underestimate the fluxes between 3–8 μm by a factor ∼10 as shown in Fig. 3.17(c).

The near-IR maps in Figs. 3.4(a)–(c) show that the near-IR band images are well reproduced. However, Fig. 3.5 shows that the small scales closer to the star position probed by the speckle observation are not well reproduced. In general, most models with a cavity density of the same order as the best-fitting model do not fit this observation. A model with similar cavity properties but with a

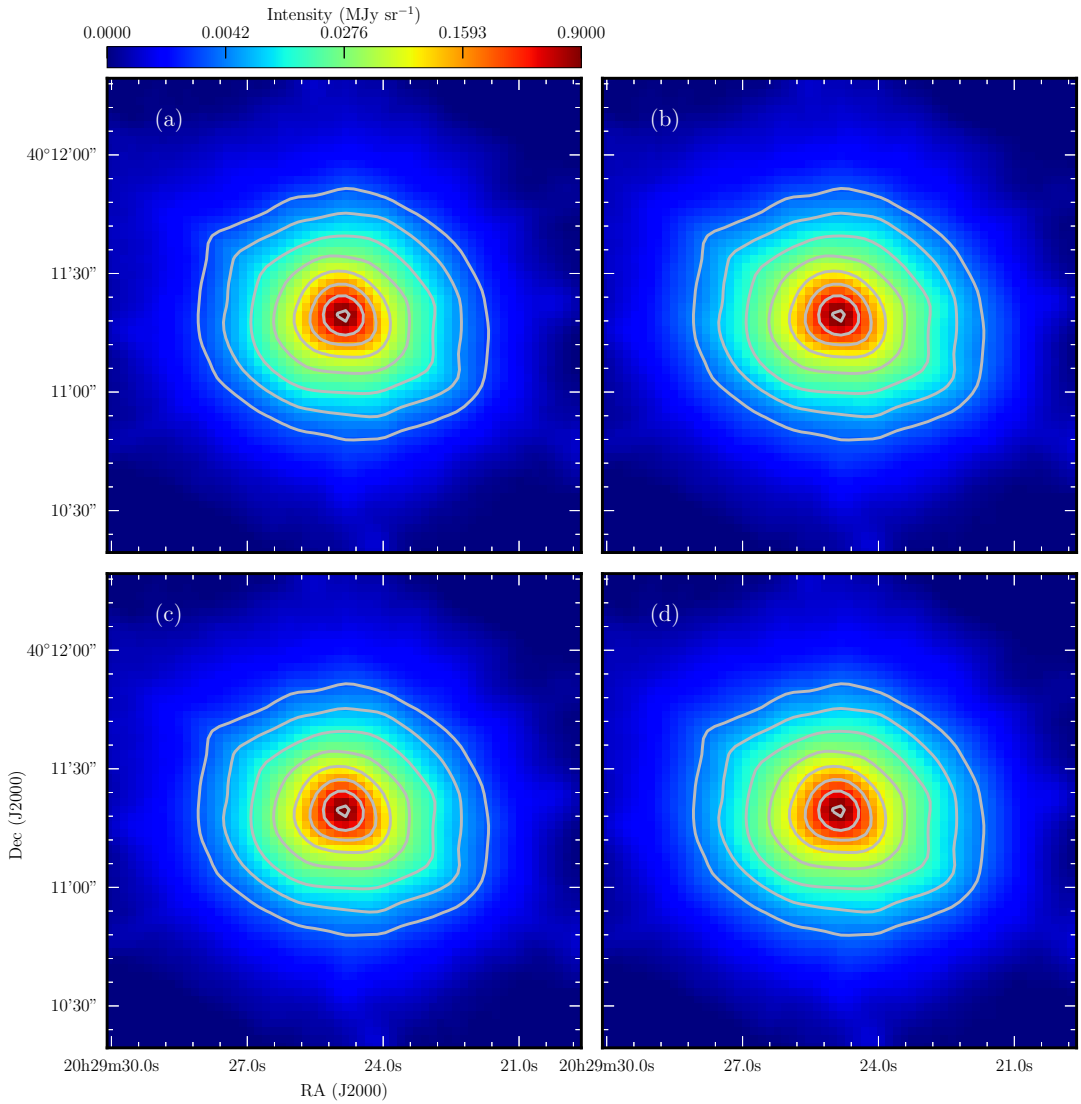

Figure 3.12: 70 μm models with different inclination and opening angles compared to the best best-fitting model ($i = 30°$ and $\theta_{\rm cav} = 28°$, contours). (a) is the best-fitting model observed at an inclination angle of 20° and (b) the same model at 40°. (c) and (d) are models with the same input parameters as the best-fitting one but with half opening angles of 25° and 35°, respectively. All images have been normalised to the peak intensity and have the same color scale. The contours levels are 0.003, 0.006, 0.013, 0.031, 0.072 0.167, 0.385 and 0.891 in peak intensity scale.

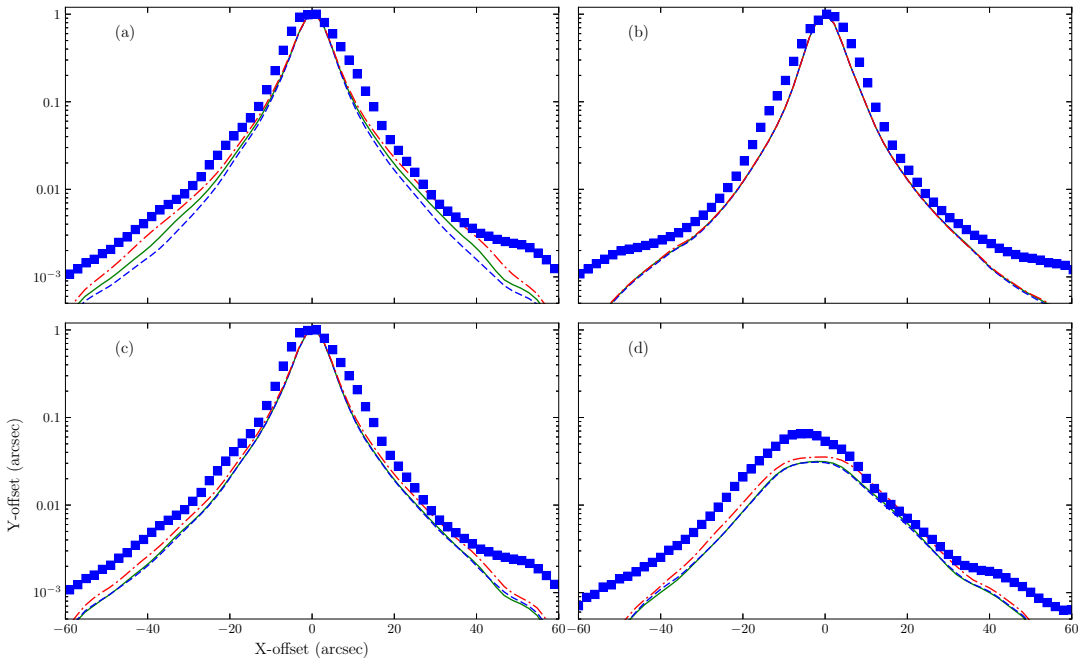

Figure 3.13: 70 μm slices of the images in Fig. 3.12. The blue squares show the observed data and have errors smaller than the size of the points. The left column shows an horizontal slice through the peak, i.e. along the outflow cavity, whilst the right column shows a vertical slice. (a) and (b) show the change in these slices at 20° (dashed blue line), 30° (continuous green line) and 40° (dot-dashed red line) inclination angles (cf. Fig. 3.12a and b). (c) and (d) show the slices at 25° (dashed blue line), 28° (continuous green line) and 35° (dot-dashed red line) half opening angles (cf. Fig. 3.12c and d). The slices in (d) where taken at an 16 arcsec offset west from the peak. Note that the different centre of the slices in (d) is due to the PA of the outflow cavity.

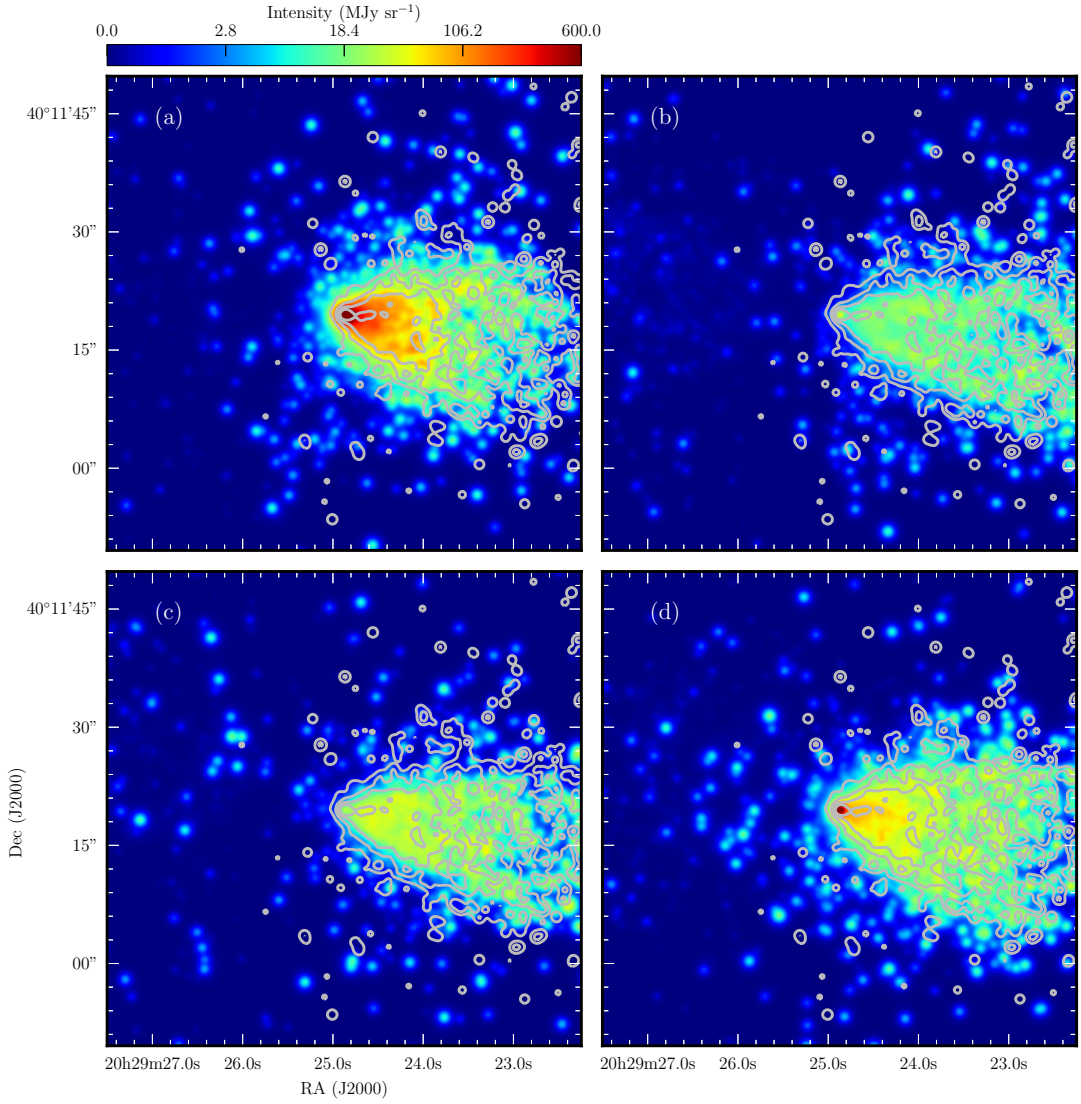

Figure 3.14: H-band models with different inclination and opening angles compared to the best best-fitting model ($i = 30°$ and $\theta_{\rm cav} = 28°$, contours). Contour levels are 3, 10, 25 and 50 MJy sr^{-1}. (a) is the best-fitting model observed at an inclination angle of 20° and (b) the same model at 40°. Note the change in the extension and intensity level of the cavity. (c) and (d) are models with the same input parameters as the best-fitting one but with half opening angles of 25° and 35°, respectively. A clearer view of the effect of changing the opening angle in the cavity emission intensity level is shown in Fig. 3.15. All images are in the same intensity scale.

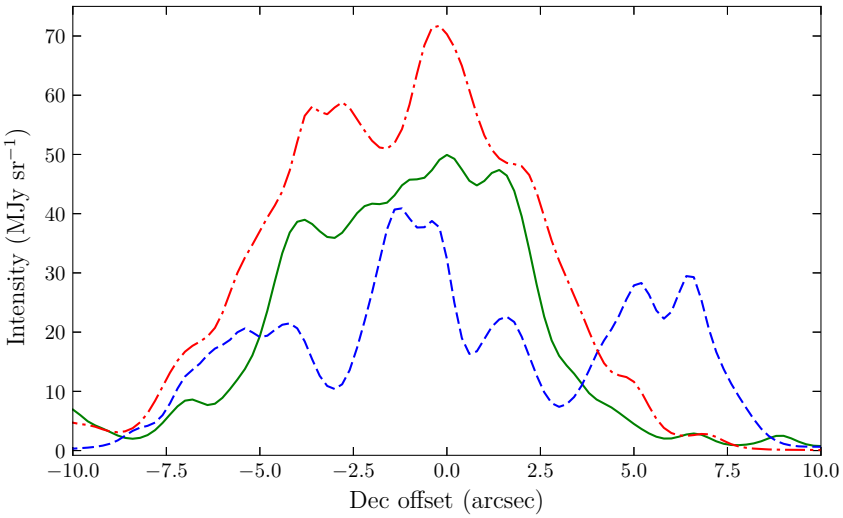

Figure 3.15: Vertical H-band slice across the outflow cavity at a distance of 5 arcsec west from the emission peak and averaged over a 1.2 arcsec slit. The continuous green line shows the best-fitting model ($\theta_{\rm cav} = 28°$), the dashed blue line shows the slice for a model with $\theta_{\rm cav} = 25°$ (cf. Fig. 3.14c) and the dot-dashed red line shows the slice for a model with $\theta_{\rm cav} = 35°$ (cf. Fig. 3.14d).

density a factor $\sim 10^{-3}$ smaller can improve the fit as shown in Fig. 3.19. The latter however underestimate the SED mid-IR fluxes, as is shown in Fig. 3.17(d), and do not fit the near-IR images as there is less (scattered) emission from dust in the cavity.

At 450 μm, the best model overestimates the emission at larger scales as shown in Fig. 3.7. The same happens in all the A and B models, whilst C models with WD01 dust are able to reproduce this profile but not the near-IR observations. At 850 μm, most of the models reproduce the radial profile relatively well. These two fits are unaffected by the inclination angle. However, an analysis of the observed images shows that the observed source is more elongated along the cavity at both wavelengths, but this is not seen in the models.

The PdBI extended array visibilities are well fitted as shown in Fig. 3.8(b).

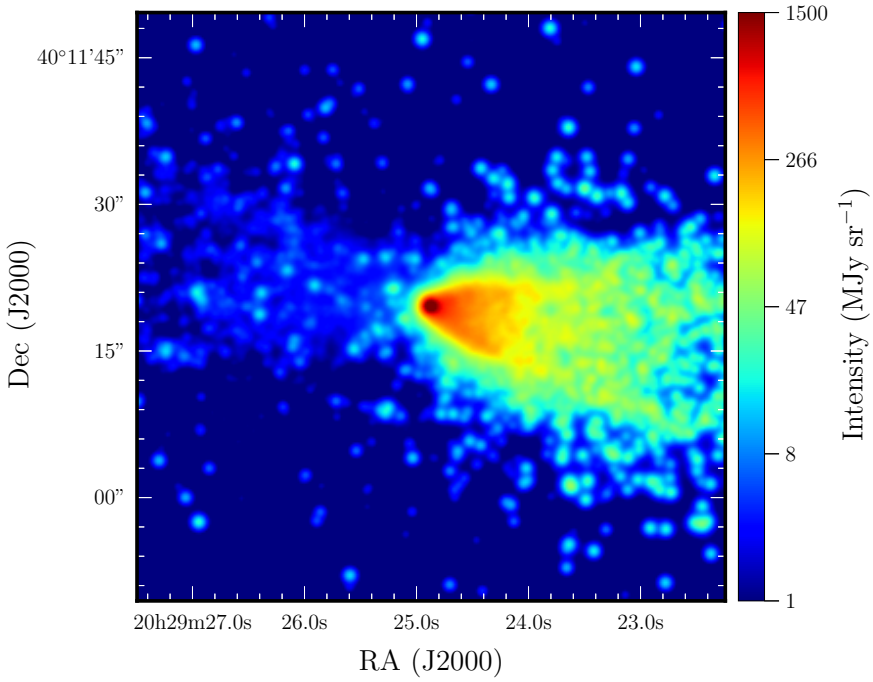

Figure 3.16: UKIRT K-band model image at 40° inclination angle (cf. Fig. 3.4c).

Figs. 3.20(c) and (d) shows that models with WD01 dust are able to improve the fit for baselines smaller than ∼150 kλ. For longer baselines, Fig. 3.21 shows that the intensity is determined mainly by the mass of the disc, 1 $M_{\odot}$ in the best-fitting model. In addition, Fig. 3.22 shows that the PdBI 1.3 mm visibilities decrease with increasing centrifugal radius at a constant disc mass, but the changes are less sensitive to this parameter than the mass. The best-fitting model underestimates the observed 1.3 mm visibilities at large spatial scales (smaller uv distances). In the NOEMA compact array observation (Fig. 3.8a) this is observed in most models. However, Figs. 3.20(a) and (b) shows that those models with WD01 dust give an improvement of the fit, but they do not fit the short wavelengths ($\lambda < 12$ μm) of the SED as shown in Fig. 3.17(c).

CLEAN images were produced from the 1.3 mm visibilities and are shown

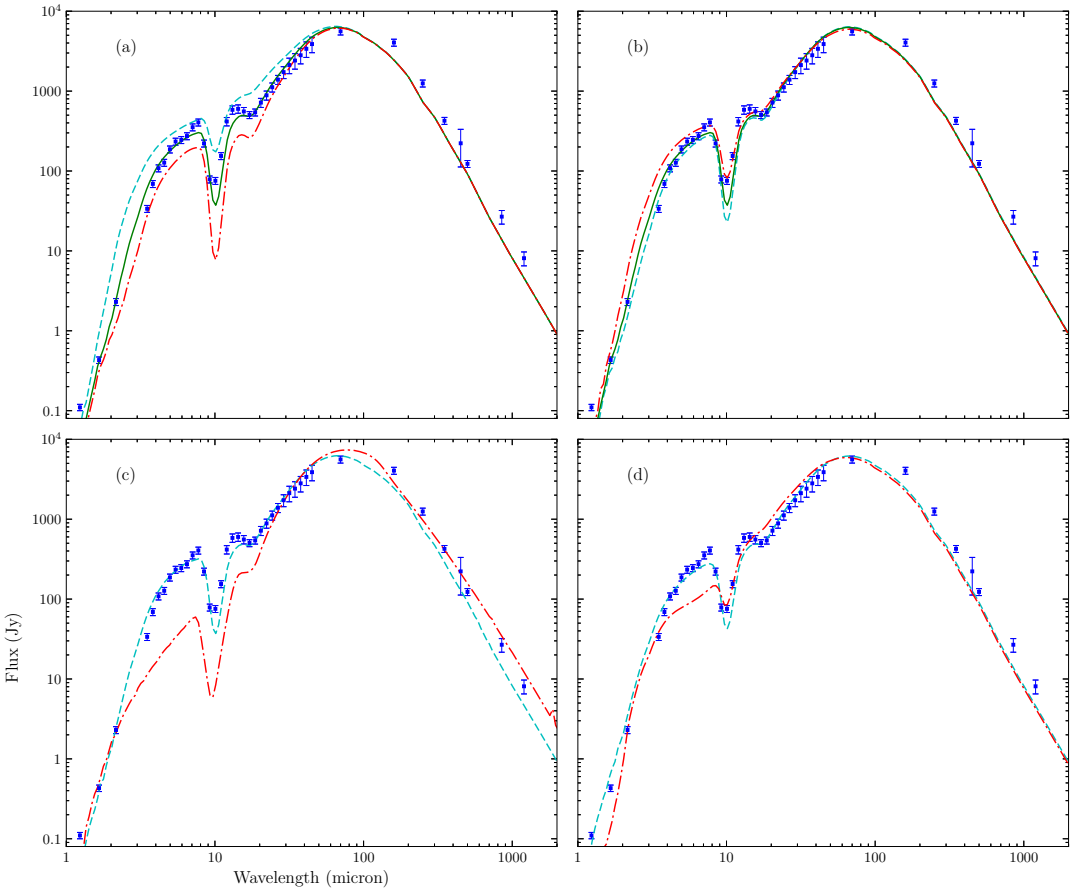

Figure 3.17: SED comparison for different models. The blue squares show the observed SED and the best-fitting model in continuous green line (only (a) and (b)). (a) shows the SEDs of the best-fitting model (cf. $i = 30°$) as observed with 20° and 40° inclination angles in dashed cyan and dash-dotted red lines, respectively. (b) dashed cyan line shows a model with the same input parameters as the best-fitting model (cf. $\theta_{\rm cav} = 28°$) but with a 25° half opening angle whilst the dot-dashed red line shows the same model but with a 35° opening angle. (c) shows a comparison between models with OHM92 (dashed cyan line) and WD01 (dot-dashed red line) dust in the envelope. (d) shows the change in the SED when the cavity reference density is decreased from $1.2{\times}10^{-21}$ g cm^{-3} (dashed cyan line) to $2{\times}10^{-24}$ g cm^{-3} (dot-dashed red line).

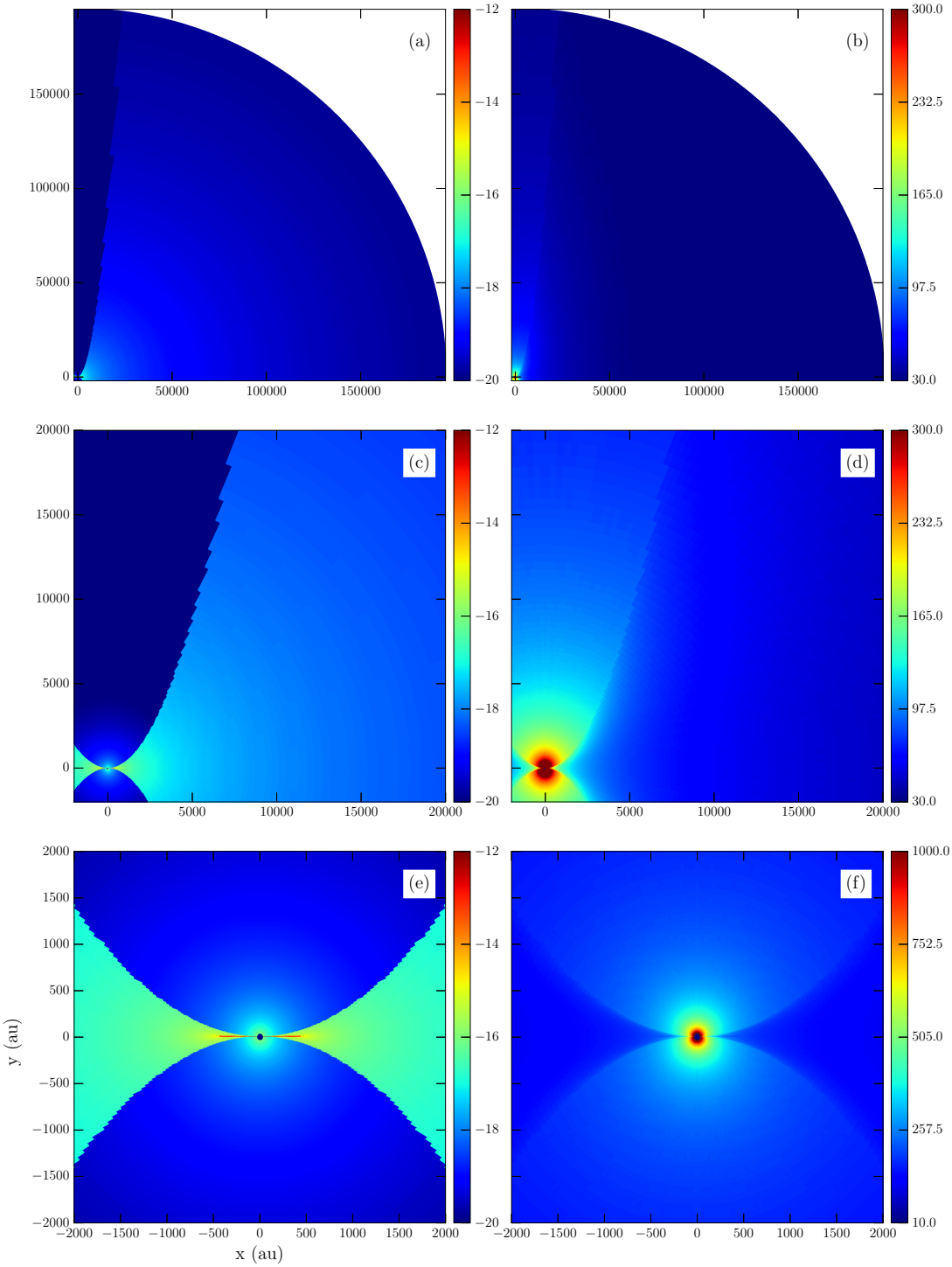

Figure 3.18: Density and temperature distributions of the best-fitting model. The logarithm of the density in units of g cm^{-3} is plotted in the left column and the temperature in units of K in the right column.

Table 3.7: Parameters of the best-fitting model.

Parameter	Value	Constrained by
Distance	3.3±0.1 kpc	Fixed
Position angle (PA)	259°	Fixed
Inclination angle (i)	30°±5°	SED + near-IR
Stellar temperature ($T_\star$)	18000 K	–
Stellar luminosity ($L_\star$)	1.6×10^5 $L_\odot$	SED
Inner radius ($R_{\rm in}$)	36 au	SED + Speckle
Outer radius ($R_{\rm out}$)	200000 au	Submm
Envelope infall rate ($\dot{M}_{\rm env}$)	$(1.4 \pm 0.2) \times 10^{-3}$ $M_\odot$ yr^{-1}	SED + (sub)mm
Envelope dust	OHM92	–
Centrifugal radius ($R_{\rm c}$)	440±200 au	SED+PdBI
Disc mass ($M_{\rm d}$)	1.0±0.5 $M_\odot$	PdBI
Disc scale-height at $r = 100$ au (h_0)	0.6 au	–
Disc flaring exponent (α)	2.25	–
Disc vertical density exponent (β)	1.25	–
Disc dust	OHM92	–
Cavity opening angle[a] ($2\theta_{\rm cav}$)	57°±10°	Near-IR
Cavity shape exponent ($b_{\rm cav}$)	2.0	–
Cavity density exponent (e)	2.0	–
Cavity reference density[a] ($\rho_{\rm cav}$)	1.4×10^{-21} g cm^{-3}	near-IR+SED
Cavity dust	KMH	–

[a] Defined at a height $z = 10^4$ au.

in Fig. 3.23. Due to the apparent presence of two sources south of VLA 3, the NOEMA image was fitted with three 2-D Gaussian components and the results are listed in Table 3.9. At $\sim 10^4$ au scales, as mapped by the NOEMA 1.3 mm compact configuration observations in Fig. 3.23(a), the model FWHM is $3\farcs6 \times 3\farcs2$ PA= 328°±3° as obtained from a 2-D Gaussian fit. This is slightly more extended than the observed size in Table 3.9 and has a different orientation. The presence of at least one source to the south of VLA 3, as shown in Fig. 3.23, may also contaminate the submm observations making them look more elongated than they really are. The position of one of these sources is close to VLA 1 and its total flux (∼0.1 Jy) is consistent with the value predicted from the VLA 1 radio spectral index ($\alpha = 0$, Johnston *et al.* 2013). A more complete modelling of VLA 3 including the contribution of VLA 1 is beyond the scope of this thesis.

Table 3.8: Overall ranking and reduced χ^2 values for the best-fitting models of each type.

Type	Rank[a]	70 μm	SED	J	H	K		450 μm	850 μm	1.3 mm		χ^2	$\langle\chi^2\rangle$
						UKIRT	Speckle			PdBI	NOEMA		
A	777	174	7.3	24.1	68.3	347	28.1	17.2	0.47	56.5	1650	146	166
B	1020	158	7.7	23.6	74.6	404	32.0	17.3	0.51	147	2140	167	206
C	956	335	20.3	23.9	119.6	514	2.1	3.6	0.10	34.8	665	219	139
Best-fitting model by χ^2													
A	1161	108	13.3	27.2	87.1	195	31.1	20.0	0.63	156	2280	103	199
Best-fitting model by $\langle\chi^2\rangle$													
A	1066	129	17.5	27.3	82.5	305	21.5	22.7	0.47	355	938	138	136

[a] Average weighted ranking as described in Section 3.3.1.

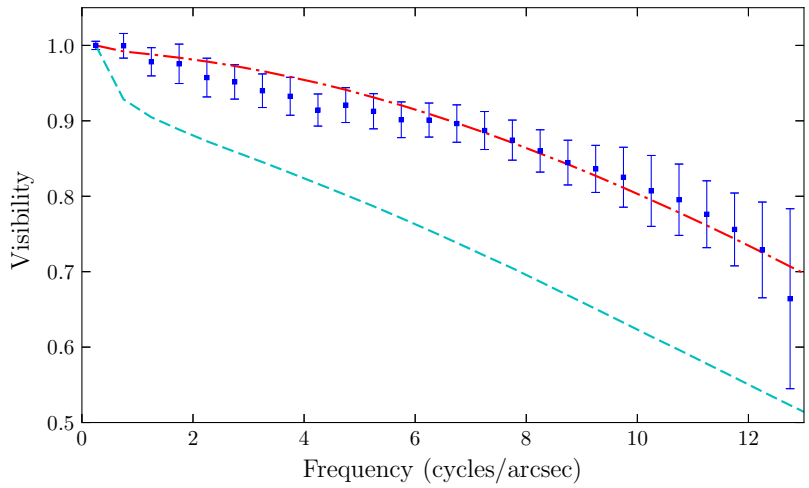

Figure 3.19: K-band speckle visibility profiles for models with different cavity density. The dashed cyan line shows the visibility profile for a model with a cavity reference density $\rho_{\rm cav} = 1.2 \times 10^{-21}$ g cm^{-3} whilst the dot-dashed red line shows the profile for a similar model but with $\rho_{\rm cav} = 2 \times 10^{-24}$ g cm^{-3}.

Fig. 3.23(b) shows the degree of agreement between the observations and model at ∼100 au scales as mapped at 1.3 mm. It shows a good agreement between the size and intensity scales. The orientation angle of the lower contours are however slightly off, with the model oriented perpendicular to the outflow cavity. This has also been observed at 3.6 cm, where the position angle of jet is 90° (Johnston *et al.* 2013). The offset between the small scale orientation derived

Table 3.9: Measured properties of NOEMA 1.3 mm sources.

Source	RA (J2000)	Dec (J2000)	Size[a] (arcsec)	PA (deg)	Peak flux (Jy beam^{-1})	Total flux (Jy)
VLA 3	20 29 24.864	40 11 19.51	3.3 × 2.4	267±2	0.2	0.4
VLA 1	20 29 24.627[b]	40 11 15.22[b]	2.9 × 2.0	18±7	0.05	0.08
VLA 3S[c]	20 29 24.901	40 11 15.64	4.9 × 3.3	49±5	0.06	0.3

Notes. The three components were fitted simultaneously. Units of RA are hour, minutes and seconds and units of Dec are degrees, arcmin and arcsec.
[a] Observed size.
[b] Position was fixed to obtain a good fit.
[c] Tentative source south of VLA 3. See next chapter for more detail.

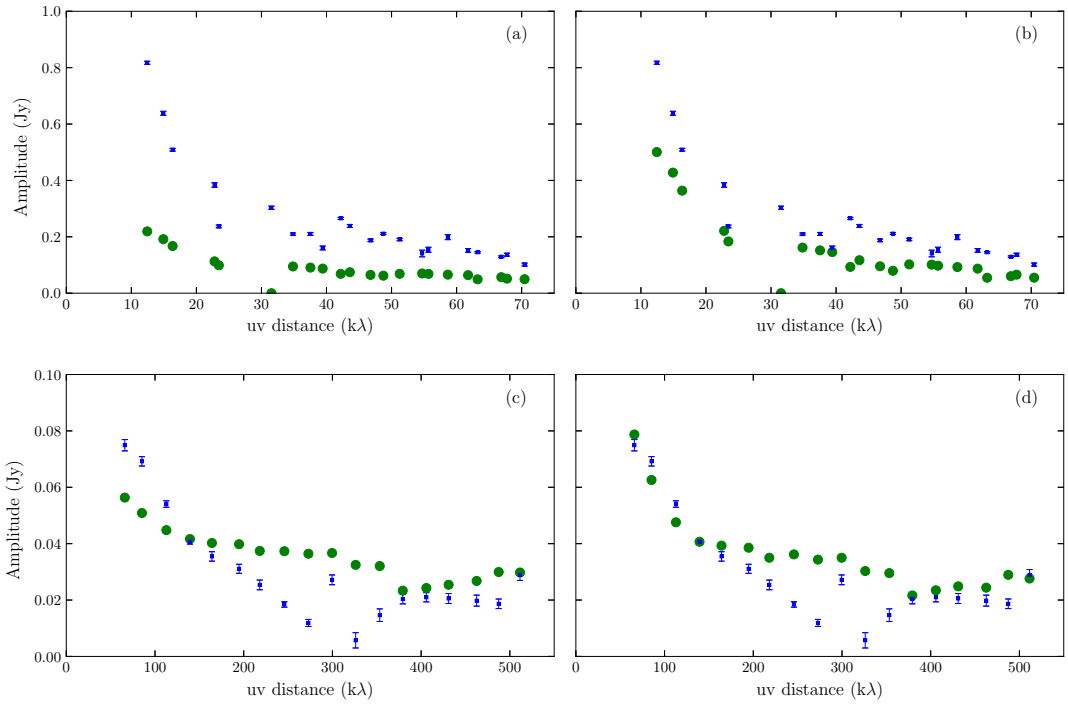

Figure 3.20: 1.3 mm visibilities for models with different dust in the envelope. Observed visibilities are shown in blue squares whilst the models are shown in green circles. (a) and (b) show the NOEMA compact array observations for models with OHM92 and WD01 dust, respectively. The same models are plotted in (c) and (d) but for the PdBI extended array visibilities.

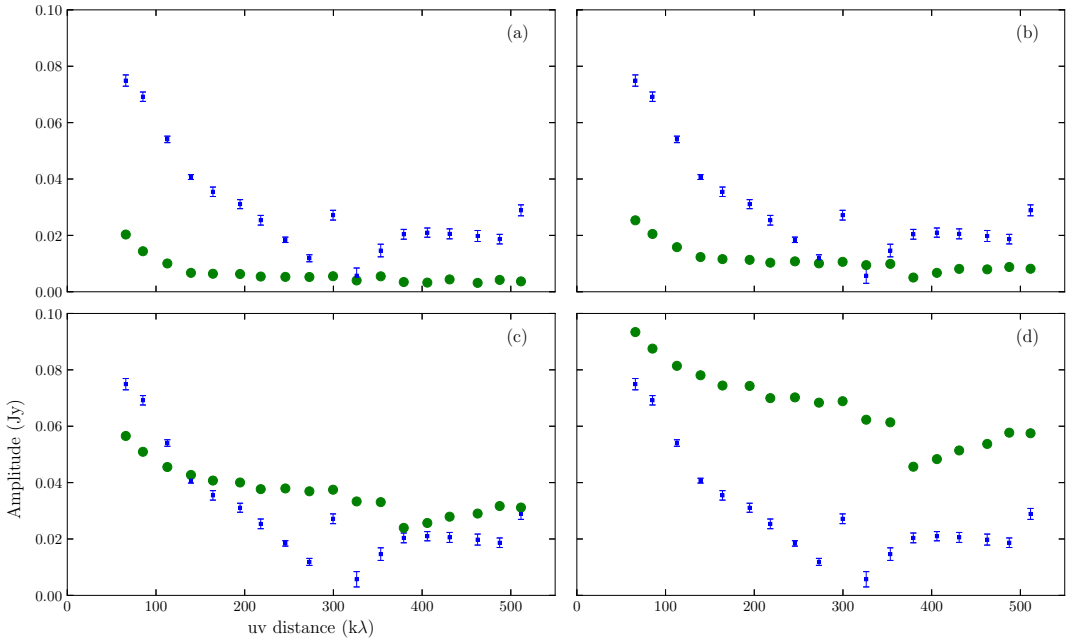

Figure 3.21: PdBI 1.3 mm visibilities for models with different disc mass and constant centrifugal radius (440 au). Observed visibilities are shown in blue squares whilst the models are shown in green circles. (a)–(d) show models with disc mass $M_{\rm d} = 0.25$, 0.5, 2 and 4 $\mathrm{M}_{\odot}$.

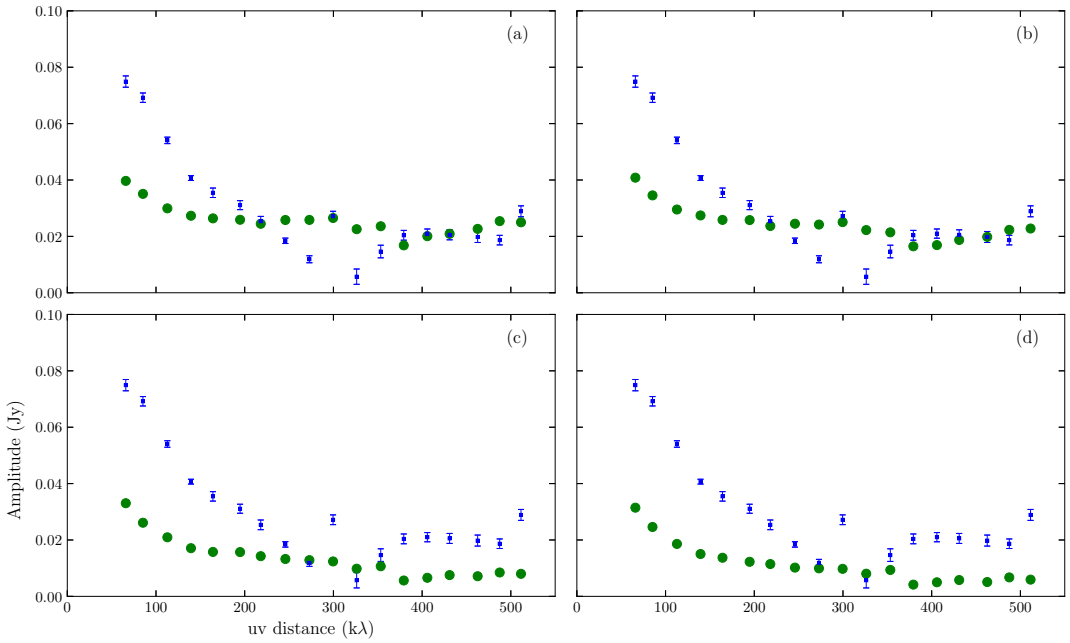

Figure 3.22: PdBI 1.3 mm visibilities for models with different centrifugal (disc) radius and constant disc mass (1 $M_{\odot}$). Observed visibilities are shown in blue square whilst the models are shown in green circles. (a)–(d) show models with centrifugal radius $R_{\rm c}$ = 100, 250, 800 and 1000 au.

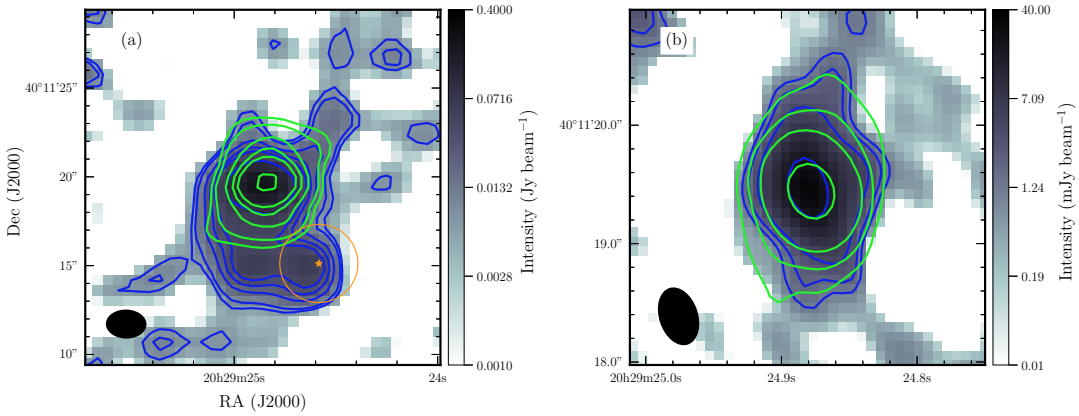

Figure 3.23: Observed (colour scale and blue contours) and model (green contours) NOEMA and PdBI 1.3 mm CLEAN images. The NOEMA compact configuration observation is shown in (a) and the levels are 7, 10, 20, 30, 40 and 80 mJy beam^{-1}. The orange star and circle show the position and 3.6 cm deconvolved size (∼4.4 arcsec; Johnston *et al.* 2013) of VLA 1. PdBI extended configuration observation is shown in (b) and the levels are 1.2, 2, 4 and 20 mJy beam^{-1}. The observed beam is shown in the bottom left corner.

from the jet and the large scale cavity may be due to precession of the disc/jet.

3.4.1 Parameters validity range and uncertainties

A coarse grid of models varying one of the parameters of the best-fitting model was calculated. This was done for parameters that can be well constrained by the observations available: inclination angle, cavity opening angle, envelope infall rate, disc mass and centrifugal radius. In order to evaluate the uncertainties in key parameters two approaches were used. In the first one, the weighted average reduced χ^2 value is used, with the same weights as for the average ranking, and their values against each parameter are shown in Fig. 3.24. In the second approach, the reduced χ^2 values for each observation constraining each parameter as listed in Table 3.7 were used and are shown in Figs. 3.25–3.27.

Good fits to the J, H-band data and SED can be obtained with inclination angles in the 25–35° range as shown in Figs. 3.26(a), (c) and 3.25(a), whilst higher inclinations can also provide good fits to the K-band data (cf. Fig. 3.26e). Models with inclination angles of 40° may fit the SED mid-IR regime slightly better. However, the red shifted outflow cavity becomes visible in the H and K-bands which is not seen in the data. At lower inclination angles the emission close to the source is more extended than observed in the near-IR bands. As will be discussed in Section 3.5, the average reduced χ^2 is driven mainly by the observations with higher χ^2 values, e.g. the K-band and 70 μm data, resulting in a flatter χ^2 distribution towards larger inclination angles as seen in Fig. 3.24(a). Based on this analysis, an uncertainty of 5° is estimated for the inclination angle based on the observations with lower χ^2 values.

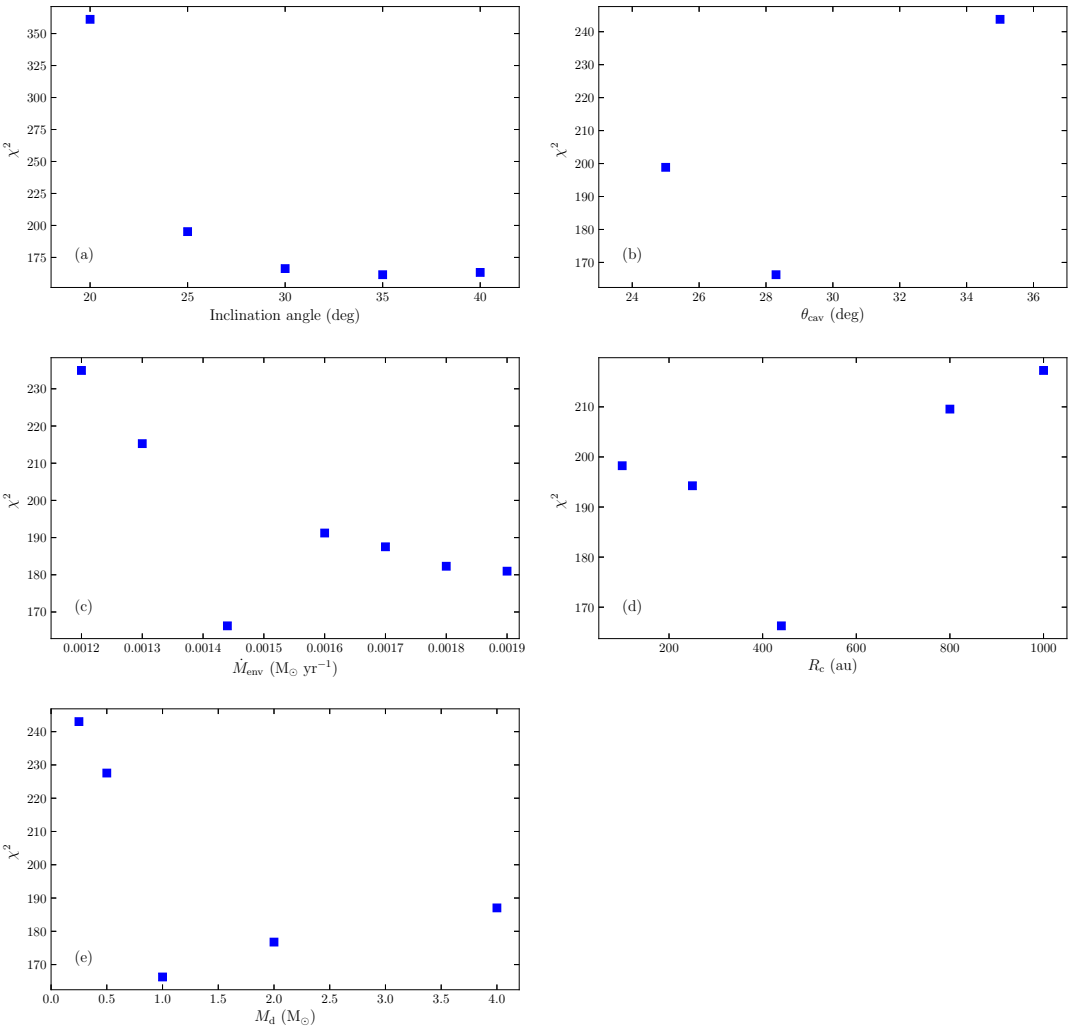

Figure 3.24: Average reduced χ^2 as a function of key parameters. The χ^2 were obtained by averaging the χ^2 values of the observations for models with all the parameters fixed to the best-fitting model except for the inclination angle in (a), cavity opening angle in (b), envelope infall rate in (c), disc radius in (d) and disc mass in (e).

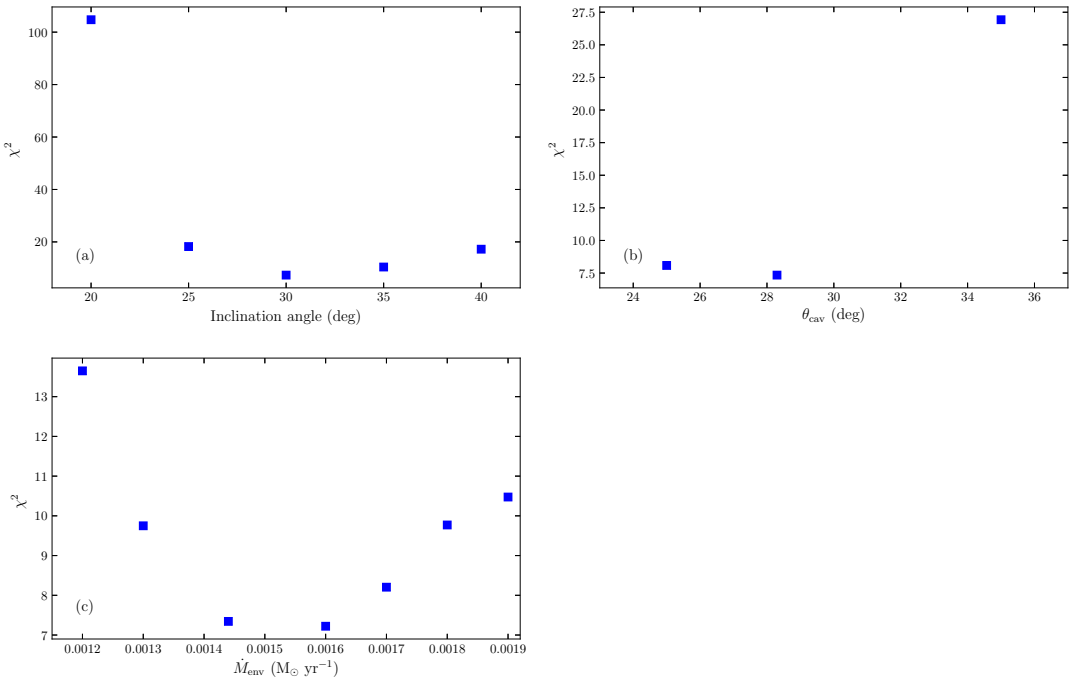

Figure 3.25: SED reduced χ^2 as a function of the (a) inclination angle, (b) cavity half opening angle and (c) envelope infall rate.

In general, depending on the cavity density and shape, cavity opening angles in the sampled high end (70–80°) can improve the fit to some observations, e.g. the 70 μm image, but they do not fit the near-IR images as well as narrower opening angles. For the best-fitting model, the average χ^2, SED, H and K-bands χ^2 show that the opening angle is constrained as shown in Figs. 3.24(b), 3.25(b) and 3.26(d) and (f), respectively. An error for the opening angle of 10° can be estimated from these observations. Fig. 3.26(b) show that the J-band observation is not constraining this parameter.

Given the inclination angle, the centrifugal radius and the dust model, the envelope infall rate is relatively well constrained within $\sim 10 - 20$ per cent of the best-fitting model. This is shown in Fig. 3.24(c) where all the parameters

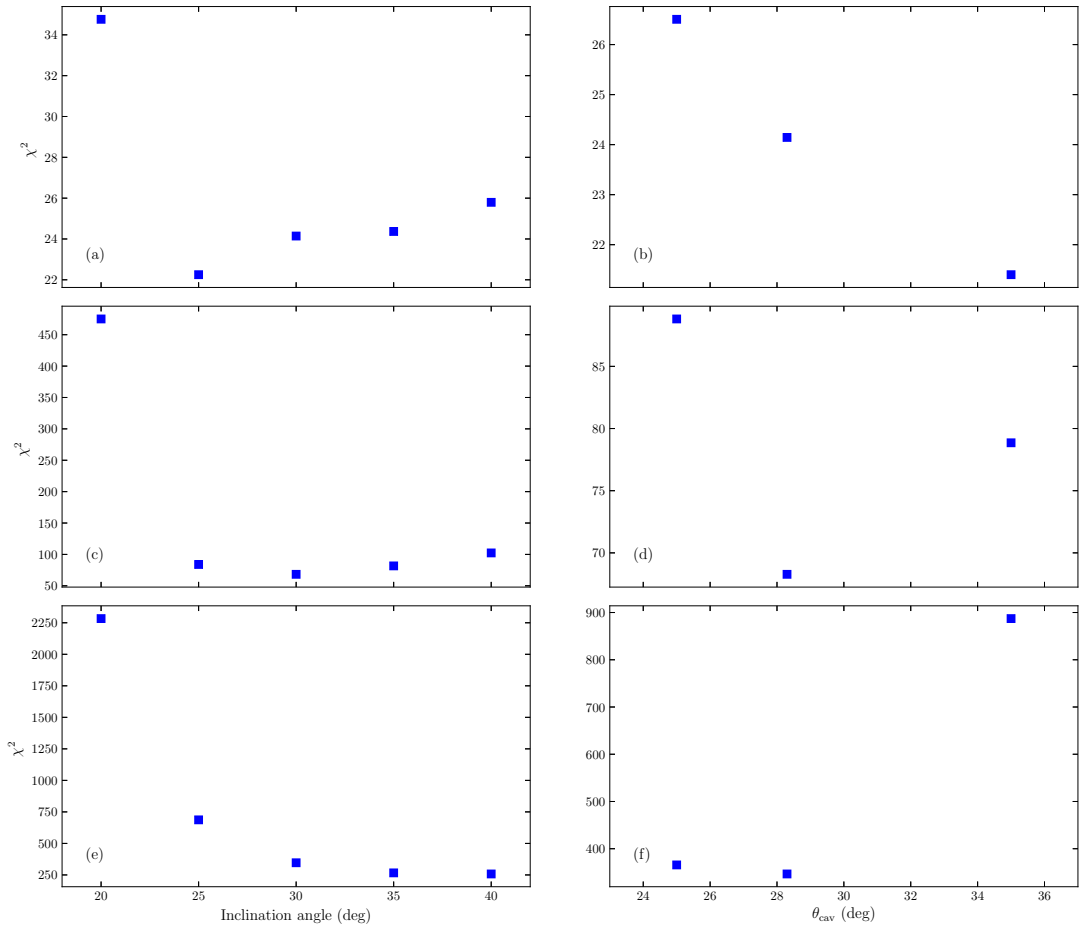

Figure 3.26: Near-IR reduced χ^2 as a function of the inclination and cavity opening angles. (a) and (b) show the J-band values, (c) and (d) the H-band values, and (e) and (f) the K-band values.

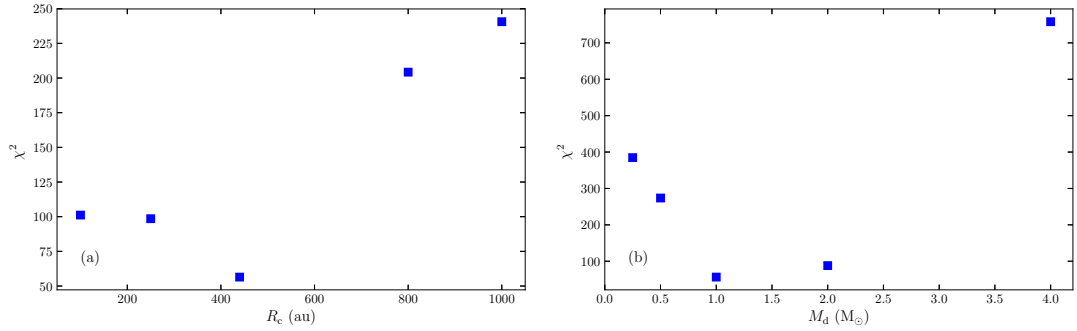

Figure 3.27: PdBI 1.3 mm reduced χ^2 as a function of (a) the centrifugal radius and (b) the disc mass.

of the best-fitting model were fixed and models with different infall rate were calculated. As described above, higher values produce a deeper silicate feature whilst lower values underestimate the submm flux. Thus the SED can provide a better estimation of the error of this parameter. From Fig. 3.25(c) an error of 0.2×10^{-3} $M_\odot$ yr^{-1} is estimated, i.e. roughly 15 per cent the best-fitting model value. As expected, models with higher submm dust opacities, such as WD01, require a lower accretion rate, i.e. lower envelope mass, to match the submm points, but still within ∼20 per cent of the best-fitting model value. Another parameter that determines the envelope mass is its radius which is constrained mainly by the 850 μm intensity radial profile. Values between $\sim 1.5 - 2.5 \times 10^5$ au fit this profile at least up to 40 arcsec.

Models with centrifugal radius between 200–500 au generally provide the best fits. Fig. 3.24(d) shows that for the best-fitting model parameters, this range goes at least between 200–800 au. The fit to the PdBI 1.3 mm data shown in Fig. 3.27(a) shows a similar result. Thus an error of 200 au is estimated for the centrifugal radius. Meanwhile, Fig. 3.28(a) shows a comparison between the ranks of different models with a range of centrifugal radius based on the best-

fitting model (also shown), i.e. the closer to the centre the better the fit is. For a fixed disc mass, Fig. 3.28(a) shows that a disc with smaller radius improve the 70 μm and the J-band fit, whilst a larger radius improve the submm and J-band fits.

A disc mass uncertainty of 0.5 $M_{\odot}$ is estimated from Fig. 3.24(e) for a fixed disc radius. A similar error can be derived from Fig. 3.27(b) in order to fit well the smallest scales sampled at 1.3 mm, which can not be fitted by models without a disc. Fig. 3.28(a) shows that a disc with a larger radius and mass can improve the fit of some (sub)mm observations. However, they overestimate the 1.3 mm visibilities between $\sim 100 - 350$ kλ. Discs with W02-3 dust and masses as low as 0.25 $M_{\odot}$ provide a similar fit to the best-fitting model. Although models with different flaring, scale height and vertical density exponent were calculated (cf. Section 3.3.2), none of them improved the overall fit. Since most of the observations are not sensitive enough to these parameters, an accurate validity range cannot be given.

Stellar parameters are difficult to constrain since the proto-stellar emission cannot be observed directly in the near-IR. By taking into account the ratios of dust extinction/emission and scattering from the best-fitting model, an attempt to constrain the stellar temperature by using the highest resolution near-IR point source data was carried out. The near-IR data used and the apertures where these ratios were measured are presented in Table 3.10, where the data have been scaled as described in Section 3.2 and model images were convolved with the respective observed PSF. Scattered photons account for the 40–50 per cent of the emission in the K-band and $\sim$70 per cent in the H-band, whilst dust emission accounts for most of the rest of the emission in both bands. This does not allow constraints

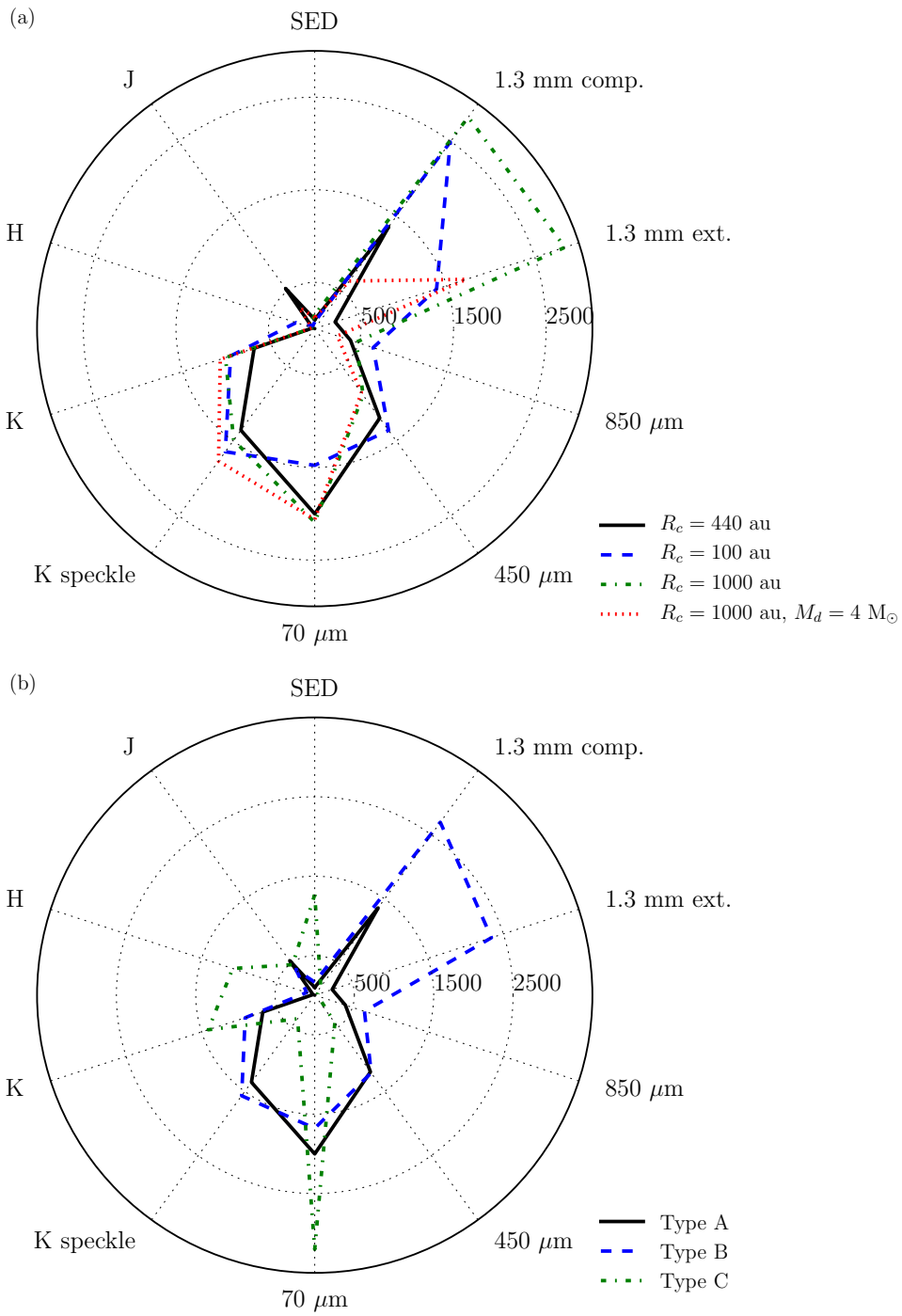

Figure 3.28: Comparison between the rank of each modelled observation for different models. The radial scale is the overall rank of each observation. (a) shows a comparison between the best-fitting model (black continuous line) and models with different disc radius and mass. (b) shows a comparison between the best-fitting model for each density distributions used (models type A, B and C). Table 3.8 lists their respective reduced χ^2.

Table 3.10: Near-IR flux contributions derived from the best-fitting model.

Obs.	Aperture (arcsec)	$F_{\rm obs}$ (Jy)	$F_{\rm tot}$ (Jy)	$F_{\rm d-emit}$ (Jy)	$F_{\rm s-emit}$ (Jy)	$F_{\rm d-scat}$ (Jy)	$F_{\rm s-scat}$ (Jy)
Speckle	0.54	1.35	1.04	0.60	3.9×10^{-3}	0.43	1.5×10^{-3}
HST	0.4	0.54	0.19	0.097	8.5×10^{-4}	0.09	4.2×10^{-4}
NIRI H	2.0	0.045	0.012	2.8×10^{-3}	4.5×10^{-5}	8.3×10^{-3}	6.4×10^{-5}

Notes. $F_{\rm obs}$ and $F_{\rm tot}$ are the observed and model total fluxes respectively. The fluxes for each components are defined in HYPERION as:
$F_{\rm d-emit}$: photons that were last emitted from dust and did not undergo any subsequent interaction.
$F_{\rm s-emit}$: same as $F_{\rm d-emit}$ but for source photons, i.e. stellar photons.
$F_{\rm d-scat}$: photons that were last emitted from dust and were subsequently scattered.
$F_{\rm s-scat}$: same as $F_{\rm d-scat}$ but for source photons.

to be put on the stellar temperature due to the low amount of stellar photons as predicted by the model. Furthermore, the aperture sizes are well outside of the sublimation radius as they trace emission at radial distances of ∼600 au in the best case, thus the emission is still dominated by dust emission/scattering.

3.4.2 Other density distributions

Fig. 3.28(b) shows a comparison between the rank of the different types of model densities (A, B or C) for each observation modelled, and their reduced χ^2 are listed in Table 3.8. The common parameters between the best-fitting type B model are equivalent to the overall best-fitting model ones, i.e. they are identical except for the density distribution of the disc and the addition of the accretion luminosity. This model has an accretion luminosity of ∼20 $L_\odot$. Fig. 3.28 shows that the main difference with the best-fitting model is the fit to the 1.3 mm visibilities. In these observations, the amplitudes are underestimated by the model.

The best-fitting type C model has the same inclination angle of the best-fitting model. It fits relatively well the speckle, submm and mm observations.

The envelope has a mass of 1.5×10^3 $M_\odot$ and the density in the cavity is lower ($\rho_{0,\mathrm{cav}} = 5 \times 10^{-23}$ g cm^{-3}) and decreases at a shallower rate ($e = 1.5$) than the best-fitting model. The latter causes a dip in the near- and mid-IR fluxes and less extended emission in the near-IR bands. Its disc radius is half the best-fitting model one. In general, this type of models do not fit well the 70 μm image.

3.5 Discussion

3.5.1 70 μm morphology

The detailed RT modelling here presented has shown that the bipolar outflow cavities play an important role in reproducing the 70 μm observations. The modelling has allowed the fit of the extended emission at the aforementioned wavelength and the SED. The observed and model 70 μm images are elongated along the cavity axis. The results in Figs. 3.9 and 3.11 imply that the warm/hot dust in the envelope cavity walls bring an important contribution to the emission at 70 μm. Furthermore, the temperature distribution in Fig. 3.18 shows that cavity walls are being heated by the stellar radiation escaping through the outflow cavity more than other regions of the envelope. The figure also shows that the dust in the cavity is hotter than the walls, however there is less dust in the cavity. Hence the contribution of the envelope cavity wall is more important at 70 μm, which is also shown in the SED.

In the models of Zhang *et al.* (2013) the 70 μm is extended along the outflow direction. The origin of the extended emission in their models is due to dust in the outflow at distances larger than the core radius, otherwise the emission is

dominated by the cavity walls of the core. They used a wide cavity angle ($\sim$100°) thus at an inclination of 30° the observer is looking directly to the source hence the emission of the cavity walls in their models is relatively symmetrical. In the best-fitting model the line of sight passes through a section of the envelope.

3.5.2 Physical properties

The physical properties derived from the modelling are consistent with the current picture of AFGL 2591, but the density is better constrained. The disc mass is consistent with the mass range given by Wang *et al.* (2012, 1–3 $M_{\odot}$), even though they derived the disc mass from the total flux at 1.3 mm. However, the disc radius is smaller than the one they derived from the 1.3 mm continuum ($\sim$1300 au at 3.3 kpc). A model with a disc radius of 1000 au requires a disc mass of 4 $M_{\odot}$ in order to fit the 1.3 mm visibilities for uv distances larger than 350 kλ as the best-fitting model does. Although this model is ranked second during the modelling and is consistent with the estimates of Wang *et al.* (2012), it does not improve enough the fit to the other wavelengths (cf. Fig. 3.28). Johnston *et al.* (2013) obtained disc radii, which were also fixed to the centrifugal radius, of 3.5×10^4 and 2.7×10^3 au for their envelope with disc and control models, respectively. Although both radii seems to be well constrained by their modelling, the former one is larger than the resolution of 2MASS ($\sim$3 arcsec, i.e. $\sim$10000 au) whilst the latter is twice the radius of the 1.3 mm emission. These larger radii may have been needed in order to explain the extension of the 2MASS profiles close to the star. Larger radii may have also been needed in order to increase the SED mid-IR fluxes to compensate for their larger inclination angles (see below).

Johnston *et al.* (2013) could not constrain the disc mass as they did not fit the mm interferometric data.

The inclination with respect to the line of sight is consistent with the values in the literature (30–45°, e.g. Hasegawa & Mitchell 1995; van der Tak *et al.* 2006) which are generally found based on geometrical considerations, and it is constrained between 30–40°. Larger values like those found by Johnston *et al.* (2013) are discarded by the modelling since at 40° the red shifted outflow cavity starts to emit in the near-IR. This discrepancy may be explained by the data and methods used. Although the red shifted cavity is observed in the models at higher inclinations, the intensity is much lower than the peak or the blue shifted cavity. Hence the red shifted cavity emission will be negligible due to the lower surface brightness sensitivity of the 2MASS observations. Johnston *et al.* (2013) fitted the SED and 2MASS slices, thus their opening angle is not well constrained as they showed (cf. their fig. 4) and is degenerated with the inclination angle. Another reason the models rule out higher inclinations is that they require a larger envelope mass to compensate for the lower luminosity in order to fit the submm fluxes, and higher inclinations produce a deeper silicate feature which do not fit the mid-IR spectrum.

The inner radius radius is ∼3 times smaller than the one found by Preibisch *et al.* (2003) and Johnston *et al.* (2013) models. Although the sublimation radius was allowed to change in order to obtain a maximum dust temperature of 1600 K in the inner radius, the sublimation radii of the models did not increase noticeably. Smaller inner radii, near the sublimation radius, are also not strongly ruled out by Johnston *et al.* (2013). In order to analyse the effect of a larger inner radius on the near-IR observations, a modified version of the best-fitting model was

calculated with a larger inner radius. This model did not improve the fit to the speckle visibilities. Moreover, the fit to the H-band observation is worse than the best-fitting model.

The parabolic shape of the cavity can help to explain the wider cavity opening angle close to the star as observed in maser emission (Sanna *et al.* 2012). The density in the cavity is also consistent with the one expected for an outflow (e.g. Matzner & McKee 1999) and the opening angle is consistent with previous results (e.g. CS line modelling by van der Tak *et al.* 1999, maser emission from Sanna *et al.* 2012). Due to the lack of data, previous modelling of MYSOs used a constant small density (or empty) in the cavity (e.g. de Wit *et al.* 2010). This is not preferred in the modelling, as a constant density tends to produce more extended emission in the near-IR than observed. For a fixed cavity density distribution exponent, the density is determined mainly by the near-IR observations and the near/mid-IR regime of the SED. If the gas in the cavity is expanding isotropically the outflow rate $\dot{M}_{\rm out}$ can be described as:

$$\dot{M}_{\rm out} = 4\pi r^2 v_{\rm out} \rho_{\rm cav} \tag{3.13}$$

with $v_{\rm out}$ the outflow velocity and $\rho_{\rm cav}$ the cavity mass density at radius r. The outflow rate is roughly 10 per cent the accretion rate $\dot{M}_{\rm acc}$ (e.g. Beuther *et al.* 2002b). If the accretion rate is $\dot{M}_{\rm acc} = \dot{M}_{\rm env}$, an outflow velocity $v_{\rm out} = 175$ km s^{-1} is obtained by solving eq. 3.13 with the values in Table 3.7. This velocity is within the range assumed by Preibisch *et al.* (2003) for the expansion of the loops (100–500 km s^{-1}) based on the ^{12}CO line wings in the observations of van der Tak *et al.* (1999). Fig. 3.29 uses eq. 3.13 to compare the density in the cavity at the

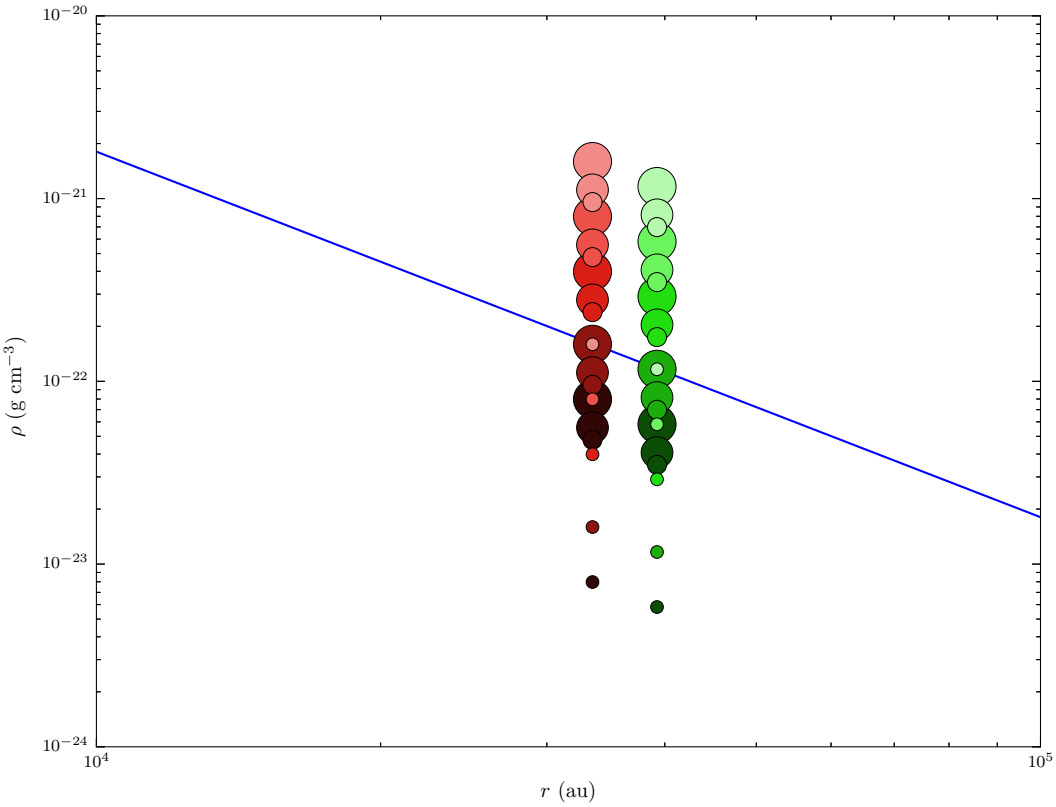

Figure 3.29: Outflow cavity density distribution from the model (blue line) and from solving eq. 3.13 at the near-IR loops distances for different velocities and envelope infall rates. Colours from lighter to darker represent outflow velocities of 25, 50, 100, 250, 500 km s^{-1}. Point sizes from larger to smaller represent infall rates of 2×10^{-3}, 1.4×10^{-3}, 1.2×10^{-3}, 2×10^{-4} M$_\odot$ yr^{-1}. The outflow rate was assumed to be 10 per cent the envelope infall rate. The loops projected distances are 8.8 arcsec (shades of red points) and 10.3 arcsec (shades of green points) according to Preibisch *et al.* (2003). The loops were assumed to be in the cavity walls thus the inclination used was 60°.

loops distances for different outflow velocities and envelope infall rates. For the RT model cavity density, the figure shows that the outflow velocity should be in the range 200–300 km s^{-1} for infall rates within 20 per cent the best-fitting model one.

In general, the 450 μm and 850 μm images from the modelling are not elongated along the cavity axis. For the best-fitting model, the major-to-minor axis

ratio of 2-D Gaussians fitted to the model images is ∼1 at both wavelengths, instead of ∼1.3 as observed (cf. Section 3.2). Elongation along the cavity axis was predicted by de Wit *et al.* (2010) for 350 μm observations of the MYSO W33A, but this is not observed in the modelling at pc scales. However, their source has a larger inclination angle (60° for their best-fitting model) and their cavity has a constant density distribution of $\rho \approx 2 \times 10^{-20}$ g cm^{-3}. As stated in Section 3.2, changes in the PSF may also help to explain why the models are not elongated.

3.5.3 Best-fitting model selection

In the previous chapter arguments raised by different authors (Jørgensen *et al.* 2002; Williams *et al.* 2005) in favour of using the ranking of models in order to select the model that fits different types of data were presented. To summarise, they argue that there is not a correct way to combine the χ^2 values of different data sets because they may not independent (especially if the SED is included), different parameters are constrained by different observations and the numerical scales of the χ^2 values between different data sets are different. In order to explore this further, a total reduced χ^2 and an average reduced χ^2 were calculated and the best-fitting models were selected. The best-fitting models χ^2 for these selection are listed in Table 3.8. In what follows the results for the best-fitting model of type A models will be discussed.

The best-fitting model as selected by the total reduced χ^2 has the same parameters as the best-fitting model ($i = 30°$, $\theta_{\rm cav} = 28°$ and $L = 1.6 \times 10^5$ L$_\odot$) but its inclination and cavity opening angles are higher ($i = 40°$ and $\theta_{\rm cav} = 35°$), and its luminosity is lower ($L = 1.4 \times 10^5$ L$_\odot$). As was shown in Section 3.4 and

in Table 3.8 higher inclination and opening angles are preferred by the 70 μm observations but not by the J- and H-band ones, and the SED. It can also be seen in Table 3.8 that better χ^2 values than in the best-fitting model by ranking are obtained in those observations with a higher number of points, namely the UKIRT K-band and 70 μm observations. Hence, this method for selecting the best-fitting model is dominated by the observations with larger number of points.

The best-fitting model selected by the average χ^2 has similar parameter as the one selected by ranking. The most different parameters are the disc dust and mass (W02-3 dust and $M_{\rm d} = 0.5$ M$_\odot$, cf. OHM92 and $M_{\rm d} = 1$ M$_\odot$), the cavity shape exponent ($b_{\rm cav} = 1.5$, cf. $b_{\rm cav} = 2$) and inclination angle ($i = 40°$, cf. $i = 30°$). As argued, the higher inclination produced a worse fit to some near-IR observations and the SED than the model selected by ranking. In general this method gives more weight to observations which have in general a high χ^2 value, namely the 70 μm and 1.3 mm NOEMA observations. It also reflects the difference in χ^2 scale between the different observations. If all the observations were well fitted ($\chi^2 \sim 1$) then this best-fitting model should be the same as the ranking one.

In general the method used in this thesis is independent of the intrinsic χ^2 scale of each observations and the number of points of each one. Overall the best-fitting model selected by ranking provides a good fit for key observations and its total and average χ^2 values are relatively close to the best-fitting ones selected by these two χ^2. The disadvantage of the ranking is that it reduces the difference between models with a large difference in χ^2 or increases it for models with similar χ^2.

3.5.4 Dust size distribution and grain growth

In order to explore the change in dust from within the envelope or disc, spectral indices were derived based on dust emission at different scales from single dish and interferometric observations in the radio/submm regime. The former traces cold dust located in the large scale envelope, whilst the latter trace scales of few 1000 au. The dust optical depth is assumed to follow a power law $\tau \propto \nu^{\beta}$ in this regime (optically thin). If it is further assumed that the emission is in the Rayleigh-Jeans regime, the fluxes are then $F_{\nu} \propto \nu^{\beta+2} \propto \nu^{\alpha}$. Fig. 3.30 shows the observations made at different scales and the indices α of the power law fitted to the single dish, mm and radio interferometry data individually.

Dust models with shallower emissivity index (e.g. WD01, see Table 3.6) fit the $\lambda > 70$ μm regime of the SED better than dust with steeper spectral indices (e.g. KMH, OHM92). This is supported by the emissivity index derived from single dish observations ($\beta = 1.2$ from Fig. 3.30). However, shallower emissivity index models, i.e. models with larger grains (cf. Table 3.6), are not good at fitting the mid-IR regime and show an excess in emission along the cavity in the near-IR images because larger grains scatter more photons.

The dust emissivity index derived from interferometric observations is $\beta = 0.2$. This shallower emissivity index implies that larger grains are responsible for the mm disc emission, thus it may be evidence of grain growth in the denser regions, i.e. the disc, of the MYSO. Although the best-fitting model favours a disc with smaller grains, a similar model with a disc mass of $M_{\rm d} = 0.25$ $\rm M_{\odot}$ and larger dust grains is ranked fourth in the model list. Therefore, dust models with larger grains can also produce results consistent with the observations.

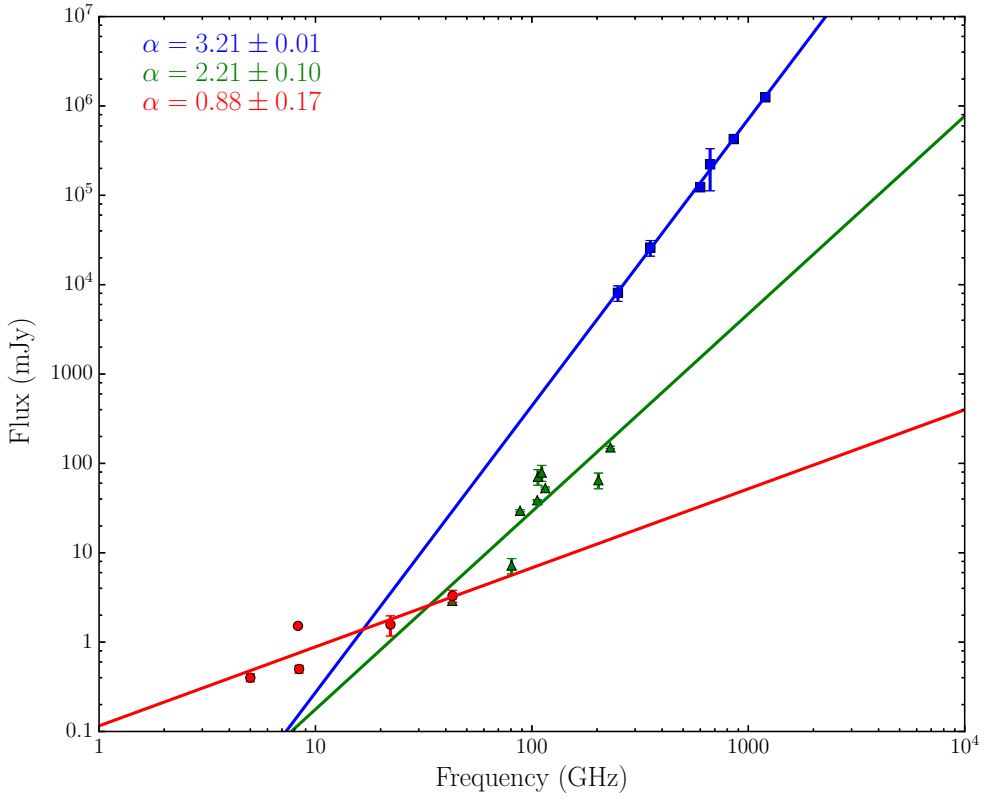

Figure 3.30: SED of the cm/submm regime as observed at different scales. Blue squares fluxes correspond to single dish observations and are presented in Table 3.4. Green triangles come from mm interferometric observations from van der Tak *et al.* (1999), Johnston *et al.* (2013) and Wang *et al.* (2012). Red circles are radio/mm interferometric observations from Campbell (1984), Tofani *et al.* (1995), Trinidad *et al.* (2003), van der Tak & Menten (2005) and Johnston *et al.* (2013). The slopes of the fitted lines are listed in the upper left corner, then the dust emissivity slope is $\beta = \alpha - 2$.

The spectral index of radio/mm observations and 3.6 cm observations (e.g. Trinidad *et al.* 2003; Johnston *et al.* 2013) points towards the presence of a jet with $\alpha \sim 0.6$. Hence, the spectral index from mm interferometry may be shallower if the contribution of the jet/wind emission is subtracted, which will depend on the turnover frequency of the jet emission.

The presence of different dust models to those used here is also supported by modelling of near-IR polarimetric observations of Simpson *et al.* (2013). They

found that elongated dust grains rather than spherical ones can reproduce their observations better. Therefore, the dust optical properties may be different depending on the physical conditions at different positions, e.g. dust in the cavity walls is being shocked by the outflows or dust in colder regions may develop ice mantles. This may allow dust with $\beta = 1.5$ to be present in colder regions of the envelope, thus improving the fit of the submm observations, and dust with $\beta = 2.0$ to exist in hotter or shocked regions like the cavity walls, which may improve the mid-IR fit.

3.5.5 The Ulrich solution limitations

The Ulrich analytical solution for the accretion problem is able to reproduce some of the observed features. However, one model that can fit all the observations together could not be found. The limitations on the physics included in the Ulrich solution does not allow for better results. Additionally, the simplicity of the models, where the clumpiness of the cavity or the presence of nearby sources are not taken into account, also limits the quality of the fit.

The large amount data available for this source and other MYSOs, will allow the use of more complex theoretical models. These models should solve self-consistently the hydrodynamic equations to obtain the density distribution and include more physics, like radiation feedback (e.g. Cunningham *et al.* 2011; Kuiper *et al.* 2015).

3.6 Conclusions

The extended nature of the *Herschel* 70 μm observations can be explained as the result of dust emission from the outflow cavity, whose walls are heated by the radiation escaping through the less dense cavity medium. Spatially resolved dust continuum images between 1 to 1300 μm and the SED were used to study the dust density and temperature distributions of the prototypical MYSO AFGL 2591.

The presence of a disc is needed in order to fit the 1.3 mm visibilities. This disc has a mass of 1 $M_{\odot}$. The best-fitting model consists of an Ulrich envelope a flared disc and bipolar outflow cavities with properties consistent with previous results. The 450 μm and K-band speckle interferometry observations were not fitted well by the models.

The physical limitations of the Ulrich solution, together with the simplicity of the models, do not allow an improvement in the fit. 3-D self-consistent theoretical models should be tested in order to improve the fit to the observations. This, in addition to high-resolution data from current and future surveys, will allow a more complete study of MYSOs.

The dust emissivity indexes change from 1.2 to 0.2 between observations tracing the large scale and the small scale, respectively. This is consistent with an increase of the dust grain size towards denser regions, which may be evidence of grain growth in the disc.

Chapter 4

Gas velocity distribution of AFGL 2591

4.1 Introduction

The well constrained density and temperature distributions from the previous chapter allows the study of the kinematics of AFGL 2591 with a much more limited number of free parameters. To study the velocity distribution of its circumstellar material, molecular line observations are essential. As one of the most studied MYSOs, there are a copious amounts of molecular line observations towards AFGL 2591. Early observations CO and HCO^+ allowed the study of the geometry and direction of the molecular outflow (e.g. Lada *et al.* 1984; Hasegawa & Mitchell 1995) and were interpreted as a jet within a large scale outflow. Near-IR H_2 emission has also been observed and denotes the presence of shocked gas along the predicted outflow direction (Poetzel *et al.* 1992).

The kinematics of the outflow and the inner region have been studied by

several authors. The blue shifted radial velocity of the jet is constrained between 200–500 km s^{-1} as measured from the line wings of the Herbig-Haro objects (Poetzel *et al.* 1992) and ^{12}CO (van der Tak *et al.* 1999). The $C^{18}O$ observations of Johnston *et al.* (2013) show evidence of Hubble-like expansion of the blue shifted emission towards the outflow. Hubble-like expansion and rotation at disc scales (< 5000 au) was also found from PdBI observations of HDO and $H_2^{18}O$ by Wang *et al.* (2012). The rotation at these scales seems to be sub-Keplerian and anti-clockwise looking down from the blue shifted cavity. Wang *et al.* (2012) argue that these water isotopologues are closer to the surface of a disc-like structure, thus the expansion motion is a result of the interaction of the stellar radiation/wind, and infall occurs in the inner region of the disc where these molecules are depleted. Similarly, their SO_2 observations trace material affected more by the wind than the rotation.

The change in the abundance for different molecules in AFGL 2591 has also been addressed by several authors. Benz *et al.* (2007) used the spherically symmetric abundance models of Stäuber *et al.* (2005) to fit their CS and SO interferometric (sub-arcsec resolution) observations, and concluded that X-ray emission from the protostar is needed to produce a better fit. Kaźmierczak-Barthel *et al.* (2015) studied the emission of 25 molecules observed with the Heterodyne Instrument for the Far-Infrared (HIFI) by *Herschel*. They found that the emission from some molecules can be better described by abundances with a jump at 100 or 230 K, which were then fitted by a theoretical chemical model. Their theoretical model fitted relatively well the abundance jumps in molecules like H_2O and NH_3, and predicted a chemical age of 10–50 kyr. The first jump at 100 K is related to the evaporation of ices (van Dishoeck & Blake 1998) whilst the second

jump at temperatures $T > 230$ K is important for N-bearing molecules due to less formation of N_2 (Boonman *et al.* 2001). Far UV and X-ray radiation, which penetrates a thin layer in the cavity walls, can also enhance the abundance of several diatomic molecules observed in the far-IR and (sub)mm as shown by the chemical modelling of Bruderer *et al.* (2009, 2010). Thus molecules can trace the distribution and velocity of gas for the different density components. Since the density distribution of AFGL 2951 has already been constrained in the previous chapter, the velocity distribution can be studied, particularly at intermediate scales ($\sim$10000 au), i.e. the inner envelope, where the gas motions have not been modelled in detail. These scales are key to understand the infall process and how the gas is accreted into the disc and then the star.

Methyl cyanide, CH_3CN, has been proven to be a good disc and rotation tracer (e.g. Beuther *et al.* 2005; Johnston *et al.* 2015). It is a symmetrical top molecule, as such radiative transitions can only occur within each K ladder and the relative populations of each K ladder is a measure of the kinetic temperature, T_K (Cummins *et al.* 1983). Total angular momentum, J, transitions occur at relatively close frequencies for consecutive K levels (Loren & Mundy 1984), thus allowing the study of T_K in a single spectrum. It has a critical density of $\sim 10^7$ cm^{-3} at 100 K (Bell *et al.* 2014), hence it can be used as a thermometer of the dense inner $\sim$5000 au region of AFGL 2591.

In this chapter CH_3CN observations are used to study the kinematics of the envelope of AFGL 2591. The observations are presented in Section 4.2. In Section 4.3 physical properties like the temperature and column density are studied by fitting the data with 1-D constant density models. The velocity distribution and CH_3CN abundance constrained by the continuum model are studied through

RT modelling in Section 4.4 and the results discussed in Section 4.5. Finally, the conclusions are presented in Section 4.6.

4.2 Observations

AFGL 2591 was observed in the most compact configuration of NOEMA as part of the CORE[1] program. These observations cover the methyl cyanide K ladder of the J=12–11 transition between K=0–5, as shown in the peak spectrum in Fig. 4.1. The spectral resolution of the observations was 1.95 MHz ($\sim$2.7 km s^{-1} at 218 GHz), while the beam size was $2\farcs6 \times 1\farcs8$ PA=87°. The average noise measured in a annulus of sky along all channels is $\sigma_{\rm rms}$ = 30 mJy beam^{-1} per channel, and it can range roughly between $10 - 50$ mJy beam^{-1} at different channels.

The data were reduced by the CORE team, and zeroth and first moments maps for each line are shown in Figs. 4.2 and 4.3. The first moment maps were calculated considering all data with fluxes larger than $5\sigma_{\rm rms} = 0.15$ Jy beam^{-1} per channel over a range of spectral channels covering the lines. The local standard of rest (LSR) velocity measured by Kaźmierczak-Barthel *et al.* (2014, -5.5 ± 0.5 km s^{-1}) over 24 lines in *Herschel*/HIFI observations was used to shift the velocities, so zero velocity corresponds to the line systemic velocity. As expected, higher K lines have more compact emission as they trace hotter material.

The zeroth moment maps show further evidence of two sources towards the south of VLA 3, as they are located in local intensity peaks. Fig. 4.4 shows the position of the radio sources with respect to the methyl cyanide ones. The

[1] `http://www2.mpia-hd.mpg.de/core/Overview.html`

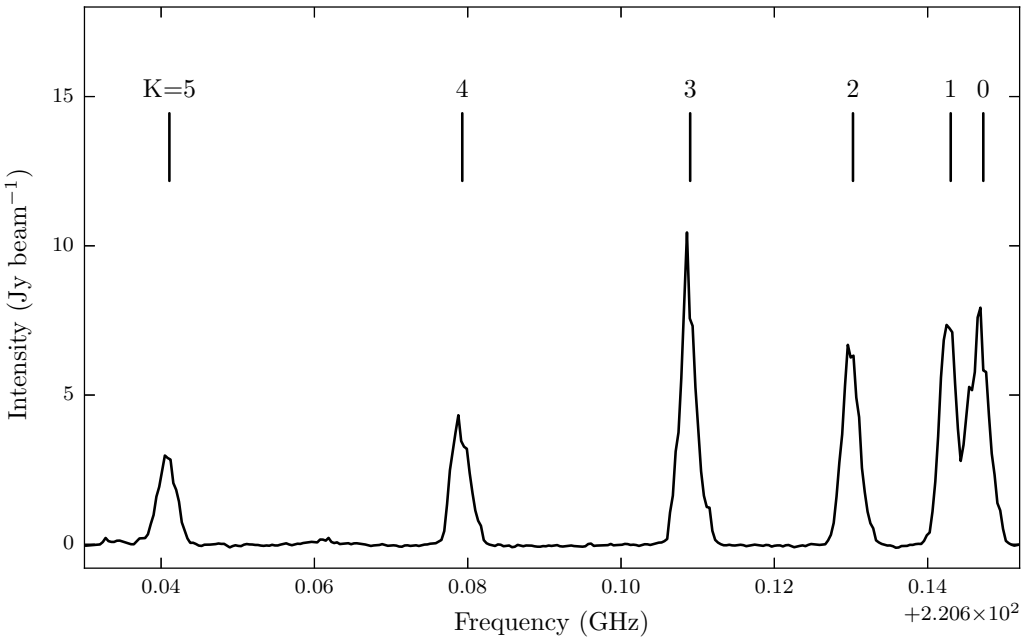

Figure 4.1: Peak spectrum showing the methyl cyanide K-ladder.

source towards the south west has already been identified as VLA 1 from the continuum analysis in the previous chapter, and in Fig. 4.4 it can be seen that the methyl cyanide emission coincides with emission from the eastern hemisphere of this source. This is consistent with VLA 1 being a slightly cometary H II region with the ionising gas expanding towards the less dense gas in the west. The source immediately south of VLA 3, which will be referred to as VLA 3S, has an intensity peak which is shifted ∼2 arcsec towards the south east from the continuum peak. This source does not have radio emission as shown in Fig. 4.4 and has not been detected in the IR, thus its nature is as yet unknown but it could be a very young low-mass source. Fig. 4.3 also shows that the velocity structures of the three sources are different.

Table 4.1 lists measured properties from a 2-D Gaussian fit to each zeroth mo-

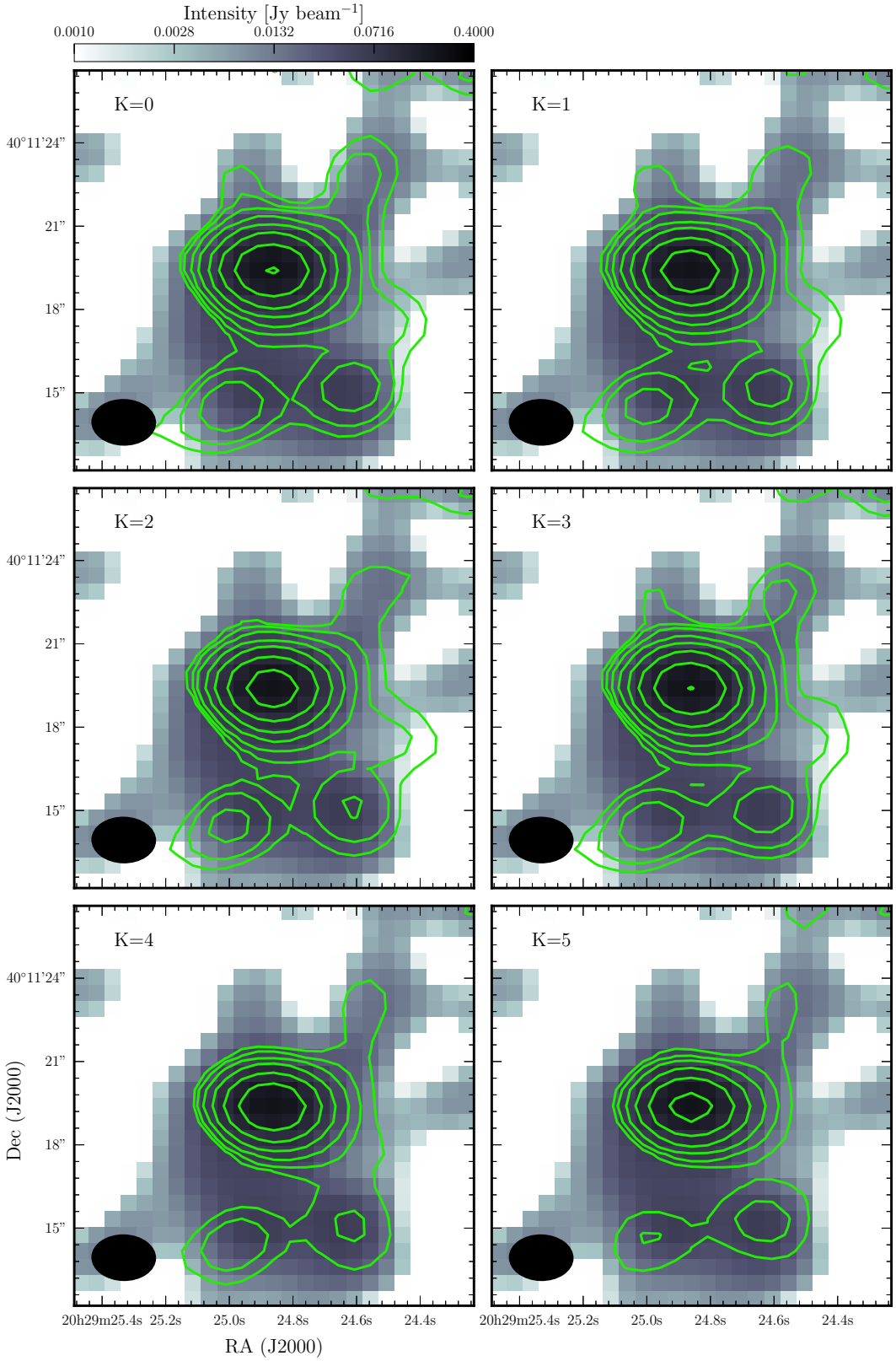

Figure 4.2: Zeroth moment maps of CH_3CN J=12–11 for K=0–5. Continuum is plotted in colour scale. Contour levels are 0.5, 0.9, 1.6, 3.0, 5.4, 9.7, 18, 32 Jy beam^{-1} km s^{-1}. Beam size is shown in the bottom left corner

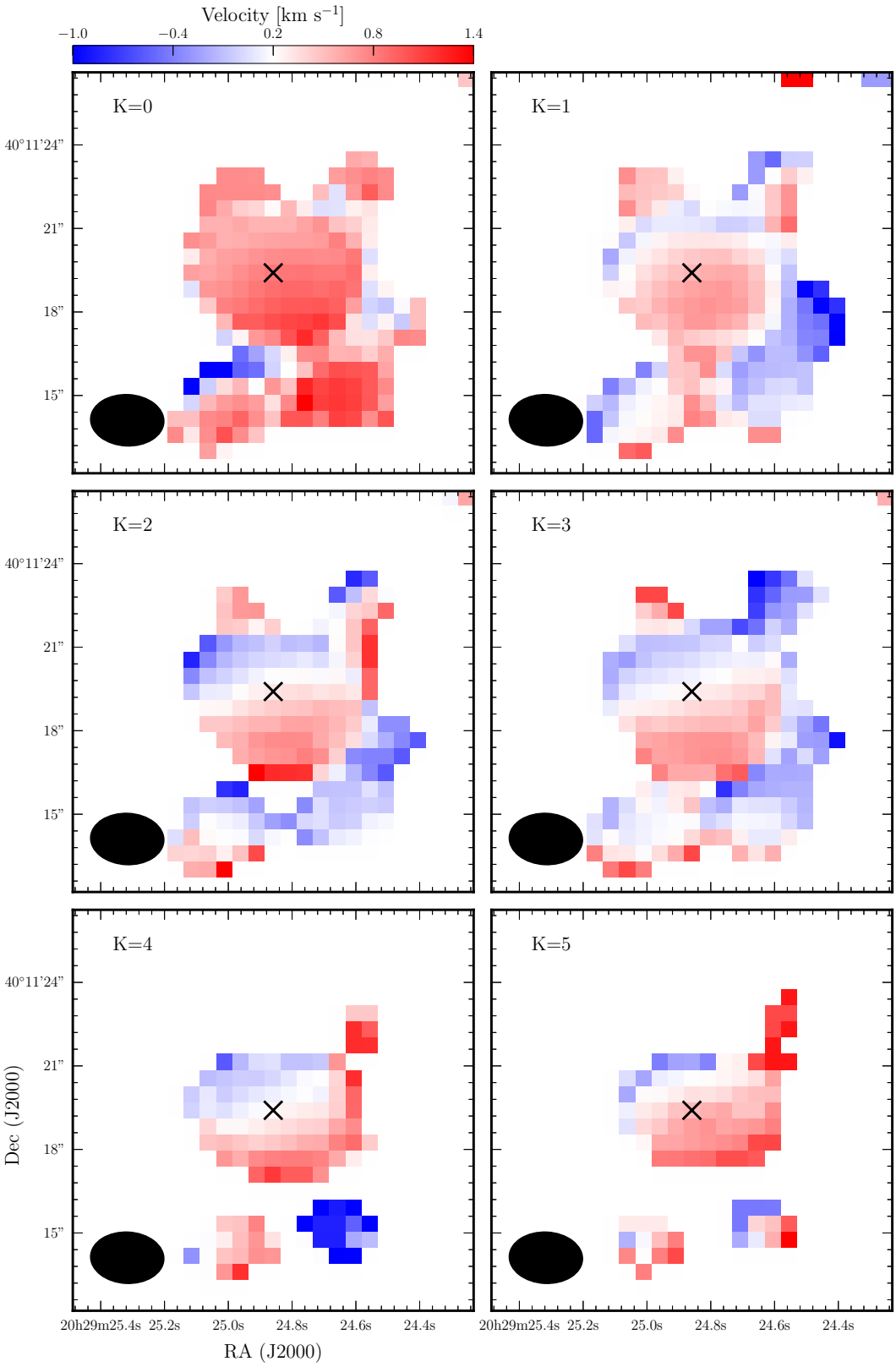

Figure 4.3: First moment maps of CH_3CN J=12–11 for K=0–5. Lines corresponding to K=0 and 1 are blended, thus the first moment map for K=0 do not show the same range as higher K lines. The position of the radio continuum source is marked with a black cross and the beam size is shown in the bottom left corner. Zero velocity correspond to the systemic velocity in the LSR system ($v_{\rm LSR} = -5.5$ km s^{-1}).

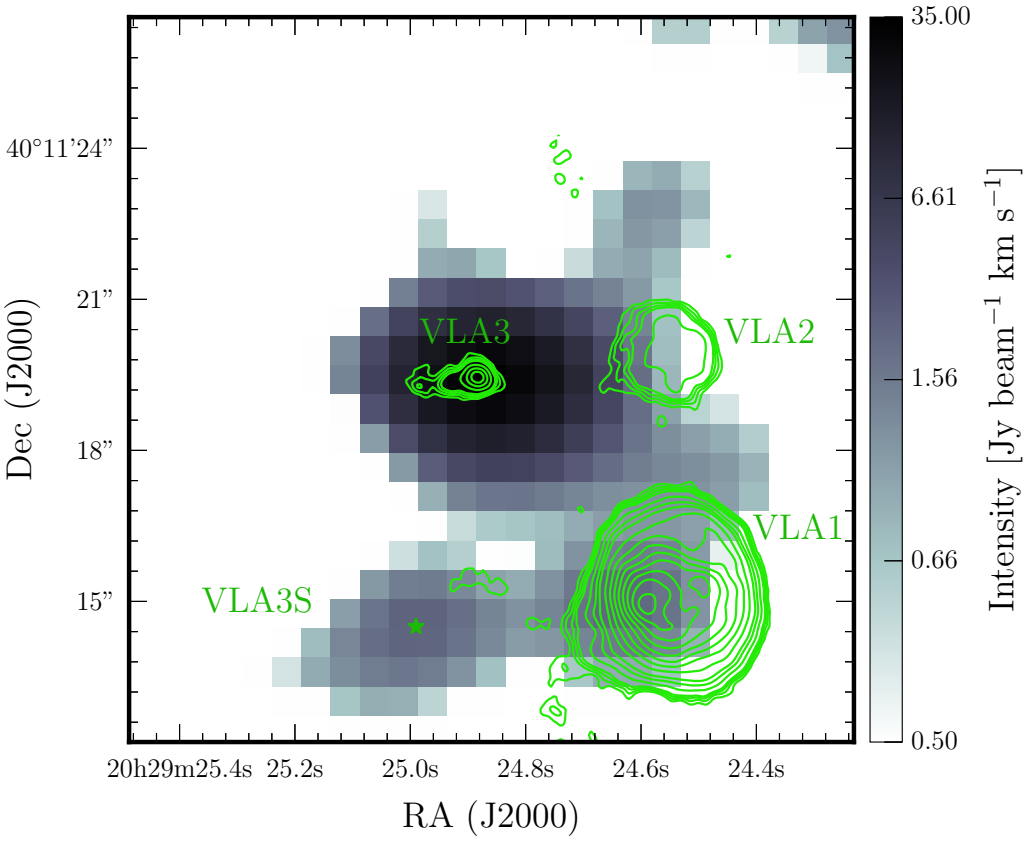

Figure 4.4: VLA 3.6 cm continuum emission (contours) from Johnston *et al.* (2013) superimposed to the K=3 zeroth moment map (grey scale). Sources are labelled and the position of VLA 3S is marked with a star. Following Johnston *et al.* (2013), contours are –3, 3, 4, 5, 7, 10, 15, 20, 30–100×30 μJy beam^{-1}.

ment map. The fit was done for each source within boxes to isolate their emission. An attempt to fit all the sources simultaneously did not produce good results due to the extended emission of VLA 3 towards the other sources. The observed size of VLA 3 decreases slightly with K, and the source is partially resolved. The orientation of the source seems to agree with the large scale orientation of the near-IR images, but the beam is oriented in the same direction. In fact, the deconvolved PAs shown in Table 4.2 have large errors, thus the orientation is mostly affected by the beam. The sizes of VLA 1 and VLA 3S appear to be

larger because they are fainter objects, hence producing a flatter Gaussian, and the emission from the other sources has not been subtracted. The scatter in PA values of VLA 1 are a consequence of the beam size.

4.3 Physical properties of the gas

4.3.1 Methodology

In order to obtain some physical properties of the gas (e.g. temperature), the methyl cyanide K ladder was fitted by using the program CASSIS. This program uses a Markov chain Monte Carlo (MCMC) which samples the parameter space in order to minimise the χ^2 between the observed and synthetic spectra. The parameters defining the synthetic models are listed in Table 4.3. CASSIS calculates spectra under the LTE approximation, or the non-LTE approximation by using the RT code RADEX (van der Tak *et al.* 2007). In order to find the kinetic temperature and gas opacity, RADEX separates the collisional and radiative statistical calculations. First, it calculates the optical depth in the optically thin limit. Then, it uses these values to calculate escape probability for a homogeneous medium and finds the level populations. This two calculations are repeated until the level populations of the radiative and collisional transitions converge.

The spectra from the data cube were first extracted and their flux units converted into main beam temperature $T_{\rm mb}$. In order to limit the region to analyse, only spectra with at least one line with a flux higher than 0.25 Jy beam^{-1} were considered in the fit. Additionally, CASSIS requires an estimate of each line rms and the flux calibration error. The first was estimated from boxes around the

Table 4.1: Zeroth moment 2-D Gaussian fit measured parameters.

K	Frequency (GHz)	E_u^a (K)	RA (J2000)	Dec (J2000)	Peak (Jy beam^{-1} km s^{-1})	$T_{\rm B}^b$ (K)	Flux (Jy km s^{-1})	Major (arcsec)	Minor (arcsec)	PA (deg)
					VLA 3					
0	220.74726	68.87	20 29 24.864	40 11 19.41	32.7±0.6	40.9	39.3±0.7	2.87±0.03	2.04±0.05	87.1±0.9
1	220.74301	76.01	20 29 24.861	40 11 19.38	26.4±0.5	37.9	31.6±0.6	2.85±0.03	2.04±0.05	86.8±1.0
2	220.73026	97.44	20 29 24.861	40 11 19.39	24.5±0.6	34.5	28.9±0.7	2.82±0.04	2.03±0.06	86.1±1.3
3	220.70902	133.16	20 29 24.861	40 11 19.39	32.1±0.6	53.9	37.8±0.7	2.81±0.04	2.03±0.05	84.7±1.1
4	220.67929	183.15	20 29 24.861	40 11 19.36	16.2±0.4	22.3	18.3±0.5	2.81±0.05	1.96±0.07	84.6±1.3
5	220.64108	247.40	20 29 24.856	40 11 19.36	12.4±0.3	15.3	13.7±0.4	2.86±0.05	1.93±0.07	87.7±1.3
					VLA 1					
0	220.74726	68.87	20 29 24.62	40 11 15.5	2.3±0.3	2.7	3.8±0.5	3.2±0.3	2.6±0.3	137±14
1	220.74301	76.01	20 29 24.62	40 11 15.5	1.9±0.3	3.3	3.3±0.4	3.1±0.3	2.7±0.3	140±15
2	220.73026	97.44	20 29 24.62	40 11 15.6	1.6±0.3	2.3	3.4±0.5	3.5±0.4	3.0±0.3	151±17
3	220.70902	133.16	20 29 24.63	40 11 15.4	2.1±0.3	2.9	4.1±0.6	3.4±0.4	2.8±0.3	136±15
4	220.67929	183.15	20 29 24.63	40 11 15.5	1.0±0.2	1.3	2.1±0.3	3.7±0.4	2.8±0.3	2.7±9.5
5	220.64108	247.40	20 29 24.63	40 11 15.4	1.2±0.1	1.1	2.0±0.2	3.2±0.2	2.6±0.3	110±9
					VLA 3S					
0	220.74726	68.87	20 29 24.99	40 11 14.5	2.6±0.3	2.8	3.2±0.3	3.2±0.2	1.9±0.3	114±4
1	220.74301	76.01	20 29 24.99	40 11 14.5	2.1±0.2	3.1	2.8±0.3	3.2±0.2	2.0±0.2	113±4
2	220.73026	97.44	20 29 24.99	40 11 14.5	2.1±0.3	2.9	2.3±0.3	2.9±0.3	1.8±0.3	117±6
3	220.70902	133.16	20 29 24.98	40 11 14.5	2.5±0.3	3.4	3.2±0.4	3.3±0.2	1.9±0.3	110±4
4	220.67929	183.15	20 29 24.98	40 11 14.4	1.5±0.3	1.4	1.7±0.3	3.0±0.3	1.8±0.4	111±6
5	220.64108	247.40	20 29 24.97	40 22 14.6	1.0±0.2	1.3	1.2±0.2	3.2±0.3	1.8±0.4	110±6

Notes. The units of RA are hours, minutes and seconds and the units of Dec. are degrees, arcmin and arcsec.

[a] From the Leiden Atomic and Molecular Database (LAMDA; Schöier *et al.* 2005).

[b] Brightness temperature at the line peak at the position of the zeroth moment peak.

Table 4.2: Deconvolved 2-D Gaussian fit sizes for VLA 3.

K	Major (arcsec)	Minor (arcsec)	PA (deg)
0	1.14±0.08	0.86±0.12	87±175
1	1.09±0.09	0.88±0.13	83±173
2	1.00±0.13	0.84±0.19	73±79
3	1.01±0.13	0.80±0.18	58±41
4	1.00±0.17	0.61±0.37	69±31
5	1.12±0.14	0.55±0.43	90±176

lines and vary between 0.04–0.06 K, where the higher the K line the higher the error. The relative flux calibration error was fixed to 20 per cent.

Different approaches were used to fit the spectra and are summarised in Table 4.3. For the LTE approximation, models with one- or two-components were used. For the two-component approach three sub-approaches were followed. In the first one, the parameters of each component were constrained as shown in Table 4.3. In the second, the results for the FWHM and $\Delta v_{\rm LSR}$ from the one-component approach were fixed in the second step. In the third approach, a colder component was fitted first to the K=0–3 lines and then a hotter and denser component was fitted to the whole spectra.

In the non-LTE approximation, only models with one component were calculated as this approximation is more time consuming. A slab geometry was used for these models. The LTE approximation in CASSIS does not require any assumption about the geometry of the source because it uses the MCMC sampled temperatures and column densities to derive the observed temperature.

The size parameter in Table 4.3 is the source size and is used to calculate the beam dilution, which is defined in CASSIS as:

$$\Omega = \frac{\theta^2}{\theta^2 + \theta_{\rm B}^2} \tag{4.1}$$

Table 4.3: Parameter constraints of the modelling with CASSIS.

Components	N	Code	$N(CH_3CN)$ (cm^{-2})	$n(H_2)^a$ (cm^{-3})	T^b (K)	Size (arcsec)	Δv (km s^{-1})	Δv^c_{LSR} (km s^{-1})
1 component	1	M1C	1×10^{13}–1×10^{18}	1×10^{3}–1×10^{9}	10–500	0–1.2	1–7	-2–2
2 components	1	M2C1a	1×10^{13}–1×10^{15}		10–150	0–1.2	1–7	-2–2
	2	M2C2a	1×10^{15}–1×10^{18}		150–800	0–1	1–7	-2–2
2 components	1	M2C1b	1×10^{13}–1×10^{15}		10–150	0–1.2	fixed to M1C results	
	2	M2C2b	1×10^{15}–1×10^{18}		150–800	0–1.2	fixed to M1C results	
2 components	1	M2C1c	1×10^{13}–1×10^{18}		10–120	0–1.2	1–7	-2–2
	2	M2C2c	M2C1c result–1×10^{18}		120–800	0–M2C1c size	1–7	-2–2

[a] Only for the non-LTE case.

[b] Excitation temperature, T_{ex}, for LTE and kinetic temperature, T_k, for non-LTE.

[c] Difference with respect to $v_{LSR} = -5.5$ km s^{-1}.

where θ is the source size and $\theta_{\rm B}$ is the beam size derived from the configuration files specific for each telescope, which include its diameter/largest baseline. In this case, the baseline used was calculated to match the resolution of the observations. The observed flux calculated by CASSIS is then $S_\nu = \Omega I_\nu$.

4.3.2 Results

LTE modelling

The results of the LTE modelling are shown in Figs. 4.5–4.7 for models M1C and M2Ca. In general all the models present similar trends and χ^2 values, thus the results for the other two component models are in Appendix A. As expected, hotter and denser regions are located close to the emission peak and all the parameters are within the limits set for the MCMC algorithm for most spectra. However, the χ^2 maps show a region to the east of the emission that is not well fitted by any of the models.

All the models require at least one component which is centrally concentrated with a peak column density close to the emission peak. For the models with two components, this corresponds to the hotter component whilst the colder component shows a flatter density distribution, except for model M2Cc where the second (hotter) component is flatter probably due to the wider limits in column density for each component. This can be interpreted as the colder component being emission from the large scale envelope, and the hotter from regions closer to the star and, at some degree, the outflow cavity. However, the reduced χ^2 maps are similar for all the models, hence in what follows the results regarding the most centrally concentrated component will be discussed.

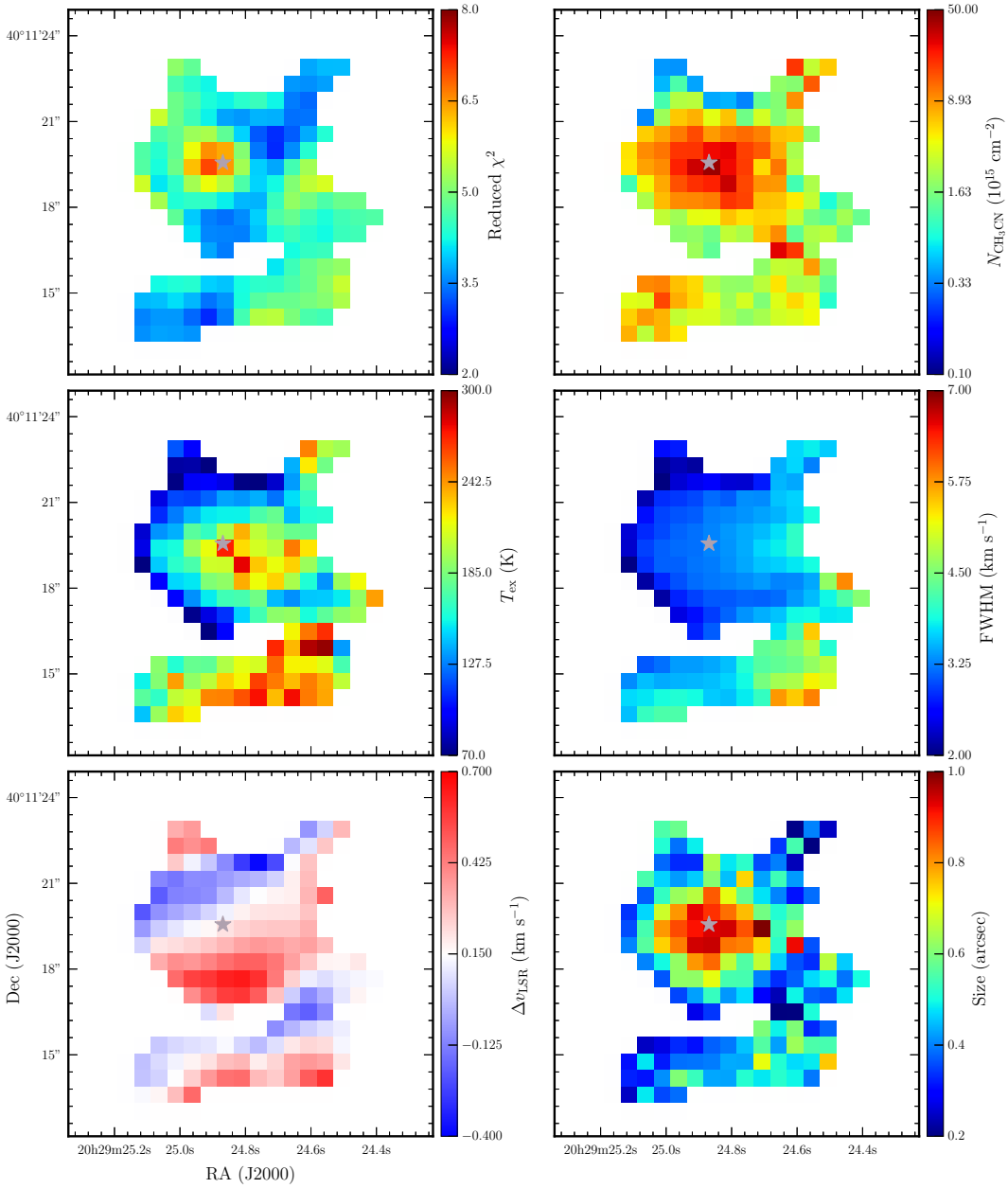

Figure 4.5: One LTE component model (model M1C) results. The star marks the position of the radio continuum source from Trinidad *et al.* (2003)

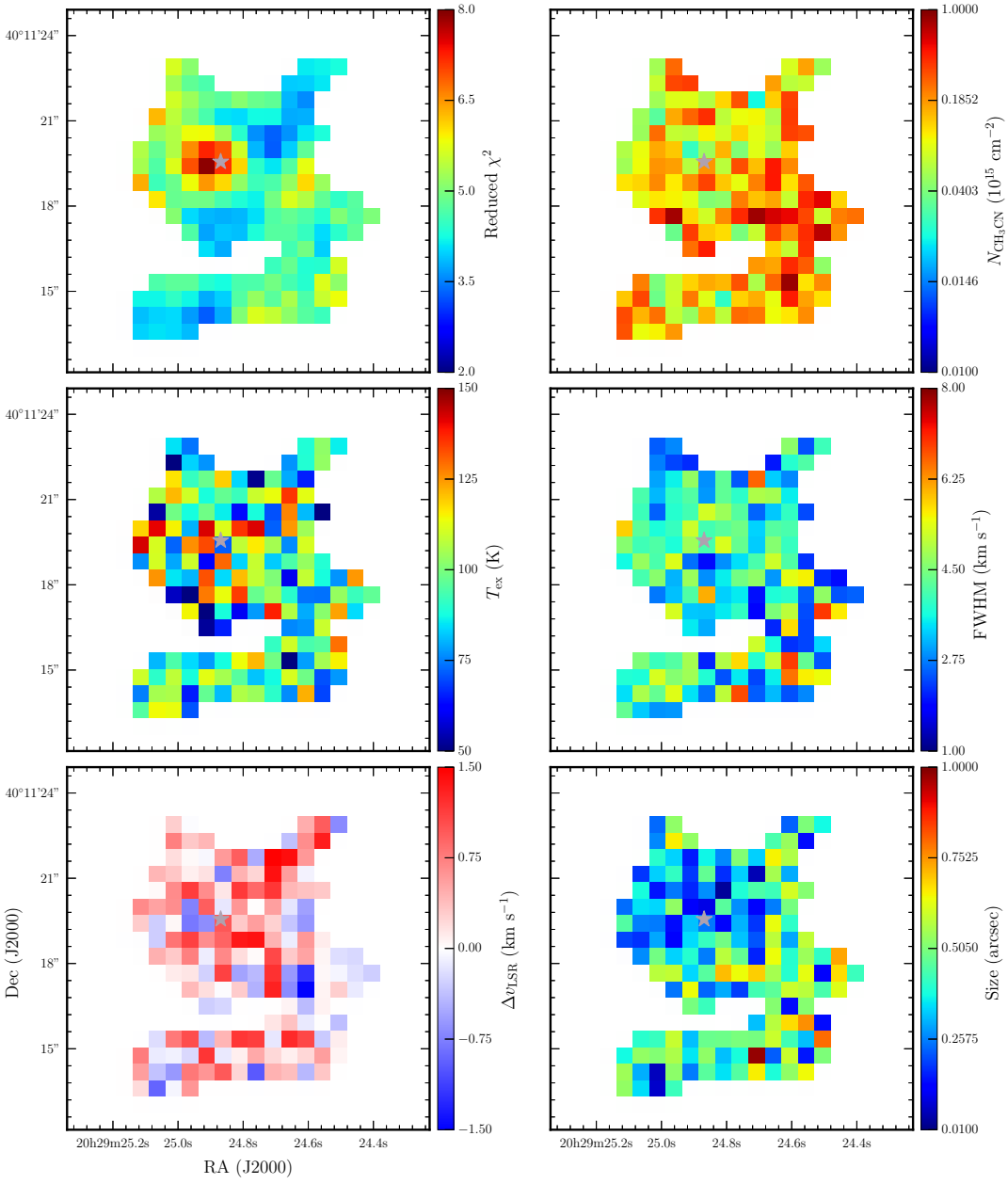

Figure 4.6: First component results for the LTE model M2C1a. χ^2 value is the same for M2C1a and M2C2a.

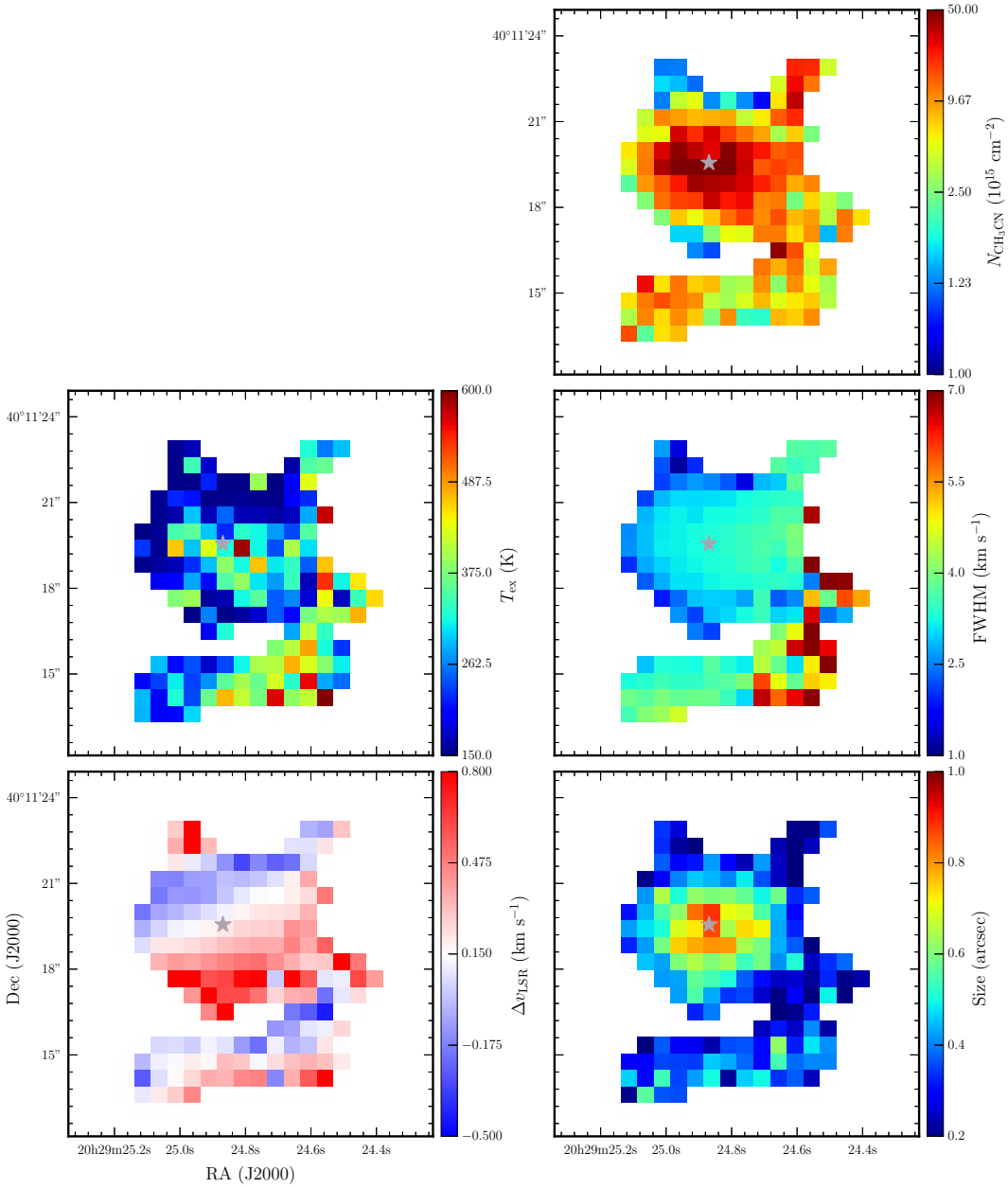

Figure 4.7: Second component results for the LTE model M2C2a.

The peak column density for VLA 3 is 4.2×10^{16} cm^{-3} in the M1C model, and is located at the position of the source. The average column density inside a region with radius 2 arcsec is 1.5×10^{16} cm^{-3}. An approximate value of the H_2 column density can be obtained from the continuum map in the optically thin limit (e.g. Morales *et al.* 2009):

$$N_{H_2} = \frac{S_\nu R_{gd}}{\Omega_B B_\nu(T_d)\kappa_\nu \mu m_H} \tag{4.2}$$

with S_ν the observed dust continuum flux and Ω_B the beam area. If eq. 4.2 is solved with a dust temperature $T_d = 190$ K (see below), a dust opacity $\kappa_{1.3mm} = 1$ cm^2 g^{-1}, a mean molecular weight $\mu = 2.3$ and a gas-to-dust ratio $R_{gd} = 100$, a peak H_2 column density value of 2.0×10^{23} cm^{-3} and an average of 9.9×10^{22} cm^{-3} within the same 2 arcsec region are obtained. Hence the methyl cyanide abundance is 2.1×10^{-7} for the peak value and 1.5×10^{-7} for the average.

The excitation temperature for the M1C model in VLA 3 peaks at the source position and has a value of 271 K. In a region of radius 2 arcsec the minimum temperature is 120 K and the average is 190 K. In general the hotter component of the two component models does not peak at the position of the continuum peak. The peak in temperature closest to the source position in the M2C2b is similar to the M1C model (238 K) whilst for M2C2a and M2C2c the peak temperature is 587 and 658 K, respectively.

The FWHM of the line gets wider along the blue shifted outflow direction. This may be due to turbulent motion of the gas in the outflow. The red shifted outflow direction does not show the same trend, probably because the emission is optically thick towards that side. However, the fit is worse towards the red shifted

outflow direction as shown by the reduced χ^2 maps, hence this result should be taken with caution. The line velocity maps of VLA 3 are consistent with the first moment maps in Fig. 4.3.

The sizes obtained from the modelling are smaller than the beam size of the observations and the deconvolved angular size derived from continuum observations ($\sim$2.0 arcsec from Table 3.9). The less beam diluted areas are located towards the denser regions. As the flux is proportional to the beam dilution factor Ω and proportional to the column density in the optically thin regime, the size and the column density parameters may be degenerate. Models with a fixed size of 2.5 arcsec, which is close to the observed continuum size and larger than the beam size thus minimising the beam dilution, were calculated under the LTE approach with a one component model. However, the same trends for the other parameters and similar reduced χ^2 maps were obtained, but the peak column density was $\sim$10 per cent lower than in the free size parameter approach.

The VLA 1 and VLA 3S regions show a different temperature and velocity structure. As expected for an H II region, VLA 1 has wider lines due to turbulent gas expansion and is hotter than the other two regions. A velocity similar to VLA 3 is observed in the north-east to south-west direction, which can be due to rotation or expansion of the gas for the bluer north-east side. If VLA 1 and 3 are in the same region, i.e. from material with the same initial angular momentum direction, then the observed gradient may be due to rotation. A similar velocity gradient is observed towards VLA 3S, which may imply that it belongs to the same region. VLA 1 also has a lower column density in comparison to the other two regions, which is consistent with it being optically thin at mm/radio wavelengths as found by e.g. Trinidad *et al.* (2003) at 3.6 cm. VLA 3S peaks in temperature

and column density at the same position in the M1C map. The peak temperature is 240 K and its column density is $1.6{\times}10^{16}$ cm^{-3}, hence is slightly colder and less dense than VLA 3.

Non-LTE modelling

The results for the non-LTE modelling with one component are shown in Fig. 4.8. These results are similar to those obtained from the LTE modelling, which can be seen by comparing the χ^2 maps. The H_2 density varies by two orders of magnitude but there is not a clear distribution. The average value within a region of radius 2 arcsec centred in the continuum peak position is $n_{H_2} = 1.1 \times 10^7$ cm^{-3} but with most values in the $10^6 - 10^7$ cm^{-3} range, which is consistent with the values expected from the continuum RT model ($n_{H_2} > 10^6$ cm^{-3} within 5000 au).

The optical depths obtained from the RADEX models are shown in Fig. 4.9 for each line. The lines tend to be thicker towards the red shifted outflow lobe. This is consistent with that side having a larger column of gas due to the geometry of the source derived in the previous section. As previously stated, this should be taken with caution as that region is not well fitted by the models. The lines are also thinner towards VLA 1 for all the values of K.

4.4 Radiative transfer modelling

4.4.1 Fitting procedure

Models for the K=3 and 5 lines were calculated using the line RT code MOLLIE (Keto & Rybicki 2010). The former line is the most prominent one and where

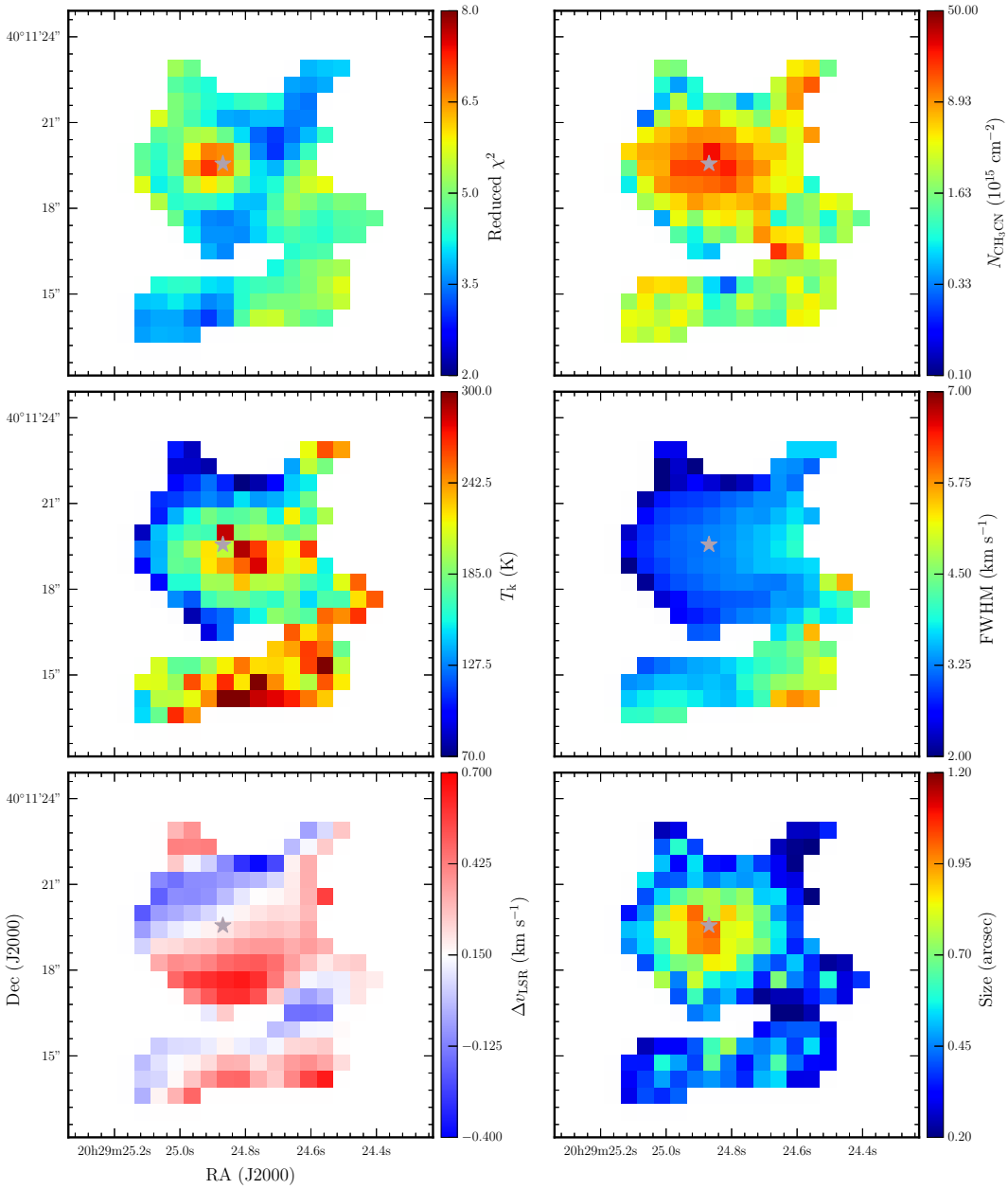

Figure 4.8: One non-LTE component model (model M1C) results.

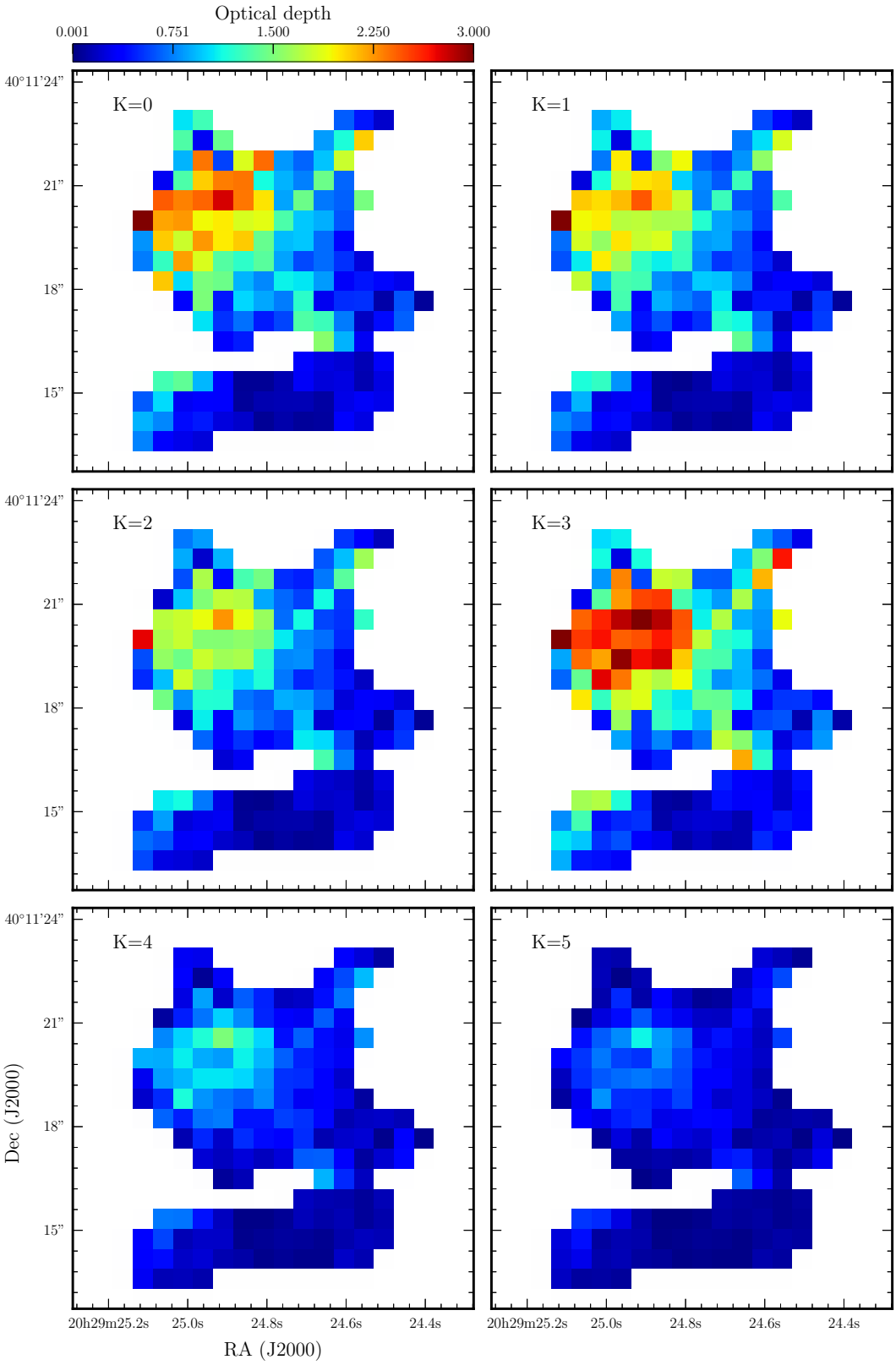

Figure 4.9: Optical depth maps for each line obtained from RADEX.

the velocity pattern is clearest as shown in Fig. 4.3, whilst the latter line traces the hottest material out of all the lines. The code requires grids describing the density, temperature and velocity distributions of the collisional partner (H_2), the abundance of the molecule with respect to the total gas density and the width of the line. MOLLIE calculates the molecular line emission at different velocities, i.e. produces a data cube, under the LTE approximation for CH_3CN. Since the radiation field (the gas temperature) was already calculated in the previous chapter and the LTE approximation is used, MOLLIE only uses the ray tracing method to produce the images.

For the modelling, three nested grids with increasing resolution on the region close to the star were used. In order to optimise the computer resources, the grids were defined with 32^3, 40^3 and $64 \times 64 \times 14$ cells from large to small scale, respectively. The former covers a size of $3.9{\times}10^5$ au, the second grid a size of $1{\times}10^5$ au and the latter a size of 1000 au in the x-y plane. The smallest scale this grid can resolve is 15.6 au.

The density and temperature distributions were taken from the continuum RT modelling. The density values were calculated on each point of the grid using the equations in Section 3.3, whilst the temperature values were obtained from the closest point on the HYPERION grid. Since the line RT grid is coarser than the continuum RT grid, the values at heights smaller than the cell size of each grid were averaged for distances smaller than the disc radius. This increases the temperature in the central region, which is not resolved by the observations but it determines the flux scale at the centre of the line. Without this correction the values would have been otherwise underestimated by the cavity values.

The same was applied to the velocity distribution, which was calculated at

each point of the grid. For the envelope, the Ulrich envelope velocity distribution was used. Unlike HYPERION, the velocity components of the envelope inside the disc radius were set to zero because the Ulrich solution is undefined at the centrifugal radius resulting in a large increase in velocity. This produces a discontinuity in the velocity distribution but at scales which are not resolved by the observations. The 3-D components of the envelope velocity distribution are given in spherical coordinates by:

$$v_r(r,\theta) = -\left(\frac{GM_\star}{r}\right)^{1/2}\left(1+\frac{\mu}{\mu_0}\right)^{1/2} \tag{4.3}$$

$$v_\theta(r,\theta) = \left(\frac{GM_\star}{r}\right)^{1/2}(\mu_0-\mu)\left(\frac{\mu_0+\mu}{\mu_0\sin\theta}\right)^{1/2} \tag{4.4}$$

$$v_\phi(r,\theta) = \phi_{\rm dir}\left(\frac{GM_\star}{r}\right)^{1/2}\frac{\sin\theta_0}{\sin\theta}\left(1-\frac{\mu}{\mu_0}\right)^{1/2} \tag{4.5}$$

where $\phi_{\rm dir}$ parametrises the direction of rotation, i.e. has a value of ± 1.

The outflow velocity was modelled with a Hubble expansion law:

$$v_r(r) = v_0\frac{r}{r_0} \tag{4.6}$$

where v_0 is the velocity at $r_0 = 10^4\cos^{-1}\theta_{\rm c}$ au with $\theta_{\rm c}$ the half opening angle of the cavity like in the continuum modelling. This velocity distribution was used by Wang *et al.* (2012) to interpret the molecular emission from the PdBI 1.3 mm observations at a smaller scale.

For the disc, the azimuthal velocity was parametrised as in Shakura & Sunyaev

(1976), which is described in cylindrical coordinates by:

$$v_\phi(\varpi) = \phi_{\rm dir}\sqrt{\frac{GM_\star}{\varpi}} \tag{4.7}$$

The other two components of the velocity were set to zero in order to limit the number of parameters in the fit and because the disc is not resolved in the observations.

MOLLIE includes a line width parameter which was set to the sum in quadrature of the thermal speed of sound and a turbulence velocity. The turbulence velocity $v_{\rm nth}$ was varied during the modelling (see below).

Following the studies of other molecules presented above (e.g. Kaźmierczak-Barthel *et al.* 2015), the methyl cyanide abundance was defined as a step function of the temperature. This approach has also been used for methyl cyanide in other studies (e.g. Johnston *et al.* 2015). The abundance function is then defined as:

$$\xi(T) = \begin{cases} \xi_0 & \text{if } T < T_0 \\ \xi_1 & \text{if } T_0 \leqslant T \leqslant T_1 \\ \xi_2 & \text{if } T > T_1 \end{cases} \tag{4.8}$$

This approach is consistent with the change in abundance due to thermal desorption of molecules from dust grains in the evolution of hot cores when the temperature increases with time (e.g. Viti *et al.* 2004). Several temperature values were explored to match the extension of the zeroth moment map and the ratios between the K=3 and 5 lines, with increasing number of temperature steps from 0 to 2. It was found that 2 temperature steps are better to explain these

observations, and the temperatures were then fixed to $T_0 = 80$ K and $T_1 = 100$ K, and the abundance $\xi_0 = 5 \times 10^{-12}$. ξ_1 and ξ_2 were varied during the modelling (see below).

The model images were rotated and then synthetic observations were calculated with CASA. The synthetic images included thermal noise which approximately matches that observed. The K=3 line first moment map in Fig. 4.10(a) shows that, if the velocity structure was completely due to rotation, the rotation axis will be oriented roughly at a PA = 286°. However, as pointed out by Wang *et al.* (2012), expansion or infalling motions can change the perceived position of the rotation angle. The orientation of the disc plane as derived from a Gaussian fit to the 1.3 mm continuum observations is PA = 6° (Wang *et al.* 2012) which is nearly perpendicular to the radio jet orientation (deconvolved PA = 97 ± 6° from a 2-D Gaussian fit to the 3.6 cm observation of Johnston *et al.* 2013 in Fig. 4.4). Therefore, the small scale rotation axis does not have the same orientation as the large scale outflow cavity. Then the orientation of the model rotation axis was set to PA = 276°, i.e. perpendicular to the disc plane.

Similar to the continuum modelling, the best-fitting model was chosen by averaging the ranking of: the reduced χ^2 of the peak spectra for K=3 and 5 with a weight of 1/3 for each one, and reduced χ^2 of slices along and perpendicular to the small scale rotation axis of the first moment map of K=3 with a weight of 1/6 for each one. The weight for each slice is smaller than for each line because they are taken from the same line, i.e. similar to the K-band and 1.3 mm observations in the continuum modelling. The peak spectra were obtained from the position of the peak in the zeroth moment map, and the χ^2 were calculated by using the observed points with values larger than $5\sigma_{\rm rms}$ with $\sigma_{\rm rms} = 30$ mJy beam^{-1} for the

K=3 line and 50 mJy beam^{-1} for the K=5 line. The errors in the χ^2 calculations were equal to the noise of each line. The larger error in K=5 is because it is in a noisier section of the spectrum and has lower signal-to-noise ratio.

In order to calculate the first moment slices, the position-velocity maps (hereafter pv maps) of the K=3 line were first calculated. Fig. 4.10(a) shows the directions of the slices where the pv maps were calculated corresponding to slices of 2 arcsec width along the rotation axis (PA = 276°) and its orthogonal. The resulting pv maps are shown in Fig. 4.11. Then first moment values were obtained from the pv maps by taking the flux weighted velocity average along each offset value. The error was obtained from the propagation of errors with a flux error equal to $\sigma_{\rm rms}$ = 30 mJy beam^{-1} and velocity error equal to the channel width σ_v = 0.5 km s^{-1}. Only values with fluxes higher than $5\sigma_{\rm rms}$ = 150 mJy beam^{-1} were utilised in the slice. The slices are shown in Fig. 4.12. Due to the presence of other sources and the thermal noise added to the models, only points with an offset between –2.4 to 3 arcsec and –2.4 to 2.4 arcsec were compared between observations and models at PA = 276 and 6°, respectively.

Prior to obtaining the best-fitting model, the centroid of the observed K=3 and 5 spectral lines were aligned with all models ones. An average shift of 0.38 ± 0.02 MHz (-0.51 ± 0.03 km s^{-1}) was obtained. This value is within the errors in $v_{\rm LSR}$ (cf. Section 4.2) and equivalent to a systemic velocity of –6 km s^{-1}. This shift was applied to the observed spectral and first moment data before the calculation of the χ^2 values.

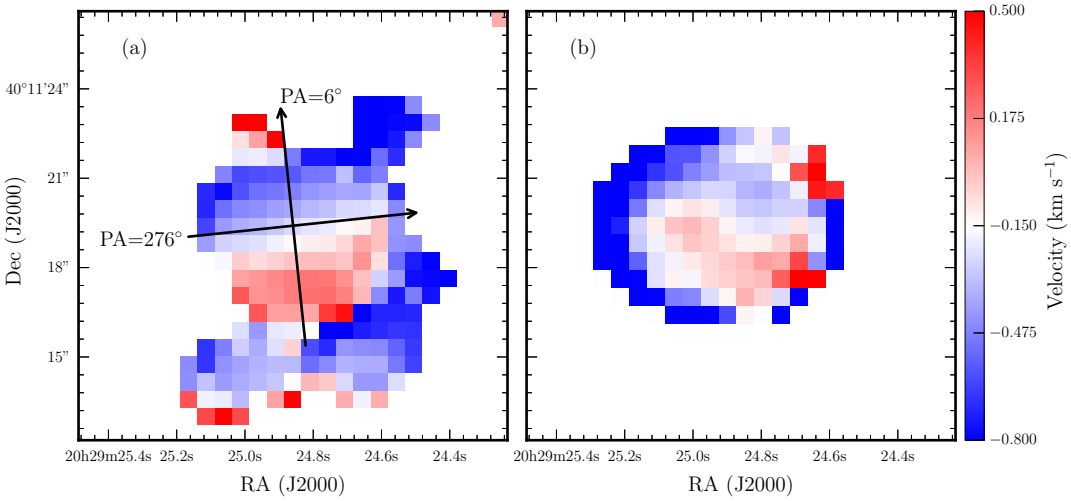

Figure 4.10: Observed first moment map for the K=3 line (a) and from the overall best-fitting model (b). Black arrows show the direction of the slices in Fig. 4.12 with the arrows pointing towards positive offsets.

Table 4.4: Values of the line modelling parameter grid.

Parameter	Values
R_c	440, 2200, 4400 au
Abundance 1 (ξ_1)[a]	1×10^{-8}, 5×10^{-8}
Abundance 2 (ξ_2)[a]	2×10^{-8}, 5×10^{-8}, 8×10^{-8}
Outflow velocity at $z = 10^4$ au (v_0)	0, 0.2, 0.5 km s^{-1}
Turbulent width (v_{nth})	0.5, 0.8, 1.0 km s^{-1}

[a] All the models in the grid have $\xi_1 < \xi_2$.

4.4.2 Parameter selection

Key parameters were varied in a grid as listed in Table 4.4. The first grid of parameters was calculated with a stellar mass $M_\star = 40$ M$_\odot$, as in the continuum modelling. However, the lines were double peaked, which is not observed. Hence the stellar mass was reduced to 20 M$_\odot$ and the envelope infall rate was scaled accordingly (cf. eq. 3.11).

Preliminary results showed that for a 40 M$_\odot$ star and a 440 au centrifugal radius the velocity distribution is dominated by inflow motions. Therefore, models with different centrifugal radii were calculated only for models with stellar mass

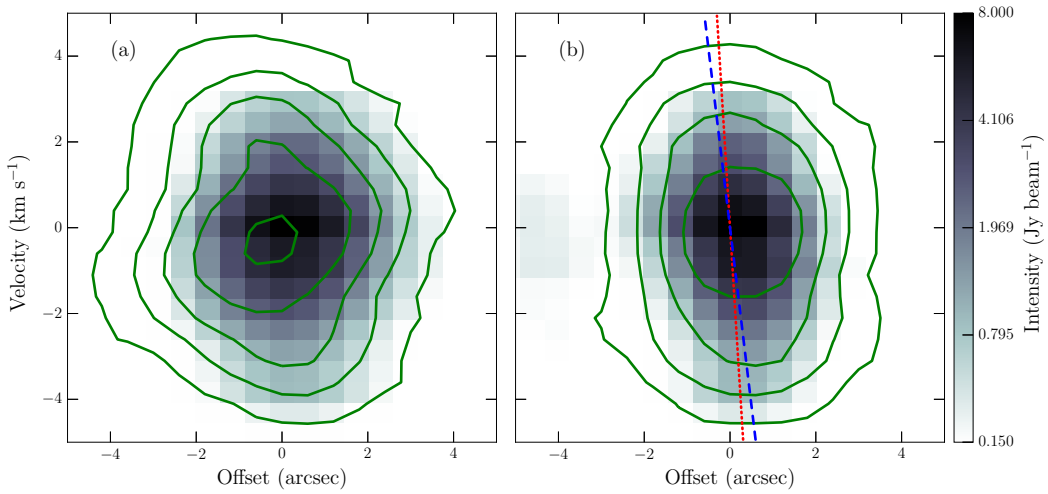

Figure 4.11: Observed position-velocity (pv) maps (grey scale) and overall best-fitting model pv maps (contours) for a position angle of (a) 276°, i.e. along the rotation axis, and (b) 6°. Contours levels are 0.15, 0.8, 2.0, 4.0 and 8.0 Jy beam^{-1}. The dashed blue and dotted red lines in (b) show the linear velocity gradient found here (8.3 km s^{-1} arcsec^{-1} at PA = 6°) and by Wang *et al.* (2012) from their HDO pv map (16.2 km s^{-1} arcsec^{-1} at PA = 0°), respectively.

of 20 $M_{\odot}$. Larger centrifugal radii were not used in the modelling because as the centrifugal radius increases the continuum fit would get worse. In these models, the disc radius was not fixed to the centrifugal radius.

The range of the abundance values is based on the results of the previous section, which are consistent with values in the literature for methyl cyanide in high-mass star forming regions (e.g Hunter *et al.* 2014; Johnston *et al.* 2015). The model abundances are shown in Fig. 4.13.

The disc velocity only changed when the stellar mass was varied. The direction of the rotation of the envelope and disc was fixed to $\phi_{\rm dir} = 1$, i.e. anticlockwise looking down from the blue shifted cavity axis as suggested by Wang *et al.* (2012) from their first moment maps of HDO, $H_2{}^{18}O$ and SO_2 line emission.

The outflow velocities were based on Johnston *et al.* (2013) who found an

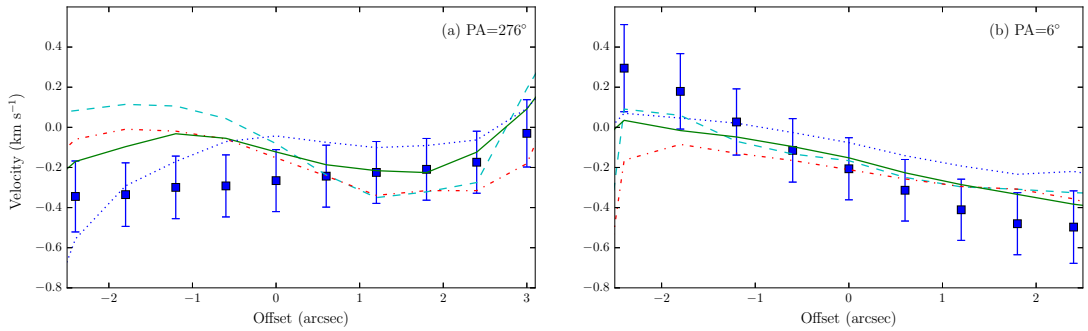

Figure 4.12: Observed (blue squares) and best-fitting models first moment slices for K=3 along the rotation axis (a) and its orthogonal direction (b) as shown in Fig. 4.10. Best-fitting models are separated by R_c with dashed cyan line for $R_c = 440$ au ($M_\star = 40$ M$_\odot$), dash-dotted red line for $R_c = 440$ au ($M_\star = 20$ M$_\odot$), continuous green line for $R_c = 2200$ au and dotted blue line for $R_c = 4400$ au.

average velocity relative to v_{LSR} of -1.2 km s^{-1} at a deprojected outflow length of 61000 au (assuming an inclination of 60°, i.e. ∼9400 au at an inclination angle of 30°) from C^{18}O line observations. Wang *et al.* (2012) found that a wind with a Hubble law constant of 10 km s^{-1} arcsec^{-1}, which is 200 times higher than the highest velocity used here (roughly 0.5 km s^{-1} per 10000 au). Such high velocity disc wind was not included here because the scale affected by it is not resolved by the methyl cyanide observations. It is worth noticing that the methyl cyanide emission do not show any signatures of outflows thus it is not expected to constrain this parameter.

4.4.3 Results

Table 4.5 lists the parameters of the best-fitting models separated by R_c and stellar mass. The overall best-fitting model is from the grid with $R_c = 2200$ au. Its velocity distribution in the input intermediate refinement grid, which is the relevant scale for the observations, is shown in Fig. 4.14. Fig. 4.15 shows the

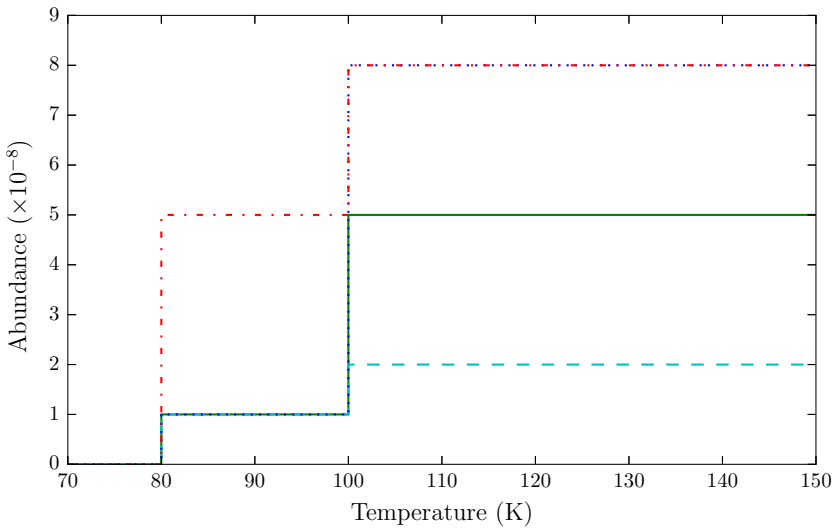

Figure 4.13: Methyl cyanide model abundances as a result of the combination of the values in Table 4.4 by using the definition from eq. 4.8.

Table 4.5: Parameters of the best-fitting models for each R_c and stellar mass combination.

Parameter	Values			
Stellar mass ($M_\star$)	40	20	20	20 $M_\odot$
Centrifugal radius (R_c)	440	440	2200	4400 au
Abundance 1 (ξ_1)	1×10^{-8}	1×10^{-8}	1×10^{-8}	1×10^{-8}
Abundance 2 (ξ_2)	2×10^{-8}	2×10^{-8}	5×10^{-8}	8×10^{-8}
Outflow velocity (v_0)	0.5	0.5	0.5	0.5 km s^{-1}
Turbulent width (v_{nth})	1.0	1.0	1.0	1.0 km s^{-1}

peak spectra of each best-fitting model for K=3 and 5, and K=0 is also shown for comparison. The best-fitting models reproduce relatively well the width of the K=3 line and the ratio between the line peak fluxes of the K=3 and 5 lines. It is also worth noticing that even though K=0 was not included in the modelling, the model and the observed lines are similar. On the other hand, the peak of the observed lines are skewed towards higher velocities with respect to the model lines. The width of the K=5 line is also not well fitted by the model.

The observed first moment slice along the rotation axis in Fig. 4.12(a) is

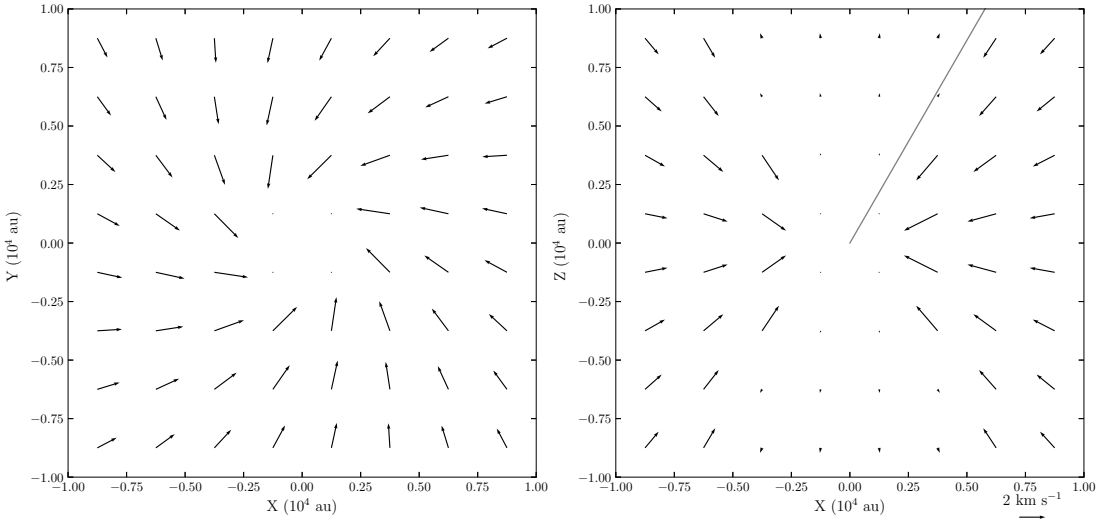

Figure 4.14: Velocity distribution of the inner 10^4 au from the input intermediate refinement grid used in the RT code of the overall best-fitting model. The velocity scale is shown in the bottom right corner. The velocities in the mid-plane with $z = 0$ (left column) range from 1.7 to 2.6 km s^{-1} from the outside, while dots close to zero have a velocity of 0.08 km s^{-1}. The velocities in the mid-plane at $y = 0$ (right column) range from 0.08 to 2.9 km s^{-1}. The continuous grey line shows the viewing angle.

relatively flat, indicating that there is not much contribution from the outflow or rotation in this direction. On the other hand, the models are not as flat as the observations, but as the centrifugal radius increases the flatter the models are. This is because as the centrifugal radius increases the infall dominated region of the envelope, where $\rho \propto r^{-1.5}$, moves outwards and in the inner envelope the rotation starts to become more important. Then the gradient of the first moment map slice orthogonal to the rotation axis increases with centrifugal radius as it can be noticed in Fig. 4.12(b) when the models with $M_\star = 20$ M$_\odot$ increase the centrifugal radius from 440 au to 2200 au. It is not clear that the same happens from 2200 au to 4400 au, however the average slope in the –2 to 2 arcsec offset range is -0.098 ± 0.003 km s^{-1} arcsec^{-1} and -0.099 ± 0.003 km s^{-1} arcsec^{-1} for the models with 2200 and 4400 au, respectively. The model shown in Fig. 4.12(b)

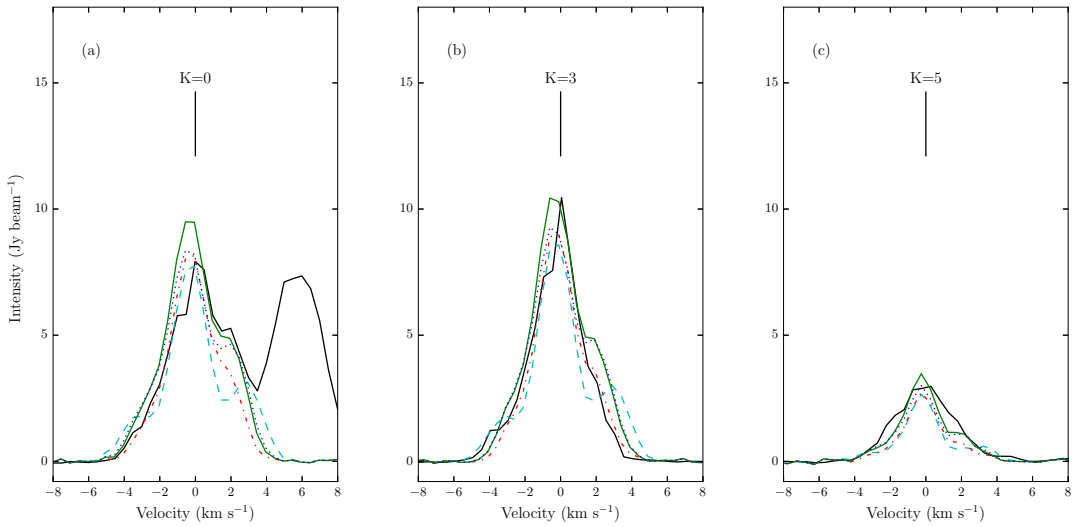

Figure 4.15: Observed (black line) and best-fitting models peak spectra for (a) K=0, (b) K=3 and (c) K=5. Best-fitting models are separated by R_c with dashed cyan line for $R_c = 440$ au ($M_\star = 40$ M$_\odot$), dash-dotted red line for $R_c = 440$ au ($M_\star = 20$ M$_\odot$), continuous green line for $R_c = 2200$ au and dotted blue line for $R_c = 4400$ au.

with $R_c = 4400$ au has slope of –0.082, thus it was probably selected because it fits better the spectral lines than the other $R_c = 4400$ au models. The noise added during the simulation of the observations also plays a role in making models with a higher slope between –2 and 2 arcsec fit the data worse even though a 5σ clipping is used, especially if the abundance is lower since these models tend to be less extended.

The best fitting models with stellar masses of 40 and 20 M$_\odot$ and $R_c = 440$ au have identical model parameters. Fig. 4.15 shows that the 20 M$_\odot$ model fits better the width of the K=3 line and does not have the high-velocity wings observed in the larger mass model. However, as a result of decreasing the mass the rotation and infall are slower which is reflected in flatter slices in Fig 4.12(b).

The best-fitting model pv maps in Fig. 4.11 show that the model is more extended than the observations, but their shapes are similar. Fig. 4.16 shows

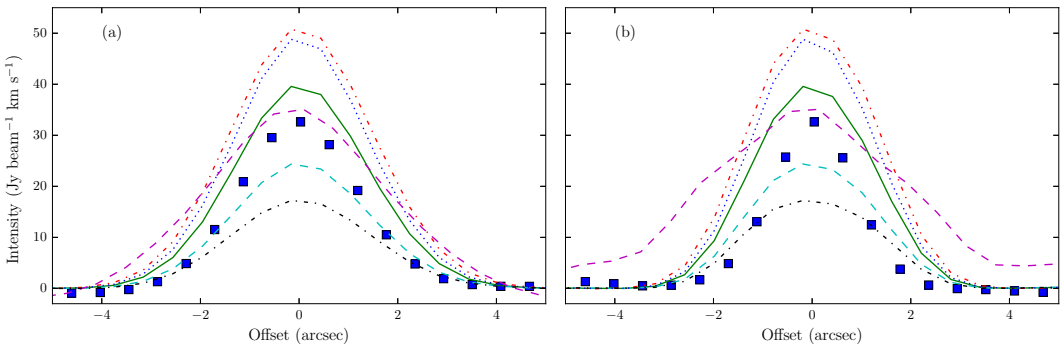

Figure 4.16: Observed (blue squares) and model zeroth moment map slices along the horizontal axis (a) and vertical axis (b) and centred in the peak. The continuous green line corresponds to the best-fitting model, the dashed cyan and dotted blue lines correspond to models with the same parameters as the best-fitting one but with the abundances shown in Fig. 4.13 for the same lines. Example models based on the best-fitting model but with other abundances are also shown: dashed magenta lines are models with a constant abundance of 5×10^{-8}, dash-dotted red lines has a constant abundance of 5×10^{-8} for $T > 80$ K and 5×10^{-12} otherwise, and dash-dotted black line has the same abundance as the best-fitting model, but with a jump at 200 K instead of 100 K.

slices of the zeroth moment map along the horizontal and vertical directions. As shown in the figure, the model emission is more extended than the observed one. If the abundance ξ_2 decreases the peak emission is underestimated but it is less extended. Whilst if the abundance ξ_2 increases the model overestimates the emission and is more extended. Table 4.5 also shows that the larger the centrifugal radius the greater the abundance. If the centrifugal radius increases then the amount of matter in the inner region decreases because the density distribution flattens for radii smaller than the centrifugal radius. Thus an increase in the abundance of the hotter gas is needed in order to match the line intensity.

The best-fitting model has an outflow reference velocity of 0.5 km s^{-1}. This is the largest velocity considered in the model grid. However, this parameter may not be well constrained because the observations do not show any clear evidence

of outflow motion in the first moment map in Fig. 4.10.

All the best-fitting models have a turbulent width of 1.0 km s^{-1}. However, close to the line peak the models tend to be wider, particularly for K=3. Since the observed lines seems to be skewed towards higher velocities, models with wider lines, i.e. larger turbulence velocity, tend to fit better. The line wings can also be well fitted by models with smaller turbulent width parameters, but they do not fit well the width of the line. Thus the turbulent width should be taken as an upper limit.

4.5 Discussion

4.5.1 The velocity distribution of gas in AFGL 2591

The analysis presented in the previous sections shows that the methyl cyanide line emission is tracing material at intermediate scales (∼5000 au) in the envelope of AFGL 2591. The velocities in the line of sight and the radiative transfer modelling imply that the molecular line emission is dominated by rotation rather than infalling or outflow material. The direction of the rotation is consistent with the observations of smaller scales made by Wang *et al.* (2012). They also found that the linear velocity gradient[1] in the HDO line pv map is 16.2 km s^{-1} $arcsec^{-1}$ at a PA = 0°. Fig. 4.11(b) shows that this agrees with the data here presented. Moreover, the linear velocity gradient from the pv map at PA = 6° is 8.3 ± 3.1 km s^{-1} $arcsec^{-1}$, which is consistent with slower rotation of the envelope in comparison to the disc. Thus the small scale rotating motion observed in other

[1]NB The linear velocity gradient is calculated from the average flux weighted offset rather than the average flux weighted velocity as is the first moment.

molecules can be connected to the large scale motion traced by methyl cyanide.

For the parameters derived from the dust continuum modelling, the Ulrich model velocity distribution is dominated by infall rather than rotation. Increasing the centrifugal radius does not solve the problem completely as the observed first moment slice gradient (0.17 km s^{-1} $arcsec^{-1}$) is higher than the models one, which reaches on average a gradient of 0.09 km s^{-1} $arcsec^{-1}$. In the dust RT modelling it was found that a higher density gradient, thus bringing more material closer to the star, was needed in order to fit the (sub)mm observations. The increase in centrifugal radius is against this.

Benz *et al.* (2007) noted that their observations of HCN molecular line emission at the continuum peak were skewed towards the red like in the observations here presented for CH_3CN, whilst other lines (e.g. SO) were skewed towards blue. They interpreted the blue skewed lines as produced by material in the inner region absorbing the red shifted emission. Their observations however trace a smaller region close to the star, thus this can be explained by an optically thick disc. On the other hand, the line RT modelling lines do not show any asymmetry close to the line centre.

Although the RT modelling here presented seems to favour models with outflow expansion velocities of 0.5 km s^{-1} at distance of 10^4 au from the central source, this value is not well constrained since the observations do not show a clear evidence of tracing outflow material. The width of the lines seems to be different in the outflow cavity than in the envelope. The wider lines are located in the outflow cavity and can be explained as turbulent motions of gas in the outflow. The emission from the region where the red shifted outflow is located do not show the same trend. It can be argued that the emission is optically thick

towards the red shifted outflow, which is consistent with the inclination of the outflow axis with respect to the line of sight being closer to face-on.

4.5.2 Temperature and molecular abundance

The excitation and kinetic temperatures derived from the fit to the data cube are within the 100–300 K range. This gas is located within a region of radius 5000 au as implied by the observed source size. This is consistent with the dust temperature distribution derived from the continuum modelling, where the bulk of the material at the aforementioned temperature range is located (cf. Fig. 3.18).

Similarly to other molecules, the methyl cyanide abundance needed to be defined as a piecewise function in order to fit the extension of the emission and the ratios between different K lines. Fig. 4.16 shows that a constant abundance model produces a much more extended emission. When only one step at $T = 80$ K is included, the peak of the zeroth moment map is overestimated, which also happens when the abundance is increased in the $80 < T < 100$ K step. Moving the second step from $T_1 = 100$ K to 200 K underestimates the peak zeroth moment, thus the $T = 100 - 200$ range is the most relevant one in order to fit the peak of the zeroth moment emission. The inclusion of a step at 230–300 K was not needed during the line RT modelling. This jump should increase the abundance of N-bearing molecules in the inner hotter regions (e.g. Rodgers & Charnley 2001). Such temperatures are reached in regions much closer to the star which are not resolved by the methyl cyanide observations here presented. Further observations with NOEMA extended configurations, i.e. higher spatial resolution, will be available and can be used to explore more in this subject.

Further refining of the RT grid is also needed in order to explore more the changes in abundance.

4.6 Conclusions

The velocity distribution from methyl cyanide CH_3CN J=12–11 emission shows that the inner envelope (scales of ∼5000 au) is rotating with a direction consistent with the disc rotation. As expected, the velocity gradient of the inner envelope is slower than the disc. The observed velocity distribution cannot be reproduced by the Ulrich model, which is dominated by infall for models with the same parameters as the ones derived from continuum RT modelling and does not rotate as fast as what the observations have shown. Therefore, the limitations of the Ulrich model does not allow a better fit to the data, and models with a higher rotation at larger radii and a steep density distribution are needed to fit the data.

The modelling of the emission shows that the gas in the blue shifted outflow has wider line wings consistent with turbulent motion. The red shifted outflow cavity does not show the same trend, maybe because it is optically thick due to the envelope material.

Chapter 5

Conclusions

5.1 Summary

In this thesis, the circumstellar matter distribution of MYSOs was studied through new high resolution observations in the IR and mm regimes. This early evolutionary stage, characterised by the presence of inflow and outflow motions and high luminosities, offers the best chance to study the formation of massive stars before the ionising radiation of the star erases the imprints left in the circumstellar matter during the accretion process. These imprints, which are the result of several physical processes, are reflected in their temperature, density and velocity distributions which in turn produce their observable properties.

The highest resolution observations in the far-IR at 70 μm to date come from the *Herschel Space Observatory*. The spatial information in such emission from MYSOs had been little studied as most previous data were unresolved. Using data from the *Herschel*/Hi-GAL survey, a study of the observational properties at 70 μm of a sample of three MYSOs was conducted. Hi-GAL observations were

made at a high scan velocity, which resulted in a PSF smeared along the scan direction. First, the observations of two fields at Galactic latitude $l = 30°$ and $50°$ were analysed to characterise the 70 μm PSF. This analysis showed that the observations of the asteroid Vesta, which were made during the science verification phase, describe well the PSF and have a higher signal-to-noise ratio than PSF stars candidates in the two Hi-GAL fields analysed.

Based on this result, it was then investigated whether three relatively isolated MYSOs were resolved or not at 70 μm. This study showed that isolated sources with higher $\sqrt{L}/d$ have a higher probability of being resolved, especially if they are observed at lower scan speeds where the PSF is sharper and more symmetrical. 1-D models of the SED and the 70 μm emission favour models with shallower power law density exponents. Shallower exponents are expected in the inner regions (thousand au scales) of rotationally flattened envelopes, but this is unlikely given the extension of the 70 μm emission. Thus the emission needs to be analysed with non-spherically symmetric models to determine whether the extended emission is due to rotation flattening or emission from outflow cavities.

To test this, the nature of the 70 μm emission of the MYSO AFGL 2591 was studied. *Herschel*/HOBYS observations with a slower scan speed were used, which resolve the source at 70 μm. The 3-D RT modelling of the source showed that the 70 μm emission is extended due to emission along the envelope cavity walls. These are irradiated by the photons escaping through the emptier outflow cavity.

As part of the RT modelling of AFGL 2591, constraints from other high-resolution observations across the spectrum were utilised to produce a temperature and density distribution. The density distribution consisted of an Ulrich

rotationally flattened envelope, a disc of 1 $M_{\odot}$ and paraboloidal bipolar outflow cavities. The images produced by the RT code reproduce relatively well most of the observations. The temperature distribution shows that the temperature is higher in the cavity walls than inside the envelope at a constant radius from the star.

The spectral index of mm interferometry observations tracing emission from the disc is shallower than the spectral index from single dish observations tracing the envelope emission. This may be produced by a change in dust size which can be the result of grain growth in the disc.

Then the velocity distribution of the inner envelope of AFGL 2591 was studied through the methyl cyanide line emission. The emission comes from material at temperatures up to 300 K, thus tracing a region of few thousand au. The radial velocity maps showed that the gas is rotating in the same direction as it does at smaller scales, but with a slower linear velocity gradient. There was no evidence of methyl cyanide motion in the outflow other than the lines having larger widths due to turbulent motions. Therefore, methyl cyanide on these scales is useful for tracing how material gets on to the disc.

To study the velocity distribution of the inner envelope, 3-D line radiative transfer modelling was used to fit the methyl cyanide observations. The models followed the Ulrich prescription for the velocities of a slowly rotating envelope under gravitational collapse. This model was not able to reproduce the observed first moment velocity gradient perpendicular to the rotation axis with the same parameters from the continuum modelling or with a lower stellar mass and a larger centrifugal radius than the continuum model.

The results presented here have shown the limitations of the Ulrich envelope

model. Some of the findings are contradictory between the line and continuum modelling. For instance, their centrifugal radius are different because the continuum models require a steeper density distribution down to smaller radii whilst the line models require more rotation at larger radii. In addition, the small scale orientation of the outflow/jet, and consequently the rotation axis, is different to the orientation of the large scale outflow cavities and the Herbig-Haro objects observed towards the blue shifted cavity. This is probably the result of precession of the outflow, which may be caused by the presence of a yet unknown companion. Changes in jet direction have already been observed in multi-epoch radio observations of other MYSOs (e.g. Rodríguez *et al.* 2008). VLA 1 and VLA 3S are unlikely to be causing the precession due to their large projected distances. These features limit the capacity to fit all the observations simultaneously with a single model. However, simulations including more physical processes (e.g. magnetic fields) may be able to explain these features.

5.2 Future prospects

5.2.1 AFGL 2591 modelling

In the previous chapters, several solutions or improvements have been proposed for the RT modelling of AFGL 2591 in order to fit the observations better. Here they are discussed.

A better density distribution. The Ulrich model is limited in the description of the continuum and the line observations. Other density distributions (e.g. power law distribution) do not show better results either. In addition, the

density distribution presented here is not self-consistent in the sense that there are discontinuities in the density distribution, e.g. going from the envelope to the disc. Thus self-consistent models that include more physical processes are needed. For instance, a proper treatment of infalling motions can solve the discontinuities in the density and velocity distributions where the material is accreted from the envelope into the disc. This will be important when new observations of methyl cyanide at smaller scales become available (see below). As important as infall are outflows due to their effect on the cavity wall structure and probably the dust/molecular composition and kinematics inside the bipolar cavities and their walls. These can be constrained by the observations presented here and molecular line observations tracing outflows (e.g. SiO, $C^{18}O$). Magnetic fields can also help to explain the current observations by solving the centrifugal radius discrepancy (see next section).

Dust models distribution. The distribution of dust models should consider the physical conditions, namely density and temperature, in different regimes. The physical conditions should determine the optical properties of the dust. Dust in the coldest regions of the envelope can develop ice mantles, whilst in the outflow and its cavity walls grains may be smaller due to shocks. In the disc the dust size may increase towards the midplane because of grain growth, as the decrease in dust emissivity index from the large scale envelope to the disc has shown (cf. Section 3.5.4). Furthermore, Maud & Hoare (2013) also found a shallower dust emissivity index from mm interferometry observations of the MYSO S140–IRS1, which was also interpreted as grain

growth in the disc.

The continuum and line should be fitted simultaneously. Here the continuum results have been used as an input of the line RT modelling. As part of the latter, parameters which define the envelope density, e.g. the centrifugal radius, have been changed to improve the results. The next step should be to compute new sets of continuum models including the line modelling results, and see if these can improve the fit or if other parameters need to be changed to obtain a better fit. The best model should be that obtained by several iterations between continuum and line modelling.

Best-fitting model selection. In this thesis data and models were compared under different approaches (e.g. comparing radial profiles, images). Better ways to compare models and data need to be explored to add more accurate spatial constraints to the models. The synthetic model observations should be simulated following as close as possible the observations conditions, and different ways to compare with the data should be considered, e.g. how the images are aligned or the goodness of fit statistic used (χ^2, mean absolute deviation or other). Some of the observations were normalised and then compared. This makes them statistically independent from the SED, and focus in the distribution of the material. However, they provide less information on which density structure (star, envelope, cavity or disc) needs to be modified to improve the fit because all the models are normalised to the same value at the same position. Whether to use one or the other should depend on the information available (i.e. how accurate the simulated observations can be done) and the goodness of fit method used. In

addition, the search of the best fitting-model needs to be improved. Due to the large amount of observations with different resolutions, developing a grid of models may not be the best approach in terms of time and computing resources. The approach followed here may leave some parameters under-explored, whilst the genetic algorithm followed by Johnston *et al.* (2013) may find a local minimum of the χ^2 minimisation if there are not enough observations to constrain the models or if the initial parameters are far from the 'real' ones. Finally, a good visualization of the goodness of fit statistic as a function of the model parameters and/or the observations fitted is needed in order to see more precisely were changes in the parameters can improve the fit.

Improving the line RT modelling. As part of the CORE project new observations at higher resolution will be available in the 1.3 mm band with the same spectral setup. In addition, IRAM 30 m observations with the same spectral setup are already available. Thus, these observations and the ones presented here will connect the kinematics of the extended and inner envelope with that of the disc as observed by a single molecule. Similar scale range can be achieved by ALMA in a single observation for MYSOs in the southern hemisphere. This range in scales will require a better grid in the line RT modelling, thus larger computing resources will be required.

More observations. Observations at intermediate scales in the 850 μm band of NOEMA will connect the large scale envelope mapped by SCUBA with the inner envelope. These are important because they should resolve the inner region better than the 1.3 mm observations presented here, thus showing

whether the elongation observed in the SCUBA observations is due to the outflow cavities or, e.g., a large scale non-spherical envelope. Additionally, the nature of VLA 3S can be investigated further with these observations, e.g. by constraining its dust temperature. High sensitivity and resolution observations are also needed in the 20–40 GHz regime in order to separate the disc and jet components (e.g. with the expanded VLA). This will allow to determine the turnover frequency of the jet SED and then subtract its contribution to the mm interferometry observations, thus constraining the dust emissivity index of the disc. It will also confirm the jet and disc orientations.

Ultimately, the amount of data available for this and other MYSOs is enough for testing more realistic models from simulations which include more physical processes than the Ulrich model.

5.2.2 Towards a unified model for MYSOs

The findings of this thesis show that any model that attempts to reproduce observations of MYSOs should have an envelope, a disc and bipolar outflow cavities. In the case of AFGL 2591, the line RT model contradicts the continuum model based on the Ulrich solution by requiring a steeper density distribution down to radii smaller than the centrifugal radius derived from the line RT modelling. The overall result is that the inner envelope is rotating faster than what is expected from the continuum model, which has a smaller centrifugal radius. One physical process that can make this possible is the presence of magnetic fields.

Simulations with magnetic fields and radiation transfer show promising re-

sults. The simulations of early stages in the formation of high-mass stars calculated by Commerçon *et al.* (2011) show that magnetic fields and radiation can reduce the fragmentation during early stages in the formation of massive stars. Furthermore, the magneto hydrodynamic simulations of Myers *et al.* (2013), which explore a larger time evolution of a collapsing core with an initial power law density distribution index of –1.5, show that magnetic fields can remove angular momentum from the infalling material through magnetic braking whilst still forming a massive star (20 $M_{\odot}$). Their models can still form an accretion disc but their radii are <50 au, thus smaller than the one of AFGL 2591. These models also show that the matter is accreted into the disc from filaments which have collapsed within the envelope at scales of 5000 au in the mid-plane. However, these models do not include feedback from an outflow.

The non-magnetic simulations by Klassen *et al.* (2016) succeed in producing a Keplerian disc but they focus on 1000 au scales, thus in the transition from the envelope to disc. They also have a higher rotational to kinetic energy ratio than Myers *et al.* (2013) by a factor of $\sim 5 - 30$, and impose an initial solid body rotation. The 2-D simulations of Kuiper *et al.* (2015, 2016) show the effect of radiation on the outflow cavity and its widening from an initially slowly rotating core. The cavity distributions in these models resemble the near-IR observations of AFGL 2591. However, they do not include magnetic fields and they also start from solid body rotation.

Further simulations that combine a good description of outflows and include magnetic fields may be able to explain the observations of MYSOs. These numerical simulations need to be compared with data in order to improve simulations and finally determine which physical processes dominate the formation of massive

stars.

Appendix A

LTE modelling results

Figs. A.1–A.4 show the results for the LTE modelling with CASSIS for the models with two components M2Cb and M2Cc (cf. Table 4.3).

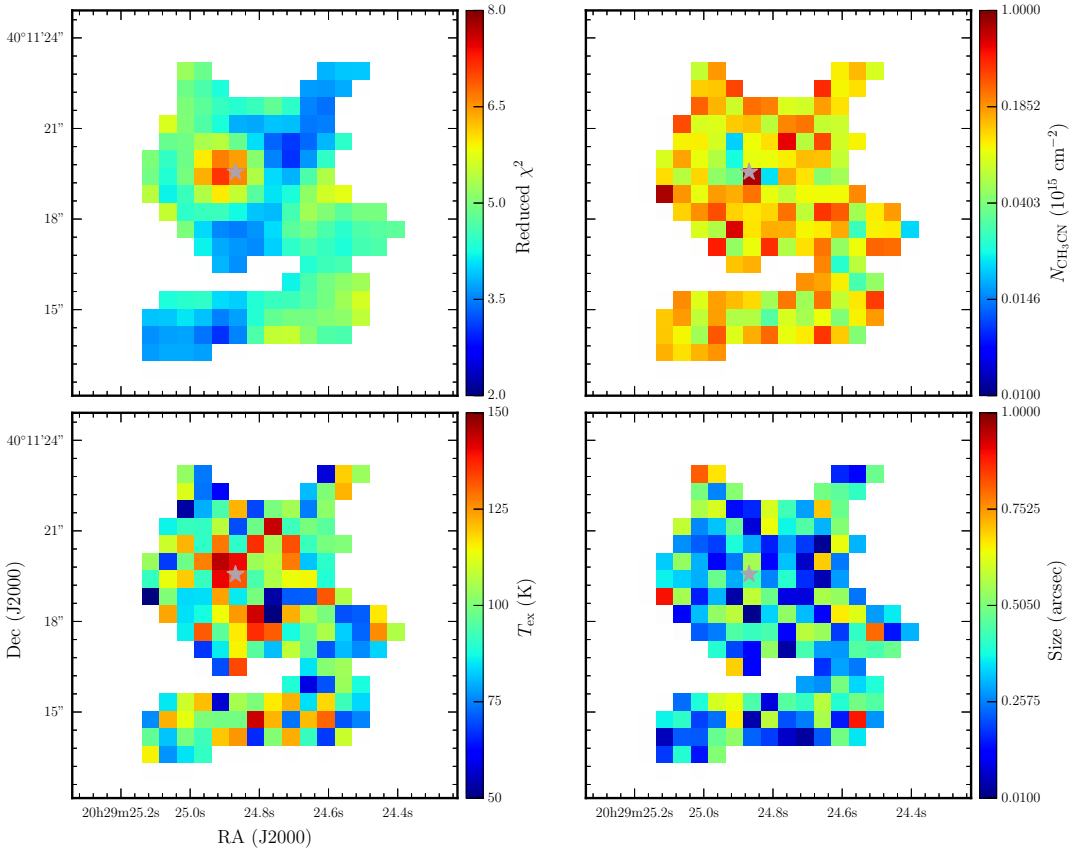

Figure A.1: First component results for the LTE model M2C1b. χ^2 value is the same for M2C1b and M2C2b. FWHM and $v_{\rm LSR}$ values are fixed to those in Fig. A.1.

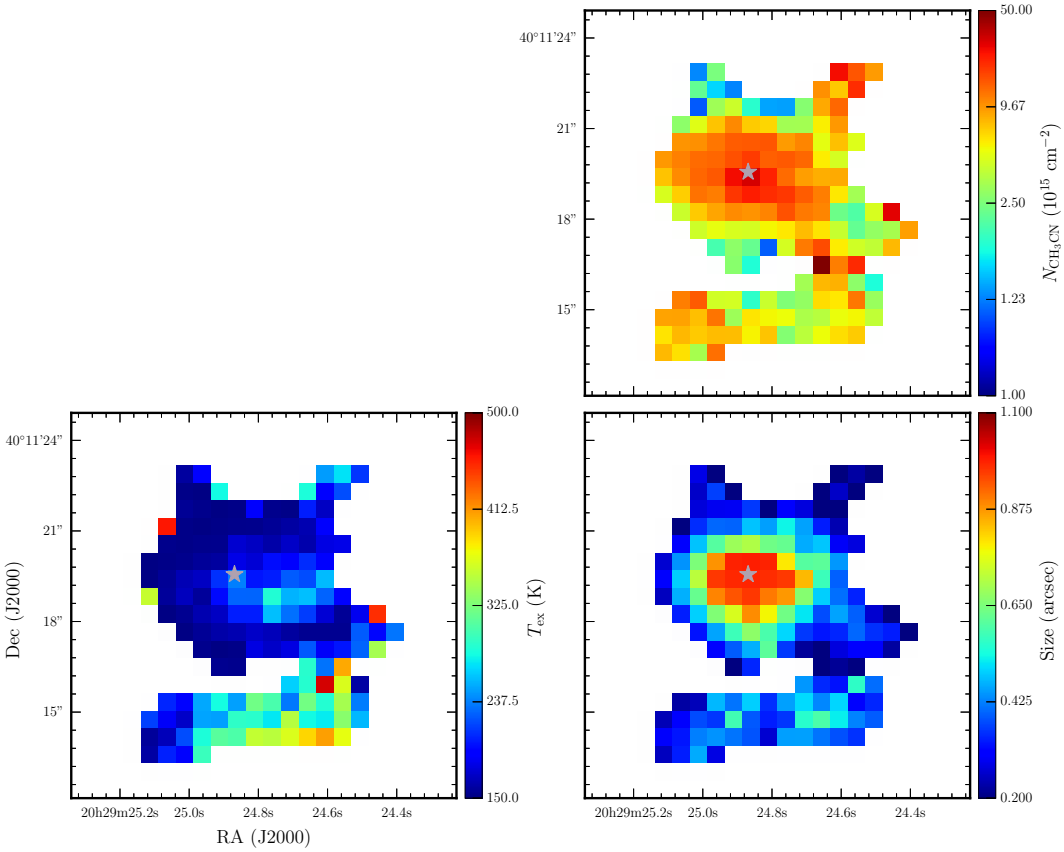

Figure A.2: Second component results for the LTE model M2C2b.

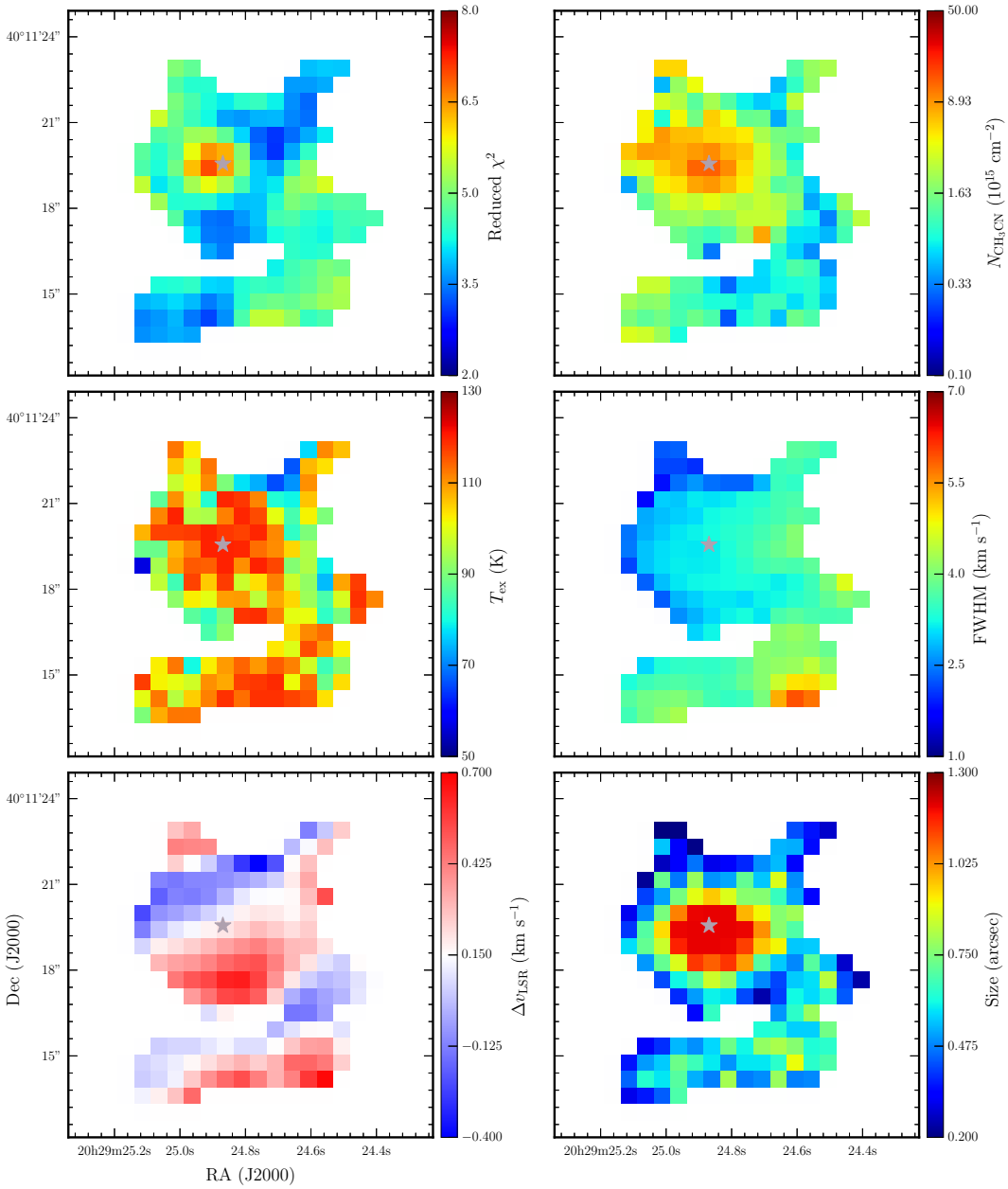

Figure A.3: First component results for the LTE model M2C1c.

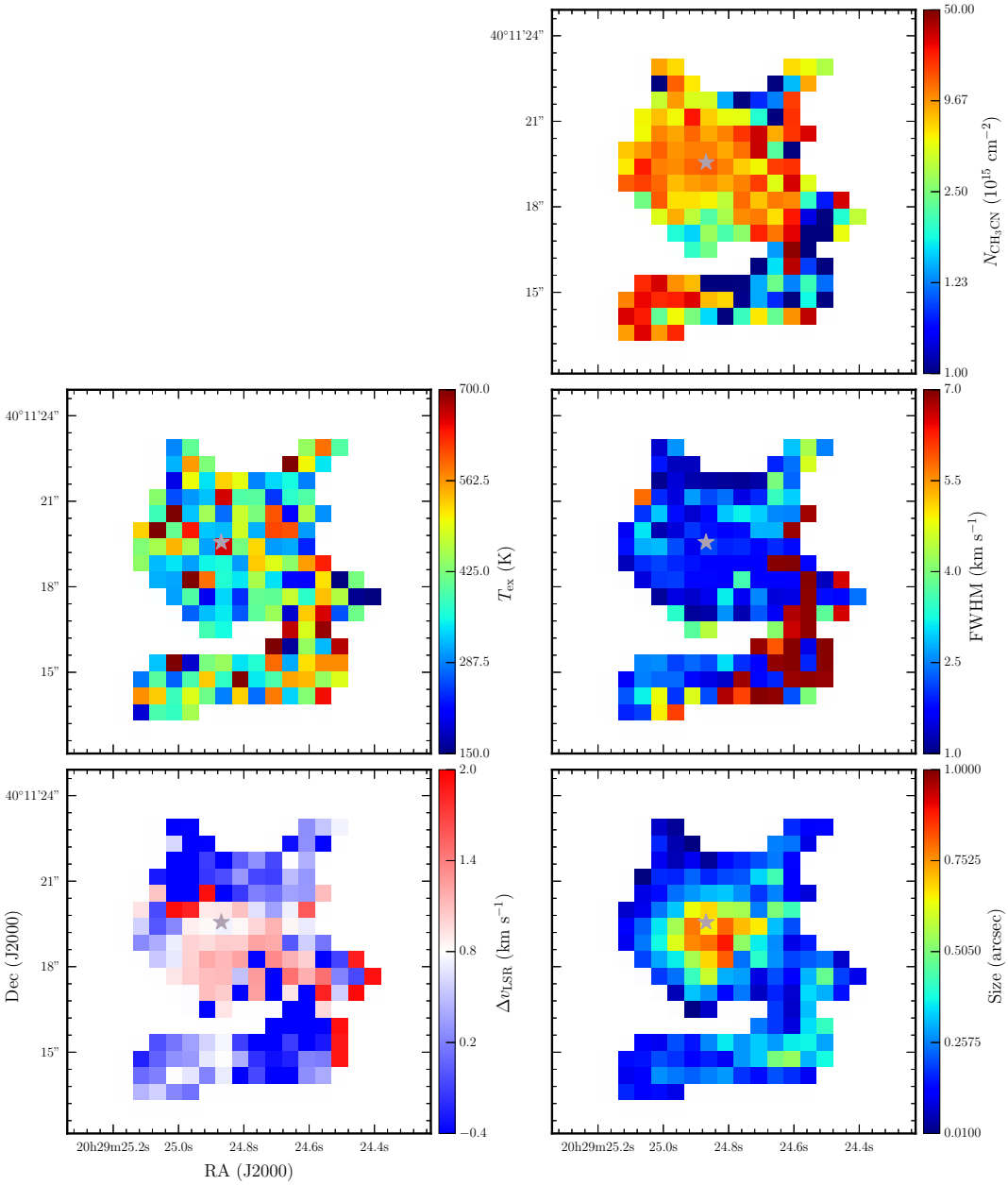

Figure A.4: Second component results for the LTE model M2C2c.

References

Alvarez, C., Hoare, M. & Lucas, P. (2004). Constraints in the circumstellar density distribution of massive Young Stellar Objects. *A&A*, **419**, 203–213. 79, 81

Alves, J., Lombardi, M. & Lada, C.J. (2007). The mass function of dense molecular cores and the origin of the IMF. *A&A*, **462**, L17–L21. 3

André, P. (1994). Observations of protostars and protostellar stages. In T. Montmerle, C.J. Lada, I.F. Mirabel & J. Tran Thanh Van, eds., *The Cold Universe*, 179. 9

Andre, P., Ward-Thompson, D. & Barsony, M. (1993). Submillimeter continuum observations of Rho Ophiuchi A - The candidate protostar VLA 1623 and prestellar clumps. *ApJ*, **406**, 122–141. 8

Arce, H.G., Shepherd, D., Gueth, F., Lee, C.F., Bachiller, R., Rosen, A. & Beuther, H. (2007). Molecular Outflows in Low- and High-Mass Star-forming Regions. *Protostars and Planets V*, 245–260. 4

Banerjee, R. & Pudritz, R.E. (2007). Massive Star Formation via High Accretion Rates and Early Disk-driven Outflows. *ApJ*, **660**, 479–488. 13

Bell, T.A., Cernicharo, J., Viti, S., Marcelino, N., Palau, A., Esplugues, G.B. & Tercero, B. (2014). Extended warm gas in Orion KL as probed by methyl cyanide. *A&A*, **564**, A114. 121

Beltrán, M.T., Brand, J., Cesaroni, R., Fontani, F., Pezzuto, S., Testi, L. & Molinari, S. (2006a). Search for massive protostar candidates in the southern hemisphere. II. Dust continuum emission. *A&A*, **447**, 221–233. 44

Beltrán, M.T., Cesaroni, R., Codella, C., Testi, L., Furuya, R.S. & Olmi, L. (2006b). Infall of gas as the formation mechanism of stars up to 20 times more massive than the Sun. *Nature*, **443**, 427–429. 4, 11

Benz, A.O., Stäuber, P., Bourke, T.L., van der Tak, F.F.S., van Dishoeck, E.F. & Jørgensen, J.K. (2007). Energetic radiation and the sulfur chemistry of protostellar envelopes: submillimeter interferometry of AFGL 2591. *A&A*, **475**, 549–558. 120, 153

Beuther, H., Schilke, P., Menten, K.M., Motte, F., Sridharan, T.K. & Wyrowski, F. (2002a). High-Mass Protostellar Candidates. II. Density Structure from Dust Continuum and CS Emission. *ApJ*, **566**, 945–965. 44, 48

Beuther, H., Schilke, P., Sridharan, T.K., Menten, K.M., Walmsley, C.M. & Wyrowski, F. (2002b). Massive molecular outflows. *A&A*, **383**, 892–904. 4, 111

Beuther, H., Zhang, Q., Sridharan, T.K. & Chen, Y. (2005). Testing the Massive Disk Scenario for IRAS 18089-1732. *ApJ*, **628**, 800–810. 121

Bjorkman, J.E. & Wood, K. (2001). Radiative Equilibrium and Temperature Correction in Monte Carlo Radiation Transfer. *ApJ*, **554**, 615–623. 18

Blandford, R.D. & Payne, D.G. (1982). Hydromagnetic flows from accretion discs and the production of radio jets. *MNRAS*, **199**, 883–903. 13

Boley, P.A., Linz, H., van Boekel, R., Henning, T., Feldt, M., Kaper, L., Leinert, C., Müller, A., Pascucci, I., Robberto, M., Stecklum, B., Waters, L.B.F.M. & Zinnecker, H. (2013). The VLTI/MIDI survey of massive young stellar objects . Sounding the inner regions around intermediate- and high-mass young stars using mid-infrared interferometry. *A&A*, **558**, A24. 14, 29

Bondi, H. & Hoyle, F. (1944). On the mechanism of accretion by stars. *MNRAS*, **104**, 273. 12

Bonnell, I.A., Bate, M.R., Clarke, C.J. & Pringle, J.E. (2001). Competitive accretion in embedded stellar clusters. *MNRAS*, **323**, 785–794. 12

Bonnor, W.B. (1956). Boyle's Law and gravitational instability. *MNRAS*, **116**, 351. 7

Boonman, A.M.S., Stark, R., van der Tak, F.F.S., van Dishoeck, E.F., van der Wal, P.B., Schäfer, F., de Lange, G. & Laauwen, W.M. (2001). Highly Abundant HCN in the Inner Hot Envelope of GL 2591: Probing the Birth of a Hot Core? *ApJ*, **553**, L63–L67. 121

Brinch, C., Crapsi, A., Jørgensen, J.K., Hogerheijde, M.R. & Hill, T. (2007). A deeply embedded young protoplanetary disk around L1489 IRS observed by the Submillimeter Array. *A&A*, **475**, 915–923. 8

Bruderer, S., Benz, A.O., Doty, S.D., van Dishoeck, E.F. & Bourke, T.L. (2009). Multidimensional Chemical Modeling of Young Stellar Objects. II. Irradiated Outflow Walls in a High-Mass Star-Forming Region. *ApJ*, **700**, 872–886. 121

Bruderer, S., Benz, A.O., Stäuber, P. & Doty, S.D. (2010). Multidimensional Chemical Modeling of Young Stellar Objects. III. The Influence of Geometry on the Abundance and Excitation of Diatomic Hydrides. *ApJ*, **720**, 1432–1453. 121

Cabrit, S., Raga, A. & Gueth, F. (1997). Models of Bipolar Molecular Outflows. In B. Reipurth & C. Bertout, eds., *Herbig-Haro Flows and the Birth of Stars*, vol. 182 of *IAU Symposium*, 163–180. 13

Campbell, B. (1984). New radio sources at AFGL 2591 - Young cluster or single star? *ApJ*, **287**, 334–337. 116

Campbell, M.F., Butner, H.M., Harvey, P.M., Evans, N.J., II, Campbell, M.B. & Sabbey, C.N. (1995). High-Resolution Far-Infrared Observations and Radiative-Transfer Models of W3 IRS 4 and IRS 5. *ApJ*, **454**, 831. 28

Cantó, J., Raga, A.C. & Williams, D.A. (2008). The interaction of a YSO outflow with the surrounding molecular cloud core. *Rev. Mex. Astron. Astrofis.*, **44**, 293–300. 79

Cesaroni, R., Neri, R., Olmi, L., Testi, L., Walmsley, C.M. & Hofner, P. (2005). A study of the Keplerian accretion disk and precessing outflow in the massive protostar IRAS 20126+4104. *A&A*, **434**, 1039–1054. 4, 15

Cesaroni, R., Massi, F., Arcidiacono, C., Beltrán, M.T., McCarthy, D., Kulesa, C., Boutsia, K., Paris, D., Quirós-Pacheco, F. & Xompero, M. (2013). A close-up view of a bipolar jet: Sub-arcsecond near-infrared imaging of the high-mass protostar IRAS 20126+4104. *A&A*, **549**, A146. 14, 16

Cesaroni, R., Galli, D., Neri, R. & Walmsley, C.M. (2014). Imaging the disk around IRAS 20126+4104 at subarcsecond resolution. *A&A*, **566**, A73. 15, 16

Chini, R., Kruegel, E. & Kreysa, E. (1986). Dust emission spectra from star-forming regions. *A&A*, **167**, 315–324. 49

Churchwell, E. (2002). Ultra-Compact HII Regions and Massive Star Formation. *ARA&A*, **40**, 27–62. 3, 5

Churchwell, E., Babler, B.L., Meade, M.R., Whitney, B.A., Benjamin, R., Indebetouw, R., Cyganowski, C., Robitaille, T.P., Povich, M., Watson, C. & Bracker, S. (2009). The Spitzer/GLIMPSE Surveys: A New View of the Milky Way. *PASP*, **121**, 213–230. 44

Commerçon, B., Hennebelle, P. & Henning, T. (2011). Collapse of Massive Magnetized Dense Cores Using Radiation Magnetohydrodynamics: Early Fragmentation Inhibition. *ApJ*, **742**, L9. 165

Contreras, Y., Schuller, F., Urquhart, J.S., Csengeri, T., Wyrowski, F., Beuther, H., Bontemps, S., Bronfman, L., Henning, T., Menten, K.M., Schilke, P., Walmsley, C.M., Wienen, M., Tackenberg, J. & Linz, H. (2013). ATLASGAL - compact source catalogue: 330° $< \ell <$ 21°. *A&A*, **549**, A45. 26, 41, 44

Cooper, H.D.B., Lumsden, S.L., Oudmaijer, R.D., Hoare, M.G., Clarke, A.J., Urquhart, J.S., Mottram, J.C., Moore, T.J.T. & Davies, B. (2013). The RMS survey: near-IR spectroscopy of massive young stellar objects. *MNRAS*, **430**, 1125–1157. 26, 29

Crutcher, R.M. (1999). Magnetic Fields in Molecular Clouds: Observations Confront Theory. *ApJ*, **520**, 706–713. 6

Crutcher, R.M. (2005). Magnetic fields and massive star formation. In R. Cesaroni, M. Felli, E. Churchwell & M. Walmsley, eds., *Massive Star Birth: A Crossroads of Astrophysics*, vol. 227 of *IAU Symposium*, 98–107. 10

Crutcher, R.M. & Troland, T.H. (2000). OH Zeeman Measurement of the Magnetic Field in the L1544 Core. *ApJ*, **537**, L139–L142. 6

Crutcher, R.M., Hakobian, N. & Troland, T.H. (2009). Testing Magnetic Star Formation Theory. *ApJ*, **692**, 844–855. 6

Cummins, S.E., Green, S., Thaddeus, P. & Linke, R.A. (1983). The kinetic temperature and density of the Sagittarius B2 molecular cloud from observations of methyl cyanide. *ApJ*, **266**, 331–338. 121

Cunningham, A.J., Klein, R.I., Krumholz, M.R. & McKee, C.F. (2011). Radiation-hydrodynamic Simulations of Massive Star Formation with Protostellar Outflows. *ApJ*, **740**, 107. 12, 117

Davies, B., Hoare, M.G., Lumsden, S.L., Hosokawa, T., Oudmaijer, R.D., Urquhart, J.S., Mottram, J.C. & Stead, J. (2011). The Red MSX Source survey: critical tests of accretion models for the formation of massive stars. *MNRAS*, **416**, 972–990. 5, 12, 80

de Wit, W.J., Hoare, M.G., Oudmaijer, R.D. & Mottram, J.C. (2007). VLTI/MIDI 10 μm Interferometry of the Forming Massive Star W33A. *ApJ*, **671**, L169–L172. 29

de Wit, W.J., Hoare, M.G., Fujiyoshi, T., Oudmaijer, R.D., Honda, M., Kataza, H., Miyata, T., Okamoto, Y.K., Onaka, T., Sako, S. & Yamashita, T. (2009). Resolved 24.5 micron emission from massive young stellar objects. *A&A*, **494**, 157–178. 14, 16, 24, 30, 34, 43, 44, 48, 49

de Wit, W.J., Hoare, M.G., Oudmaijer, R.D. & Lumsden, S.L. (2010). The origin of mid-infrared emission in massive young stellar objects: multi-baseline VLTI observations of W33A. *A&A*, **515**, A45. 24, 29, 45, 74, 79, 84, 111, 113

de Wit, W.J., Hoare, M.G., Oudmaijer, R.D., Nürnberger, D.E.A., Wheelwright, H.E. & Lumsden, S.L. (2011). Mid-infrared interferometry towards the massive young stellar object CRL 2136: inside the dust rim. *A&A*, **526**, L5. 29

Di Francesco, J., Johnstone, D., Kirk, H., MacKenzie, T. & Ledwosinska, E. (2008). The SCUBA Legacy Catalogues: Submillimeter-Continuum Objects Detected by SCUBA. *ApJS*, **175**, 277–295. 26, 41, 44, 72

Draine, B.T. (2003). Interstellar Dust Grains. *ARA&A*, **41**, 241–289. 21

Draine, B.T. & Lee, H.M. (1984). Optical properties of interstellar graphite and silicate grains. *ApJ*, **285**, 89–108. 43

Dullemond, C.P., Hollenbach, D., Kamp, I. & D'Alessio, P. (2007). Models of the Structure and Evolution of Protoplanetary Disks. *Protostars and Planets V*, 555–572. 8

Ebert, R. (1955). Über die Verdichtung von H I-Gebieten. Mit 5 Textabbildungen. *Z. Astrophys.*, **37**, 217. 7

Eisner, J.A., Hillenbrand, L.A., Carpenter, J.M. & Wolf, S. (2005). Constraining the Evolutionary Stage of Class I Protostars: Multiwavelength Observations and Modeling. *ApJ*, **635**, 396–421. 8

Gies, D.R. (2003). Masses and other parameters of massive binaries. In K. van der Hucht, A. Herrero & C. Esteban, eds., *A Massive Star Odyssey: From Main Sequence to Supernova*, vol. 212 of *IAU Symposium*, 91. 10

Hasegawa, T.I. & Mitchell, G.F. (1995). CO J = 3–2 and HCO + J = 4–3 Observations of the GL 2591 Molecular Outflow. *ApJ*, **451**, 225. 56, 57, 110, 119

Hatchell, J., Fuller, G.A., Millar, T.J., Thompson, M.A. & Macdonald, G.H. (2000). SCUBA imaging of high mass star formation regions. *A&A*, **357**, 637–650. 69

Henning, T., Schreyer, K., Launhardt, R. & Burkert, A. (2000). Massive young stellar objects with molecular outflows. *A&A*, **353**, 211–226. 4

Hill, T., Motte, F., Didelon, P., Bontemps, S., Minier, V., Hennemann, M., Schneider, N., André, P., Men'shchikov, A., Anderson, L.D., Arzoumanian, D., Bernard, J.P., di Francesco, J., Elia, D., Giannini, T., Griffin, M.J., Könyves, V., Kirk, J., Marston, A.P., Martin, P.G., Molinari, S., Nguyen Luong, Q., Peretto, N., Pezzuto, S., Roussel, H., Sauvage, M., Sousbie, T., Testi, L., Ward-Thompson, D., White, G.J., Wilson, C.D. & Zavagno, A. (2011). Filaments and ridges in Vela C revealed by Herschel: from low-mass to high-mass star-forming sites. *A&A*, **533**, A94. 2

Hoare, M.G. & Franco, J. (2007). Massive Star Formation. *Astrophysics and Space Science Proceedings*, **1**, 61. 5, 12

Hoare, M.G., Roche, P.F. & Glencross, W.M. (1991). Submillimetre emission and the dust content of compact H II regions. *MNRAS*, **251**, 584–599. 49

Hofner, P., Cesaroni, R., Olmi, L., Rodríguez, L.F., Martí, J. & Araya, E. (2007). Sub-arcsecond resolution radio continuum observations of IRAS 20126+4104. *A&A*, **465**, 197–205. 15, 16

Hosokawa, T., Yorke, H.W. & Omukai, K. (2010). Evolution of Massive Protostars Via Disk Accretion. *ApJ*, **721**, 478–492. 12

Hunter, T.R., Brogan, C.L., Cyganowski, C.J. & Young, K.H. (2014). Subarcsecond Imaging of the NGC 6334 I(N) Protocluster: Two Dozen Compact Sources and a Massive Disk Candidate. *ApJ*, **788**, 187. 146

Ivezic, Z. & Elitzur, M. (1997). Self-similarity and scaling behaviour of infrared emission from radiatively heated dust - I. Theory. *MNRAS*, **287**, 799–811. 21, 40, 43, 52

Johnston, K.G., Shepherd, D.S., Robitaille, T.P. & Wood, K. (2013). The standard model of low-mass star formation applied to massive stars: a multi-wavelength picture of AFGL 2591. *A&A*, **551**, A43. 56, 57, 58, 59, 60, 62, 71, 72, 79, 81, 82, 85, 86, 94, 96, 99, 109, 110, 116, 120, 126, 143, 146, 163

Johnston, K.G., Robitaille, T.P., Beuther, H., Linz, H., Boley, P., Kuiper, R., Keto, E., Hoare, M.G. & van Boekel, R. (2015). A Keplerian-like Disk around the Forming O-type Star AFGL 4176. *ApJ*, **813**, L19. 24, 121, 142, 146

Johnstone, D., Wilson, C.D., Moriarty-Schieven, G., Joncas, G., Smith, G., Gregersen, E. & Fich, M. (2000). Large-Area Mapping at 850 Microns. II. Analysis of the Clump Distribution in the ρ Ophiuchi Molecular Cloud. *ApJ*, **545**, 327–339. 7

Jørgensen, J.K., Schöier, F.L. & van Dishoeck, E.F. (2002). Physical structure and CO abundance of low-mass protostellar envelopes. *A&A*, **389**, 908–930. 44, 113

Kahn, F.D. (1974). Cocoons around early-type stars. *A&A*, **37**, 149–162. 10

Kaźmierczak-Barthel, M., van der Tak, F.F.S., Helmich, F.P., Chavarría, L., Wang, K.S. & Ceccarelli, C. (2014). The HIFI spectral survey of AFGL 2591 (CHESS). II. Summary of the survey. *A&A*, **567**, A53. 122

Kaźmierczak-Barthel, M., Semenov, D.A., van der Tak, F.F.S., Chavarría, L. & van der Wiel, M.H.D. (2015). The HIFI spectral survey of AFGL 2591 (CHESS). III. Chemical structure of the protostellar envelope. *A&A*, **574**, A71. 120, 142

Keto, E. & Rybicki, G. (2010). Modeling Molecular Hyperfine Line Emission. *ApJ*, **716**, 1315–1322. 137

Kim, S.H., Martin, P.G. & Hendry, P.D. (1994). The size distribution of interstellar dust particles as determined from extinction. *ApJ*, **422**, 164–175. 84

Klassen, M., Pudritz, R.E., Kuiper, R., Peters, T. & Banerjee, R. (2016). Simulating the Formation of Massive Protostars. I. Radiative Feedback and Accretion Disks. *ApJ*, **823**, 28. 165

Kolpak, M.A., Jackson, J.M., Bania, T.M., Clemens, D.P. & Dickey, J.M. (2003). Resolving the Kinematic Distance Ambiguity toward Galactic H II Regions. *ApJ*, **582**, 756–769. 2

Kroupa, P. (2001). On the variation of the initial mass function. *MNRAS*, **322**, 231–246. 3

Krumholz, M.R., McKee, C.F. & Klein, R.I. (2005). How Protostellar Outflows Help Massive Stars Form. *ApJ*, **618**, L33–L36. 12

Krumholz, M.R., Klein, R.I. & McKee, C.F. (2012). Radiation-hydrodynamic Simulations of the Formation of Orion-like Star Clusters. II. The Initial Mass Function from Winds, Turbulence, and Radiation. *ApJ*, **754**, 71. 11

Kuiper, R., Klahr, H., Beuther, H. & Henning, T. (2010). Circumventing the Radiation Pressure Barrier in the Formation of Massive Stars via Disk Accretion. *ApJ*, **722**, 1556–1576. 12

Kuiper, R., Yorke, H.W. & Turner, N.J. (2015). Protostellar Outflows and Radiative Feedback from Massive Stars. *ApJ*, **800**, 86. 117, 165

Kuiper, R., Turner, N.J. & Yorke, H.W. (2016). Protostellar Outflows and Radiative Feedback from Massive Stars. II. Feedback, Star-formation Efficiency, and Outflow Broadening. *ApJ*, **832**, 40. 165

Kurtz, S., Cesaroni, R., Churchwell, E., Hofner, P. & Walmsley, C.M. (2000). Hot Molecular Cores and the Earliest Phases of High-Mass Star Formation. *Protostars and Planets IV*, 299–326. 4

Lada, C.J., Thronson, H.A., Jr., Smith, H.A., Schwartz, P.R. & Glaccum, W. (1984). The nature of AFGL 2591 and its associated molecular outflow Infrared and millimeter-wave observations. *ApJ*, **286**, 302–309. 119

Lada, E.A., Depoy, D.L., Evans, N.J., II & Gatley, I. (1991). A 2.2 micron survey in the L1630 molecular cloud. *ApJ*, **371**, 171–182. 3

Laor, A. & Draine, B.T. (1993). Spectroscopic constraints on the properties of dust in active galactic nuclei. *ApJ*, **402**, 441–468. 83

Larson, R.B. (1972). The evolution of spherical protostars with masses 0.25 M_solar to 10 M_solar. *MNRAS*, **157**, 121. 7

Larson, R.B. (1981). Turbulence and star formation in molecular clouds. *MNRAS*, **194**, 809–826. 11

Larson, R.B. & Starrfield, S. (1971). On the formation of massive stars and the upper limit of stellar masses. *A&A*, **13**, 190–197. 10

Lee, C.F., Ho, P.T.P., Hirano, N., Beuther, H., Bourke, T.L., Shang, H. & Zhang, Q. (2007). HH 212: Submillimeter Array Observations of a Remarkable Protostellar Jet. *ApJ*, **659**, 499–511. 8

Loren, R.B. & Mundy, L.G. (1984). The methyl cyanide hot and warm cores in Orion - Statistical equilibrium excitation models of a symmetric-top molecule. *ApJ*, **286**, 232–251. 121

Lucas, P.W., Hoare, M.G., Longmore, A., Schröder, A.C., Davis, C.J., Adamson, A., Bandyopadhyay, R.M., de Grijs, R., Smith, M., Gosling, A., Mitchison, S., Gáspár, A., Coe, M., Tamura, M., Parker, Q., Irwin, M., Hambly, N., Bryant, J., Collins, R.S., Cross, N., Evans, D.W., Gonzalez-Solares, E., Hodgkin, S., Lewis, J., Read, M., Riello, M., Sutorius, E.T.W., Lawrence, A., Drew, J.E., Dye, S. & Thompson, M.A. (2008). The UKIDSS Galactic Plane Survey. *MNRAS*, **391**, 136–163. 26

Lucy, L.B. (1999). Computing radiative equilibria with Monte Carlo techniques. *A&A*, **344**, 282–288. 18, 20, 72

Lumsden, S.L., Hoare, M.G., Oudmaijer, R.D. & Richards, D. (2002). The population of the Galactic plane as seen by MSX. *MNRAS*, **336**, 621–636. 25

Lumsden, S.L., Hoare, M.G., Urquhart, J.S., Oudmaijer, R.D., Davies, B., Mottram, J.C., Cooper, H.D.B. & Moore, T.J.T. (2013). The Red MSX Source Survey: The Massive Young Stellar Population of Our Galaxy. *ApJS*, **208**, 11. 25, 26, 79

Lutz, D. (2012). Herschel internal document picc-me-tn-03. PACS Photometer Point Spread Function (`http://herschel.esac.esa.int/twiki/pub/Public/PacsCalibrationWeb/bolopsf_20.pdf`). 33, 60, 62

Mac Low, M.M. & Klessen, R.S. (2004). Control of star formation by supersonic turbulence. *Reviews of Modern Physics*, **76**, 125–194. 3

Mathis, J.S., Rumpl, W. & Nordsieck, K.H. (1977). The size distribution of interstellar grains. *ApJ*, **217**, 425–433. 10, 43, 84

Matzner, C.D. & McKee, C.F. (1999). Bipolar Molecular Outflows Driven by Hydromagnetic Protostellar Winds. *ApJ*, **526**, L109–L112. 111

Maud, L.T. & Hoare, M.G. (2013). Resolving the Dust Disk in the Prototype Ionized Disk Wind Source S140-IRS1. *ApJ*, **779**, L24. 59, 161

Maud, L.T., Hoare, M.G., Gibb, A.G., Shepherd, D. & Indebetouw, R. (2013). High angular resolution millimetre continuum observations and modelling of S140-IRS1. *MNRAS*, **428**, 609–624. 14, 24, 59

McDonald, M., Courteau, S., Tully, R.B. & Roediger, J. (2011). A survey of 286 Virgo cluster galaxies at optical griz and near-IR H band: surface brightness profiles and bulge-disc decompositions. *MNRAS*, **414**, 2055–2068. 64

McKee, C.F. & Ostriker, E.C. (2007). Theory of Star Formation. *ARA&A*, **45**, 565–687. 3, 6

McKee, C.F. & Tan, J.C. (2002). Massive star formation in 100,000 years from turbulent and pressurized molecular clouds. *Nature*, **416**, 59–61. 11

McKee, C.F. & Tan, J.C. (2003). The Formation of Massive Stars from Turbulent Cores. *ApJ*, **585**, 850–871. 11

McLaughlin, D.E. & Pudritz, R.E. (1996). A Model for the Internal Structure of Molecular Cloud Cores. *ApJ*, **469**, 194. 7

McMullin, J.P., Waters, B., Schiebel, D., Young, W. & Golap, K. (2007). CASA Architecture and Applications. In R.A. Shaw, F. Hill & D.J. Bell, eds., *Astronomical Data Analysis Software and Systems XVI*, vol. 376 of *Astronomical Society of the Pacific Conference Series*, 127. 78

Minchin, N.R., Hough, J.H., McCall, A., Aspin, C., Hayashi, S.S., Yamashita, T. & Burton, M.G. (1991). Near-infrared imaging polarimetry of bipolar nebulae. II - GL 2591. *MNRAS*, **251**, 508–521. 57

Moffat, A.F.J. (1969). A Theoretical Investigation of Focal Stellar Images in the Photographic Emulsion and Application to Photographic Photometry. *A&A*, **3**, 455. 64

Molinari, S., Swinyard, B., Bally, J., Barlow, M., Bernard, J.P., Martin, P., Moore, T., Noriega-Crespo, A., Plume, R., Testi, L., Zavagno, A., Abergel, A., Ali, B., Anderson, L., André, P., Baluteau, J.P., Battersby, C., Beltrán, M.T., Benedettini, M., Billot, N., Blommaert, J., Bontemps, S., Boulanger, F., Brand, J., Brunt, C., Burton, M., Calzoletti, L., Carey, S., Caselli, P., Cesaroni, R., Cernicharo, J., Chakrabarti, S., Chrysostomou, A., Cohen, M., Compiegne, M., de Bernardis, P., de Gasperis, G., di Giorgio, A.M., Elia, D., Faustini, F., Flagey, N., Fukui, Y., Fuller, G.A., Ganga, K., Garcia-Lario, P., Glenn, J., Goldsmith, P.F., Griffin, M., Hoare, M., Huang, M., Ikhenaode, D., Joblin, C., Joncas, G., Juvela, M., Kirk, J.M., Lagache, G., Li, J.Z., Lim, T.L., Lord, S.D., Marengo, M., Marshall, D.J., Masi, S., Massi, F., Matsuura, M., Minier, V., Miville-Deschênes, M.A., Montier, L.A., Morgan, L., Motte, F., Mottram, J.C., Müller, T.G., Natoli, P., Neves, J., Olmi, L., Paladini, R., Paradis, D., Parsons, H., Peretto, N., Pestalozzi, M., Pezzuto, S., Piacentini, F., Piazzo, L., Polychroni, D., Pomarès, M., Popescu, C.C., Reach, W.T., Ristorcelli, I., Robitaille, J.F., Robitaille, T., Rodón, J.A., Roy, A., Royer, P., Russeil, D., Saraceno, P., Sauvage, M., Schilke, P., Schisano, E., Schneider, N., Schuller, F., Schulz, B.,

Sibthorpe, B., Smith, H.A., Smith, M.D., Spinoglio, L., Stamatellos, D., Strafella, F., Stringfellow, G.S., Sturm, E., Taylor, R., Thompson, M.A., Traficante, A., Tuffs, R.J., Umana, G., Valenziano, L., Vavrek, R., Veneziani, M., Viti, S., Waelkens, C., Ward-Thompson, D., White, G., Wilcock, L.A., Wyrowski, F., Yorke, H.W. & Zhang, Q. (2010a). Clouds, filaments, and protostars: The Herschel Hi-GAL Milky Way. *A&A*, **518**, L100. 31

Molinari, S., Swinyard, B., Bally, J., Barlow, M., Bernard, J.P., Martin, P., Moore, T., Noriega-Crespo, A., Plume, R., Testi, L., Zavagno, A., Abergel, A., Ali, B., André, P., Baluteau, J.P., Benedettini, M., Berné, O., Billot, N.P., Blommaert, J., Bontemps, S., Boulanger, F., Brand, J., Brunt, C., Burton, M., Campeggio, L., Carey, S., Caselli, P., Cesaroni, R., Cernicharo, J., Chakrabarti, S., Chrysostomou, A., Codella, C., Cohen, M., Compiegne, M., Davis, C.J., de Bernardis, P., de Gasperis, G., Di Francesco, J., di Giorgio, A.M., Elia, D., Faustini, F., Fischera, J.F., Fukui, Y., Fuller, G.A., Ganga, K., Garcia-Lario, P., Giard, M., Giardino, G., Glenn, J.., Goldsmith, P., Griffin, M., Hoare, M., Huang, M., Jiang, B., Joblin, C., Joncas, G., Juvela, M., Kirk, J., Lagache, G., Li, J.Z., Lim, T.L., Lord, S.D., Lucas, P.W., Maiolo, B., Marengo, M., Marshall, D., Masi, S., Massi, F., Matsuura, M., Meny, C., Minier, V., Miville-Deschênes, M.A., Montier, L., Motte, F., Müller, T.G., Natoli, P., Neves, J., Olmi, L., Paladini, R., Paradis, D., Pestalozzi, M., Pezzuto, S.,

Piacentini, F., Pomarès, M., Popescu, C.C., Reach, W.T., Richer, J., Ristorcelli, I., Roy, A., Royer, P., Russeil, D., Saraceno, P., Sauvage, M., Schilke, P., Schneider-Bontemps, N., Schuller, F., Schultz, B., Shepherd, D.S., Sibthorpe, B., Smith, H.A., Smith, M.D., Spinoglio, L., Stamatellos, D., Strafella, F., Stringfellow, G., Sturm, E., Taylor, R., Thompson, M.A., Tuffs, R.J., Umana, G., Valenziano, L., Vavrek, R., Viti, S., Waelkens, C., Ward-Thompson, D., White, G., Wyrowski, F., Yorke, H.W. & Zhang, Q. (2010b). Hi-GAL: The Herschel Infrared Galactic Plane Survey. *PASP*, **122**, 314–325. 27, 30, 31

Morales, E.F.E., Mardones, D., Garay, G., Brooks, K.J. & Pineda, J.E. (2009). A Multiwavelength Study of Young Massive Star-Forming Regions. III. Mid-Infrared Emission. *ApJ*, **698**, 488–501. 19, 135

Motte, F. & André, P. (2001). The circumstellar environment of low-mass protostars: A millimeter continuum mapping survey. *A&A*, **365**, 440–464. 7

Motte, F., Bontemps, S., Schilke, P., Schneider, N., Menten, K.M. & Broguière, D. (2007). The earliest phases of high-mass star formation: a 3 square degree millimeter continuum mapping of Cygnus X. *A&A*, **476**, 1243–1260. 72

Motte, F., Zavagno, A., Bontemps, S., Schneider, N., Hennemann, M., di Francesco, J., André, P., Saraceno, P., Griffin, M., Marston, A., Ward-Thompson, D., White, G., Minier, V., Men'shchikov, A., Hill, T., Abergel, A., Anderson, L.D., Aussel,

H., Balog, Z., Baluteau, J.P., Bernard, J.P., Cox, P., Csengeri, T., Deharveng, L., Didelon, P., di Giorgio, A.M., Hargrave, P., Huang, M., Kirk, J., Leeks, S., Li, J.Z., Martin, P., Molinari, S., Nguyen-Luong, Q., Olofsson, G., Persi, P., Peretto, N., Pezzuto, S., Roussel, H., Russeil, D., Sadavoy, S., Sauvage, M., Sibthorpe, B., Spinoglio, L., Testi, L., Teyssier, D., Vavrek, R., Wilson, C.D. & Woodcraft, A. (2010). Initial highlights of the HOBYS key program, the Herschel imaging survey of OB young stellar objects. *A&A*, **518**, L77. 27, 55

Mottram, J.C., Hoare, M.G., Lumsden, S.L., Oudmaijer, R.D., Urquhart, J.S., Sheret, T.L., Clarke, A.J. & Allsopp, J. (2007). The RMS survey: mid-infrared observations of candidate massive YSOs in the southern hemisphere. *A&A*, **476**, 1019–1111. 25

Mottram, J.C., Hoare, M.G., Davies, B., Lumsden, S.L., Oudmaijer, R.D., Urquhart, J.S., Moore, T.J.T., Cooper, H.D.B. & Stead, J.J. (2011a). The RMS Survey: The Luminosity Functions and Timescales of Massive Young Stellar Objects and Compact H II Regions. *ApJ*, **730**, L33. 5, 10, 26

Mottram, J.C., Hoare, M.G., Urquhart, J.S., Lumsden, S.L., Oudmaijer, R.D., Robitaille, T.P., Moore, T.J.T., Davies, B. & Stead, J. (2011b). The Red MSX Source survey: the bolometric fluxes and luminosity distributions of young massive stars. *A&A*, **525**, A149. 24, 26, 40

Mouschovias, T.C. & Spitzer, L., Jr. (1976). Note on the collapse of magnetic interstellar clouds. *ApJ*, **210**, 326. 6

Mueller, K.E., Shirley, Y.L., Evans, N.J., II & Jacobson, H.R. (2002). The Physical Conditions for Massive Star Formation: Dust Continuum Maps and Modeling. *ApJS*, **143**, 469–497. 23, 48, 49

Myers, A.T., McKee, C.F., Cunningham, A.J., Klein, R.I. & Krumholz, M.R. (2013). The Fragmentation of Magnetized, Massive Star-forming Cores with Radiative Feedback. *ApJ*, **766**, 97. 165

Offner, S.S.R., Clark, P.C., Hennebelle, P., Bastian, N., Bate, M.R., Hopkins, P.F., Moraux, E. & Whitworth, A.P. (2014). The Origin and Universality of the Stellar Initial Mass Function. *Protostars and Planets VI*, 53–75. 3

Ossenkopf, V., Henning, T. & Mathis, J.S. (1992). Constraints on cosmic silicates. *A&A*, **261**, 567–578. 84

Paradis, D., Veneziani, M., Noriega-Crespo, A., Paladini, R., Piacentini, F., Bernard, J.P., de Bernardis, P., Calzoletti, L., Faustini, F., Martin, P., Masi, S., Montier, L., Natoli, P., Ristorcelli, I., Thompson, M.A., Traficante, A. & Molinari, S. (2010). Variations of the spectral index of dust emissivity from Hi-GAL observations of the Galactic plane. *A&A*, **520**, L8. 49

Parkin, E.R., Pittard, J.M., Hoare, M.G., Wright, N.J. & Drake, J.J. (2009). The interactions of winds from massive young stellar objects: X-ray emission, dynamics and cavity evolution. *MNRAS*, **400**, 629–645. 57

Pelletier, G. & Pudritz, R.E. (1992). Hydromagnetic disk winds in young stellar objects and active galactic nuclei. *ApJ*, **394**, 117–138. 8

Plunkett, A.L., Arce, H.G., Corder, S.A., Dunham, M.M., Garay, G. & Mardones, D. (2015). Assessing Molecular Outflows and Turbulence in the Protostellar Cluster Serpens South. *ApJ*, **803**, 22. 8

Poetzel, R., Mundt, R. & Ray, T.P. (1992). Herbig-Haro outflows associated with high-luminosity young stellar objects - AFGL 2591 and MWC 1080. *A&A*, **262**, 229–247. 57, 58, 119, 120

Preibisch, T., Balega, Y.Y., Schertl, D. & Weigelt, G. (2003). Bispectrum speckle interferometry of the massive protostellar outflow source AFGL 2591. *A&A*, **412**, 735–743. 57, 58, 59, 65, 77, 79, 110, 111, 112

Price, S.D., Egan, M.P., Carey, S.J., Mizuno, D.R. & Kuchar, T.A. (2001). Midcourse Space Experiment Survey of the Galactic Plane. *AJ*, **121**, 2819–2842. 44

Pudritz, R.E. & Norman, C.A. (1983). Centrifugally driven winds from contracting molecular disks. *ApJ*, **274**, 677–697. 13

Pudritz, R.E., Rogers, C.S. & Ouyed, R. (2006). Controlling the collimation and rotation of hydromagnetic disc winds. *MNRAS*, **365**, 1131–1148. 13

Pudritz, R.E., Ouyed, R., Fendt, C. & Brandenburg, A. (2007). Disk Winds, Jets, and Outflows: Theoretical and Computational Foundations. *Protostars and Planets V*, 277–294. 13

Rathborne, J.M., Jackson, J.M. & Simon, R. (2006). Infrared Dark Clouds: Precursors to Star Clusters. *ApJ*, **641**, 389–405. 4

Reipurth, B., Yu, K.C., Rodríguez, L.F., Heathcote, S. & Bally, J. (1999). Multiplicity of the HH 111 jet source: it Hubble Space Telescope NICMOS images and VLA maps. *A&A*, **352**, L83–L86. 8

Richer, J.S., Shepherd, D.S., Cabrit, S., Bachiller, R. & Churchwell, E. (2000). Molecular Outflows from Young Stellar Objects. *Protostars and Planets IV*, 867. 4

Robitaille, T.P. (2011). HYPERION: an open-source parallelized three-dimensional dust continuum radiative transfer code. *A&A*, **536**, A79. 19, 72

Robitaille, T.P., Whitney, B.A., Indebetouw, R., Wood, K. & Denzmore, P. (2006). Interpreting Spectral Energy Distributions from Young Stellar Objects. I. A Grid of 200,000 YSO Model SEDs. *ApJS*, **167**, 256–285. 24

Robitaille, T.P., Whitney, B.A., Indebetouw, R. & Wood, K. (2007). Interpreting Spectral Energy Distributions from Young Stellar Objects. II. Fitting Observed SEDs Using a Large Grid of Precomputed Models. *ApJS*, **169**, 328–352. 26

Rodgers, S.D. & Charnley, S.B. (2001). Chemical Differentiation in Regions of Massive Star Formation. *ApJ*, **546**, 324–329. 154

Rodríguez, L.F., Moran, J.M., Franco-Hernández, R., Garay, G., Brooks, K.J. & Mardones, D. (2008). The Collimated Jet Source in IRAS 16547-4247: Time Variation, Possible Precession, and Upper Limits to the Proper Motions Along the Jet Axis. *AJ*, **135**, 2370–2379. 160

Roy, A., Ade, P.A.R., Bock, J.J., Chapin, E.L., Devlin, M.J., Dicker, S.R., France, K., Gibb, A.G., Griffin, M., Gundersen, J.O., Halpern, M., Hargrave, P.C., Hughes, D.H., Klein, J., Marsden, G., Martin, P.G., Mauskopf, P., Morales Ortiz, J.L., Netterfield, C.B., Noriega-Crespo, A., Olmi, L., Patanchon, G., Rex, M., Scott, D., Semisch, C., Truch, M.D.P., Tucker, C., Tucker, G.S., Viero, M.P. & Wiebe, D.V. (2011). The Balloon-borne Large Aperture Submillimeter Telescope (BLAST) 2005: A 10 deg^2 Survey of Star Formation in Cygnus X. *ApJ*, **727**, 114. 72

Roy, A., André, P., Palmeirim, P., Attard, M., Könyves, V., Schneider, N., Peretto, N., Men'shchikov, A., Ward-Thompson, D., Kirk, J., Griffin, M., Marsh, K., Abergel, A., Arzoumanian, D., Benedettini, M., Hill, T., Motte, F., Nguyen Luong, Q., Pezzuto, S., Rivera-Ingraham, A., Roussel, H., Rygl, K.L.J., Spinoglio, L., Stamatellos, D. & White, G. (2014). Reconstructing the density and temperature structure of prestellar cores from Herschel data: A case study for B68 and L1689B. *A&A*, **562**, A138. 71

Rybicki, G.B. & Lightman, A.P. (1986). *Radiative Processes in Astrophysics*. 17, 18

Rygl, K.L.J., Brunthaler, A., Sanna, A., Menten, K.M., Reid, M.J., van Langevelde, H.J., Honma, M., Torstensson, K.J.E. & Fujisawa, K. (2012). Parallaxes and proper motions of interstellar masers toward the Cygnus X star-forming complex. I. Membership of the Cygnus X region. *A&A*, **539**, A79. 56

Sadavoy, S.I., Di Francesco, J., Johnstone, D., Currie, M.J., Drabek, E., Hatchell, J., Nutter, D., André, P., Arzoumanian, D., Benedettini, M., Bernard, J.P., Duarte-Cabral, A., Fallscheer, C., Friesen, R., Greaves, J., Hennemann, M., Hill, T., Jenness, T., Könyves, V., Matthews, B., Mottram, J.C., Pezzuto, S., Roy, A., Rygl, K., Schneider-Bontemps, N., Spinoglio, L., Testi, L., Tothill, N., Ward-Thompson, D., White, G., JCMT, t. & Herschel Gould Belt Survey Teams (2013). The Herschel and JCMT Gould Belt Surveys: Constraining Dust Properties in the Perseus B1 Clump with PACS, SPIRE, and SCUBA-2. *ApJ*, **767**, 126. 19, 71

Salpeter, E.E. (1955). The Luminosity Function and Stellar Evolution. *ApJ*, **121**, 161. 3

San José-García, I., Mottram, J.C., van Dishoeck, E.F., Kristensen, L.E., van der Tak, F.F.S., Braine, J., Herpin, F., Johnstone, D., van Kempen, T.A. & Wyrowski, F. (2016). Linking low- to high-mass young stellar objects with Herschel-HIFI observations of water. *A&A*, **585**, A103. 24

Sanna, A., Reid, M.J., Carrasco-González, C., Menten, K.M., Brunthaler, A., Moscadelli, L. & Rygl, K.L.J. (2012). Clustered Star Formation and Outflows in AFGL 2591. *ApJ*, **745**, 191. 57, 111

Schneider, N., Bontemps, S., Motte, F., Blazere, A., André, P., Anderson, L.D., Arzoumanian, D., Comerón, F., Didelon, P., Di Francesco, J., Duarte-Cabral, A., Guarcello, M.G., Hennemann,

M., Hill, T., Könyves, V., Marston, A., Minier, V., Rygl, K.L.J., Röllig, M., Roy, A., Spinoglio, L., Tremblin, P., White, G.J. & Wright, N.J. (2016). Globules and pillars in Cygnus X. I. Herschel far-infrared imaging of the Cygnus OB2 environment. *A&A*, **591**, A40. 56, 60

Schöier, F.L., van der Tak, F.F.S., van Dishoeck, E.F. & Black, J.H. (2005). An atomic and molecular database for analysis of submillimetre line observations. *A&A*, **432**, 369–379. 23, 128

Shakura, N.I. & Sunyaev, R.A. (1976). A theory of the instability of disk accretion on to black holes and the variability of binary X-ray sources, galactic nuclei and quasars. *MNRAS*, **175**, 613–632. 141

Shu, F., Najita, J., Ostriker, E., Wilkin, F., Ruden, S. & Lizano, S. (1994). Magnetocentrifugally driven flows from young stars and disks. 1: A generalized model. *ApJ*, **429**, 781–796. 8, 13

Shu, F.H. (1977). Self-similar collapse of isothermal spheres and star formation. *ApJ*, **214**, 488–497. 7

Shu, F.H., Ruden, S.P., Lada, C.J. & Lizano, S. (1991). Star formation and the nature of bipolar outflows. *ApJ*, **370**, L31–L34. 14

Simpson, J.P., Whitney, B.A., Hines, D.C., Schneider, G., Burton, M.G., Colgan, S.W.J., Cotera, A.S., Erickson, E.F. & Wolff, M.J. (2013). Aligned grains and inferred toroidal magnetic fields in the envelopes of massive young stellar objects. *MNRAS*, **435**, 3419–3436. 57, 65, 116

Skrutskie, M.F., Cutri, R.M., Stiening, R., Weinberg, M.D., Schneider, S., Carpenter, J.M., Beichman, C., Capps, R., Chester, T., Elias, J., Huchra, J., Liebert, J., Lonsdale, C., Monet, D.G., Price, S., Seitzer, P., Jarrett, T., Kirkpatrick, J.D., Gizis, J.E., Howard, E., Evans, T., Fowler, J., Fullmer, L., Hurt, R., Light, R., Kopan, E.L., Marsh, K.A., McCallon, H.L., Tam, R., Van Dyk, S. & Wheelock, S. (2006). The Two Micron All Sky Survey (2MASS). *AJ*, **131**, 1163–1183. 44

Smith, R.J., Longmore, S. & Bonnell, I. (2009). The simultaneous formation of massive stars and stellar clusters. *MNRAS*, **400**, 1775–1784. 12

Smith, R.J., Shetty, R., Stutz, A.M. & Klessen, R.S. (2012). Line Profiles of Cores within Clusters. I. The Anatomy of a Filament. *ApJ*, **750**, 64. 12

Sridharan, T.K., Williams, S.J. & Fuller, G.A. (2005). The Direct Detection of a (Proto)Binary/Disk System in IRAS 20126+4104. *ApJ*, **631**, L73–L76. 14

Stahler, S.W. & Palla, F. (2005). *The Formation of Stars*. 6

Stahler, S.W., Shu, F.H. & Taam, R.E. (1980). The evolution of protostars. I - Global formulation and results. *ApJ*, **241**, 637–654. 8

Stäuber, P., Doty, S.D., van Dishoeck, E.F. & Benz, A.O. (2005). X-ray chemistry in the envelopes around young stellar objects. *A&A*, **440**, 949–966. 120

Tamura, M. & Yamashita, T. (1992). Infrared morphology of mass outflow from GL 2591. *ApJ*, **391**, 710–718. 57

Tan, J.C. (2015). Comparison of Low-Mass and High-Mass Star Formation. *ArXiv e-prints*. 12

Tan, J.C., Beltrán, M.T., Caselli, P., Fontani, F., Fuente, A., Krumholz, M.R., McKee, C.F. & Stolte, A. (2014). Massive Star Formation. *Protostars and Planets VI*, 149–172. 12

Terebey, S., Shu, F.H. & Cassen, P. (1984). The collapse of the cores of slowly rotating isothermal clouds. *ApJ*, **286**, 529–551. 8

Tofani, G., Felli, M., Taylor, G.B. & Hunter, T.R. (1995). Exploring the engines of molecular outflows. Radio continuum and H_2_O maser observations. *A&AS*, **112**, 299. 116

Tomisaka, K. (2000). The Evolution of the Angular Momentum Distribution during Star Formation. *ApJ*, **528**, L41–L44. 8

Trinidad, M.A., Curiel, S., Cantó, J., D'Alessio, P., Rodríguez, L.F., Torrelles, J.M., Gómez, J.F., Patel, N. & Ho, P.T.P. (2003). Observations of Water Masers and Radio Continuum Emission in AFGL 2591. *ApJ*, **589**, 386–396. 56, 61, 116, 132, 136

Trinidad, M.A., Curiel, S., Migenes, V., Patel, N., Torrelles, J.M., Gómez, J.F., Rodríguez, L.F., Ho, P.T.P. & Cantó, J. (2005). Very Large Array Simultaneous 1.3 cm Continuum and H_2O Maser Observations toward IRAS 20126+4104. *AJ*, **130**, 2206–2211. 15

Trinidad, M.A., Curiel, S., Estalella, R., Cantó, J., Raga, A., Torrelles, J.M., Patel, N.A., Gómez, J.F., Anglada, G., Carrasco-González, C. & Rodríguez, L.F. (2013). Formation and evolution of the water maser outflow event in AFGL 2591 VLA 3-N. *MNRAS*, **430**, 1309–1323. 56

Ulrich, R.K. (1976). An infall model for the T Tauri phenomenon. *ApJ*, **210**, 377–391. 8, 73, 76

Urquhart, J.S., Busfield, A.L., Hoare, M.G., Lumsden, S.L., Clarke, A.J., Moore, T.J.T., Mottram, J.C. & Oudmaijer, R.D. (2007a). The RMS survey. Radio observations of candidate massive YSOs in the southern hemisphere. *A&A*, **461**, 11–23. 25

Urquhart, J.S., Busfield, A.L., Hoare, M.G., Lumsden, S.L., Oudmaijer, R.D., Moore, T.J.T., Gibb, A.G., Purcell, C.R., Burton, M.G. & Marechal, L.J.L. (2007b). The RMS survey. ^{13}CO observations of candidate massive YSOs in the southern Galactic plane. *A&A*, **474**, 891–901. 26

Urquhart, J.S., Busfield, A.L., Hoare, M.G., Lumsden, S.L., Oudmaijer, R.D., Moore, T.J.T., Gibb, A.G., Purcell, C.R., Burton, M.G., Maréchal, L.J.L., Jiang, Z. & Wang, M. (2008). The RMS survey. ^{13}CO observations of candidate massive YSOs in the northern Galactic plane. *A&A*, **487**, 253–264. 26

Urquhart, J.S., Hoare, M.G., Purcell, C.R., Lumsden, S.L., Oudmaijer, R.D., Moore, T.J.T., Busfield, A.L., Mottram, J.C. & Davies,

B. (2009). The RMS survey. 6 cm continuum VLA observations towards candidate massive YSOs in the northern hemisphere. *A&A*, **501**, 539–551. 25

Urquhart, J.S., Hoare, M.G., Lumsden, S.L., Oudmaijer, R.D., Moore, T.J.T., Mottram, J.C., Cooper, H.D.B., Mottram, M. & Rogers, H.C. (2012). The RMS survey: resolving kinematic distance ambiguities towards a sample of compact H II regions using H I absorption. *MNRAS*, **420**, 1656–1672. 26

van der Tak, F.F.S. & Menten, K.M. (2005). Very compact radio emission from high-mass protostars. II. Dust disks and ionized accretion flows. *A&A*, **437**, 947–956. 116

van der Tak, F.F.S., van Dishoeck, E.F., Evans, N.J., II, Bakker, E.J. & Blake, G.A. (1999). The Impact of the Massive Young Star GL 2591 on Its Circumstellar Material: Temperature, Density, and Velocity Structure. *ApJ*, **522**, 991–1010. 57, 111, 116, 120

van der Tak, F.F.S., Walmsley, C.M., Herpin, F. & Ceccarelli, C. (2006). Water in the envelopes and disks around young high-mass stars. *A&A*, **447**, 1011–1025. 24, 57, 110

van der Tak, F.F.S., Black, J.H., Schöier, F.L., Jansen, D.J. & van Dishoeck, E.F. (2007). A computer program for fast non-LTE analysis of interstellar line spectra. With diagnostic plots to interpret observed line intensity ratios. *A&A*, **468**, 627–635. 127

van Dishoeck, E.F. (2003). Chemical Changes During Star Formation: High vs. Low-mass YSOs. In C.L. Curry & M. Fich, eds., *SFChem 2002: Chemistry as a Diagnostic of Star Formation*, 201. 4

van Dishoeck, E.F. & Blake, G.A. (1998). Chemical Evolution of Star-Forming Regions. *ARA&A*, **36**, 317–368. 120

Vázquez-Semadeni, E., Kim, J., Shadmehri, M. & Ballesteros-Paredes, J. (2005). The Lifetimes and Evolution of Molecular Cloud Cores. *ApJ*, **618**, 344–359. 6

Viti, S., Collings, M.P., Dever, J.W., McCoustra, M.R.S. & Williams, D.A. (2004). Evaporation of ices near massive stars: models based on laboratory temperature programmed desorption data. *MNRAS*, **354**, 1141–1145. 142

Wang, K.S., van der Tak, F.F.S. & Hogerheijde, M.R. (2012). Kinematics of the inner thousand AU region around the young massive star AFGL 2591-VLA3: a massive disk candidate? *A&A*, **543**, A22. 59, 70, 71, 81, 109, 116, 120, 141, 143, 146, 147, 152

Wang, P., Li, Z.Y., Abel, T. & Nakamura, F. (2010). Outflow Feedback Regulated Massive Star Formation in Parsec-Scale Cluster-Forming Clumps. *ApJ*, **709**, 27–41. 12

Weingartner, J.C. & Draine, B.T. (2001). Dust Grain-Size Distributions and Extinction in the Milky Way, Large Magellanic Cloud, and Small Magellanic Cloud. *ApJ*, **548**, 296–309. 21, 84

Wheelwright, H.E., de Wit, W.J., Oudmaijer, R.D., Hoare, M.G., Lumsden, S.L., Fujiyoshi, T. & Close, J.L. (2012). Probing the envelopes of massive young stellar objects with diffraction limited mid-infrared imaging. *A&A*, **540**, A89. 14, 24, 30, 49

Whitney, B.A. (2011). Monte Carlo radiative transfer. *Bulletin of the Astronomical Society of India*, **39**, 101–127. 18

Whitney, B.A., Wood, K., Bjorkman, J.E. & Wolff, M.J. (2003). Two-dimensional Radiative Transfer in Protostellar Envelopes. I. Effects of Geometry on Class I Sources. *ApJ*, **591**, 1049–1063. 75

Whitney, B.A., Indebetouw, R., Bjorkman, J.E. & Wood, K. (2004). Two-Dimensional Radiative Transfer in Protostellar Envelopes. III. Effects of Stellar Temperature. *ApJ*, **617**, 1177–1190. 80

Wilcock, L.A., Kirk, J.M., Stamatellos, D., Ward-Thompson, D., Whitworth, A., Battersby, C., Brunt, C., Fuller, G.A., Griffin, M., Molinari, S., Martin, P., Mottram, J.C., Peretto, N., Plume, R., Smith, H.A. & Thompson, M.A. (2011). The initial conditions of high-mass star formation: radiative transfer models of IRDCs seen in the Herschel Hi-GAL survey. *A&A*, **526**, A159. 4

Wiles, B., Lo, N., Redman, M.P., Cunningham, M.R., Jones, P.A., Burton, M.G. & Bronfman, L. (2016). Scaled up low-mass star formation in massive star-forming cores in the G333 giant molecular cloud. *MNRAS*, **458**, 3429–3442. 24

Williams, J.P., Blitz, L. & McKee, C.F. (2000). The Structure and Evolution of Molecular Clouds: from Clumps to Cores to the IMF. *Protostars and Planets IV*, 97. 2, 3

Williams, S.J., Fuller, G.A. & Sridharan, T.K. (2005). The circumstellar environments of high-mass protostellar objects. II. Dust continuum models. *A&A*, **434**, 257–274. 23, 44, 48, 49, 76, 78, 113

Wolfire, M.G. & Cassinelli, J.P. (1987). Conditions for the formation of massive stars. *ApJ*, **319**, 850–867. 10

Wood, K., Wolff, M.J., Bjorkman, J.E. & Whitney, B. (2002). The Spectral Energy Distribution of HH 30 IRS: Constraining the Circumstellar Dust Size Distribution. *ApJ*, **564**, 887–895. 83, 84

Yorke, H.W. (1986). The dynamical evolution of H II regions - Recent theoretical developments. *ARA&A*, **24**, 49–87. 5

Yorke, H.W. & Sonnhalter, C. (2002). On the Formation of Massive Stars. *ApJ*, **569**, 846–862. 10, 13

Zhang, Q. (2005). Massive star disks. In R. Cesaroni, M. Felli, E. Churchwell & M. Walmsley, eds., *Massive Star Birth: A Crossroads of Astrophysics*, vol. 227 of *IAU Symposium*, 135–144. 54

Zhang, Y. & Tan, J.C. (2011). Radiation Transfer of Models of Massive Star Formation. I. Dependence on Basic Core Properties. *ApJ*, **733**, 55. 59

Zhang, Y., Tan, J.C. & McKee, C.F. (2013). Radiation Transfer of Models of Massive Star Formation. II. Effects of the Outflow. *ApJ*, **766**, 86. 59, 108

Zinnecker, H. & Yorke, H.W. (2007). Toward Understanding Massive Star Formation. *ARA&A*, **45**, 481–563. 1, 3